Alma Mater Studiorum – Università di Bologna

Dottorato di ricerca in
Fisica
Ciclo XXXIV

Settore Concorsuale: 02/A1 - Fisica Sperimentale delle Interazioni Fondamentali
Settore Scientifico disciplinare: FIS/01 - Fisica Sperimentale

Search for direct *CP* violation in charm neutral meson decays at LHCb

Presentata da: Serena Maccolini

Coordinatore Dottorato
Prof. Michele Cicoli

Supervisore
Dott. Stefano Perazzini

Co-supervisore
Prof. Angelo Carbone

Esame finale anno 2022

There is a crack in everything
That's how the light gets in

Anthem
Leonard Cohen, 1992

Abstract

A search for time-integrated violation of the *CP* symmetry, $\mathcal{A}^{CP}(K^-K^+)$, in the Cabibbo-suppressed $D^0 \to K^-K^+$ decays is performed at the LHCb detector using proton-proton collisions recorded from 2015 to 2018 at the centre of mass energy of 13 TeV. The data used corresponds to an integrated luminosity of 5.7 fb^{-1}. The flavour of the charm mesons is defined from the charge of the pion in $D^{*+} \to D^0\pi^+$ and $D^{*-} \to \overline{D}^0\pi^-$ decays. Nuisance asymmetries are constrained from $D^{*+} \to D^0(\to K^-\pi^+)\pi^+$, $D^+ \to K^0_S\pi^+$, $D^+ \to K^-\pi^+\pi^+$, $D_s^+ \to K^0_S K^+$ and $D_s^+ \to \phi\pi^+$ decays. The $\mathcal{A}^{CP}(K^-K^+)$ asymmetry is measured to be

$$\mathcal{A}^{CP}(K^-K^+) = [6.8 \pm 5.4\,(\text{stat}) \pm 1.6\,(\text{syst})] \cdot 10^{-4},$$

in agreement with the previous LHCb results and the current world average. This represents the world's most precise measurement of this quantity to date. Combining $\mathcal{A}^{CP}(K^-K^+)$ with the time-integrated *CP* asymmetry difference, $\Delta A_{CP} = \mathcal{A}^{CP}(K^-K^+) - \mathcal{A}^{CP}(\pi^-\pi^+)$, and the time-dependent *CP* asymmetry, ΔY, measured with $D^0 \to K^-K^+$ and $D^0 \to \pi^-\pi^+$ decays, the direct *CP* asymmetries in $D^0 \to K^-K^+$ and $D^0 \to \pi^-\pi^+$ decays, a^d_{KK} and $a^d_{\pi\pi}$, result to be

$$\begin{aligned} a^d_{KK} &= (7.7 \pm 5.7) \cdot 10^{-4}, \\ a^d_{\pi\pi} &= (23.2 \pm 6.1) \cdot 10^{-4}, \end{aligned}$$

where the errors include systematic and statistical uncertainties and the correlation between the two values is $\rho(a^d_{KK}, a^d_{\pi\pi}) = 0.88$. The values differ from zero for 1.4 and 3.8 standard deviations, respectively. In particular, $a^d_{\pi\pi}$ shows an evidence for direct *CP* violation in $D^0 \to \pi^-\pi^+$ decays.

In this thesis, a preliminary study regarding the performance evaluation for a future silicon tracker around the interaction region (Vertex Locator) for Upgrade-II is also reported. In particular, the possibility of using a 3D silicon sensor developed within the TimeSpot project is explored. Considering a preliminary parametrisation of the sensor with a time resolution per pixel of 50 ps, the track reconstruction efficiency of charged particles is estimated to be 97% while the fake track rate is 1.6%. Those preliminary results are not far from the current performance of the LHCb-Upgrade VELO detector and show the importance of time measurements for a vertex detector working in the High-Luminosity era.

Contents

Introduction

The current understanding of fundamental interactions between elementary particles is summarised in the Standard Model of particle physics. It has been developed from the 1960's onwards by many theoretical physicists on the basis of the quantum mechanics and quantum field theories developed in the 1920's. The Standard Model predictions have been challenged by many experiments and no significant discrepancy has been observed so far.

However, there are phenomena in Nature which are not described by the Standard Model. A series of open questions needs to be answered: How did antimatter particles disappear in the early Universe leading to the matter-antimatter asymmetry observed? What is the nature of dark matter and dark energy, which make up 95% of the energy in the Universe? How to incorporate a coherent description of gravity into a quantum-mechanical framework? In general, the Standard Model alone has not any response. In particular, it can not explain the inflationary epoch.

Answering some of these questions is the main goal of the Large Hadron Collider (LHC), the biggest for size, price, and energy particle accelerator built in the world. The discovery of the Higgs boson by the ATLAS and CMS experiments was one of the biggest milestones in particle physics as it was the last missing particle of the Standard Model. These experiments are designed to measure high p_{T} decay products that could indicate the direct production of new particles. This is a complementary approach with respect to the one used by the LHCb experiment. It measures the existence of such new particles indirectly, through their virtual quantum effects. One of the main goals of the LHCb experiment is the study of *CP*-violating effects in the decay of charm and beauty hadrons. *CP* violation refers to differences between particle and antiparticle decays and it is allowed by the Standard Model. However, unexpected results could point to new physics. In this context, the study of the charm physics is particularly interesting as it forms the only probe of *CP* violation in the up-type quark sector.

Because of the required experimental precision, *CP* violation in the charm sector has only been observed recently [1]. This result has lead to a lively discussion in the theory community, where it is debated whether the magnitude of *CP* violation is compatible with the Standard Model. In fact, precise estimates are plagued by long-distance physics contributions. Moreover, it renewed the interest in charm physics from the experimental side.

The discovery measurement considers the difference of two time-integrated *CP* asymmetries of Cabibbo suppressed D^0 decays, $\Delta A_{CP} = \mathcal{A}^{CP}(D^0 \to K^-K^+) - \mathcal{A}^{CP}(D^0 \to \pi^-\pi^+)$. The result is $\Delta A_{CP} = (-15.4 \pm 2.9) \cdot 10^{-4}$ corresponding to a difference from zero of more than five standard deviations. The work presented in this thesis reports the measurement of the individual *CP* asymmetry in $D^0 \to K^-K^+$, *i.e.* $\mathcal{A}^{CP}(K^-K^+)$, with the full dataset of events collected by LHCb during Run 2. Finally, the direct *CP* asymmetries in $D^0 \to K^-K^+$ and $D^0 \to \pi^-\pi^+$ decays, a^d_{KK} and $a^d_{\pi\pi}$, are obtained from the combination of $\mathcal{A}^{CP}(K^-K^+)$ with the time-integrated *CP* asymmetry difference ΔA_{CP} and the time-dependent *CP* asymmetry ΔY.

The expected uncertainty on $\mathcal{A}^{CP}(K^-K^+)$ at the end of Run 2 is about $7 \cdot 10^{-4}$. This value is further improved in the current analysis thanks to the combination of more control channels to extract the *CP* asymmetry from the raw asymmetry measured in $D^0 \to K^-K^+$ decays. Moreover, in this novel strategy the systematic error is kept under control and the uncertainty of the measurement is statistically dominated. This will allow to easily reproduce the measurement on the future data samples that are being collected by the LHCb experiment.

LHCb is now transitioning for an upgraded version of the detector (LHCb Upgrade) aimed to work at increased luminosity and energy in the center of mass. Moreover, a possible LHCb Upgrade-II of the detector to begin operation after Run 4, is also considered. The success in the performance of the Vertex Locator in the extremely harsh scenario of the High-Luminosity LHC is essential to achieve important results. In particular, the Vertex Locator should be able to reconstruct (and distinguish) efficiently and accurately primary and decay vertices. The introduction of the time information in the design for the future VELO has as the main goal to improve the primary vertex separation together with the correct assignment of the primary vertex to "long-living" hadrons.

Recently, the TimeSpot collaboration has developed an interesting 3D silicon sensor with a per-pixel resolution of about 15 ps, suited for high radiation environments with the goal of being applied in future 4D tracking devices. In this thesis, a preliminary performance study on a possible Upgrade-II Vertex Locator using the TimeSpot sensor is also reported. This represents a first step towards the introduction of time information in a LHCb detector.

The thesis is structured as follows. Chapter 1 reports a brief description of the theoretical aspects related to the measurement of *CP* violation in charm decays. In Chapter 2, the LHCb detector, the experimental apparatus which provided the data used for the experimental result, is described. The measurement of $\mathcal{A}^{CP}(K^-K^+)$ is explained in Chapter 3 and includes the final combination with all the LHCb measurements for the calculation of the direct *CP* violation parameters. The presented results are still blind, since the analysis has not finished the internal review of the LHCb collaboration. Chapter 4 is dedicated to the study of the Vertex Locator performances in Upgrade-II scenario with

the TimeSpot sensor. Conclusions are discussed in the last chapter.

Chapter 1

CP violation in charm decays

1.1 Historical overview

The concept of symmetry holds a special place in particle theory as the recognition of a symmetry gives insight into the fundamental physics. Three discrete symmetries are considered in particle physics: parity, charge and time reversal. Parity, or space inversion, is the reflection in the origin of the space coordinates of a particle (*i.e.* the three space dimensions x, y and z become, respectively, $-x$, $-y$ and $-z$). Charge-conjugation (C) is a mathematical operation that transforms a particle into an antiparticle, inverting the sign of all charges (such as electric charge) while leaving unaffected all other quantities (and in particular space-time related ones such as position, momentum and spin). It implies that every charged particle has an oppositely charged antimatter counterpart, while the antiparticle of an electrically neutral particle may be identical to the particle, as in the case of the neutral π meson. The time reversal (T) represents the inversion of time coordinate t into $-t$. In this thesis, the role of CP violation, which is the violation of the combined conservation laws associated with charge conjugation and parity by the weak nuclear force, will be underlined.

Before 1950s, it was assumed that the P, C and T operators were symmetric for the electromagnetic, strong and weak interactions. However, a series of discoveries brought the physicists to alter significantly their assumption. In particular, the theoretical physicists C. N. Yang and T. D. Lee, in 1956, showed that there was no evidence supporting parity invariance in weak interactions [2]. Experiments conducted in the late 1950s in both nuclear and pion's beta decay [3, 4] verified that parity was violated. Moreover, they revealed that charge conjugation symmetry was also broken for these decay processes. A subsequent experiment made by Goldhaber et al. [5], in 1958, showed that the neutrino is left-handed, *i.e.* its spin is anti-parallel with respect to its momentum. It was soon pointed out that the independent application of P or C operators to the left-handed neutrino (ν_L) led to physical states not observed in nature, right-handed

neutrino (ν_R) or left-handed anti-neutrino ($\bar{\nu}_L$), respectively. However, the application of the *CP* operator to the ν_L led to the observed $\bar{\nu}_R$. For this reason it was thought that the *CP* symmetry was indeed conserved. This point was supported by the local T invariance derived from Mach's principle and from the CPT invariance that is natural in Lorentz–invariant quantum field theories [6, 7], *i.e.* no *CP* violation is then allowed if T violation is not found.

Subsequently, in 1964, Cronin and Fitch observed long lived neutral K mesons, usually decaying into three pions, a *CP* eigenstate with negative eigenvalue, decaying into two pions, a *CP* eigenstate with positive eigenvalue. This proved that also the *CP* symmetry was not conserved by weak interactions [8]. At that time, the C and P symmetry violations were incorporated in the basic structure of the unified electroweak theory by representing the left–handed and the right–handed fermions as a doublet and a singlet of the symmetry group $SU(2)_L \times U(1)_Y$. The theory was originally proposed by S. Glashow, S. Weinberg and A. Salam [9–11] to describe the leptons and then extended to the quarks by Nicola Cabibbo, in 1963, by introducing a mixing angle θ_C (the so-called Cabibbo angle). The hypothesis that the state that couples to the up quark via charged-current weak interaction is a superposition of down-type quarks (*i.e.* $d' = d\cos\theta_C + s\sin\theta_C$), arose to preserve the universality of the weak interaction [12]. Few years later, in 1970, Glashow, J. Iliopoulos and L. Maiani [13] proposed to explain the non-observation of flavour-changing neutral current (FCNC) processes with the existence of a fourth quark, the charm, discovered in 1974 [14, 15]. Before 1973, the model foresaw *CP* and T invariance with no explanation of the observed neutral K mesons phenomenology. This was an open problem until M. Kobayashi and T. Maskawa [16] noticed that *CP* violation could be allowed in the electroweak model, by the presence of a single unremovable complex phase in the charged current interactions of quarks, if there were a third generation of quarks. The existence of the bottom quark was established a few years later in 1977 [17], while the sixth quark, the top, was discovered later in 1995 [18, 19].

The Cabibbo-Kobayashi-Maskawa formalism (CKM) has proven to be very successful in explaining and predicting *CP* violation in different decays. Since its discovery in the K meson system in 1964, a systematic study of the *CP* violation phenomenon has been carried out by a number of experiments in beauty and charm decays. Historically, *CP* violation has been discovered in a indirect way through the study of flavour oscillations of neutral mesons. The existence of *CP* violation in the decays of B^0 mesons was demonstrated by the BaBar and Belle experiments in 2011 [20, 21] while the first observation of *CP* violation in B_s^0 decays was reported in 2013 by the LHCb collaboration [22]. The first evidence for $D^0 - \overline{D}^0$ mixing was reported in 2007 by the B-factories [23, 24] while *CP* violation in the charm sector has been observed in 2019 by the LHCb collaboration [1]. This result has lead to a lively discussion in the theory community, where it is debated whether the magnitude of *CP* violation is compatible with the Standard Model (see Section 1.5.2).

The phenomenology of *CP* violation is particularly interesting since it was indicated

as one of the necessary conditions to explain in a dynamical way the generation of the matter-antimatter asymmetry observed in the Universe [25]. Today, the Standard Model (SM) of particle physics encompasses only two sources of *CP* violation. The first originates from the strong-interaction Lagrangian [26]. However, upper bounds of the electric dipole moment of the neutron constrain the coefficient of this *CP*-violating Lagrangian term to be less than 10^{-10} [27]. This is referred to as the "strong *CP* problem", which has motivated the proposal of the existence and the search of new particles or interactions such as the axion. The only source of *CP* violation measured so far is a single complex phase in the CKM matrix, that quantifies the interaction of the W^- boson with quarks. However, while the CKM paradigm has been tested successfully in the decay of down-type quarks in K and B mesons, it is too small to explain the observed matter-antimatter asymmetry [28–30], suggesting the existence of additional sources of *CP* violation beyond the SM. One possible source, which will be tested in the next few years, is *CP* violation in the oscillation probabilities of neutrinos [31]. Another possibility is given by *CP*-violating interactions of new particles, which can influence the decay of SM particles via virtual interactions, even in the case that their masses are much larger than those that can be currently produced directly at colliders like the Large Hadron Collider at CERN [32]. The latter category can be tested with high-precision measurements of *CP* violation in the decay of SM particles. The measurement presented in this thesis falls into this experimental category. The background information necessary to understand the unique role and potential of searches of *CP* violation in the decay of the charm mesons in the context of precision measurements of the SM is provided in the next sections.

1.2 *CP* violation in the Standard Model and beyond

The SM describes the interactions between elementary particles, that form the fundamental building blocks of matter. The theory describes these elementary particles interacting via the strong, electromagnetic and weak forces while the gravitational force is excluded. The strong interaction binds the constituents of nucleons and forms a nucleus out of them. The electromagnetic interaction holds electrons and nuclei together to form atoms, molecules and solid state bodies. Finally, the weak interaction describes decays of particles leading, for example, to radioactivity.

Within the mathematical framework of the SM, particles and forces are the observable manifestations of scalar, vector or spinor fields which interact with each other according to a well-defined set of rules. The quanta of the scalar and vector fields are bosons, which are defined by their integer spin quantum number and which "carry" forces from one place to another. The bosons include the scalar Higgs particle, the strong force vectors, called gluons, and the electroweak vectors $W^{\pm}$, Z^0, and γ. The quanta of the spinor fields are fermions, which have half-integer spins and are categorised as quarks or

leptons. The leptons can be observed directly, and comprise the electron (e), the muon (μ), the tau (τ), and their neutrinos ($\nu_{e,\mu,\tau}$). The quarks do not exist apart[1], but make up all other observable massive particles, which are called hadrons. Quarks come in six flavours: up (u), down (d), strange (s), charm (c), bottom (b) and top (t). Quarks and leptons (except neutrinos) are charged, and each particle has a partner of opposite charge, which is referred to as its antiparticle. Fundamental particles acquire their masses via the Higgs mechanism. The exceptions are the photon and gluon, which are massless, and perhaps the neutrinos[2]. Most of the mass of the more common composite hadrons such as the proton and neutron results from the strong forces binding their constituent quarks together, rather than from their masses.

Mathematically, the Standard Model is defined as a model of elementary particles and their interactions by the local invariance of the Lagrangian with respect to the transformation of the symmetry group

$$G_{SM} = SU(3)_C \times SU(2)_L \times U(1)_Y, \tag{1.1}$$

where the $SU(3)_C$ is the non-abelian algebra of the strong forces and the electroweak part is described by $SU(2)_L \times U(1)_Y$ through the Glashow–Weinberg–Salam theory [9–11]. Fermions are divided in three generations, each consisting of five representations

$$Q^I_{Li}(3,2)_{+1/6}, \quad u^I_{Ri}(3,1)_{+2/3}, \quad d^I_{Ri}(3,1)_{-1/3}, \quad L^I_{Li}(1,2)_{-1/2}, \quad \ell^I_{Ri}(1,1)_{-1}. \tag{1.2}$$

The notations mean that, for example, the left-handed quarks, Q^I_L, are in a triplet (3) of the $SU(3)_C$ group, a doublet (2) of $SU(2)_L$ and carry hypercharge $Y = 2(Q_{EM} - T_3) = +1/6$. The super-script I denotes interaction eigenstates. The sub-script $i = 1, 2, 3$ is the flavour (or generation) index. The Higgs boson is represented as the scalar multiplet

$$\phi(1,2)_{+1/2}, \tag{1.3}$$

defined as

$$\phi = \begin{pmatrix} \phi^+ \\ \phi^0 \end{pmatrix}, \tag{1.4}$$

which assumes the vacuum expectation value (VEV)

$$\langle \phi \rangle = \begin{pmatrix} 0 \\ \frac{v}{\sqrt{2}} \end{pmatrix}. \tag{1.5}$$

Thus, is often parametrized as

$$\phi = e^{i\frac{\sigma_i}{2}\theta_i} \begin{pmatrix} 0 \\ \frac{v+H^0}{\sqrt{2}} \end{pmatrix}, \tag{1.6}$$

[1]The only exception is the top quark, which may decay via electroweak interaction before it hadronizes.

[2]As it will be seen in the next pages, neutrinos are massless in the SM. However, the observation of neutrino mixing [33] demonstrates that this is not the case.

where σ_i are the Pauli's matrices, θ_i are three real fields and H^0 is the Higgs boson field. The non-zero vacuum expectation generates a spontaneous breaking of the gauge group

$$G_{SM} \to SU(3)_C \times U(1)_{EM}. \tag{1.7}$$

The Standard Model Lagrangian, $\mathcal{L}_{SM}$, is the most general renormalizable Lagrangian that is consistent with the gauge symmetry G_{SM} of Eq. 1.1. It can be divided to four parts:

$$\mathcal{L}_{SM} = \mathcal{L}_{kinetic} + \mathcal{L}_{gauge} + \mathcal{L}_{Higgs} + \mathcal{L}_{Yukawa}. \tag{1.8}$$

The kinetic term has the form $i\bar{\psi}\gamma_\mu D^\mu \psi$ where γ_μ are the Dirac matrices, ψ and $\bar{\psi} = \psi^\dagger\gamma^0$ are a Dirac spinor and its adjoint. D^μ is the covariant derivative which has replaced ∂^μ in order to maintain gauge invariance and it is defined as

$$D^\mu = \partial^\mu + ig_s G_a^\mu L_a + igW_b^\mu T_b + ig'B^\mu Y. \tag{1.9}$$

Here G_a^μ are the eight gluon fields, W_b^μ the three weak interaction bosons and B^μ the single hypercharge boson. The L_a's are $SU(3)_C$ generators (the 3×3 Gell-Mann matrices $1/2\,\lambda_a$ for triplets, 0 for singlets), the T_b's are $SU(2)_L$ generators (the 2×2 Pauli matrices $1/2\,\tau_b$ for doublets, 0 for singlets), and Y are the $U(1)_Y$ charges. For example, for the left-handed quarks Q_L^I, one has

$$\begin{aligned}\mathcal{L}_{kinetic}(Q_L) &= i\overline{Q_{Li}^I}\gamma_\mu D^\mu Q_{Li}^I, \\ &= i\overline{Q_{Li}^I}\gamma_\mu \left(\partial^\mu + \frac{i}{2}g_s G_a^\mu \lambda_a + \frac{i}{2}gW_b^\mu \tau_b + \frac{i}{6}g'B^\mu\right) Q_{Li}^I,\end{aligned} \tag{1.10}$$

that represents the free propagation of the fermion and the interactions with a generic field A^μ (*e.g.* B^μ) in the form of a charged current $-J_\mu$ (*e.g.* $-\frac{1}{6}g'\overline{Q_{Li}^I}\gamma_\mu Q_{Li}^I$). This part of the interaction Lagrangian is always *CP* conserving.

The second term describes the self-interactions of the gauge fields and is written as

$$-\mathcal{L}_{gauge} = \frac{1}{4}\left(G_a^{\mu\nu}G_{a\,\mu\nu} + W_b^{\mu\nu}W_{b\,\mu\nu} + B^{\mu\nu}B_{\mu\nu}\right), \tag{1.11}$$

where $G_a^{\mu\nu}$, $W_b^{\mu\nu}$ and $B_{\mu\nu}$ are the Yang-Mills tensors, defined as

$$\begin{aligned} G_a^{\mu\nu} &= \partial_\mu G_a^\nu - \partial_\nu G_a^\mu + g_s f^{abc} G_b^\mu G_c^\nu, \\ W_b^{\mu\nu} &= \partial_\mu W_b^\nu - \partial_\nu W_b^\mu + g\varepsilon^{bcd} W_c^\mu W_d^\nu, \\ B^{\mu\nu} &= \partial_\mu B^\nu - \partial_\nu B^\mu. \end{aligned} \tag{1.12}$$

Although there exists an additional term (*i.e.* a gauge-invariant and renormalizable operator) that could introduce *CP* violation, $\mathcal{L}_{gauge}$ is assumed to be *CP* invariant [34].

The Higgs potential, which describes the scalar self-interactions, is given by

$$\mathcal{L}_{Higgs} = \mu^2\phi^\dagger\phi - \lambda(\phi^\dagger\phi)^2, \tag{1.13}$$

where λ is the Higgs self-coupling strength and $\mu = v\sqrt{\lambda}$. For the Standard Model scalar sector, where there is a single doublet, this part of the Lagrangian is also *CP* conserving. For extended scalar sector, such as that of a two Higgs doublet model, $\mathcal{L}_{Higgs}$ can be *CP* violating. Even in case that it is *CP* symmetric, it may lead to spontaneous *CP* violation.

The Yukawa interactions between the fermions and the scalar field are given by

$$-\mathcal{L}_{Yukawa} = +Y^d_{ij}\overline{Q^I_{Li}}\phi d^I_{Rj} + Y^u_{ij}\overline{Q^I_{Li}}\tilde{\phi}u^I_{Rj} + Y^\ell_{ij}\overline{L^I_{Li}}\phi\ell^I_{Rj} + h.c., \tag{1.14}$$

where $\tilde{\phi} = i\sigma_2\phi^\dagger$, Y^f are 3×3 complex matrices and *h.c.* stands for the hermitian conjugate terms. This part of the Lagrangian is, in general, *CP* violating as further described.

After the electroweak symmetry breaking by a non–zero vacuum expectation value v of the Higgs field (see Eq. 1.5)), the Yukawa terms in Eq. 1.14 give rise (upon the replacement $\mathfrak{Re}(\phi^0) \to (v+H^0)/\sqrt{2}$) to the mass matrices of quarks and charged leptons

$$-\mathcal{L}_M = (M_d)_{ij}\overline{d^I_{Li}}d^I_{Rj} + (M_u)_{ij}\overline{u^I_{Li}}u^I_{Rj} + (M_\ell)_{ij}\overline{\ell^I_{Li}}\ell^I_{Rj} + h.c., \tag{1.15}$$

where $M_f = \frac{v}{\sqrt{2}}Y^f$ and the $SU(2)_L$ doublets are decomposed into their components

$$Q^I_{Li} = \begin{pmatrix} u^I_{Li} \\ d^I_{Li} \end{pmatrix}, \quad L^I_{Li} = \begin{pmatrix} \nu^I_{Li} \\ \ell^I_{Li} \end{pmatrix}. \tag{1.16}$$

Since the SM neutrinos have no Yukawa interactions, they are predicted to be massless[3].

The mass basis corresponds, by definition, to diagonal mass matrices. One can always find unitary matrices V_{fL} and V_{fR} such that

$$V_{fL}M_fV^\dagger_{fR} = M^{diag}_f, \tag{1.17}$$

with M^{diag}_f diagonal and real. The mass eigenstates are then identified as

$$\begin{aligned} d_{Li} &= (V_{dL})_{ij}d^I_{Lj}, \quad & d_{Ri} &= (V_{dR})_{ij}d^I_{Rj}, \\ u_{Li} &= (V_{uL})_{ij}u^I_{Lj}, \quad & u_{Ri} &= (V_{uR})_{ij}u^I_{Rj}, \\ \ell_{Li} &= (V_{\ell L})_{ij}\ell^I_{Lj}, \quad & \ell_{Ri} &= (V_{\ell R})_{ij}\ell^I_{Rj}, \\ \nu_{Li} &= (V_{\nu L})_{ij}\nu^I_{Lj}. \end{aligned} \tag{1.18}$$

[3]This is mere a consequence of the fact that in the SM there are no "sterile" right–handed neutrinos, $\nu^I_{Ri}(1,1)_0$, thus it is impossible to produce Dirac mass terms of the form $\bar{\nu}^I_{Li}\nu^I_{Ri}$. Therefore, the established observations of neutrino masses [33] necessarily call for an extension of the Standard Model.

Since the SM neutrinos are massless, $V_{\nu L}$ is arbitrary.

The Lagrangian of charged current interactions (that are the interactions of the charged $SU(2)_L$ gauge bosons $W^{\pm}_{\mu} = \frac{1}{\sqrt{2}}(W^1_{\mu} \mp iW^2_{\mu})$) for quarks, described by Eq. 1.10 in the interaction basis, have a different form in the mass basis:

$$-\mathcal{L}_{W^{\pm}} = \frac{g}{\sqrt{2}} \overline{u_{Li}} \gamma^{\mu} (V_{uL} V^{\dagger}_{dL})_{ij} d_{Lj} W^{+}_{\mu} + h.c.. \tag{1.19}$$

The unitary 3×3 matrix,

$$V_{CKM} = V_{uL} V^{\dagger}_{dL}, \quad (V_{CKM} V^{\dagger}_{CKM} = 1), \tag{1.20}$$

is the Cabibbo-Kobayashi-Maskawa (CKM) mixing matrix for quarks [12, 16]. By convention, the elements of V_{CKM} are written as follows

$$V_{CKM} = \begin{pmatrix} V_{ud} & V_{us} & V_{ub} \\ V_{cd} & V_{cs} & V_{cb} \\ V_{td} & V_{ts} & V_{tb} \end{pmatrix}. \tag{1.21}$$

A unitary $n \times n$ matrix depends on n^2 real independent parameters. However, regarding the CKM matrix, $2n-1$ parameters out of n^2 can be eliminated through the rephrasing of the n up-type and n down-type fermion fields (*i.e.* changing all fermions by the same phase obviously does not affect V_{CKM}), yielding to $(n-1)^2$ physical parameters: $n(n-1)/2$ real angles and $(n-1)(n-2)/2$ complex phases. For $n = 2$, *i.e.* two families, there is just one mixing angle that yields the Cabibbo matrix

$$V_C = \begin{pmatrix} \cos\theta_C & \sin\theta_C \\ -\sin\theta_C & \cos\theta_C \end{pmatrix}. \tag{1.22}$$

For $n = 3$, there are instead four physical parameters, namely three Euler angles and one phase δ. It is the latter that provides the gateway for *CP* violation (*i.e.* $\mathcal{L}_W \neq CP\mathcal{L}_W(CP)^{\dagger}$. In the standard parametrization, the elements of the CKM matrix are written as follows:

$$V_{CKM} = \begin{pmatrix} c_{12}c_{13} & s_{12}c_{13} & s_{13}e^{-i\delta} \\ -s_{12}c_{23} - c_{12}s_{23}s_{13}e^{i\delta} & c_{12}c_{23} - s_{12}s_{23}s_{13}e^{i\delta} & s_{23}c_{13} \\ s_{12}s_{23} - c_{12}c_{23}s_{13}e^{i\delta} & -c_{12}s_{23} - s_{12}c_{23}s_{13}e^{i\delta} & c_{23}c_{13} \end{pmatrix}, \tag{1.23}$$

where $c_{ij} \equiv \cos\theta_{ij}$, $s_{ij} \equiv \sin\theta_{ij}$ and θ_{ij} are the three real mixing parameters.

As a result of the fact that V_{CKM} is not diagonal, the $W^{\pm}$ gauge boson couple also to quark (mass eigenstates) of different generations. Within the Standard Model, this is the only source of *flavour-changing* interactions. In principle, there could be additional sources of flavour mixing (and *CP* violation) in the lepton sector and in Z^0 interactions, but within the Standard Model context this does not happen.

The current knowledge of the modules of the CKM matrix elements, as obtained by Particle Data Group [31] using the prescription of Refs. [35, 36], is the following:

$$V_{CKM} = \begin{pmatrix} 0.97401 \pm 0.00011 & 0.22650 \pm 0.00048 & 0.00361^{+0.00011}_{-0.00009} \\ 0.22636 \pm 0.00048 & 0.97320 \pm 0.00011 & 0.04053^{+0.00083}_{-0.00061} \\ 0.00854^{+0.00023}_{-0.00016} & 0.03978^{+0.00082}_{-0.00060} & 0.999172^{+0.00024}_{-0.00035} \end{pmatrix}. \tag{1.24}$$

The observed hierarchy $|V_{ub}| << |V_{cb}| << |V_{us}|$, $|V_{cd}| << 1$ allows to expand V_{CKM} in powers of $\lambda = |V_{us}| = \sin\theta_C$, as firstly realized by Wolfenstein [37]. The expansion up to $\mathcal{O}(\lambda^3)$ is given by:

$$V_{CKM} = \begin{pmatrix} 1 - \frac{\lambda^2}{2} & \lambda & A\lambda^3(\rho - i\eta) \\ -\lambda & 1 - \frac{\lambda^2}{2} & A\lambda^2 \\ A\lambda^3(1 - \rho - i\eta) & -A\lambda^2 & 1 \end{pmatrix} + \mathcal{O}(\lambda^4). \tag{1.25}$$

where $\lambda \approx 0.23$, $A \approx 0.82$, $\rho \approx 0.12$, $\eta \approx 0.36$ [31] are the four mixing parameters. In such representation, one clearly sees that the CKM matrix is a very special unitary matrix. It is almost diagonal and symmetric, and the matrix elements get smaller moving away from the diagonal. The weak decays are classified into Cabibbo favoured (CF), Cabibbo suppressed (CS) or double Cabibbo suppressed (DCS) decays, depending on the lowest power of λ that appears in any of their decay amplitudes being zero, one or two, respectively.

1.2.1 *CP* violation in meson decays

Having introduced these preliminary notions, the conditions of observing *CP* violation in hadron decays can be presented. Let us consider the decay amplitudes of an initial hadron, whose state is denoted by $|D\rangle$, into a general final state $|f\rangle$, and its *CP*-conjugate amplitude, describing the decay of its antiparticle into the *CP*-conjugated final state,

$$A_f \equiv \langle f|\mathcal{H}|D\rangle, \quad \bar{A}_{\bar{f}} \equiv \langle \bar{f}|\mathcal{H}|\overline{D}\rangle, \tag{1.26}$$

where $\mathcal{H}$ is the effective Hamiltonian governing the decay. In general, two types of phases can enter in the amplitudes contributing to the transitions of Eq. 1.26. The *strong phases* that do not change their sign under *CP* transformation, while *weak phases* do. This is a consequence of the observation that all phases due to strong interactions, which arise for example from rescattering[4] processes, are invariant under *CP* transformations. Conversely, the only measured source of *CP*-odd phases in the SM is given by the complex phase δ of the CKM matrix, and thus pertains to the weak interaction. In fact, if a given matrix element V^{ij}_{CKM} appears in A_f, the corresponding element entering in $\bar{A}_{\bar{f}}$ is seen from Eq. 1.19 to be $(V^{ij}_{CKM})^*$, which is obtained from V^{ij}_{CKM} with the substitution

[4]Non-perturbative quantum-chromo dynamics (QCD) interactions involving on-shell particles.

$\delta \to -\delta$. In quantum mechanics, the strong and weak phases of an amplitude are not observable, since only the amplitudes magnitude and the phase differences between different amplitudes are. However, most decay processes receive contributions from multiple amplitudes,

$$A_f = \sum_j |A_j| e^{i(\delta_j + \phi_j)}, \qquad \bar{A}_{\bar{f}} = \sum_j |A_j| e^{i(\delta_j - \phi_j)}, \tag{1.27}$$

where δ_j and ϕ_j are the strong and weak phases, respectively. *CP* relates A_f and $\bar{A}_{\bar{f}}$ and any violation is expressed as a non-zero value of the *CP* asymmetry, defined as

$$\mathcal{A}_{CP} = \frac{|A_f|^2 - |\bar{A}_{\bar{f}}|^2}{|A_f|^2 + |\bar{A}_{\bar{f}}|^2}. \tag{1.28}$$

CP violation appears as a result of interference among various terms in the decay amplitude. In fact, to observe *CP* violation there must be a contribution from at least two processes with both different weak and strong phases in order to have a non vanishing interference term

$$|A_f|^2 - |\bar{A}_{\bar{f}}|^2 = -2 \sum_{i,j} |A_i||A_j| \sin(\delta_i - \delta_j) \sin(\phi_i - \phi_j). \tag{1.29}$$

The size of *CP* violation is determined by the differences of the phases, as well by the ratio of the product of the magnitudes of the amplitudes responsible of *CP* violation in numerator of Eq. 1.28 to the squared magnitude of the largest amplitudes in the denominator,

$$|A_f|^2 + |\bar{A}_{\bar{f}}|^2 = \sum_i |A_i|^2 + \sum_{i \neq j} |A_i||A_j| \cos(\delta_i - \delta_j) \cos(\phi_i - \phi_j). \tag{1.30}$$

Although *CP* violation can be measured in the decay of many particles, neutral flavoured meson decays are enriched by the possibility of having particle-antiparticle transitions. For a better understanding of this phenomenology, the mixing of neutral mesons is described in the next section.

1.3 Mixing of neutral mesons

In the SM there are exactly four neutral mesons (plus their antiparticles) that are unable to decay into lighter particles via the electromagnetic or strong interaction, namely the K^0 ($d\bar{s}$), D^0 ($c\bar{u}$), B^0 ($d\bar{b}$) and B_s^0 ($s\bar{b}$) mesons. The flavour eigenstates listed above are not mass eigenstates of the effective Hamiltonian $\mathcal{H}$ that governs their time evolution. As a consequence, flavoured neutral mesons have a non-zero probability of oscillating into their antiparticles via a $\Delta F = 2$ transition, which changes their flavour quantum numbers

by two units, before decaying. This phenomenon is commonly named as *mixing*. This section presents the formalism to describe the evolution of a generic flavoured neutral meson M^0, both employing the standard phenomenological parametrisation [31] and the theoretical parametrisation [38, 39]. Finally, the mixing phenomelogy of the four flavoured neutral mesons is briefly described.

1.3.1 Formalism

Let us consider an initial state that is a pure superposition of the neutral flavour eigenstates M^0 and $\overline{M}^0$ where M^0 stands for K^0, D^0, B^0 or B_s^0, at time equal to zero,

$$|\psi(0)\rangle = a(0)|M^0\rangle + b(0)|\overline{M}^0\rangle. \tag{1.31}$$

The time evolution of this state is determined by the Schrödinger equation,

$$i\frac{d}{dt}|\psi(t)\rangle = \mathcal{H}|\psi(t)\rangle, \tag{1.32}$$

where $\mathcal{H}$ is the Hamiltonian governing its dynamics and $|\psi(t)\rangle$ is a linear superposition of M^0, $\overline{M}^0$ and all the final states $|f_k\rangle$ in which these two mesons can decay,

$$|\psi(t)\rangle \equiv a(t)|M^0\rangle + b(t)|\overline{M}^0\rangle + \sum_k c_k(t)|f_k\rangle. \tag{1.33}$$

If the times t under consideration are much larger than the typical time scale of the strong interaction, the problem can be solved with a simplified formalism using the Wigner-Weisskopf approximation [40]. The evolution of the state in the $M^0 - \overline{M}^0$ subspace is described with a 2×2 effective Hamiltonian $\mathbf{H}$,

$$i\frac{d}{dt}\begin{pmatrix} a(t) \\ b(t) \end{pmatrix} = \begin{pmatrix} H_{11} & H_{12} \\ H_{21} & H_{22} \end{pmatrix}\begin{pmatrix} a(t) \\ b(t) \end{pmatrix}. \tag{1.34}$$

This Hamiltonian is non-hermitian, reflecting the fact that the probability is not conserved in the $M^0 - \overline{M}^0$ subspace (the two mesons can decay). However, it can be convenient splitting the Hamiltonian into a Hermitian and an anti-Hermitian part,

$$\mathbf{H} = \mathbf{M} - \frac{i}{2}\mathbf{\Gamma}, \tag{1.35}$$

where $\mathbf{M} \equiv (\mathbf{H} + \mathbf{H}^\dagger)/2$ and $\mathbf{\Gamma} \equiv i(\mathbf{H} - \mathbf{H}^\dagger)$ are the hermitian mass and decay matrices, which describe dispersive transitions through virtual (off-shell) intermediate states, and absorptive transitions through real (on-shell) intermediate states, respectively. In general, $\mathbf{H}$ is defined by eight free parameters and if the interactions described by $\mathbf{H}$ are invariant under some combinations of discrete transformations, further relations among

the matrix elements of $\mathbf{M}$ and $\mathbf{\Gamma}$ hold. The CPT invariance is assumed in the following and implies $M_{11} = M_{22} \equiv M$ and $\Gamma_{11} = \Gamma_{22} \equiv \Gamma$. Under this assumption, which is motivated by the central role of the CPT invariance in the formulation of the quantum field theory and by the conservation of the CPT symmetry in all measurements performed to date, the expressions to describe the M^0 mixing are greatly simplified.

Phenomenological parametrisation

The normalised eigenstates of $\mathbf{H}$ are given by

$$|M_{1,2}\rangle \equiv p|M^0(t)\rangle \pm q|\bar{M}^0(t)\rangle, \tag{1.36}$$

where p and q are complex numbers satisfying $|p|^2 + |q|^2 = 1$ and

$$\left(\frac{p}{q}\right) = \frac{H_{21}}{H_{12}} = \frac{M_{12}^* - i/2\Gamma_{12}^*}{M_{12} - i/2\Gamma_{12}}. \tag{1.37}$$

As the matrix $\mathbf{H}$ is not hermitian, $|M_1\rangle$ and $|M_2\rangle$ are not necessary orthogonal. These interaction eigenstates evolve according to $|M_{1,2}\rangle = e^{-\omega_{1,2}t}|M_{1,2}(0)\rangle$, where the eigenvalues $\omega_{1,2} \equiv \omega_0 \mp 1/2\Delta\omega$ are conveniently split into a real and an imaginary part,

$$\omega_{1,2} \equiv M_{1,2} - \frac{i}{2}\Gamma_{1,2}, \tag{1.38}$$

corresponding to the masses and decay widths of the two eigenstates. The averages of the masses and of the decay widths are equal to the diagonal matrix elements of $\mathbf{M}$ and $\mathbf{\Gamma}$,

$$\omega_0 = \frac{M_1 + M_2}{2} - \frac{i}{2}\frac{\Gamma_1 + \Gamma_2}{2} = M - \frac{i}{2}\Gamma, \tag{1.39}$$

while their differences $\Delta M = M_2 - M_1$ and $\Delta\Gamma = \Gamma_2 - \Gamma_1$, or equivalently $\Delta\omega \equiv \Delta M - i/2\Delta\Gamma$, satisfy

$$H_{12}H_{21} = \frac{1}{4}(\Delta M - \frac{i}{2}\Delta\Gamma)^2. \tag{1.40}$$

The mass and width differences of the eigenstates can be parametrised in units of the average decay width, through the two dimensionless mixing parameters

$$x \equiv \frac{\Delta M}{\Gamma} \text{ and } y \equiv \frac{\Delta\Gamma}{2\Gamma}. \tag{1.41}$$

The time evolution of a particle $|M^0(t)\rangle$ and $|\overline{M}^0(t)\rangle$ created in its flavour eigenstate M^0 and $\overline{M}^0$, respectively, at time zero are given by

$$\begin{aligned} |M^0(t)\rangle &= g_+(t)|M^0(0)\rangle + \frac{q}{p}g_-(t)|\overline{M}^0(0)\rangle, \\ |\overline{M}^0(t)\rangle &= g_+(t)|\overline{M}^0(0)\rangle + \frac{p}{q}g_-(t)|M^0(0)\rangle, \end{aligned} \tag{1.42}$$

with

$$g_{\pm}(t) \equiv \frac{e^{-i\omega_1 t} \pm e^{-i\omega_2 t}}{2}. \tag{1.43}$$

The probability of observing at time t the same particle that was produced in its flavour eigenstate at time $t = 0$ is equal to

$$|\langle M^0(t)|M^0(t)\rangle|^2 = |\langle \overline{M}^0(t)|\overline{M}^0(t)\rangle|^2 = |g_+(t)|^2, \tag{1.44}$$

whereas the probabilities of observing particles with opposite flavour quantum numbers are

$$\begin{aligned} |\langle \overline{M}^0(t)|M^0(t)\rangle|^2 &= |\frac{q}{p}|^2 |g_-(t)|^2, \\ |\langle M^0(t)|\overline{M}^0(t)\rangle|^2 &= |\frac{p}{q}|^2 |g_-(t)|^2, \end{aligned} \tag{1.45}$$

with

$$|g_{\pm}(t)|^2 = \frac{1}{2} e^{-\Gamma t} \left[\cosh(y\Gamma t) \pm \cos(x\Gamma t)\right]. \tag{1.46}$$

Thus, the probability of the M^0 and $\overline{M}^0$ mesons to preserve their flavour quantum numbers as a function of time is the same for both mesons, whereas the probability to oscillate into their antiparticle can be different, provided that $|q/p| \neq 1$ and that at least one of the mixing parameters x and y is different from zero.

In this parametrisation, a convention choice is needed to resolve the ambiguity arising from the definitions of $|M_1\rangle$ and $|M_2\rangle$ in Eq. 1.36, which can be interchanged by redefining $q \to -q$. For example, the ambiguity can be solved by defining $|M_2\rangle$ as the short-lived eigenstate or, equivalently, by forcing the y parameter to be positive. Once this convention choice is done, all ambiguities are removed, apart from the phase of q and p. In fact, their relative phase still depends on the convention for the *CP* transformation of the M^0 and $\overline{M}^0$ mesons.

Theoretical parametrisation

The results of the previous section can be obtained also by using an alternative parametrisation, introduced in Refs. [38, 39], which is convention-independent and quantifies directly the magnitudes and the phase difference between the dispersive and absorptive transition amplitudes. In particular, the theoretical mixing parameters and the mixing phase are defined as

$$x_{12} \equiv \frac{2|M_{12}|}{\Gamma}, \quad y_{12} \equiv \frac{|\Gamma_{12}|}{\Gamma}, \quad \phi_{12} \equiv \arg\left(\frac{M_{12}}{\Gamma_{12}}\right), \tag{1.47}$$

and are all observable quantities. While x_{12} and y_{12} are *CP*-even observables, ϕ_{12} is a *CP*-odd weak phase.

The theoretical and phenomenological mixing parameters are related as

$$x^2 - y^2 = x_{12}^2 - y_{12}^2, \tag{1.48}$$
$$xy = x_{12} y_{12} \cos\phi_{12}, \tag{1.49}$$
$$|q/p|^{\pm 2}\,(x^2 + y^2) = x_{12}^2 + y_{12}^2 \pm 2 x_{12} y_{12} \sin\phi_{12}, \tag{1.50}$$

equalising the expressions for $H_{12}H_{21}$, $|H_{12}|^2$ and $|H_{21}|^2$ in terms of the two sets of mixing parameters (Eqs. 1.37 and 1.40).

The ratio $|p/q|$ is measured to be very close to unity for all flavoured neutral mesons, corresponding to very small values of $\sin(\phi_{12})$. Therefore, the x_{12} and y_{12} parameters are equal to the magnitude of the x and y parameters up to corrections quadratic in $\sin(\phi_{12})$. Finally, $|q/p| - 1$ is approximately equal to

$$\left|\frac{q}{p}\right| - 1 \approx \frac{x_{12} y_{12}}{x_{12}^2 + y_{12}^2} \sin(\phi_{12}), \tag{1.51}$$

up to corrections quadratic in $\sin(\phi_{12})$.

1.3.2 Phenomenology

The formalism introduced in the previous section describes the mixing of all K^0, D^0, B^0 and B_s^0 mesons. However, the phenomenology, which is governed by the size of the mixing parameters x and y summarised in Table 1.1, varies considerably among different particles. This is displayed in Figure 1.1, where the probability for a meson to preserve its flavour quantum numbers or to change it, oscillating into its antiparticle given by Eq. 1.46, is plotted as a function of time.

These different behaviours can be traced down to largely different interactions contributing to the matrix elements responsible for the transitions M_{12} and Γ_{12}. These are fourth-order interactions in the weak coupling, and are usually classified in two categories, namely *short-distance* and *long-distance* contributions, depending on whether they receive significant contributions from long-distance non-perturbative QCD interactions or not. In particular, while short-distance amplitudes involve the exchange of

System	x	y
K^0-$\overline{K}^0$ [31]	-0.946 ± 0.004	0.99650 ± 0.00001
D^0-$\overline{D}^0$ [41, 42]	$(0.398^{+0.056}_{-0.054})\%$	$(0.63 \pm 0.07)\%$
B^0-$\overline{B}^0$ [42]	0.769 ± 0.004	$(-0.1 \pm 1.0)\%$
B_s^0-$\overline{B}_s^0$ [42]	26.89 ± 0.07	$(-12.9 \pm 0.6)\%$

Table 1.1: Value of the mixing parameters of the four flavoured neutral mesons.

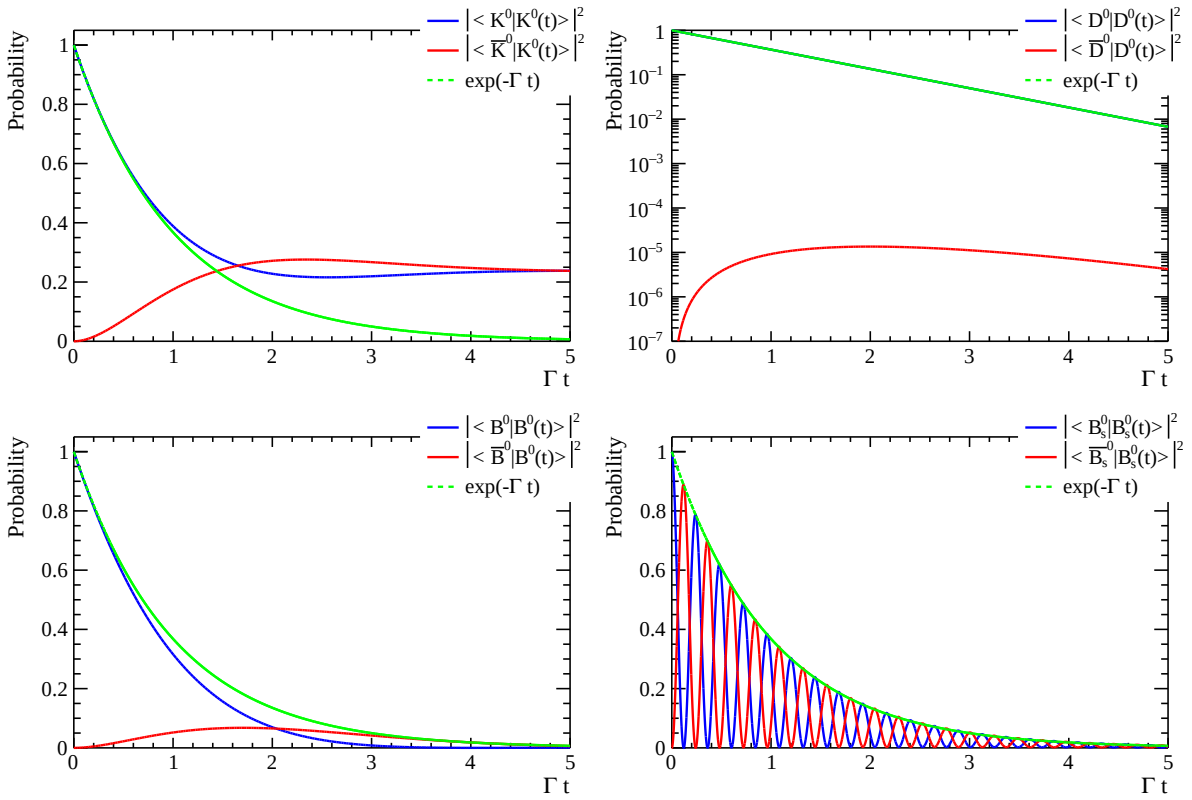

Figure 1.1: Probability for a neutral flavoured meson (red) to oscillate in its relative antimeson or (blue) to preserve its flavour quantum numbers as a function of time, under the assumption that $|q/p| = 1$. The exponential function that would be observed in absence of mixing is drawn as well as a green-dashed line. The plots correspond, from left to right and from top to bottom, to K^0, D^0 (in logaritmic scale), B^0 and B_s^0 mesons.

virtual particles off the mass shell only, and can be calculated with good precision, long-distance amplitudes can be significantly enhanced by the exchange of hadrons on the mass shell, as shown in Figure 1.2, and pose several challenges to theory predictions.

Box diagrams responsible for the $\Delta F_1 = -2$, $\Delta F_2 = 2$ neutral currents that provoke the mixing of mesons with $F_1\overline{F}_2$ flavour content, similar to those of Figure 1.2 (left), are roughly proportional to $\lambda^q_{F_1F_2}(\lambda^{q'}_{F_1F_2})^*(m_q/m_W)^2$, where $\lambda^q_{F_1F_2} \equiv V_{qF_1}V^*_{qF_2}$ and q and q' are the internal quarks of the diagram, with q the lightest one [43]. The absence of $\Delta F = 2$ transitions at tree level and the suppression of possible contributions from loops involving light quarks is known as GIM mechanism [13] and follows from the unitarity of the CKM matrix.

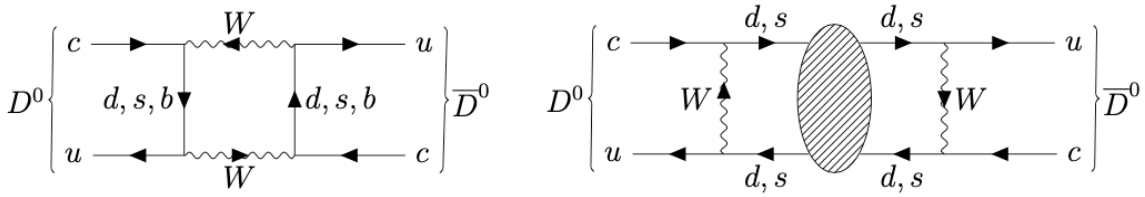

Figure 1.2: Feynman diagrams of (left) short-distance and (right) long-distance contributions to D^0 mixing. In the right diagram, the blob stands for low-energy QCD interactions, possibly involving the exchange of hadrons on the mass shell.

B mesons mixing

For B^0 and B_s^0 mesons, the only relevant contribution to mixing involves the exchange of two internal top quarks, owing to the breaking of the suppression of the GIM mechanism with $m_t/m_W \approx 1$ (while $m_q/m_W << 1$ for $q \neq t$), and to the favourable hierarchy of the relevant CKM-matrix elements ($\lambda_{bs}^t \approx \lambda_{bs}^c >> \lambda_{bs}^u$ and $\lambda_{bd}^t \approx \lambda_{bd}^c \approx \lambda_{bd}^u$). Moreover, these amplitudes are nearly completely short-distance, since the large B masses are off the region of hadronic resonances. Since the top-quark exchanges are off the mass shell, in the SM the magnitude of M_{12} (and of the x parameter) of B mesons is expected to be much larger than that of Γ_{12} (and of the y parameter). In addition, since $|V_{td}|$ is much smaller than $|V_{ts}|$, the magnitude of the mixing parameters of the B_s^0 meson is larger than that of the B^0 meson, and its oscillations are much faster. Finally, in the approximation of negligible CP violation in mixing, $\phi_{12} \approx \pi$, implying opposite signs for x and y, and the ratio x/y is the same for B^0 and B_s^0 mesons. The fact that the width difference is smaller for B^0 than for B_s^0 mesons can be understood considering the total branching fractions of B_q^0 decays that are shared with $\overline{B}_q^0$ decays. These are dominated by $b \to c\bar{c}q$ transitions, which are Cabibbo favoured for B_s^0 decays ($q = s$) and Cabibbo suppressed for B^0 decays ($q = d$).

K mesons mixing

A completely different dynamics is at play in K^0 mixing. Since the K^0 mass is of the same order of many hadronic resonances, the contributions to Γ_{12} are dominated by long-distance amplitudes. In particular, the y parameter is approximately equal to unity, since, neglecting CP-violating effects of the order of 10^{-3}, only the approximately CP-even K eigenstate can decay into two pions, whereas the semileptonic decays and the decays into three pions of the approximately CP-odd eigenstate have very low rates owing to phase-space suppression. On the contrary, only approximately 20% of the M_{12} amplitude is due to long-distance contributions. However, unlike in B mixing, the short-distance contributions to M_{12} involving charm quarks are larger than those due to top

quarks, owing to the large CKM suppression ($\lambda_{sd}^t/\lambda_{sd}^c << m_c/m_t$).

D^0 mesons mixing

The interactions governing the mixing of D^0 mesons, which are the only flavoured neutral mesons where the mixing of up-type quarks can be observed, are very different from those of K and B systems. The size of mixing is here extremely small, as shown in Figure 1.1, owing to a severe suppression which is due to two accidental features. First, the masses of the internal down-type quarks in the box diagrams, which break the GIM cancellation at loop level, are much smaller than that of the top quark (the largest mass is $m_b/m_W \approx 5\%$). Second, considering the hierarchy of the CKM-matrix elements, the third generation of quarks is nearly decoupled from the first two. In fact, $\lambda_{cu}^b/\lambda_{cu}^s \approx \lambda_{cu}^b/\lambda_{cu}^d << \Lambda/m_b$, where Λ is a dynamical hadronic scale of order Λ_{QCD} that replaces $m_{s,d}$ in the evaluation of box diagrams with internal s and d quarks (the charm-quark mass is not distant from that of light-quarks hadronic resonances and long-distance effects can not be neglected). Both x and y mixing parameters of the D^0 mesons are experimentally less than 1% [44]. However, while the y parameter has been measured to differ significantly from zero in 2007, the x parameter has been found to differ from zero only recently with the observation of the mass difference between neutral charm-meson eigenstates [41], in 2021 by the LHCb experiment.

1.4 Classification of *CP* violation

The phenomenology of *CP* violation is particularly rich in flavoured neutral mesons, thanks to the fact that weak and strong phases can appear both in the mixing or in the decay amplitudes. Depending on which of these factors is responsible for *CP* violation, *CP*-violating effects are conventionally classified into three categories, introduced below.

CP violation in the decay

The *CP violation in the decay* arises if the magnitude of the decay amplitudes of *CP*-conjugated processes are different. It is defined as

$$a_f^d = \frac{|A_f|^2 - |\bar{A}_{\bar{f}}|^2}{|A_f|^2 + |\bar{A}_{\bar{f}}|^2}, \tag{1.52}$$

and is the only type of *CP* violation that can be observed in charged hadrons.

CP violation in the mixing

The *CP violation in the mixing* occurs if the probability of the M^0 meson to oscillate after a time t into its antiparticle $\overline{M}^0$ is different from the *CP*-conjugate process, where

a $\overline{M}^0$ mesons oscillates into a M^0 meson. This happens if the magnitude of the ratio of the coefficients of M^0 and $\overline{M}^0$ in the expressions of the mass eigenstates (Eq. 1.42) differs from unity, *i.e.*

$$\left|\frac{q}{p}\right| \neq 1. \tag{1.53}$$

In the theoretical parametrisation, it corresponds to the condition

$$\frac{x_{12}y_{12}}{x_{12}^2+y_{12}^2}\sin(\phi_{12}) \neq 0, \tag{1.54}$$

from Eq. 1.51.

CP violation in the interference between decay and mixing

The *CP violation in the interference* arises only for final states accessible by both M^0 and $\overline{M}^0$ mesons, *e.g.* via Cabibbo-favoured and doubly-Cabibbo-suppressed processes for M^0 and $\overline{M}^0$ and vice versa. It is due to the interference between the decay without mixing $M^0 \to f$ and the decay following mixing $M^0 \to \overline{M}^0 \to f$. This condition occurs if

$$\mathfrak{Im}\left(\frac{q}{p}\frac{\bar{A}_f}{A_f}\right) + \mathfrak{Im}\left(\frac{q}{p}\frac{\bar{A}_{\bar{f}}}{A_{\bar{f}}}\right) \neq 0. \tag{1.55}$$

In the theoretical parametrisation, it corresponds to the condition

$$\frac{\sin(2\phi_{12})}{\cos(2\phi_{12}) + y_{12}^2/x_{12}^2} \neq 0, \tag{1.56}$$

from Ref. [39].

1.5 *CP* violation in $D^0 \to h^- h^+$ decays

The discussion is now focused on the measurement of the *CP* asymmetry with the Cabibbo suppressed (CS) decay of D^0 and $\overline{D}^0$ mesons into two charged hadrons, namely the $D^0 \to K^-K^+$ and $D^0 \to \pi^-\pi^+$ decays. The measurement of a^d_{KK} and $a^d_{\pi\pi}$ is the main subject of this thesis.

The time-integrated asymmetry for the *CP* final states $f = K^-K^+, \pi^-\pi^+$ can be written as a function of the decay time rates as

$$\mathcal{A}^{CP}(D^0 \to f) \equiv \frac{\int \Gamma(D^0(t) \to f)\epsilon(t)dt - \int \Gamma(\overline{D}^0(t) \to f)\epsilon(t)dt}{\int \Gamma(D^0(t) \to f)\epsilon(t)dt + \int \Gamma(\overline{D}^0(t) \to f)\epsilon(t)dt}, \tag{1.57}$$

with $\epsilon(t)$ being the decay time acceptance. This quantity does not correspond to a^d_f because of additional contributions arising from the neutral meson mixing.

In the following, the time-dependent decay rates for $D^0 \to h^- h^+$ are described with the theoretical parametrisation as in Ref. [45]. Finally, the theoretical predictions together with the current experimental status are reported.

1.5.1 Time-dependent decay rates

Let us denote the amplitudes of D^0 and $\overline{D}^0$ decays into a final state f as

$$A_f \equiv \langle f|\mathcal{H}|D^0\rangle, \quad \bar{A}_f \equiv \langle f|\mathcal{H}|\overline{D}^0\rangle, \tag{1.58}$$

where $\mathcal{H}$ is the $|\Delta C| = 1$ weak-interaction effective Hamiltonian that governs the decay of D^0 mesons. The time-dependent rates if D^0 and $\overline{D}^0$ decays into the final state f are equal to

$$\Gamma(D^0 \to f, t) = \mathcal{N}_f |\langle f|\mathcal{H}|D^0(t)\rangle|^2, \quad \Gamma(\overline{D}^0 \to f, t) = \mathcal{N}_f |\langle f|\mathcal{H}|\overline{D}^0(t)\rangle|^2, \tag{1.59}$$

where $\mathcal{N}_f$ is a common, time-independent normalisation factor that includes the result of the phase-space integration. By employing the definitions of Eq. 1.58, the last equation can be written as

$$\begin{aligned} \Gamma(D^0 \to f, t) &= \mathcal{N}_f \, |A_f \langle D^0|D^0(t)\rangle + \bar{A}_f \langle \overline{D}^0|D^0(t)\rangle|^2, \\ \Gamma(\overline{D}^0 \to f, t) &= \mathcal{N}_f \, |\bar{A}_f \langle \overline{D}^0|\overline{D}^0(t)\rangle + A_f \langle D^0|\overline{D}^0(t)\rangle|^2, \end{aligned} \tag{1.60}$$

where the first and second term of the sums correspond to decays without and with flavour oscillations, respectively, which can interfere giving rise to *CP* violation in the interference.

The analogue of all the expressions and definitions given above for the final state f, can be obtained for the *CP* conjugate final state $\bar{f}$ by substituting $f \to \bar{f}$. Note that the normalisation factor $\mathcal{N}_f$ is shared between the D^0 and $\overline{D}^0$ decays widths separately for each final state f and, in addition, is equal for the f and $\bar{f}$ final states, *i.e.* $\mathcal{N}_f = \mathcal{N}_{\bar{f}}$.

Cabibbo suppressed final states

In this section f indicates either of the two CS final states K^-K^+ and $\pi^-\pi^+$. Since the final states are *CP*-even eigenstates A_f is equal to $A_{\bar{f}}$ and no strong phase appears between them. The *CP*-violating dispersive and absorptive weak phases are defined as

$$\phi_f^M \equiv \arg\left(\frac{M_{12}}{|M_{12}|}\frac{A_f}{\bar{A}_f}\right) \text{ and } \phi_f^\Gamma \equiv \arg\left(\frac{\Gamma_{12}}{|\Gamma_{12}|}\frac{A_f}{\bar{A}_f}\right), \tag{1.61}$$

respectively, and satisfy $\phi_f^M - \phi_f^\Gamma = \phi_{12}$. The time-dependent decay time rates are conveniently parametrised as

$$\begin{aligned} \Gamma(D^0(t) \to f) &= e^{-\tau}|A_f|^2 \left(1 + c_f^+ \, \tau\right), \\ \Gamma(\overline{D}^0(t) \to f) &= e^{-\tau}|\bar{A}_f|^2 \left(1 + c_f^- \, \tau\right), \end{aligned} \tag{1.62}$$

up to first order in the mixing parameters, where $\tau \equiv \Gamma t$ and the parameters $c_f^{\pm}$ satisfy

$$c_f^{\pm} = \mp x_{12} \sin\phi_f^M - y_{12} \cos\phi_f^{\Gamma} (1 \mp a_f^d), \tag{1.63}$$

in the limit of small *CP* violation. Finally, the following *CP*-odd and *CP*-even combinations of c_f^+ and c_f^-

$$\Delta Y_f \equiv \frac{c_f^+ - c_f^-}{2} \approx -x_{12} \sin\phi_f^M + y_{12} \cos\phi_f^{\Gamma} a_f^d, \tag{1.64}$$

$$y_{CP}^f \equiv -\frac{c_f^+ + c_f^-}{2} \approx y_{12} \cos\phi_f^{\Gamma}, \tag{1.65}$$

are particularly convenient from an experimental point of view, and are often employed as experimental observables insted of c_f^+ and c_f^-. To date, the latest measurements of these quantity show compatibility between the K^-K^+ and $\pi^-\pi^+$ final states. Their combination gives $\Delta Y = (-1.04 \pm 1.17) \cdot 10^{-4}$ [46] and $y_{CP} = (6.96 \pm 0.29) \cdot 10^{-3}$ [47], with ΔY in agreement with zero.

Using Eq. 1.62, Eq. 1.57 can be rewritten as

$$\mathcal{A}^{CP}(D^0 \to f) = a_f^d + \frac{\langle t \rangle_f}{\tau_D} \cdot \Delta Y_f, \tag{1.66}$$

where $\langle t \rangle_f$ is the average (acceptance dependent) decay time of the D^0 mesons in the experimental sample and τ_D is the D^0 lifetime. Given that $\langle t \rangle_f / \tau_D$ is usually in the range between 1 and 2, time-dependent *CP*-violating effects are of the order of 10^{-4} or below.

1.5.2 Theoretical prediction

For the purposes of this discussion, it is useful to parametrise the decay amplitudes of D^0 and $\overline{D}^0$ mesons into the final state f and $\bar{f}$ as

$$\begin{aligned}
A_f &\equiv A_f^0 e^{+i\phi_f^0} [1 + r_f e^{i(\delta_f + \phi_f)}], \\
A_{\bar{f}} &\equiv A_{\bar{f}}^0 e^{i(\Delta_f^0 + \phi_{\bar{f}}^0)} [1 + r_{\bar{f}} e^{i(\delta_{\bar{f}} + \phi_{\bar{f}})}], \\
\bar{A}_{\bar{f}} &\equiv A_f^0 e^{-i\phi_f^0} [1 + r_f e^{i(\delta_f - \phi_f)}], \\
\bar{A}_f &\equiv A_{\bar{f}}^0 e^{i(\Delta_f^0 - \phi_{\bar{f}}^0)} [1 + r_{\bar{f}} e^{i(\delta_{\bar{f}} - \phi_{\bar{f}})}],
\end{aligned} \tag{1.67}$$

where A_f^0 and $A_{\bar{f}}^0$ are the magnitudes of the dominant SM contributions, the ratios r_f and $r_{\bar{f}}$ are the relative magnitudes of the subleading amplitudes (either from the SM or from interactions beyond the SM) with respect to the dominant ones, ϕ_f^0 and $\phi_{\bar{f}}^0$ are unobservable weak phases, and Δ_f^0 is a strong phase. Finally, ϕ_f and $\phi_{\bar{f}}$ (δ_f and $\delta_{\bar{f}}$) are the relative weak (strong) phases between the subleading and the dominant decay

amplitudes. For CS decays into *CP*-even final states, the expression for A_f and $\bar{A}_f$ are simplified, yielding

$$\begin{aligned} A_f &\equiv A_f^0 e^{+i\phi_f^0}[1 + r_f e^{i(\delta_f+\phi_f)}], \\ \overline{A}_f &\equiv A_f^0 e^{-i\phi_f^0}[1 + r_f e^{i(\delta_f-\phi_f)}]. \end{aligned} \tag{1.68}$$

Employing these definitions, the phases ϕ_f^M and ϕ_f^Γ defined in Eq. 1.61 for CS decays can be written as

$$\phi_f^{M(\Gamma)} \approx \phi^{M(\Gamma)} + 2\phi_f^0 + 2r_f \cos\delta_f \sin\phi_f, \tag{1.69}$$

to the first order in r_f, with $\phi^{M(\Gamma)}$ being the argument of M_{12} (Γ_{12}). The *CP* violation in the decay can be easily calculated in terms of the introduced parameters, yielding

$$a_f^d \approx -2r_f \sin\delta_f \sin\phi_f, \tag{1.70}$$

to the first order in r_f.

In the SM the factors r_f and $r_{\bar{f}}$ in Eq. 1.67, and consequently the *CP* violation in the decay, can be neglected for CF and DCS decays, since these decays are not sensitive to QCD electroweak-loop and chromomagnetic dipole operators. On the contrary, the factor r_f of CS decays can not be neglected in Eq. 1.68. Here, the choice of the dominant and subleading amplitudes is convention dependent. For example, exploiting CKM unitarity, the leading CS D^0 decay amplitudes, *e.g.* Figure 1.3 (top left), could be chosen to be proportional to λ_{cu}^s, λ_{cu}^d, or their difference $\lambda_{cu}^s - \lambda_{cu}^d$. The last choice is particularly convenient as it is motivated by the U-spin flavuor symmetry[5] and represents the U-spin odd quantity $\Sigma \equiv (\lambda_{cu}^s - \lambda_{cu}^d)/2 \approx \lambda$. In the SM, the subleading amplitudes contributing to $c \to u$ transitions, *e.g.* Figure 1.3 (top right), are proportional to the U-spin even quantity $(\lambda_{cu}^s + \lambda_{cu}^d)/2 = -\lambda_{cu}^b/2 \approx -\lambda^5 A^2(\rho - i\eta)/2$, as dominated by the contribution of the internal b quark in the loop. For a discussion on the amplitudes parametrisation see Refs. [48, 49]. However, this result is general and does not depend on the chosen convention. Therefore, the factor r_f is proportional to $|\lambda_{cu}^b/\Sigma| \approx |\lambda^4 A^2(\rho - i\eta)| \approx 6.5 \cdot 10^{-4}$ [31], and the angle ϕ_f is approximately equal to $\pi - \gamma$, where the angle γ is defined as $\gamma \equiv \arg(\lambda_{cu}^b) \approx \arctan(\eta/\rho) \approx 66$ [31]. A rough upper bound on the size of *CP* violation in the decay for CS final states is thus given by $2r_f|\sin\phi_f| \approx |\lambda_{cu}^b/\Sigma| \sin\gamma \approx 5.9 \cdot 10^{-4}$. The size of *CP* violation is further suppressed by the sine of the relative strong phase between the subleading and dominant amplitudes, and by the ratio of their magnitudes. To provide predictions for these non-perturbative quantities is very challenging. The dominant amplitude A_f^0 is mostly determined by tree-level decays. On the other hand, the subleading decay amplitudes are only due to electroweak-loop diagrams or to rescattering effects. Some example of these diagrams are shown in Figure 1.3 for the $D^0 \to K^-K^+$

[5] U-spin is an approximate symmetry for the interchange of d and s quarks. It consists in a $SU(2)$ subgroup of flavour $SU(3)$, under which the (d, s) pair of quarks is a doublet, similar to (u, d) in isospin.

decay. The strong phase difference δ_f is expected to be of the order of unity due to large scattering at the charm-mass scale, and does not necessary lead to a large suppression. On the other hand, the ratio of the magnitudes of subleading to dominant amplitudes has been estimated using dynamical methods of QCD in Refs. [50–53] and is expected to lead a suppression up to one order of magnitude of the asymmetry. The predictions for the magnitudes of a^d_{KK} and $a^d_{\pi\pi}$ are accordingly in the range between 10^{-4} and 10^{-3}. However, all of the predictions rely on model assumptions, like for example the quark-hadron duality, and it cannot be excluded that the suppression is smaller due to large rescattering at the charm-mass scale, as already noted in 1989 [54]. Finally, U-spin symmetry implies that a^d_{KK} and $a^d_{\pi\pi}$ are approximately equal in magnitude and opposite in sign. However, the branching fractions of $D^0 \to K^-K^+$ and $D^0 \to \pi^-\pi^+$ differ by a factor 2.8 [31] and recent measurements show an evidence of U-spin breaking in the strong phase between $D^0 \to K^-\pi^+$ and $\overline{D}^0 \to K^-\pi^+$ decays being different from π [47], demonstrating that this approximate symmetry is not valid for D^0 meson decays and it is possible that also the rule $a^d_{KK} + a^d_{\pi\pi} = 0$ is broken.

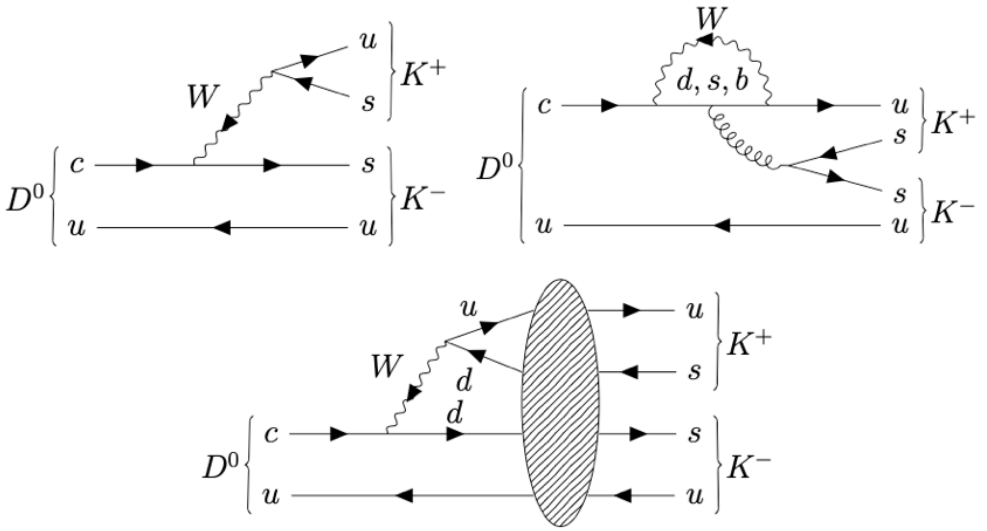

Figure 1.3: Example of Feynman diagrams contributing to the $D^0 \to K^-K^+$ decay. The tree diagram (top left) is proportional to λ^s_{cu}, while the electroweak-loop diagram (top right) is proportional to λ^q_{cu}, where q is the internal quark of the loop. Finally, the bottom diagram represents one of the possible contributions to rescattering, where the blob is a placeholder for the rescattering of the $\pi^-\pi^+$ state into the K^-K^+ final state through strong interactions and is proportional to $\lambda^d_{cu} = \lambda^b_{cu} - \lambda^s_{cu}$.

Alternative theoretical studies have been performed to estimate the size of the various topological amplitudes that contribute to the processes. They parametrise the branching

fractions and the *CP* asymmetries of all of the D final states in terms of these topological amplitudes, and fit them to their measured values [49, 54–62]. However, while the values of the branching fractions fix the size of the dominant amplitudes A_0^f, they are not able to predict the absolute size of *CP* violation, but only to relate its size among decays into different final states. In fact, the size of the electroweak-loop diagrams and of rescattering effects, which are responsible for *CP* violation, contribute only marginally to the branching fractions (or, in case of rescattering, can not be distinguished unambiguously from the tree-level-like amplitudes).

1.5.3 Current experimental status

In 2019, the LHCb collaboration reported the first observation of *CP* violation in charm-hadron decays, a new milestone in the history of particle physics, by measuring the difference between the *CP* asymmetries of $D^0 \to K^-K^+$ and $D^0 \to \pi^-\pi^+$ decays [1],

$$a^d_{KK} - a^d_{\pi\pi} = (-15.7 \pm 2.9) \cdot 10^{-4}. \tag{1.71}$$

This observable is very convenient from an experimental point of view, since most nuisance asymmetries cancel in the difference, and allows to achieve a much better precision that the measurements in the single decay channels [63, 64]. The magnitude of the measured value lies at the upper edge of the SM predictions, and challenges the predictions based on first-principle QCD dynamics [50, 53]. However, it is not excluded that the discrepancy is due to a mild enhancement of rescattering beyond expectations. This possibility has already been proposed in 2012 [49, 56, 57, 59, 60] to explain the large value of $a^d_{KK} - a^d_{\pi\pi}$ measured by the LHCb collaboration in the same year $(-8.2 \pm 2.4) \cdot 10^{-3}$ [65]. Technically, it would correspond to a mild enhancement of the subleading decay amplitudes with respect to the dominant one, and it has been explored in detail recently in Refs. [48, 66–69]. However, other authors question the possibility of such an enhancement, and attribute the effect to new interactions beyond the SM as analysed in Refs. [50, 57, 60, 70] and as further explored recently in Refs. [71–73] .

Therefore, further measurements of *CP* asymmetries in D meson decays are crucial to shed light on the dynamics underlying the measurement of $a^d_{KK} - a^d_{\pi\pi}$. In particular, measuring the *CP* asymmetries separately in the two decay channels would allow to test the U-spin predictions, which might be violated, and furnish essential informations on the nature of *CP* violation in charm decays. This is precisely the purpose of the work presented here. Specifically, the complete data set collected by the LHCb experiment during Run 2 has been analysed considering D^0 candidates from $D^{*+} \to D^0\pi^+$ decays for the measurement of a^d_{KK} and $a^d_{\pi\pi}$ as widely explained in Chapter 3. Previous determination of $\mathcal{A}^{CP}(K^-K^+)$ from the LHCb experiment are reported in Table 1.2 [63, 64]. Their combination yields

$$\mathcal{A}^{CP}(K^-K^+) = [4 \pm 12\ (\text{stat}) \pm 10\ (\text{syst})] \cdot 10^{-4}, \tag{1.72}$$

while $\mathcal{A}^{CP}(\pi^-\pi^+)$ is calculated from the measurement of the difference ΔA_{CP}=$\mathcal{A}^{CP}(K^-K^+)$-$\mathcal{A}^{CP}(\pi^-\pi^+)$ (see Table 1.3) as [64]

$$\mathcal{A}^{CP}(\pi^-\pi^+) = [7 \pm 14\ (\text{stat}) \pm 11\ (\text{syst})] \cdot 10^{-4}. \tag{1.73}$$

Because of the worse precision achievable in the measurement of $\mathcal{A}^{CP}$ in the single decay mode (K^-K^+ or $\pi^-\pi^+$), no evidence for *CP* violation has been found with these measurements so far. The expected statistical precision for this measurement is $7 \cdot 10^{-4}$, as extracted from previous determinations in Table 1.4. However, in this thesis the strategy for the analysis of Run 2 data has been deeply improved reducing the statistical uncertainty to $5.4 \cdot 10^{-4}$ and the possible systematic error below 30% of the statistical one, as will be seen in Chapter 3. Moreover, a potential U-spin symmetry breaking may enhance the size of a^d_{KK} or $a^d_{\pi\pi}$ and make an evidence of *CP* violation in one of the two decays possible.

On the other hand, it is extremely unlikely to make an observation of $\mathcal{A}^{CP}(K^-K^+)$ or $\mathcal{A}^{CP}(\pi^-\pi^+)$ different from zero with the current statistics available. Therefore, in order to access to statistically limited measurements such this and other rare processes, the average number of pp collisions per bunch crossing at LHCb will increase from 1.4 to 5 in the upcoming Run 3 and to 41 in the future Run 5 allowing the experiment to collect an integrated luminosity of 50 fb^{-1} and 300 fb^{-1} by the end of Run 4 and Run 5, respectively. As a consequence, the expected statistical precisions on $\mathcal{A}^{CP}(K^-K^+)$ at the end of the future data taking-periods are expected to improve as reported in Table 1.4. These high-precision measurements together with the other goals listed in the LHCb's physics programme [74] define the performance to be fulfilled by the upcoming and future LHCb detector.

Experiment (dataset)	$\mathcal{A}^{CP}(K^-K^+)$
LHCb Run 1 [64] (π-tagged)	$[14 \pm 15\ (\text{stat}) \pm 10\ (\text{syst})] \cdot 10^{-4}$
LHCb Run 1 [63] (μ-tagged)	$[-0.06 \pm 0.15\ (\text{stat}) \pm 0.10\ (\text{syst})]\,\%$

Table 1.2: Summary of previous measurements of *CP*-violating asymmetries in $D^0 \to K^-K^+$. All the values result compatible with zero.

Experiment (dataset)	ΔA_{CP}
LHCb Run 2 [1] (π-tagged)	$[-18.2 \pm 3.2\,(\text{stat}) \pm 0.9\,(\text{syst})] \cdot 10^{-4}$
LHCb Run 2 [1] (μ-tagged)	$[-9 \pm 8\,(\text{stat}) \pm 5\,(\text{syst})] \cdot 10^{-4}$
LHCb Run 1 [75] (π-tagged)	$[-10 \pm 8\,(\text{stat}) \pm 3\,(\text{syst})] \cdot 10^{-4}$
LHCb Run 1 [63] (μ-tagged)	$[14 \pm 16\,(\text{stat}) \pm 8\,(\text{syst})] \cdot 10^{-4}$

Table 1.3: Summary of current LHCb measurements of ΔA_{CP}.

Sample (L)	Tag	Yield $D^0 \to K^-K^+$	Yield $D^0 \to \pi^-\pi^+$	$\sigma(\Delta A_{CP})$ $[10^{-4}]$	$\sigma(\mathcal{A}^{CP}(K^-K^+))$ $[10^{-4}]$
Run 1-2 (9 fb^{-1})	Prompt	52 M	17 M	3.0	7.0
Run 1-3 (23 fb^{-1})	Prompt	280 M	94 M	1.3	3.0
Run 1-4 (50 fb^{-1})	Prompt	1 G	305 M	0.7	1.5
Run 1-5 (300 fb^{-1})	Prompt	4.9 G	1.6 G	0.3	0.7

Table 1.4: Expected signal yields and statistical precision on direct *CP* violation observables for the promptly produced samples. Reproduced from Ref. [74]

Chapter 2

The LHCb experiment at the LHC

The Large Hadron Collider beauty (LHCb) experiment [76] is dedicated to the study of heavy flavour physics at the Large Hadron Collider (LHC) [32] at CERN (Geneva). Its primary goal, as synthesized in the logo,

is to look for indirect evidence of New Physics (NP) in *CP*-violating processes and rare decays of beauty and charm hadrons.

The LHCb experiment is designed to exploit the large production cross-section of $b\bar{b}$ pairs in pp collisions at the LHC energies, measured to be $\sigma(pp \to b\bar{b}X) = (154.3 \pm 1.5 \pm 14.3)$ μb at a center of mass energy $\sqrt{s} = 13$ TeV and within the LHCb acceptance [77]. The same characteristics that make LHCb a perfect experiment for b physics are ideal for the study of c physics as well, also because the $c\bar{c}$ production cross-section is even larger than that of $b\bar{b}$, namely $\sigma(pp \to c\bar{c}X) = (2369 \pm 3 \pm 152 \pm 118)$ μb at $\sqrt{s} = 13$ TeV and within LHCb acceptance [78].

The LHCb experiment approach to the search of NP is complementary to that used by the ATLAS and CMS collaborations. Indeed, those experiments are designed to measure high p_{T} decay products that could indicate the direct production of new particles, whereas the LHCb experiment wants to measure the existence of such new particles indirectly, by means of their virtual quantum effects. Furthermore, the research is also active in other fields, like the studies of heavy-flavour spectroscopy, production of gauge bosons, and searches for new exotic particles.

2.1 The Large Hadron Collider

The LHC is a two-ring hadron collider housed in the 27 km tunnel previously constructed for the Large Electron Positron collider (LEP). It is placed 100 m underground across the border between France and Switzerland. Inside the accelerator, two high-energy beams travel at velocities close to the speed of light before they are made to collide. The beams travel in opposite directions in separate beam pipes, two tubes kept at ultra-high vacuum[1]. The accelerator is designed to collide protons up to a centre-of-mass energy of 14 TeV with an instantaneous luminosity of 10^{34} cm^{-2}s^{-1}. The LHC was successfully commissioned in 2010 for pp collisions with a 7 TeV centre-of-mass energy. It delivered $\sqrt{s} = 8$ TeV proton collisions from April 2012 until the end of Run 1 in 2013. Following the Long Shutdown 1 (LS1) in 2013–2014, it operated with $\sqrt{s} = 13$ TeV proton collisions during Run 2 from 2015 until the end of 2018. As a consequence of the coronavirus pandemic, the Long Shutdown 2 (LS2) lasted almost one year longer than foreseen delaying the start of Run 3 which is now planned for June 2022. During this period further consolidation measures have been pursued to enable the LHC to reach the beam energy of 6.8 TeV. In order to reach this energy a magnetic field with an intensity of 8.3 T is needed. This high field can only be achieved using superconducting material (NbTi) and by cooling the magnets in super-fluid helium at 1.9 K (-271.3 °C). The tunnel diameter is only 3.8 m, insufficient for the installation of two separate rings. The two rings are therefore incorporated into a single magnetic structure with two set of coils in a common yoke and cryostat. An example of the typical magnetic field emitted by the dipole magnets of the LHC is shown in Figure 2.1.

The accelerator complex at CERN is a succession of machines that accelerate particles to increasingly higher energies. Each machine boosts the energy of a beam of particles, before injecting the beam into the next machine in the sequence. Most of the other accelerators in the chain have their own experimental halls where beams are used for experiments at lower energies (*e.g.* ISOLDE, Alpha).

The proton source is a simple bottle of hydrogen gas. An electric field is used to strip hydrogen atoms of their electrons to yield protons. As it is not possible to directly accelerate protons from their quasi-rest conditions up to 6.5 TeV, it is necessary to pre-accelerate them through a complex of machines, represented in Figure 2.2. First, protons are injected in LINAC2, a linear accelerator that provides the Proton Synchrotron Booster (PSB) with proton bunches of 50 MeV energy. The PSB can accelerate protons up to 1.4 GeV; after this, the particles are injected in the Proton Synchrotron (PS), where they reach an energy of 26 GeV. Then, the PS passes them to the Super Proton Synchrotron (SPS), where they are accelerated for the last time up to an energy of 450 GeV, being injected in the LHC via two tunnels, called T12 and T18. SPS operated

[1]In order to avoid collisions with gas molecules, the vacuum pressure is about 10^{-7} Pa in the beam pipe and up to 10^{-9} Pa in the interaction points.

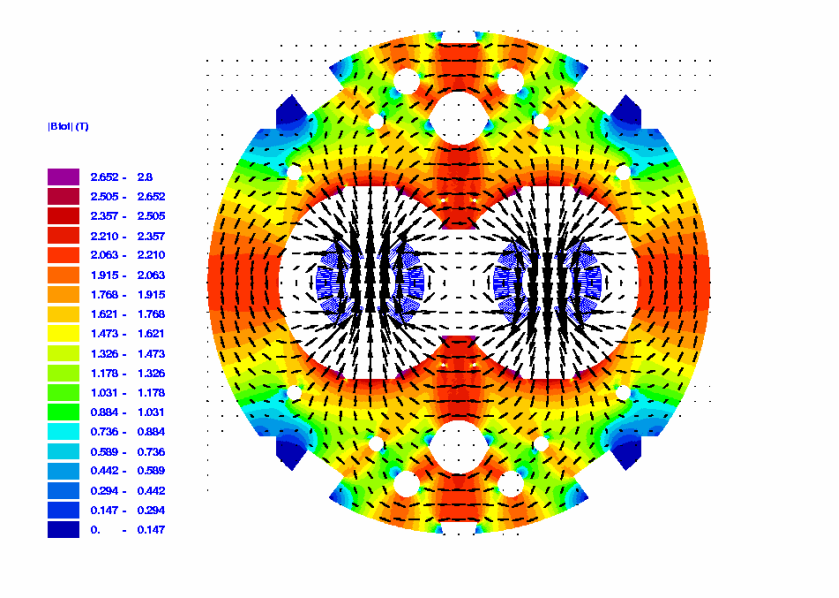

Figure 2.1: Illustration representing the typical magnetic field emitted by the dipole magnets of the LHC. The coloured portions of the diagram indicate the magnetic flux, or the amount of magnetic field passing through a given area. The arrows indicate the direction of the magnetic field. The two circles (in blue) in the centre of the diagram indicate the beam pipes for beams one and two. Notice how the arrows (direction of the magnetic field) point in opposite directions allowing to control two counter-rotating beams of protons in the same beam pipe [32].

from 1981 and 1991 as a $p\bar{p}$ collider providing beams for UA1 and UA2 experiments that discovered the $W^{\pm}$ and the Z bosons [79, 80]. In addition to LHC fills, protons can then be extracted for fixed target experiments and test beams located in the CERN North Area. After the two rings are filled, the machine is ramped to its nominal energy over about 28 min. The two beams are brought into collision inside four detectors (ALICE, ATLAS, CMS and LHCb) where the total energy at the collision point is equal to 13 TeV.

In addition to accelerating protons, the accelerator complex can also accelerate lead ions. The particle source is a 3 cm lead cylinder, which is heated to about 500 °C in order to vaporise a small number of atoms that, once partially ionised by a strong electric field, are accelerated in a linear device, in order to strip off the remaining electrons, until the ions become $^{208}Pb^{82+}$. Lead ions are then injected and accumulated in the Low Energy Ion Ring (LEIR), which transfers them to the PS. The PS accelerates the beam to 5.9 GeV/u and sends it to the SPS. The SPS accelerates the beam to 177 GeV/u and then sends it to the LHC, which accelerates it to 2.56 TeV/u. Heavy-ions collisions (Pb-Pb)

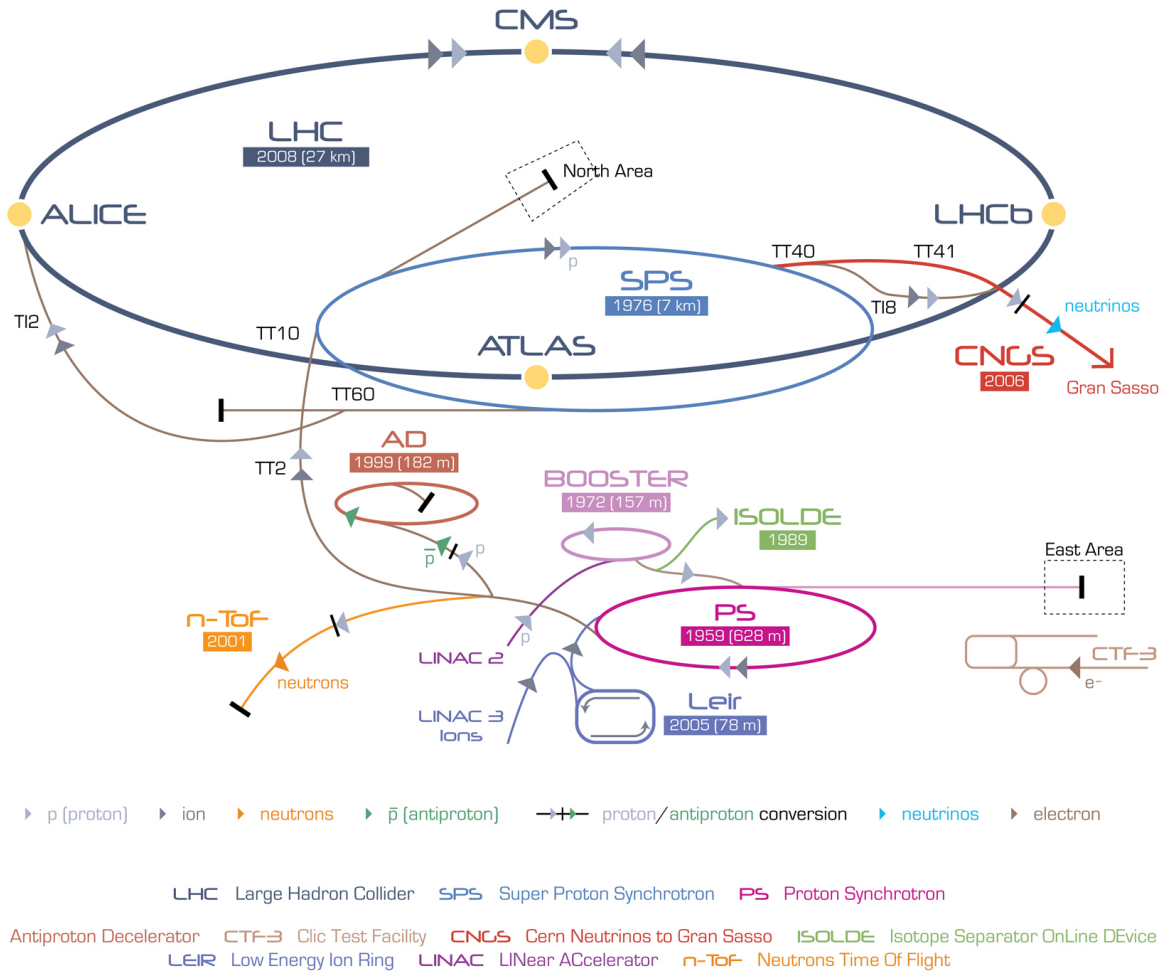

Figure 2.2: Scheme representing the CERN accelerator complex. The various machines employed to pre-accelerate the protons that will be injected in the LHC are LINAC2, PBS, PS, SPS. The accelerator complex includes the Antiproton Decelerator (AD) used for antimatter experiments like AEGIS, the Online Isotope Mass Separator (ISOLDE) facility and the CERN Neutrino to Gran Sasso (CNGS) facility for neutrino oscillations studies.

happen with a peak luminosity of 10^{27} cm^{-2}s^{-1}. This value is possible by modifying the existing obsolete Low Energy Anti-proton Ring (LEAR) into a ion accumulator (LEIR) where electron cooling is applied.

At the nominal operation regime, the LHC rings store 2808 proton bunch per ring, each of them containing 1.1^{11} protons colliding with a frequency of 40 MHz. The LHC has performed very well in these years of data taking, allowing the LHCb experiment to cross the threshold of 9 fb^{-1} of integrated luminosity over LHC Run 1 and Run 2,

collecting data with an efficiency of over 90%.

This implies that an unprecedented sample of D and B hadrons has been collected, allowing the LHCb collaboration to perform high precision measurements, improving previous results coming from BaBar, Belle and CDF collaborations and allowing the discovery of new effects in the charm and beauty sector.

2.2 The LHCb detector

The LHCb detector is a single-arm spectrometer with a forward angular coverage ranging from approximately 10 mrad to 300 (250) mrad in the bending (non-bending) plane of the dipole magnet. This geometrical acceptance corresponds to a pseudorapidity range $2 < \eta < 5$, where the pseudorapidity is defined as an approximation for the Lorentz-invariant rapidity y

$$\eta = -\ln\left(\tan\left(\theta/2\right)\right) \approx \frac{1}{2}\ln\left(\frac{\vec{p}+p_z}{\vec{p}-p_z}\right)$$

where θ is the angle between the particle and the beam line and p_z is the longitudinal momentum. This choice is justified by the fact that at high energies the B and D hadrons are predominantly produced in the same forward or backward cone. Indeed, the average imbalance in momentum of two partons that collide during a pp interaction means that the b and c quarks are produced with a strong boost along the beam line. The layout of the LHCb spectrometer is shown in Figure 2.3. The origin of the coordinate system adopted by LHCb is located at the pp interaction point, namely the primary vertex (PV). The z axis is aligned with the beam and points in the downstream direction, towards the end of the detector. The y axis points vertically upwards. The x axis points horizontally towards the centre of the LHC ring. The bending plane of the magnet is the $x-z$ plane.

Due to their relatively long lifetime, b and c-hadron decays are characterised by a displaced decay vertex, namely the secondary vertex (SV). At LHCb acceptance, a larger displacement is possible thanks to the time-dilation effect and the identification of these decays is facilitated. Nevertheless, the detector requires an excellent vertex and proper time resolution. In order to reject the background due to random combinations of tracks (combinatorial background), typical of hadronic colliders, a precise invariant-mass reconstruction is required, that implies a very good momentum resolution. Given the possibility to have topologically identical decay modes, a precise particle identification (PID) system is required, especially for charged hadrons separation. Finally, in order to collect high statistics samples and to efficiently reconstruct decays having very small branching ratios, a versatile trigger scheme has been implemented. These requirements are accomplished by the LHCb sub-detectors. They can be logically grouped in two categories based on their function.

Tracking system comprises the Vertex Locator (VELO) around the interaction point,

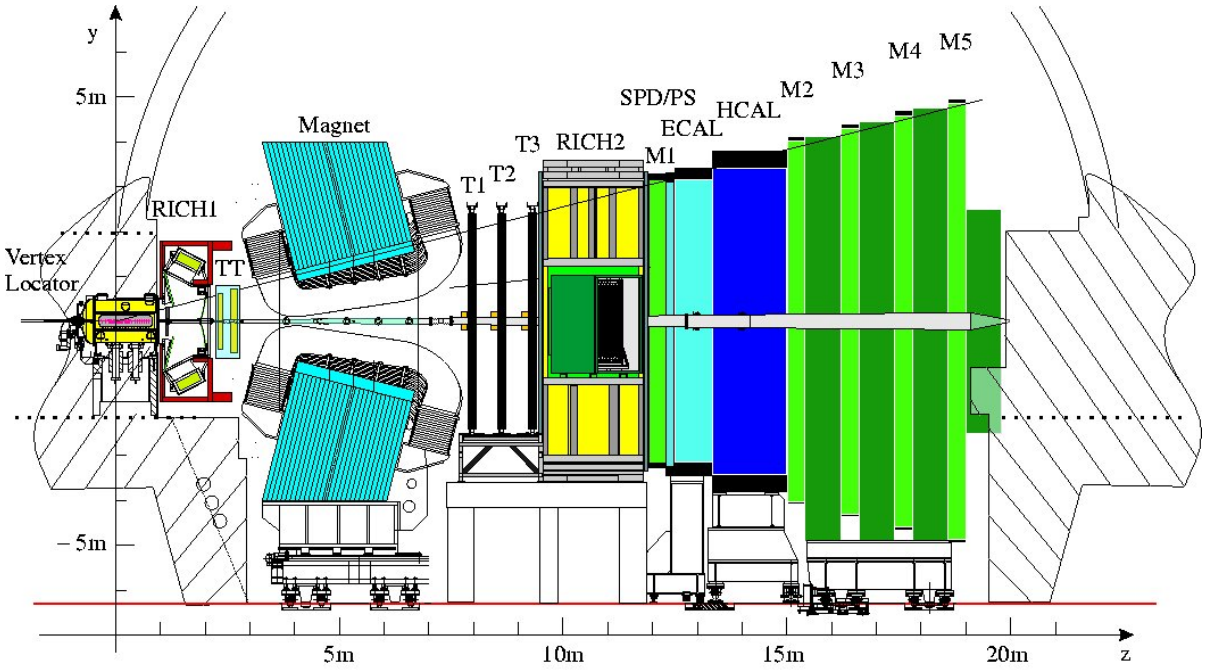

Figure 2.3: Design of the LHCb detector. From the left to the right all the sub-detectors are visible: VELO, RICH1, TT, Magnet, Tracking Stations, RICH2, ECAL, HCAL and Muon Stations.

the Tracker Turicensis (TT), and the three Tracking Stations (T1, T2 and T3) placed after the dipole magnet.

Particle identification (PID) system is composed of two Ring Imaging Cherenkov (RICH) detectors, the calorimeters system comprising the preshower (PS), the scintillating pad detector (SPD), the electromagnetic and hadronic calorimeters (ECAL and HCAL) and five muon stations (M1-M5). The first Cherenkov detector (RICH1) is placed immediately after the VELO, while the second (RICH2) is after the Tracking Stations.

A detailed description of all the sub-detectors is given in the next pages.

2.3 The LHCb tracking system

The tracking system is devoted to reconstruct the trajectories of charged particles (tracks), identify their interaction vertices and measure their momentum exploiting a magnetic field to bend them.

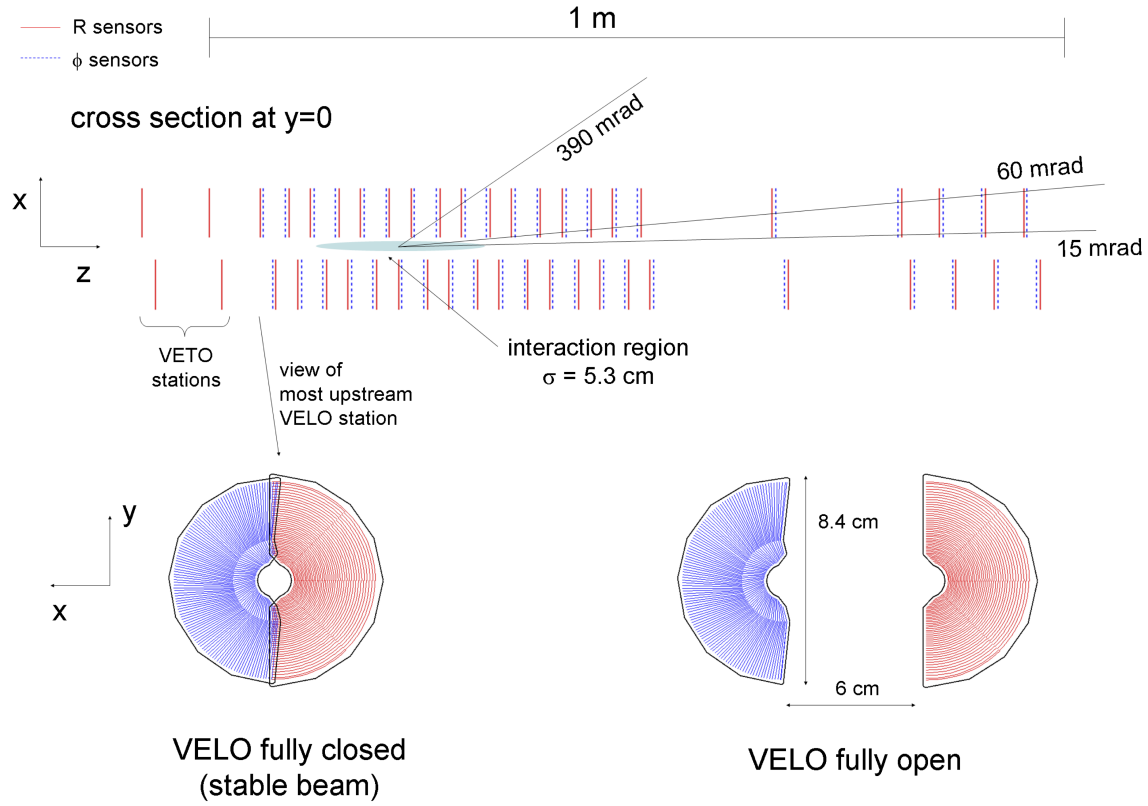

Figure 2.4: Top view of the VELO silicon sensors, with the VELO in the fully-closed mode (top). Frontal view of the modules in the closed and open mode (bottom left and bottom right, respectively) [76].

2.3.1 The Vertex Locator

Beauty (charm) hadrons at LHCb travel a distance of about 1 cm (0.3 cm) before decaying. The presence of a secondary vertex well displaced from the *pp* primary vertex is thus an important signature. For this reason and also due to the high track multiplicity in LHC collisions, it is imperative to have a vertex locator with micro-metric precision in order to select signal events and reject most of the background.

The VELO [81] is composed of 21 circular silicon modules, installed perpendicularly along the beam line, as shown in the top of Figure 2.4. In order to achieve its goals, the VELO must be located as close as possible to the LHC interaction point. It is designed to be located at ~ 7 mm from the interaction point, also considering the needs in term of radiation tolerance imposed by the severe radiation environment. Since during injection the beam is not focused enough, the VELO must be retractable to avoid damage to

the sensors. For this reason each silicon modules is divided in two halves. Before the LHC ring is filled, the two halves move away from the interaction region by 30 mm (open) and, once the beam reaches stable conditions, the two halves move back to the nominal position (closed), as can be seen in the bottom of Figure 2.4. One can notice that the two halves of a module partly overlap in the closed VELO configuration, in order to achieve a better geometrical coverage. Each half of the VELO is enclosed in a box of thin aluminium maintaining the vacuum around the sensors. The inner faces of the vessels, called RF-foils, separate the VELO vacuum from the machine vacuum, also protecting the sensors from RF background of the machine. The RF-foils are designed to minimise the material traversed by a charged particle before it crosses the sensors, in order to have a negligible impact on the VELO performance.

The modules are composed of two planes of 220 μm thick silicon micro-strip sensors able to measure the distance from the beam (radial distance, R) and the azimuthal angle ϕ of hits generated by the ionizing particles that cross the VELO. The choice of the cylindrical coordinate system was initially made with the idea of speeding up the tracks reconstruction used in the trigger. In fact, active sensors with similar ϕ values are most probably coming from the same particle. However, this feature is useful only for tracking in one dimension (R) and turned out not to be optimal. For this reason, for the design of upcoming VELO a pixel detector has been considered, as described in Section 2.7.1. The structure of such R and ϕ sensors is reported in Figure 2.5. The third coordinate z is simply given by the module position. The R-sensor strips are concentric rings with a variable pitch that increases linearly from 38 µm at the inner edge to 102 µm at the outer edge. The ϕ-sensor strips are wedge-shaped and divided into regions at $r = 17.25$ mm in order to reduce the occupancy and to avoid large strip pitches at the outer edge of the sensors, that would reduce the hit resolution. The strips have a pitch of 38 µm in the inner region (increasing to 78 µm at the outer edge), while the strips in the outer region have a pitch of 39 µm (increasing to 97 µm at the outer edge). To reduce ambiguities in the pattern recognition, the ϕ-sensor strips are 20° skewed from the radial direction in the inner region and 10° in the outer region.

The resolution on the position of the PV obtained with VELO tracks varies between 9 µm and 35 µm for the x and y coordinates, and between 50 µm and 280 µm for the z coordinate, depending on the number of tracks used to reconstruct the vertex. Typical events with 25 tracks originating from the PV have a transversal resolution of $\sim 15\,\mu$m and a longitudinal resolution of $\sim 71\,\mu$m.

Another important parameter measured by the VELO is the impact parameter (IP). The IP is defined as the distance of closest approach of the extrapolated particle trajectory to the PV and it is illustrated in Figure 2.6 on the left. It is extensively used in the physics analyses to discriminate between signal and combinatorial background tracks. Indeed, signal particles, typically produced in the decay of a b-hadron having a displaced secondary vertex, will have a higher IP with respect to the background particles coming from the primary vertex. The VELO has the highest resolution on the IP of the charged

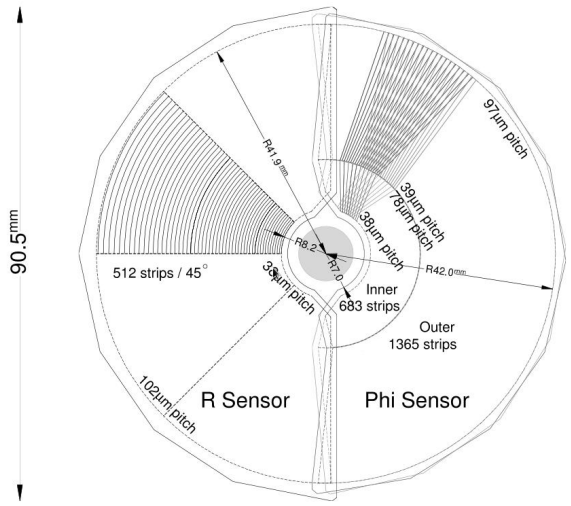

Figure 2.5: Sketch illustrating the R (left) and ϕ (right) geometry of the VELO sensors. In the ϕ-sensor, the strips on two adjacent modules are indicated, to highlight the stereo angle [76].

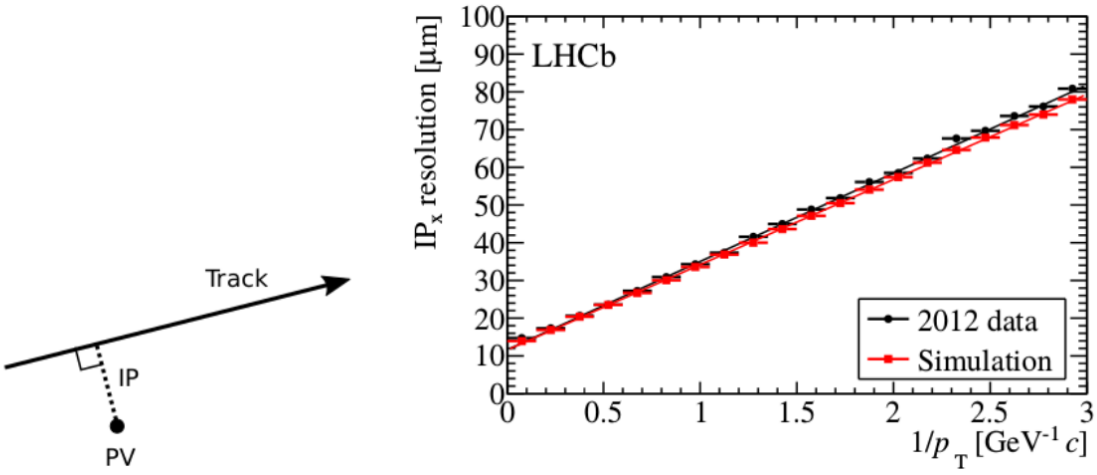

Figure 2.6: (left) Illustration of the IP (length of the dotted line) of a track (solid line) in relation to the PV. The figure is drawn in the plane containing the track and the PV. (right) IP resolution as a function of $1/p_{\mathrm{T}}$ from simulation (red) and data (black).

tracks among the LHC experiments, varying between 10 μm and 80 μm, depending on the transverse momentum of the considered track. The dominant uncertainty on the IP is due to the multiple scattering of the tracks crossing the VELO modules. Hence, an inverse relation with the p_T of the track is expected and observed, as shown in Figure 2.6 on the right.

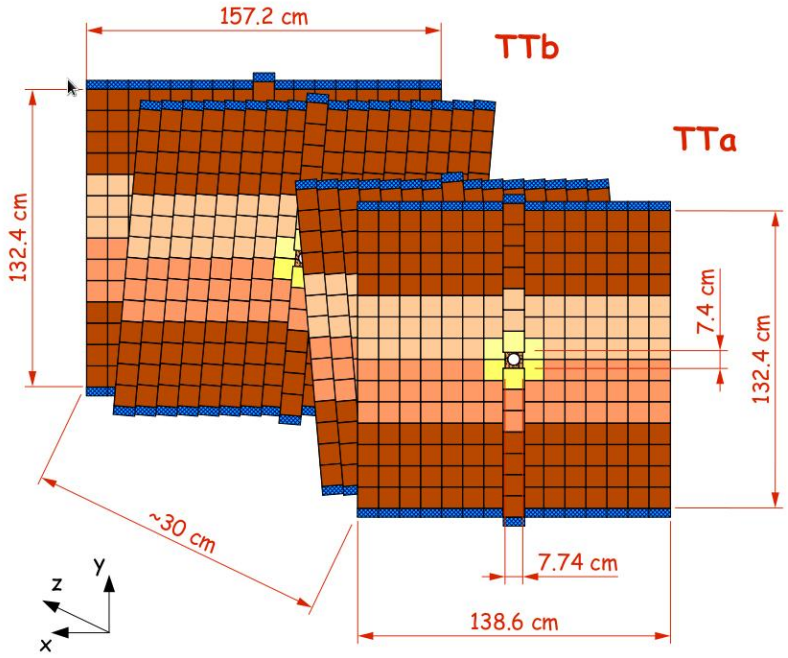

Figure 2.7: Design of the Trigger Tracker sub-detector. The first and the fourth stations have sensor parallel to the vertical plane, while the second and third stations have sensors tilted by +5° and -5°, respectively [83].

2.3.2 The Tracker Turicensis

The Tracker Turicensis[2] (TT) [82] plays an essential role in the trigger and is placed after RICH1 and immediately before the magnet. Its primary goal is to provide reference segments used to combine the track reconstructed in the tracking stations with those reconstructed in the VELO, in order to improve the momentum and coordinate resolution. In fact, in the space between the VELO and the TT stations an integrated magnetic field of 0.15 Tm is present. This allows to resolve the charge ambiguity of the particles and speed up the reconstruction process by a factor 2. The TT also permits to reconstruct the decay vertex of neutral hadrons decaying outside the VELO acceptance, such as the K^0_S or the Λ.

The system is composed by four stations, divided in two groups called TTa and TTb, respectively, at a distance of about 30 cm one from the other and placed approximately 2.4 m after the beam interaction region. A detailed scheme of this sub-detector is shown in Figure 2.7. Each of the four stations covers a rectangular region of about 120 cm in

[2]Initially named Trigger Tracker, takes the name from the University of Zurich, Turicum in latin, which gave the largest contribution to its development.

height and about 150 cm in width. A TT detector layer is composed of silicon micro-strip sensors with a 183 μm pitch, arranged in readout strips up to 38 cm long, to keep the number of readout channels low. In the first and fourth stations the strips are parallel to the vertical plane, while in the second and in the third stations they are tilted by +5° and -5°, respectively. This is done to improve the precision of the track reconstruction. The main advantage of this detector design is that all the front-end electronics and the cooling infrastructure are located outside of the acceptance of the experiment, above or below the active area of the detector.

2.3.3 The tracking stations

The three Tracking Stations T1, T2 and T3 are placed behind the magnet. They are divided in two main parts, depending on the distance from the beam pipe. The inner part of the Tracking Stations is called Inner Tracker (IT), while the outer part is called Outer Tracker (OT). They adopt different technologies to detect particles, motivated by the unbalance in the particle flux within the LHCb acceptance: the former is composed of silicon micro-strips sensors, while the latter consists of drift straw tubes.

The Inner Tracker [84] covers the region around the beam pipe and it is arranged in a cross-shaped geometry, that grants optimal coverage while conserving surface. Each station consists of four independent boxes arranged as shown in Figure 2.8. As for the TT, the first and fourth planes of the IT have the sensors parallel to the vertical plane, while the second and the third have the sensors tilted by +5° and -5°. Each IT layer consists of seven detector modules made of silicon micro-strips having a pitch of 196 µm. The side boxes have two layers, where the lower sensors are connected in series with the upper sensors to a single readout channel, while the top and the bottom boxes have only one micro-strip layer. The total IT size is about 1.2 m in the bending plane and about 40 cm in the vertical plane. Unlike the TT, the front-end electronics and the cooling systems are inside the LHCb acceptance.

The Outer Tracker [85] is a gas-filled straw tubes detector, covering about 99% of the summed surface of the T1-T3 tracker stations. For each tracking station there are four planes of straw tubes arranged in the same way as the TT and IT silicon micro-strips. Moreover, each plane is composed of two rows of tubes, arranged in a honeycomb structure, as shown in Figure 2.9. The straw tubes have a radius of 5 mm and are filled with a mixture of Ar-CF_4-CO_2. At the tube ends, locator pieces support and centre the anode wire with a precision better than 100 μm. Unlike other tracking detectors here described, the OT measures drift times rather than pulse heights. The readout time window exceeds a single LHC bunch crossing interval due to the limited drift speed of the gas mixture. The OT resolution is better than 200 μm.

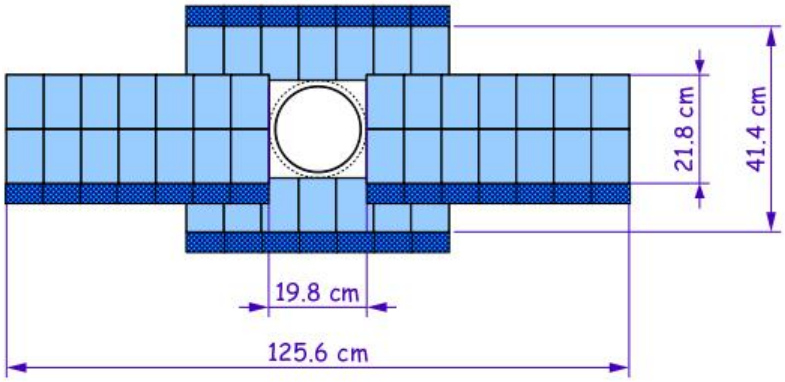

Figure 2.8: Inner Tracker layer with vertically oriented micro-strip sensors. The four boxes are arranged around the beam pipe and the individual sensors inside the boxes are visible. The deep blue part of each box represents the readout plugs [83].

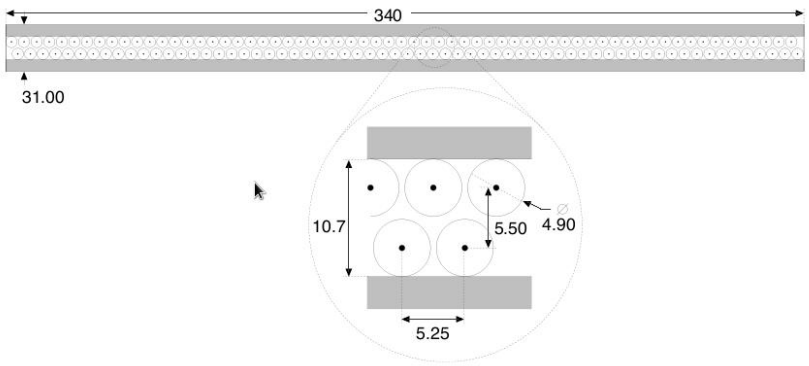

Figure 2.9: Cross section of a straw-tubes module [76].

2.3.4 The LHCb dipole magnet

All modern experiments measure particle momenta through their curvature in a given magnetic field. For this reason, the LHCb detector is provided with a warm (*i.e.* non superconducting) dipole magnet placed between the TT and the first tracking station T1, as can be seen in Figure 2.3. The magnet is formed by two coils placed with a small angle with respect to the beam axis, to increase the opening window with z in order to follow the acceptance of the LHCb detector. The main component of the magnetic field is along the y-axis as shown in Figure 2.10 and thus the xz-plane can be considered with good approximation as the bending plane. The maximum magnetic field strength is above 1 T, while its integral is about $\int \vec{B} \cdot d\vec{l} = 4$ Tm. All the tracking detectors are located outside the magnetic dipole, as shown in Figure 2.10. The magnetic field is

measured before the data-taking periods with Hall probes to obtain a precise map, which is crucial to have a good momentum resolution and consequently a good mass resolution.

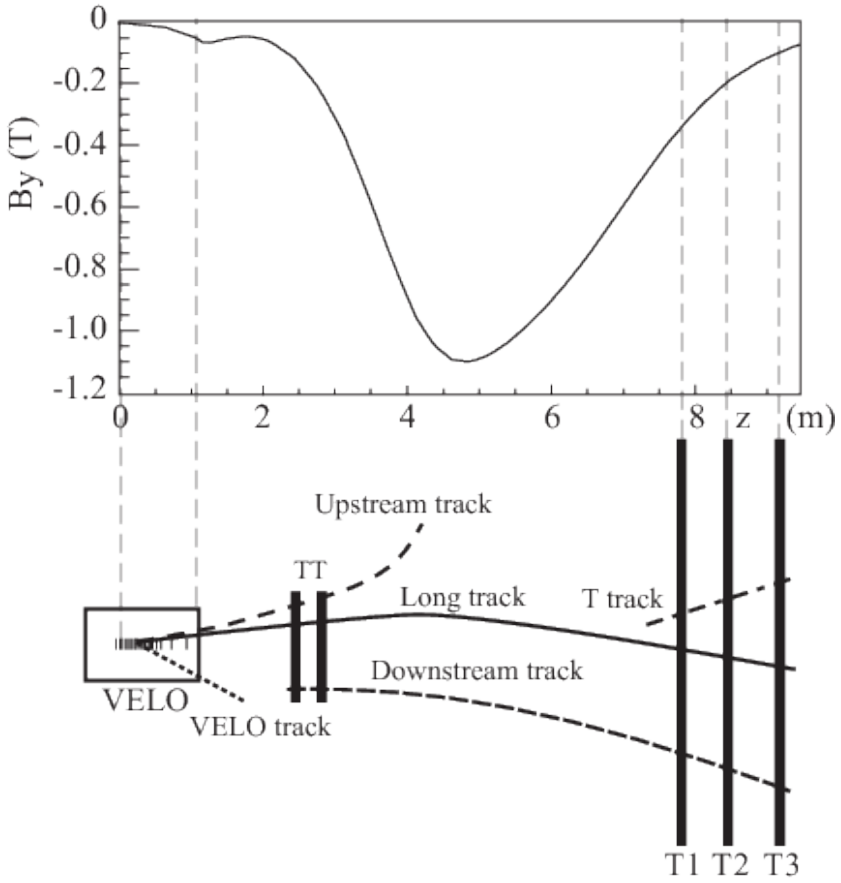

Figure 2.10: Sketch illustrating the various track types: long, VELO, upstream, downstream and T tracks. For reference the main B-field component (B_y) is plotted above as a function of the z coordinate [86].

Among the main LHC experiments, the LHCb detector has a unique feature consisting in the possibility to reverse the polarity of the magnetic field (*MagUp* or *MagDown*). This allows a precise control of the left-right asymmetries introduced by the detector. Indeed, particles hit preferentially one side of the detector, depending on their charge, thus generating non-negligible asymmetries if the detector is not completely symmetric[3]. If data samples collected with the two different polarities have approximately equal size and the operating conditions are stable enough, effects of charge asymmetries are expected

[3]This happens for the material distribution of the IT support system (structure, cables and cooling) which is found to be a source of charge asymmetry for hadrons [87].

to cancel. The magnet polarity is therefore reversed approximatively every two weeks to meet these constraints.

2.3.5 Tracking algorithm and performances

The tracks are divided in five categories, as reported in Figure 2.10.

VELO tracks: Particles generating at least three hits inside the VELO. If possible, these tracks are extended to the other subdetectors, then forming upstream or long tracks, defined below. Particles that have been produced with a wide angle with respect to the beam pipe exit from the detector geometrical acceptance just after the VELO. For most physics analyses, VELO tracks that are not extended are only used for the reconstruction of primary vertices.

Upstream tracks: These tracks are generated by particles with a low momentum, that produce hits in the VELO and in the TT, but are kicked off the geometrical acceptance of the detector by the magnetic field. However, the momentum of these particles can still be determined thanks to the residual magnetic field present between the VELO and the TT, even if the measurement is affected by a 15% relative uncertainty.

Downstream tracks: Long lived neutral particles can decay between the VELO and the TT, producing charged particles that generate hits only in the TT and in the tracking stations. These are the so-called downstream tracks.

T tracks: Particles generating hits only in the tracking stations. If possible, these tracks are extended to long tracks or downstream tracks.

Long tracks: They are made out of hits in both the VELO and the tracking stations. Long tracks must meet the requirements for both a T track and VELO track. When possible, hits from the TT are added, improving the momentum resolution. Long tracks have an accurate momentum measurement and form the main track type used in physics analyses. For particles with $p < 10$ GeV/c, a momentum resolution of $\delta p/p \approx 0.5\%$ is achieved, increasing to 1.0% at 200 GeV/c.

Long tracks are reconstructed with two algorithms: the first extrapolates VELO segment to the tracking stations, adding to the track the compatible hits in the TT. The second matches VELO and tracking station segments one to each other, extrapolating VELO segments in the forward direction and tracking station segments in the backward direction. Downstream tracks are reconstructed starting from tracking station segments and then adding the compatible hits in the TT to those segments. Upstream tracks are obtained extrapolating VELO segments to the TT, adding compatible hits and requiring a non-compatibility with any of the tracking station segments.

To protect against incorrectly reconstructed tracks, which are called "ghosts" and are composed of unrelated hits, all tracks must satisfy a number of quality requirements. They are based on the χ^2 from the track fitting, the kinematic properties and the number of hits for each tracking detector. Finally, a clone-killer algorithm compares the reconstructed tracks, two by two: if a pair of tracks shares more than a fixed percentage of hits they are considered clones and only that with more hits (or the best χ^2) is stored.

2.4 The LHCb particle identification system

In this section all the LHCb sub-detectors used for the particles identification (PID) are described. They consists in two Ring Imaging Cherenkov (RICH1 and RICH2) detectors, the electromagnetic calorimeter (ECAL), the hadronic calorimeter (HCAL) and finally the muon stations.

2.4.1 The RICH detectors

Particle identification is of fundamental importance in *CP* violation measurements. The LHCb experiment exploits two RICH detectors, the first one installed immediately after the VELO and the second one positioned after the tracking stations, to discriminate between charged pions, kaons and protons in a momentum range from few GeV/c up to about 150 GeV/c. Cherenkov light detectors exploit the light emitted by particles that travel in a medium faster than light in the same medium. The relation between the Cherenkov photon emission angle $\theta_{\check{c}}$ and the refraction index n of the radiator is

$$\cos\left(\theta_{\check{c}}\right) = \frac{1}{\beta n}, \tag{2.1}$$

where $\beta = v/c$ is the particle velocity relative to the speed of light in the vacuum. The Cherenkov light emission only occurs when the particle exceeds the threshold value of $\beta_{th} = 1/n$ (*i.e.* $\theta_{\check{c}} = 0$) while each radiator has a maximum emission angle $\theta_{\check{c}}^{max} = \arccos\left(1/n\right)$ which is obtained when $v = c$. It is evident that for particles approaching the speed of light the Cherenkov angle will saturate to $\theta_{\check{c}}^{max}$ and it is therefore necessary to have different radiators in order to discriminate particles in a wide range of momenta.

The RICH1 [76] is optimized to identify tracks with a relatively low momentum, between 1 GeV/c and about 50 GeV/c. The structure of the apparatus is reported in the left part of Figure 2.11. The geometrical acceptance (from 25 mrad to 330 mrad) of the device is enough to cover the whole LHCb detector acceptance. During Run 1, there were two different types of radiators inside RICH1: the first was a 5 cm thick Aerogel layer with $n = 1.03$, suitable for low momentum particles, while the second was gaseous (C_4F_{10}) with $n = 1.0015$ filling the remaining part of the detector and was employed to detect particles with higher momenta. The Aerogel radiator was removed

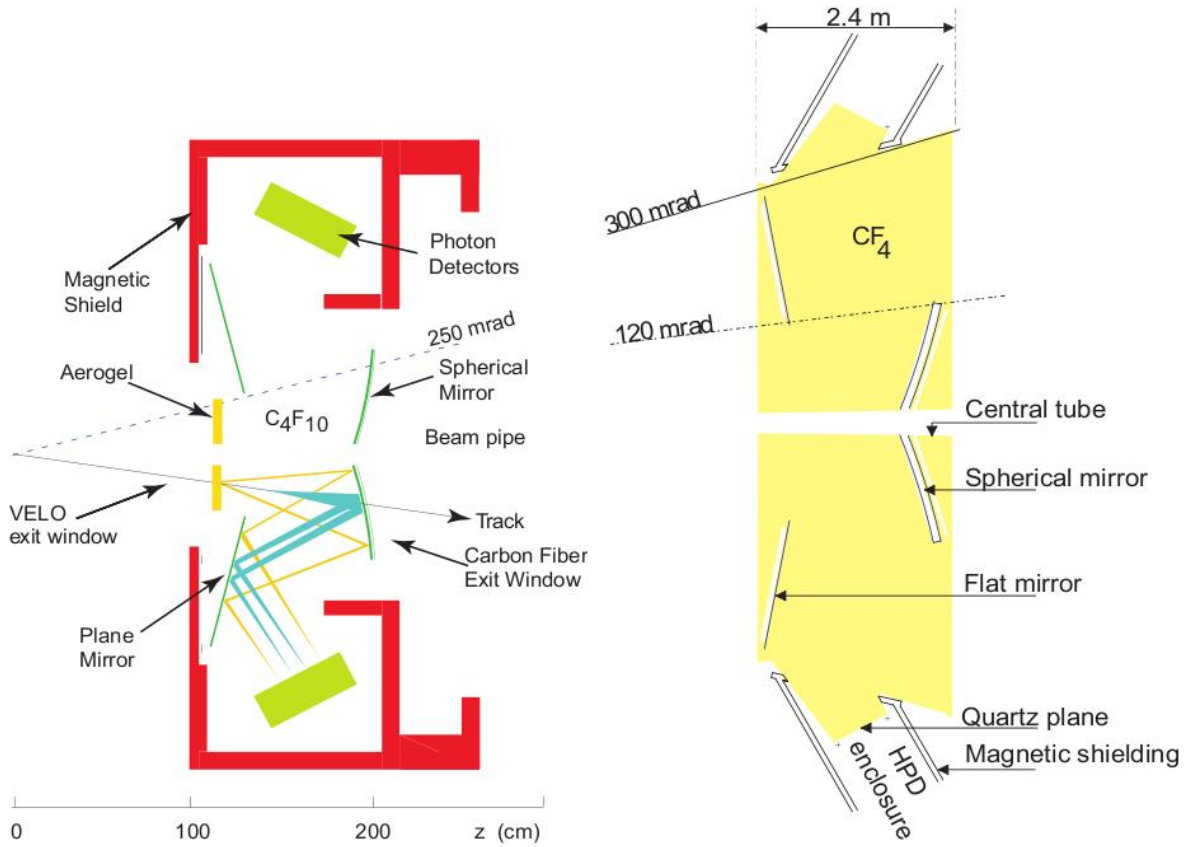

Figure 2.11: (left) Schematic view of the RICH1 sub-detector [76]. The Cherenkov light is emitted with different angles from the Aerogel (yellow) and the C_4F_{10} (light blue) radiators. (right) Schematic view of the RICH2 sub-detector, filled with CF_4 gas [76].

in the operational shut down before Run 2 as its ability to provide particle ID was compromised by the total number of photons in RICH1 in such a high track multiplicity environment [88].

The structure of the RICH2 [76] sub-detector is reported in the right part of Figure 2.11. Its geometrical acceptance, ± 120 mrad (horizontal) and ± 100 mrad (vertical), covers the region of the detector where most of high momentum particles are found. The radiator chosen is CF_4 with a refraction index $n = 1.00046$, optimal for the higher momentum, up to about 150 GeV/c.

In both the detectors, the Cherenkov light is focused, through a system of spherical and plane mirrors, onto a lattice of photo detectors, the Hybrid Photon Detector (HPD). The HPDs are placed in both the RICH sub-detectors, outside the experiment acceptance and they are shielded against the residual magnetic field. Indeed, the photo-electrons created in the photomultipliers would be bent by the residual magnetic field reducing

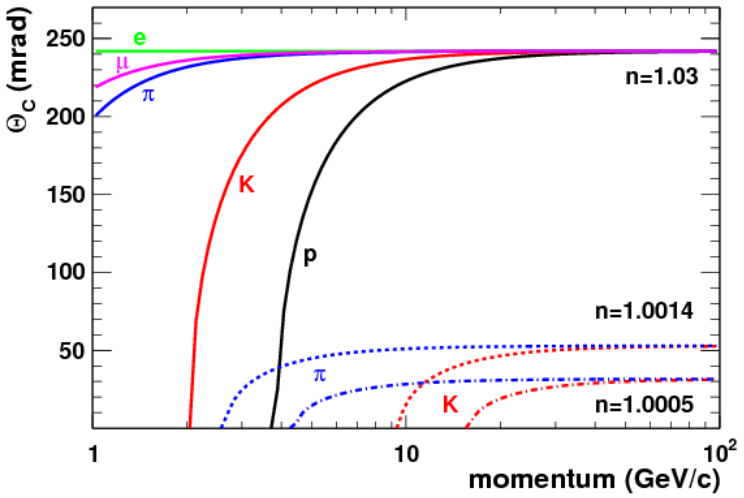

Figure 2.12: Cherenkov angles as a function of momentum for different particle species and for the three different values of the refractive index n corresponding to the three radiator materials used in the RICH setup [89].

the HPD's performances.

Particle identification method

RICH detectors are able to discriminate between the various mass hypothesis for a given particle. In fact, as shown in Figure 2.12, the photon emission angle is related to the particle mass and to its momentum. Since the Cherenkov light emission covers the full solid angle, rings with radius proportional to $\theta_{\check{c}}$ are expected on the HPD plane. Measuring the photons hit positions, it is then possible to discriminate the various mass hypotheses.

Due to an irreducible background, given by photons coming from other particles, and due to the complexity of the problem, the following approach has been chosen to achieve the best particle discrimination. For a given set of mass hypotheses, the probability for a single photon to be detected on a single HPD pixel is computed; then, the expected contribution from all sources is compared with the observed number of photons and a likelihood is calculated (the change in the likelihood value depends only on the mass hypothesis assigned to the tracks). Only five mass hypotheses are considered for the tracks detected: electron, muon, pion, kaon and proton. Since the computation of the likelihood for all tracks would be unfeasible, a different approach is adopted. In fact, the pion mass hypothesis is used for all the tracks detected and a first global likelihood is computed. Then the hypothesis is changed to e, μ, K and p for one particle at a time and the change in the global likelihood is computed. The chosen mass hypothesis is the

one that returns the maximum improvement in the global likelihood. This process is repeated for all tracks, until no improvement is observed in the likelihood value.

The discriminating variable is the so-called $\Delta \log(\mathcal{L})_{X-\pi}$ which is the difference between the logarithm of the likelihood under the X (e, μ, K or p) and π hypothesis for the observed track:

$$\Delta \log(\mathcal{L})_{X-\pi} = \log(\mathcal{L}_X) - \log(\mathcal{L}_\pi). \tag{2.2}$$

For example, a large positive value of $\Delta \log(\mathcal{L})_{K-\pi}$ corresponds to a high probability that the particle is a kaon, while a large negative value corresponds to a high probability that the particle is a pion.

The efficiency of this discriminating method had been widely studied using real data sample with high purity final states selectable only using kinematical cuts, due to their particular kinematic characteristics (*e.g.* $K^0_S \to \pi^+\pi^-$, $\Lambda^0 \to p\pi^-$, and $D^{*+} \to D^0(\to K^-\pi^+)\pi^+$).

2.4.2 The calorimeters system

The calorimeters system [90] is used to measure hadron, electron and photon energies, thus giving information for their identification. Moreover, it provides important information for the Level-0 trigger (L0), evaluating hadron, electron and photon transverse energy E_{T}. The calorimeters system is divided into four sub-detectors:

- Scintillator Pad Detector (SPD).
- Pre-Shower (PS).
- Electromagnetic Calorimeter (ECAL).
- Hadronic Calorimeter (HCAL).

A sketch of the calorimeters system and the response of each detector with the particle types is reported in Figure 2.13. Each sub-detector is divided into regions where differently sized sensors are used. SPD, PS and ECAL are divided in three regions (inner, middle and outer), while HCAL is divided only in two regions (inner and outer). The sensor size increases as the distance from the beam pipe is greater to reach a compromise between occupancy and the number of readout channels.

The SPD and the PS are auxiliary sub-detectors of the Electromagnetic calorimeter and they are placed in front of it. The SPD is used to discriminate between charged and neutral particles, as the former emit light when crossing a scintillator material while the latter do not. The PS is instead used to obtain a better discrimination between electrons and pions. Both the sub-detectors consist of scintillating pads with a thickness

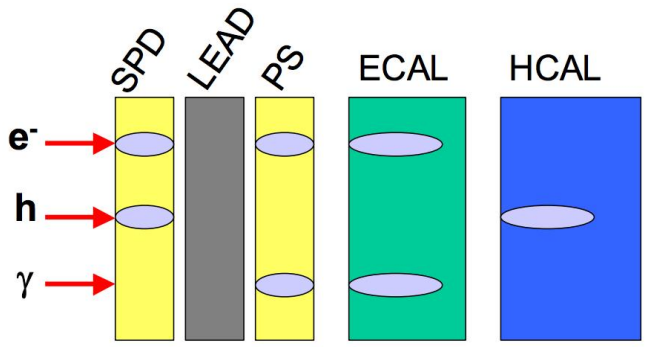

Figure 2.13: Signal deposited on the different parts of the calorimeter by an electron, a hadron and a photon [76].

of 15 mm, inter-spaced with a 2.5 radiation lengths[4] lead converter. The light produced by the scintillator material is collected using wavelength-shifting fibers (WLS). These fibers are used to transmit the light to multi-anode photomultipliers (MAPMTs) located outside the detector. The SPD and PS contain about 6000 pads each.

The ECAL is a sampling calorimeter separated in independent modules. In each module, the scintillation light is read out via WLS fibers running perpendicularly to the converter/absorber plates: this technique offer the combination of an easy assembly, good hermicity and fast time response. A sketch of the ECAL is given in Figure 2.14. Each ECAL module is composed of 66 lead converter layers (2 mm thick), each one installed between two plastic scintillator layers 4 mm thick. In total, all the layers installed in the ECAL correspond to about 25 radiation lengths and 1.1 nuclear interaction lengths[5]. The WLS fibers bring the light produced by the scintillator material to the readout photomultipliers in the back part of the module. The module size and the number of

[4]The radiation length is defined as

$$X_0 = \frac{A \cdot 716.4 \text{ g/cm}^3}{Z(Z+1)\ln(287\sqrt{Z})}$$

where A is the mass number and Z is the atomic number of the considered material. The radiation length corresponds to the distance over which the energy of an electron is reduces by a factor $1/e$ only due to radiation loss.

[5]The nuclear interaction length is defined as

$$\lambda = \frac{A}{N_A \rho \sigma_{inel}}$$

where N_A is the Avogadro constant, A is the mass number and ρ is the density of the considered material while $\sigma_{inel} \sim \sigma_{pp} A^{2/3}$ is the inelastic cross section between the particle and the nucleus. The nuclear interaction length is the mean path length required to reduce the numbers of relativistic charged particles by the factor $1/e$ as they pass through matter.

readout channels differ depending on the region where the module is installed. In the inner region each module has a section of 4×4 cm^2 and 9 readout channels. Finally, the outer region is composed of 12×12 cm^2 modules with one channel each.

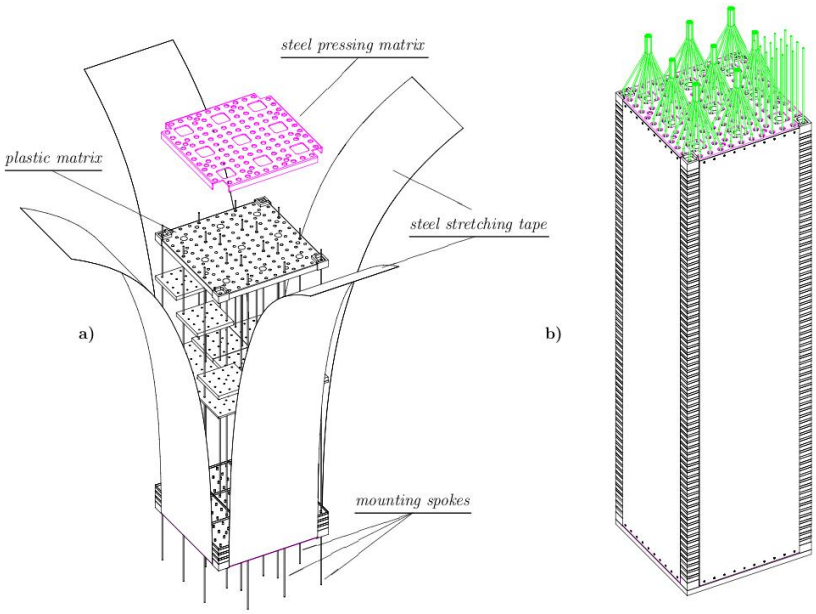

Figure 2.14: (left) Representation of an ECAL module during the assembly phase. The lead/scintillator layers are clearly visible. (right) Representation of an assembled ECAL module. The green lines connected to an end are the WLS fibers connecting the calorimeter to the photomultipliers [90].

The HCAL main task is to measure the energies of hadronic showers. This information is fundamental for the Level-0 trigger. The HCAL structure is very similar to the ECAL structure, with the difference that each module is composed of scintillator layers 4 mm thick interleaved with steel layers 16 mm thick. This corresponds to roughly 5.6 nuclear interaction lengths in total. In the inner region modules have a section of 13×13 cm^2, while in the outer region their dimensions are 26×26 cm^2.

The calorimeters system performances have been evaluated from many test beams made before the start of the data taking. Energy resolutions are given by $\sigma(E)/E = \frac{(8.5-9.5)\%}{\sqrt{E}} \oplus 0.8\%$ for ECAL and $\sigma(E)/E = \frac{(69\pm5)\%}{\sqrt{E}} \oplus (9 \pm 2)\%$ for HCAL. The ECAL calibration is achieved by reconstructing resonances decaying to two photons like $\pi^0 \to \gamma\gamma$ and $\eta \to \gamma\gamma$. Calibration of the HCAL can be realized by measuring the ratio E/p between the energy E measured in the calorimeter for a hadron with momentum p, measured by the tracking system.

2.4.3 The muon system

The final part of the LHCb detectors consists of five muon stations, that altogether form the muon sub-detector [91]. Muons with high p_{T} are very important particles since several final state products of B-hadron decay chains contain muons. The five stations (M1-M5) cover an angular acceptance of ± 300 mrad in the horizontal plane and ± 200 mrad in the vertical plane. The geometrical efficiency for the detection of muons coming from B-hadrons is nearly 46%. The first muon station M1 is placed before the calorimeters, to avoid possible muon multiple scattering effects, that could modify the particle trajectory. The remaining stations (M2-M5) are placed after the calorimeters system, at the end of the LHCb detector. A schematic view of the muon sub-detector is reported in Figure 2.15.

Each muon station is divided into four regions (R1-R4) around the beam pipe. The dimensions of the chambers increase as they are more and more distant from the beam pipe. Moreover, also the segmentation of each region increases as the distance from the beam pipe becomes grater in a ratio 1:2:4:8. In this way, the charged particle occupancy is expected to be about the same in each region. All the chambers are Multi-Wire Proportional Chambers (MWPCs), except for the inner region of the M1 station where Gas Electron Multipliers (GEMs) detectors are employed. The latter consist of three GEM foils sandwiched between anode and cathode planes. MWPCs have four overlapped gaps, each one 5 mm thick and with a distance between wires of about 2 mm. In total, the muon detector contains 1380 MWPCs.

For each hit, a straight line is extrapolated to the interaction region defining a "field of interest", that takes into account also the magnetic field kick, around such a trajectory. Hits coming from long and downstream tracks that are found around the extrapolated trajectory are fitted together to form a muon track. To consider the track as a muon it is requested to have at least two hits in M2-M5, depending on the momentum of the track. After this, complex algorithms compute the muon likelihood for each muon track, used as a particle identification discriminator.

2.5 The LHCb trigger

As already stated, the production cross-section of $b\bar{b}$ and $c\bar{c}$ pairs are quite large and together they account to about 10% of the total pp inelastic cross-section. This means that a good trigger system is needed in order to accept only the interesting events while rejecting at the same time most of the background events. The LHCb trigger has been developed to work at the bunch crossing frequency of the LHC. The only way to reach the desired performances is to divide the trigger into different levels, each processing the output of the previous [92]. The LHCb trigger system is divided into three levels.

Level-0 (L0): this is the first trigger level and it is based on custom electronics. It is

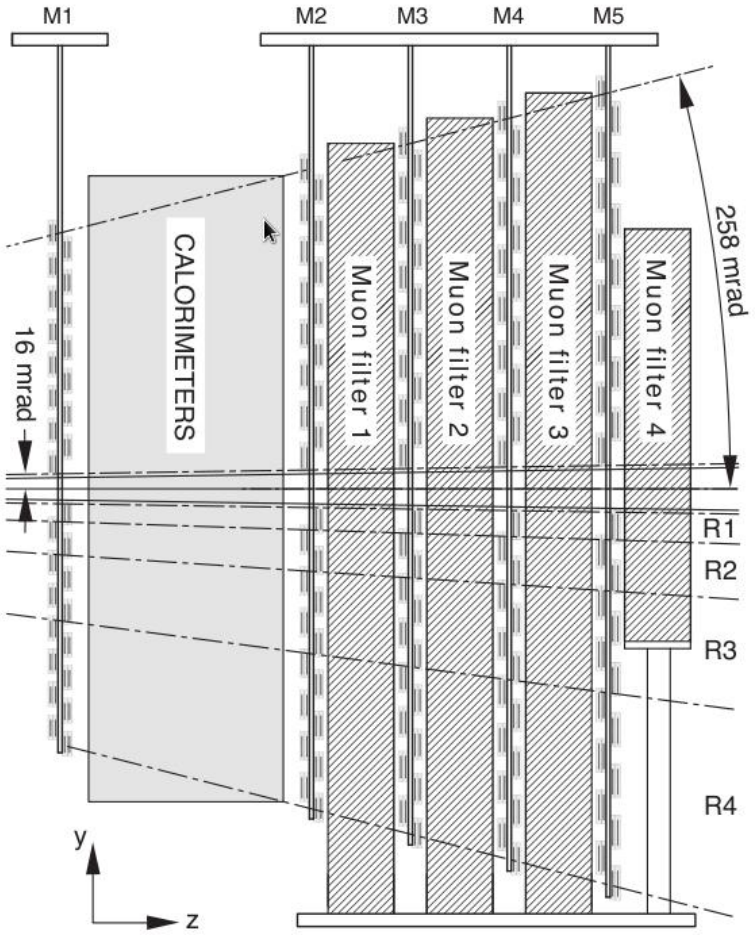

Figure 2.15: Lateral view of the muon detector. The first muon station M1 is placed before the calorimeters while the other stations are placed at the end of the LHCb detector [91].

designed to perform a first filtering of the events, reducing the input rate of about 40 MHz to an output rate of only 1 MHz.

High Level Trigger 1 (Hlt1): this is the second trigger level and it is software based. The task of Hlt1 is to filter events in an inclusive way and to reduce the rate of accepted events to 110 kHz.

High Level Trigger 2 (Hlt2): this is the last trigger level and it is completely software based. The Hlt2 applies an exclusive selection of beauty and charm decays, performing a full reconstruction of the events which is finally sent to mass storage. At the beginning of Run 1 Hlt2 operated with an output rate of about 3.5

kHz. Improvements have been made over the years and the output rate have been increased up to about 12.5 kHz.

Combinations of trigger lines for Hlt1 and L0 form a unique trigger configuration key (TCK), that is a 32 bit word pointing to the database that stores all the parameters which configure the trigger lines.

In the LHCb software framework the boolean `TIS`, `TOS` definitions are used to define whether a reconstructed track has fired a trigger line. In particular, `TOS` (Trigger On Signal) means that the particle has fired the trigger while `TIS` (Trigger Independent from Signal) means that in the event (at least) another particle has succeeded the trigger requirements. These definitions also apply to pairs of tracks where requirements on relative quantities are asked. Finally, the definition of `TOS` or `TIS` on one track t_i are extended to the combination of two or more tracks $t_1, ..., t_n$ in the LHCb software framework. While the definition for $\texttt{TOS}(t_1, ..., t_n)$ is trivial, *i.e.*

$$\texttt{TOS}(t_1, ..., t_n) = \texttt{TOS}(t_1) \text{ OR } ... \text{ OR } \texttt{TOS}(t_n), \tag{2.3}$$

the definition of $\texttt{TIS}(t_1, ..., t_n)$ can not be explicitly calculated in terms of $\texttt{TIS}(t_i)$ since it is not known if the triggering particle(s) is within $t_1, ..., t_n$ or not.

2.5.1 The Level-0 trigger

The L0 trigger uses information coming exclusively from the calorimeters system and from the muon system. In fact, at this level, the trigger decides to keep or discard events based on measures of p_{T} and E_{T} of the particles composing the event. The system uses three independent systems running in parallel:

L0Photon/Electron This trigger uses the information given by the SPD, PS and ECAL detectors. Custom boards are programmed to measure the energy of electromagnetic showers. The event is accepted if there is at least one cluster with E_{T} greater than a certain threshold.

L0Hadron This trigger exploits the information given by the HCAL detector. The way in which it works is the same as the electron/photon trigger: the event is accepted if there is at least one cluster with enough transverse energy.

L0Muon It uses the information given by the five muon stations. Tracks are reconstructed defining "field of interest" around particle hits and then connecting hits in the same field of interest. Events are accepted if at least one muon candidate has a transverse momentum exceeding a given threshold. Moreover, the trigger contains a line to select muon pairs, asking that the sum of their transverse momentum is greater than a threshold.

In the LHCb software framework the boolean `L0Global` indicates whether one of L0 trigger lines has been fired. In the measurement presented in this thesis, only the events that succeeded the `L0Global` trigger independently by the signal decay (`TIS`) have been considered, as reported in Tables 3.1 and 3.2.

2.5.2 The High Level Trigger 1

The task of this trigger level is to reduce the input rate from the L0 trigger to a more manageable level. The events are reconstructed, considering that:

- Beauty and charm hadrons and their production mechanism imply that the particles produced in their decays have a large momentum p and transverse momentum p_{T} compared to other hadrons composed by light quarks.
- The average decay length of B (D) hadrons produced at the LHC is about 1 cm (0.3 cm). As a consequence, their decay products will have a large impact parameter (IP) with respect to their primary vertex (PV).
- VELO reconstruction time is fast enough to allow the full information on the primary vertex to be used by the Hlt1.
- The full reconstruction can be performed only for a limited number of tracks due to limited time available.

The last two points are the reason why the reconstruction is divided in two steps. In the first step VELO tracks and PV are reconstructed. After this, a simplified track reconstruction is performed and forward tracks are further selected, requiring minimal p_{T} threshold. Finally, remaining tracks are fitted using a bi-directional Kalman filter[6] with outlier removal, in order to obtain an offline-quality value for the tracks (χ^2) as well as an offline-quality covariance matrix at the first state of the tracks, allowing a cut on the IP significance squared (IP χ^2). Cut on IP χ^2 is very efficient in rejecting background, while track χ^2 is suitable in rejecting ghost tracks.

In the reconstruction of charged hadrons two lines are used for trigger on single- or two-tracks. The single-track line requires the presence of at least one track with high p_{T} and large IP χ^2 with respect to the closest PV. These requirements are embedded in a multivariate variable (MVA). In particular, its parameters have slightly changed over the years of data taking (2015-2018) to reflect the available computing power and the improvements in the reconstruction algorithms. Finally, additional constraints are

[6]The Kalman filter is a recursive method for track finding and fitting. Its particularity is that the track parameters (*e.g.* momentum and direction of the track) are local and are included in the so-called state vector which evolves following the real trajectory of the particle, from the first mesure to the last, including noisy effects (*e.g.* coulomb multiple scattering and energy losses).

applied on the `GhostProbability`[7] of the track and the track χ^2. On the other hand, the two-tracks line requires the presence of two tracks of high p_{T} forming a good-quality vertex that is significantly displaced from their associated PV, defined as the PV to which the IP of the two-tracks combination is the smallest. Also in this case, the selection is based on a MVA that takes as input the χ^2 of the two-tracks vertex fit, the number of tracks with IP $\chi^2 > 16$, the sum of the p_{T} of the two tracks and their flight distance χ^2 with respect to the associated PV. In LHCb jargon, these algorithms are named `Hlt1TrackMVA` and `Hlt1TwoTrackMVA`, respectively. In the measurement of $\mathcal{A}^{CP}(K^-K^+)$, only the reconstructed decays that succeeded these trigger requirements (`TOS`) have been considered, as reported in Tables 3.1 and 3.2.

2.5.3 The High Level Trigger 2

The Hlt2 performs an event reconstruction similar to the off-line reconstruction, using also information from RICH detectors and calorimeters. The Hlt2 includes hundreds of trigger lines, which can be grouped as in the following

Exclusive designed for specific final states, requiring all particles to be reconstructed. These lines are typically used for b-hadrons and c-hadrons directly produced in pp interactions.

Inclusive designed to trigger on partially reconstructed b-hadron decays through topological requirements, for example asking at least for two charged tracks coming from a displaced decay vertex fulfilling requirements on track χ^2, IP and particle identification. Two-body objects are built requiring small distance of closest approach (DOCA) between the two particles in the final state, and in the same way n-body objects are built combining the $(n-1)$-body candidate with another particle.

During Run 2, a new data stream was introduced in Hlt2, called *Turbo stream* [93]. This stream is suitable for decays that are fully reconstructed in Hlt2. In fact, the information from the rest of the event is discarded to save storage space, in contrast to what happens for the *Full stream* (*i.e.* the default way of storing data). The sample of data used in this thesis for the measurement of $\mathcal{A}^{CP}(K^-K^+)$ comes from various Turbo stream lines, as described in Section 3.3.

[7] This variable represents the outcome of a Neutral Network used to assign a probability to the track for being a fake. It includes the following track variables: χ^2 probability of the Kalman filter, number of VELO hits, number of TT hits, η and number of tracks of the event.

2.6 Data management and computing

The basic LHCb computing model is based on a series of distributed multi-tier regional centres of different dimensions. LHCb (as well as the other three major experiment at the LHC) requires a large amount of memory disks as well as CPU power in order to store and process the data coming from the detector and to perform analysis task (*e.g.* ntuple production). The computing system is divided in different tiers dedicated to specific duties. The Tier0 is the CERN data centre and provides to LHCb about 20% of the total resources required by the experiment and it is connected to the Tier1 centres via a private network of 10 Gbit/s optical-fiber links (LHCOPN). Moreover, Tier0 stores the RAW data, also providing a copy distributed among the Tier1 centres. There are 6 LHCb Tier1 centres worldwide that are responsible for storing a proportional share of raw and reconstructed data, as well as performing large-scale processing and storing the corresponding output. Furthermore, the Tier1 centres have to distribute the data to the Tier2 centres and to store a part of the simulated data coming from them (*i.e.* Tier2 centres mainly provide CPU resources). Each Tier1 is connected to a number of Tier2 centres, usually in the same geographical area. Finally, Tier3 resources consist of clusters in research centres or university departments across the globe; they are dedicated to specific jobs needed by the research team who owns them. The whole system is collectively referred to as the World LHC Computing Grid (WLCG).

2.6.1 Data processing

The data processing involves several phases that normally follow each other in a sequential manner. The real raw data come from the detector and they are reconstructed via the online Event Filter Farm. Obviously, the first step is to collect the events of interest with an appropriate trigger system. The raw data are then processed using optimized and highly specialized algorithms implemented by the Hlts. The software applies the necessary calibration corrections during the reconstruction of the properties of the particle and imposes requirements based on physics criteria. The raw events accepted by the trigger are then transferred to the CERN Tier0 centre in order to be archived and afterwards forwarded to the Tier1 centres for further processing.

For what concerns the simulated data, the events are generated from a simulation of the LHCb detector, that includes the best understanding of the LHCb detector response, trigger response and passive material budget. The format of this type of data is the same of raw data.

Whether the data are real or simulated, they must be reconstructed in order to provide physical meaningful quantities: for example, one must determine the energy of electromagnetic and hadronic showers measuring calorimeter clusters, or hits in the tracking system have to be associated to tracks. Furthermore, the information about PID coming from the RICH sub-detectors must also be reconstructed to provide particle

identification. The reconstruction process produces a new type of data, the so-called Data Summary Tape (DST).

The information contained in the DST (tracks, energies, clusters, PID) is further analysed with specific algorithms, in order to identify candidates that could form composite particles. These algorithms are designed to select only certain categories of events (*e.g.* the `B2HH` algorithm selects only B candidates decaying to two hadrons) and are called *stripping* lines. Such lines are written for each channel of interest and they produce the output used for further analyses. The output of the stripping stage is referred to as full DST. In addition, an event tag is also created for faster reference to the selected events. The tag contains a little summary of the event characteristics together with the results of the pre-selection algorithms and a reference to the events contained in the DST data set.

In Run 2, few changes to the data flow included the possibility to perform the full event reconstruction in the trigger, thus bypassing the offline reconstruction and discarding the raw event. This new strategy is particularly interesting for charm physics that mostly suffers the trigger output rate constraints. In the *Turbo stream*, the Hlt2 directly writes out a DST containing all information necessary for analyses, and this allows an increased output rate and thus higher average efficiencies. Event pre-selection algorithms (lines) are used for data reduction and designed to identify specific decay channels.

2.7 The LHCb Upgrade-I

After the first phase of operation, from 2010 until 2018 (Run 1 and Run 2), LHCb is currently undergoing a deep upgrade of many crucial sections of the experimental setup [94]. The primary purpose of this upgrade is to take advantage of the increased number of concurrent collisions per beam crossing (pile-up), which will grow from 1.4 to about 5 in Run 3, to access rarer processes or statistically limited measurements. These new operating conditions and an increase in fast hadron fluence motivated the whole upgrade program. Also, in order to cope with more busy events, a new DAQ system, featuring flexible full-software trigger capable of full detector readout at the LHC machine clock, had to be designed, substituting both L0 hardware trigger and high level software trigger and taking decisions on the basis of the full event information. In addition, to increase the number of stored events, it is planned that the raw data will be discarded.

The new vertex detector (VELO), based on silicon pixel sensors, is a vital part of the LHCb upgrade project. It will be readout at 40 MHz and operate at luminosities up to $2 \cdot 10^{33}$ cm^{-2}s^{-1}. The sensitive pixels will be as close as 5.1 mm from the proton beams. The data rates will reach 1.2 Tbit/s, and the maximum 1-MeV neutron-equivalent fluence will reach $8 \cdot 10^{15}$ cm^{-2} at the tip of the innermost sectors. A complete description of the new VELO detector can be found in Ref. [95], while its geometry is presented in the following section.

The Upstream Tracker (UT) [96] will replace the TT, but maintains similar layout. It is based on single-sided silicon strip sensors arranged in four layers in *axial-stereo* configuration. The geometrical acceptance at small polar angles is larger and new silicon sensors with improved radiation hardness and finer granularity are mounted near the beam pipe. The front-end electronics have been redesigned in order to perform the readout at 40 MHz rate.

The IT and the OT will be replaced by the SciFi Tracker based on scintillating fibers that are read out by silicon photomultipliers. The layout and configuration of the SciFi Tracker is similar to the IT+OT configuration.

2.7.1 The VeloPix for Upgrade-I

The upgraded VELO consists of two retractable halves, each of which houses an array of 26 L-shaped silicon pixel detector modules. The two halves are enclosed in RF boxes which separate the machine vacuum from the secondary vacuum in which the modules are located. The building blocks of a module are illustrated in Figure 2.16. Each module contains four silicon sensors consisting in a row of three VeloPix ASICs. Each ASIC is composed by a grid of 256×256 pixels of pitch 55 μm, featuring an sensitive area of 14.08×14.08 mm^2. The thickness of the sensor is 200 μm. A summary of some basic parameters of the Upgrade-I VELO is presented in Table 2.1.

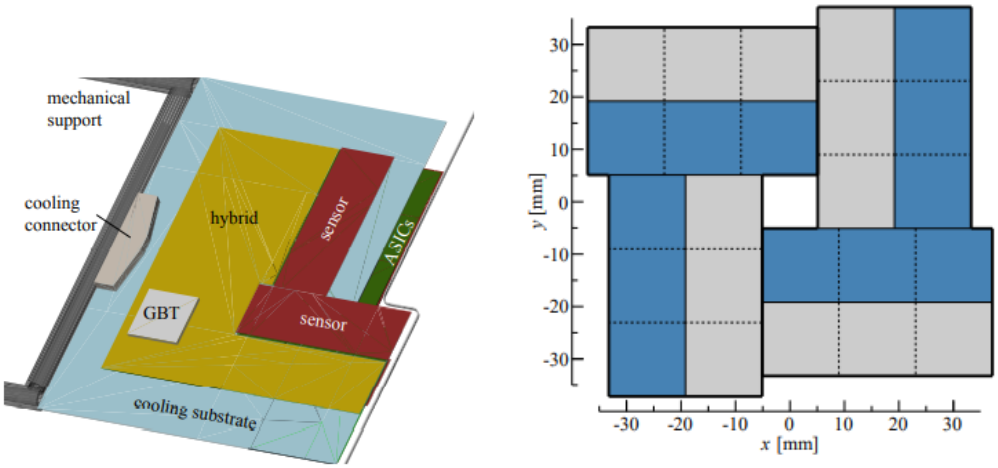

Figure 2.16: (left) Layout of a module, as implemented in the LHCb simulation framework, showing the positions of the major components, including a cross section of the RF foil at the z-position of the module. (right) Schematic layout in the transverse xy plane of each VELO station. Reproduced from Ref. [95].

.

Design parameter	Value
Number of modules	52
Number of ASICs per module	12
Number of ASICs (total)	624
Number of sensors	208
Number of pixels	41M
Number of optical links	1664
Sensor thickness	200 µm
Pixel dimensions	55×55 µm
Position of the first station upstream	-289 mm
Position of the last station downstream	751 mm
Total sensitive area	1243 cm^2
Peak total data rate	2.85 Tbit/s

Table 2.1: System parameters of the Upgrade VELO.

The two assemblies of sensor and ASICs (tiles) which are aligned vertically are mounted on opposite sides of the module, as are the two horizontal tiles. In order to ensure full coverage for angled tracks, the sensitive areas of front and back side assemblies overlap by 110 µm. As the inner horizontal tile is located on the same side

as the outer vertical tile, the latter needs to be displaced by 1 mm with respect to the inner vertical tile, resulting in a small acceptance gap. The inner tiles of left and right module form a square acceptance "hole", with the boundaries of the pixel cells closest to the beam being located at x, $y = \pm 5.1$ mm. After these considerations, a more realistic schematic for the VP detector is reported in Figure 2.17.

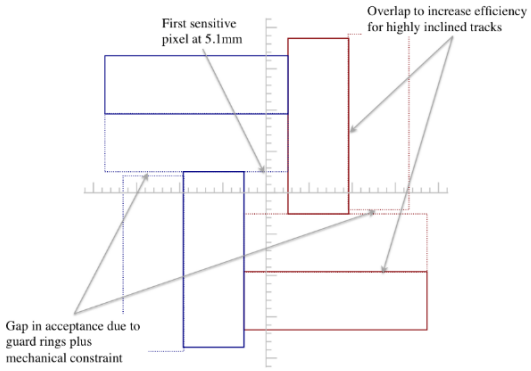

Figure 2.17: Front (x, y) view where a module of each detector half is depicted, *i.e.* they are at different z-positions. The contours of the tiles on the front (back) side of the module of the left half are drawn in solid (dotted) blue. Those of the module on the right half in red. In each module a small gap in the acceptance is visible in the horizontal plane. Tiles on opposite sides of the module are shifted to eliminate a gap for highly inclined tracks.

.

The z-layout is designed so that 99% of tracks within the nominal LHCb acceptance which originate from within $\pm 2\sigma_{lumi}$ of the interaction point cross at least four stations in the VELO. This optimised layout for the upgraded VELO is compared to the current VELO layout in Figure 2.18 and the exact module positions for the upgraded VELO are listed in Table 2.2.

2.8 The LHCb Upgrade-II and the future VELO

A second upgrade of the LHCb detector is also planned, starting operation in 2031 after the Long Shutdown 3, and running at the High-Luminosity LHC [97]. Upgrade-II of LHCb should operate at an instantaneous luminosity of $1.5 \cdot 10^{34}$ cm^{2}s^{-1} [98], which is a factor 7.5 more than Upgrade-I, and is expected to collect an integrated luminosity of $\approx$300 fb^{-1} in about 5 years. At this luminosity the number of interactions in one bunch crossing will be about 50, and the interaction vertices are spatially distributed along the beam direction with a Gaussian profile with a width of about 50 mm. Simi-

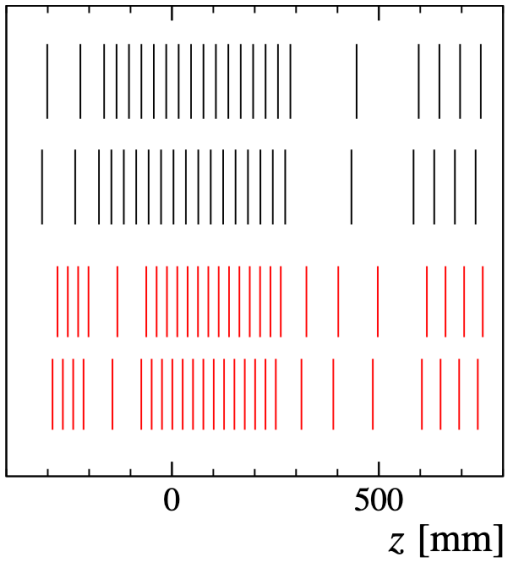

Figure 2.18: Comparison of current and upgrade VELO z-layouts. Top layout (black): current VELO. Bottom layout (red): upgrade VELO optimised with full-simulation.

.

Side	Module z position [mm]								
Left	-275.0	-250.0	-225.0	-200.0	-125.0	-50.0	-25.0	0.0	25.0
	50.0	75.0	100.0	125.0	150.0	175.0	200.0	225.0	250.0
	275.0	325.0	400.0	500.0	600.0	650.0	700.0	750.0	
Right	-287.5	-262.5	-237.5	-212.5	-137.5	-62.5	-37.5	-12.5	12.5
	37.5	62.5	87.5	112.5	137.5	162.5	187.5	212.5	237.5
	262.5	312.5	387.5	487.5	587.5	637.5	687.5	737.5	

Table 2.2: Optimised z-positions of the 52 modules of the VELO upgrade, split by side. The left side is in the positive x-direction while the right side and is in the negative x-direction. The z-positions are given in mm from the interaction point.

larly, the temporal distribution of the vertices is about 200 ps wide. To cope with this high track density and to be able to efficiently reconstruct tracks, a major upgrade of the LHCb detector is needed. Besides a new large area pixel detector after the dipole magnet, additional detectors are placed inside the magnet to enhance low momentum particle reconstruction, and also a time-of-flight detector (TORCH [99]) is added for low momentum particle identification. The key change for the experiment is, however, that timing information is added to many of the sub detectors to aid in disentangling the multitude of interaction vertices from a single bunch crossing. Timing will be added to

the RICH detectors, the calorimeter and the vertex detector, which is the subject of the work presented in Chapter 4.

The role of the VErtex LOcator (VELO) is absolutely central for the physics goals described in the Upgrade-II physics case [74]. It has to efficiently and accurately reconstruct the primary and decay vertices in a high track density environment. Besides the higher track rate and larger radiation fluence, the main challenge is to add timing to the tracks in order to obtain the same physics performance for Upgrade-II as for Upgrade-I. A few examples are given here, with reference to Figure 2.19, to underline why it is essential to maintain, and ideally to improve, the VELO Upgrade-I performance levels.

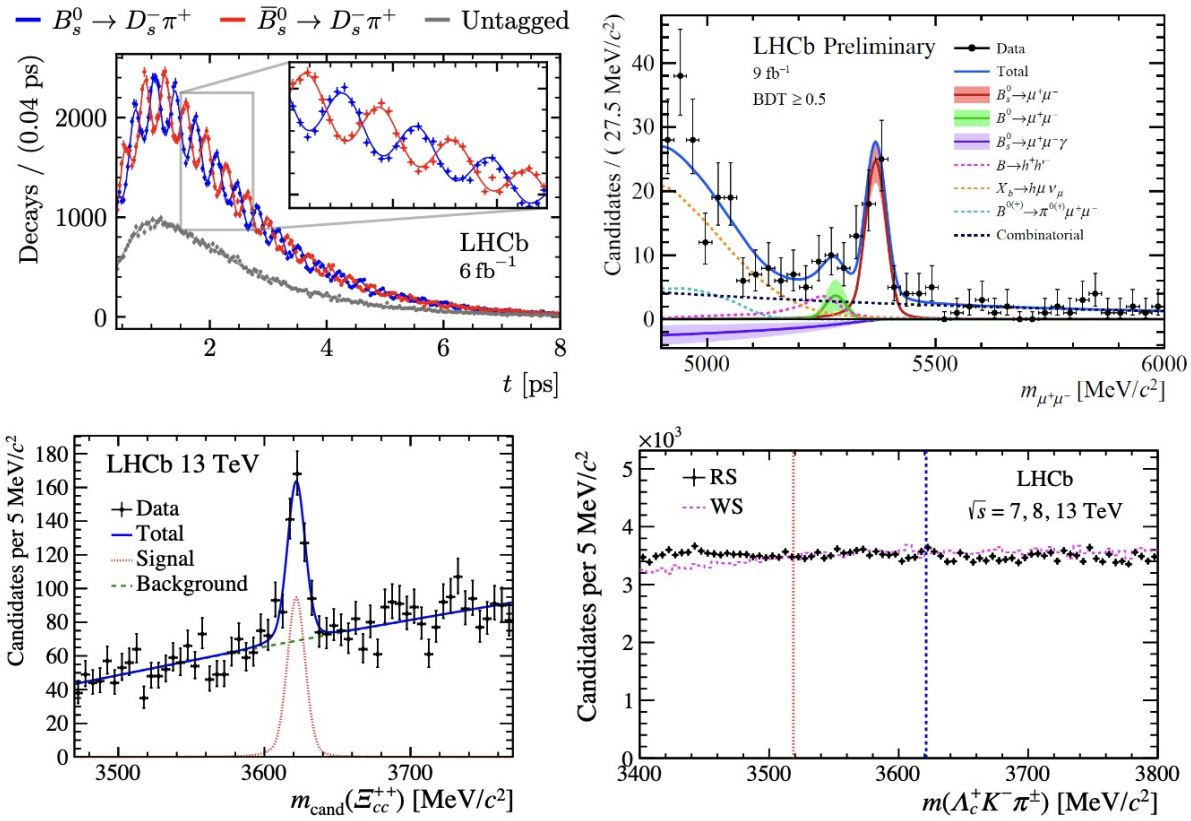

Figure 2.19: Examples of the impact of the VELO on LHCb's physics performance. (top left) B_s^0-$\overline{B}_s^0$ oscillations studied with $B_s^0 \to D_s^- \pi^+$ decays [100], (top right) the $B_s^0 \to \mu^- \mu^+$ decay [101], (bottom left) observation of the Ξ_{cc}^{++} baryon in the $\Lambda_c^+ \to K^- \pi^+ \pi^+$ final state [102], and (bottom right) search for the Ξ_{cc}^+ baryon in the $\Lambda_c^+ \to K^- \pi^+$ final state [103]

- The rate of B_s^0-$\overline{B}_s^0$ oscillations is sensitive to physics beyond the Standard Model [100]. Moreover, it is particularly critical to resolve these oscillations in order to be able

to make a number of key measurements of *CP*-violation parameters. In fact, the oscillation period of about 0.35 ps requires to determine both production and decay vertex positions with $\mathcal{O}(0.1$ mm) precision.

- Rare meson decays, such as $B_s^0 \to \mu^-\mu^+$ decays [101], provide an additional way to search for physics beyond the Standard Model. Due to their low rates — $\mathcal{O}(10^{-9})$ — the sensitivity achievable depends strongly on ability to discriminate against background formed from random combinations of tracks.

- The same arguments are even more relevant for shorter-lived particles decaying to hadronic final states, where random combinations of tracks from primary vertices can be an overwhelming background. As an example, the Ξ_{cc}^{++} lifetime is now known to be $0.256^{+0.024}_{-0.022}\,(\text{stat})\pm 0.014\,(\text{syst})$ ps [102], allowing sufficient background rejection for the observation to be achieved with Run 1 and 2 data. The Ξ_{cc}^{+} lifetime is expected to be shorter, by a factor of 2 to 4, and with the current VELO performance it is not possible to isolate Ξ_{cc}^{+} signal from background [103]. If it is possible to improve the vertexing capability with VELO Upgrade II, it will enhance significantly LHCb 's discovery prospects for particles with lifetimes of $\mathcal{O}(0.1$ ps) or less.

Figure 2.20 shows how time will help event reconstruction by separating a complete bunch crossing (left plot) into 20 ps sections (right plot). Figure 2.21 shows the primary vertex (PV) efficiency of Upgrade-II with and without timing for events with a b hadron. The PV efficiency of Upgrade-I is shown for comparison. The main goal of timing is to improve primary vertex separation. However, time will also help in assigning decay vertices to the correct primary vertex and to reduce background. Due to the forward geometry and the long flight distance of the b-hadrons, a secondary vertex, which may have only two tracks, will be geometrically compatible with many primary vertices and this is why the timing is needed. With timing, the tracks from the decay vertex will have the same timestamp as those of the primary vertex to which the decay vertex belongs and have a high probability to be time-wise significantly different from tracks originating from a different, but nearby, primary vertex.

The R&D for Upgrade-II is still in its early stages, and therefore the work presented in Chapter 4 will discuss the requirements of the detector and its challenges. Since also a detailed simulation model of the detector is still under construction, the Upgrade-I geometry and simulation parameters are considered as a starting point.

Timing information on track can be obtained by either assigning a single high resolution time measurement to each track with dedicated timing detector, or by assigning the time information to all hits constituting the track. According to the simulation studies, a track time resolution of about 20 ps is required to reach similar performance levels as in Upgrade I, while the per-hit time should be around 50 ps, where it is assumed that by combining hits a similar track timing resolution will be achieved. The timing

layer approach is chosen for the timing detectors of the ATLAS and CMS experiment that will be installed in Long Shutdown 3. As regards the future VELO a time-per-hit approach is considered as well, *i.e.* turning the VELO into a 4D-tracker. However, it is too early to favour one solution over the other and in the R&D phase, which will take place the coming years, the possible benefits and additional challenges of 4D tracker will be carefully considered.

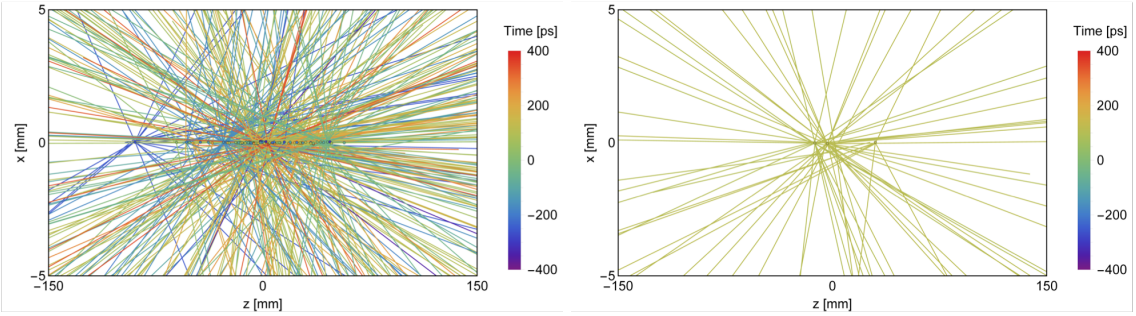

Figure 2.20: Tracks in the VELO for a typical bunch crossing at a luminosity of $1.5 \cdot 10^{34}$ $\mathrm{cm}^2\mathrm{s}^{-1}$ (left), and number of tracks in a 20 ps time slice (right).

.

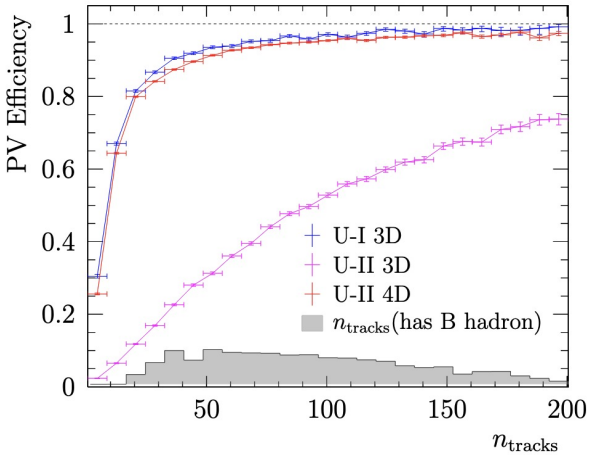

Figure 2.21: Reconstruction efficiency vs the number of tracks per primary vertex, comparing the Upgrade-I 3D reconstruction in both data conditions, and a variant using timing information to resolve the primary vertices. Reproduced from Ref. [104]

.

In terms of performance, the baseline is that the VELO for Upgrade-II should deliver at least the same performance as Upgrade-I on key parameters like efficiency, ghost

probability and impact parameter resolution. Additional benefits of 4D tracking could be the reduction of combinatorial track candidates and ghost tracks, which are relatively expensive in terms of processing time in the Event Filter Farm. This is the target of the work presented in Chapter 4, where a fast simulation for a future VELO using time information is developed and ran in Upgrade-II conditions. This work is done within the TimeSpot project where a very interesting 3D sensor has been realised in prospects of future 4D trackers.

2.8.1 The TimeSpot project

The TIME and SPace real-time Operating Tracker (TimeSpot) is an INFN project started in 2017 with the aim to provide tracking alternatives able to cope with the high luminosities expected by the harsh scenario of Hi-Lumi LHC.

The idea in the 3D sensors is that they provide fast timing due to the intrinsically short inter-electrode distance, while at the same time they provide a reasonably large signal because the sensor thickness can be much larger than the electrode distance. A further improvement of 3D sensors is the use of trenches instead of pillars, as developed by the TimeSpot collaboration [105], which reduces the effect of the non-uniform weighting field and hence makes the current response almost independent of where the track traverses the sensor. The trench 3D sensors exhibit an excellent time resolution of 15 ps when read out with high power external electronics.

The work presented in Chapter 4 is inserted in the TimeSpot work package 4 which is dedicated to the elaboration of fast-tracking algorithms and devices.

Chapter 3

Measurement of *CP* violation in charm decays

3.1 Introduction

The measurement of direct *CP* asymmetries in Cabibbo suppressed $D^0 \to K^-K^+$ and $D^0 \to \pi^-\pi^+$ decays is reported in this chapter. The analysis uses promptly produced $D^{*+} \to D^0\pi^+$ decays reconstructed in the proton-proton collision data collected by LHCb during Run 2, corresponding to $5.7\,\text{fb}^{-1}$ of integrated luminosity. High-yield samples of Cabibbo-favoured D^{*+}, D^+ and D_s^+ decays are used to subtract nuisance asymmetries due to production and detection effects. In particular, the time-integrated measurement of the *CP* asymmetry $\mathcal{A}^{CP}(K^-K^+)$ is performed. Finally, it is combined with LHCb's Run 1 and Run 2 results of $\Delta A_{CP} = \mathcal{A}^{CP}(K^-K^+) - \mathcal{A}^{CP}(\pi^-\pi^+)$, ΔY_{KK} and $\Delta Y_{\pi\pi}$ to determine the values of a^d_{KK} and $a^d_{\pi\pi}$ following

$$\mathcal{A}^{CP}(f) = a^d_f + \frac{\langle t \rangle_f}{\tau_D} \cdot \Delta Y_f, \tag{3.1}$$

with $f = KK$ or $\pi\pi$ and $\langle t \rangle_f$ the average (acceptance dependent) decay time, as explained in Section 1.5.1.

3.2 Analysis strategy

The time-integrated *CP* asymmetry in $D^0 \to K^-K^+$ decays is measured through a measurement of the raw asymmetry of D^{*+}-tagged D^0 decays,

$$A(K^-K^+) \equiv \frac{N\left(D^0 \to K^-K^+\right) - N\left(\overline{D}^0 \to K^-K^+\right)}{N\left(D^0 \to K^-K^+\right) + N\left(\overline{D}^0 \to K^-K^+\right)}, \tag{3.2}$$

which uses the pion from the D^{*+} decay (often referred to as the soft pion π^+_{soft}) to tag the flavour of the D^0 at production.

Nuisance asymmetries are expected in the production of D^{*+} mesons in pp collisions (the production asymmetry) and in the reconstruction of the soft π^+ (the pion detection asymmetry). The production asymmetry is defined as

$$A_{\text{prod}}(X) \equiv \frac{\sigma(pp \to X) - \sigma(pp \to \overline{X})}{\sigma(pp \to X) + \sigma(pp \to \overline{X})} \qquad \text{with } A_{\text{prod}}(\overline{X}) \equiv -A_{\text{prod}}(X), \tag{3.3}$$

in which $\sigma(pp \to X)$ denotes the production cross-section of D^+, D^+_s, or D^{*+} within the LHCb acceptance in 13 TeV proton-proton collisions and with $A_{\text{prod}}(X)$ being a function of X's kinematics[1]. Similarly, the detection asymmetry for particle type h is defined as

$$A_{\text{det}}(h^+) \equiv \frac{\varepsilon(h^+) - \varepsilon(h^-)}{\varepsilon(h^+) + \varepsilon(h^-)} \qquad \text{with } A_{\text{det}}(h^-) \equiv -A_{\text{det}}(h^+), \tag{3.4}$$

in which $\varepsilon(h^+)$ ($\varepsilon(h^-)$) denotes the absolute detection efficiency for the positively (negatively) charged hadron h and with $A_{\text{det}}(h^+)$ being a function of h^+'s kinematics[2]. For physics analyses, this detection efficiency typically includes contributions from the detector acceptance, track reconstruction, PID and trigger requirements.

The number of reconstructed D^0 and $\overline{D}^0$ candidates is proportional to the production rates of the D^*, branching fractions and reconstruction efficiencies (assuming they are factorizable), *i.e.*

$$N(D^0 \to K^-K^+) \propto \sigma(D^{*+})\epsilon(\pi^+_{soft})\Gamma(D^0 \to K^-K^+), \tag{3.5}$$
$$N(\overline{D}^0 \to K^-K^+) \propto \sigma(D^{*-})\epsilon(\pi^-_{soft})\Gamma(\overline{D}^0 \to K^-K^+), \tag{3.6}$$

where the reconstruction efficiency of the finale state K^-K^+ is neglected since it is shared between the two decays. According to Eq. 1.28 and Eqs. 3.3 and 3.4,

$$N(D^0 \to K^-K^+) \propto (1 + A_{\text{prod}}(D^{*+}))(1 + A_{\text{det}}(\pi^+_{soft}))(1 + \mathcal{A}^{CP}(K^-K^+)), \tag{3.7}$$
$$N(\overline{D}^0 \to K^-K^+) \propto (1 - A_{\text{prod}}(D^{*+}))(1 - A_{\text{det}}(\pi^+_{soft}))(1 - \mathcal{A}^{CP}(K^-K^+)). \tag{3.8}$$

Given these definitions, the raw asymmetry can be written as

$$A(K^-K^+) = \frac{\mathcal{A}^{CP} + A_{\text{prod}} + A_{\text{det}} + \mathcal{A}^{CP}A_{\text{prod}}A_{\text{det}}}{1 + \mathcal{A}^{CP}A_{\text{prod}} + \mathcal{A}^{CP}A_{\text{det}} + A_{\text{prod}}A_{\text{det}}}, \tag{3.9}$$

[1]When a $c\bar{c}$ pair is produced in pp collision, they hadronize to form a confined state. In this stage, each heavy quark combines with one or two lighter quarks, coming from the proton remnants or the fragmentation process of the initial interaction, to create a meson or a baryon, respectively. This leads to small differences in the number of produced mesons and anti-mesons depending on the kinematic variables of the particle, *i.e.* $\sigma(pp \to X)(\vec{p}) \neq \sigma(pp \to \overline{X})(\vec{p})$ with $\vec{p}$ being X momentum.

[2]Because of their different composition in terms of quarks, hadrons and anti-hadrons have different probability of being absorbed by the detector material. This leads to a difference in reconstruction performances depending on their momentum, *i.e.* $\varepsilon(h^+)(\vec{p}) \neq \varepsilon(h^-)(\vec{p})$ with $\vec{p}$ being h^+ momentum.

with $\mathcal{A}^{CP}$, $A_{\rm prod}$ and $A_{\rm det}$ being $\mathcal{A}^{CP}(K^-K^+)$, $A_{\rm prod}(D^{*+})$ and $A_{\rm det}(\pi^+_{soft})$, respectively. As the $A_{\rm prod}(D^{*+})$ value is expected to be $\sim$1% from the latest measurement of $A_{\rm det}(D^+)$ [106] and also $A_{\rm det}(\pi^+_{soft})$ is of the same order and $\mathcal{A}^{CP}(K^-K^+)$ is $\sim 10^{-3}$ or below (see Section 1.5.2), contributions up to $\mathcal{O}(10^{-6})$ can be neglected, yielding to the following expression for the raw asymmetry:

$$A(K^-K^+) = \mathcal{A}^{CP}(K^-K^+) + A_{\rm prod}(D^{*+}) + A_{\rm det}(\pi^+_{soft}). \tag{3.10}$$

To remove the nuisance asymmetries, additional control channels are needed with negligible *CP* asymmetry. Cabibbo favoured decays are used throughout as control channels, as *CP* violation in these decays is far smaller than the experimental reach, as explained in Section 1.5.2. The raw asymmetry in $D^0 \to K^-\pi^+$ decays is given by

$$A(K^-\pi^+) = A_{\rm prod}(D^{*+}) + A_{\rm det}(\pi^+_{soft}) + A_{\rm det}(K^-) + A_{\rm det}(\pi^+). \tag{3.11}$$

Exploiting $D^+ \to \overline{K}^0\pi^+$ and $D^+ \to K^-\pi^+\pi^+$ decays with the following raw asymmetries

$$A(K^0_{\rm S}\pi^+) = A_{\rm prod}(D^+) + A_{\rm det}(\overline{K}^0) + A_{\rm det}(\pi^+), \tag{3.12}$$
$$A(K^-\pi^+\pi^+) = A_{\rm prod}(D^+) + A_{\rm det}(K^-) + A_{\rm det}(\pi^+) + A_{\rm det}(\pi^+), \tag{3.13}$$

or using $D^+_s \to \overline{K}^0K^+$ and $D^+_s \to \phi\pi^+$ decays whose raw asymmetries are defined as

$$A(K^0_{\rm S}K^+) = A_{\rm prod}(D^+_s) + A_{\rm det}(\overline{K}^0) + A_{\rm det}(K^+), \tag{3.14}$$
$$A(\phi\pi^+) = A_{\rm prod}(D^+_s) + A_{\rm det}(\pi^+) + A_{\rm det}(\phi), \tag{3.15}$$

where $\overline{K}^0$ decays are reconstructed as $K^0_{\rm S}$ in the $\pi^-\pi^+$ final state, the measurement of $\mathcal{A}^{CP}(K^-K^+)$ is obtained. The time-integrate *CP* asymmetry for the $D^0 \to K^-K^+$ decay is calculated with the following sums and subtractions

$$\begin{aligned}\mathcal{A}^{CP}(K^-K^+)|D^+ = {} & A(K^-K^+) - A(K^-\pi^+) \\ & + A(K^-\pi^+\pi^+) - [A(K^0_{\rm S}\pi^+) - A_{\rm det}(\overline{K}^0)],\end{aligned} \tag{3.16}$$

and

$$\begin{aligned}\mathcal{A}^{CP}(K^-K^+)|D^+_s = {} & A(K^-K^+) - A(K^-\pi^+) \\ & + A(\phi\pi^+) - [A(K^0_{\rm S}K^+) - A_{\rm det}(\overline{K}^0)],\end{aligned} \tag{3.17}$$

where it is assumed that production and detection asymmetries are independent from the final state. The neutral kaon detection asymmetry $A_{\rm det}(\overline{K}^0)$ is defined as

$$A_{\rm det}(\overline{K}^0) \equiv \frac{\varepsilon(\overline{K}^0) - \varepsilon(K^0)}{\varepsilon(\overline{K}^0) + \varepsilon(K^0)}, \tag{3.18}$$

and arises from the combined effect of *CP* violation and mixing in the neutral kaon system together with the different interaction cross-section of K^0 and $\overline{K}^0$ mesons with detector material, estimated in Section 3.6 using the LHCb material map as input. $A_{\rm det}(\phi)$ is the detection asymmetry of the pair of kaons coming from the ϕ decay and is equal to zero by definition. Contribution from non-resonant components in $A_{\rm det}(\phi)$ are taken into account in the systematic uncertainty studies (Section 3.9.5). In Eqs. 3.11 to 3.15, contributions up to $\mathcal{O}(10^{-5})$ are neglected considering that $A_{\rm det}(K^-)$ and $A_{\rm det}(\pi^+)$ are expected to be $\sim$1% or less.

In general, Eqs. 3.16 and 3.17 correspond to two different measurements referred to as D^+- and D_s^+-method, respectively, and will result slightly correlated. A crucial point in this strategy is that the nuisance asymmetries depend on the kinematics of the particles involved in the decay. Hence, a good kinematic match has to be ensured to correctly subtract the nuisance asymmetries between the different decay modes in Eqs. 3.16 and 3.17. This is achieved by assigning per-candidate weights to the various datasets.

In the next sections the details on the data sample used together with the determination of the raw asymmetries and the weighting procedures are presented in Section 3.3, 3.4 and 3.5, respectively. The neutral kaon asymmetry is estimated in Section 3.6. A Monte Carlo validation is also realised to cross-check the methodology applied, as described in Section 3.8. Section 3.9 reports about the estimation of the possible systematic uncertainties. Finally, in Sections 3.11, 3.12 and 3.14 the final results and the combination with previous LHCb measurements are discussed.

3.3 Data samples and event selection

The analysis is performed using the data recorded by the LHCb detector during Run 2. The total sample corresponds to approximately $5.7\,\text{fb}^{-1}$ of integrated luminosity, split between $0.3\,\text{fb}^{-1}$, $1.7\,\text{fb}^{-1}$, $1.6\,\text{fb}^{-1}$ and $2.1\,\text{fb}^{-1}$ collected in 2015, 2016, 2017 and 2018, respectively.

Candidates for the decays of interest are reconstructed from the following exclusive Hlt2 lines using the *Turbo stream*:

$D^{*+} \to D^0(\to K^-K^+)\pi^+$	`Hlt2CharmHadDstp2D0Pip_D02KmKpTurbo`
$D^{*+} \to D^0(\to K^-\pi^+)\pi^+$	`Hlt2CharmHadDstp2D0Pip_D02KmpipTurbo`
$D^+ \to K^-\pi^+\pi^+$	`Hlt2CharmHadDpToKmPipPipTurbo`
$D^+ \to K^0_S\pi^+$	`Hlt2CharmHadDp2KS0pip_KS0LLTurbo`
$D^+_s \to K^-K^+\pi^+$	`Hlt2CharmHadDpToKmKpPipTurbo`
$D^+_s \to K^0_S K^+$	`Hlt2CharmHadDp2KS0Kp_KS0LLTurbo`

where the $K^0_S \to \pi^-\pi^+$ decays are made using pairs of pions reconstructed as long tracks (LL), which limits the effects of the neutral kaon asymmetry. The requirements applied in the online selections are reported in Tables 3.62 to 3.65 in Section 3.16.1, where the used variables include the flight distance χ^2 from the assigned PV (flight-distance χ^2), the lifetime of the particle calculated from its origin vertex (decay time), the direction angle between the momentum and the displacement vector from the PV (direction angle), the impact parameter $\chi^2_{IP}(PV)$ which is the minimum change in χ^2 when the particle is included in the vertex fit to the PV, and $\text{DLL}_{K\pi}$ is the likelihood variable provided by the RICH detector describing the probability of a track being a kaon with respect to a pion.

Given the definitions for `TIS` and `TOS`, `L0Global` and `Hlt1TrackMVA` and `Hlt1TwoTrackMVA` from Section 2.5, the following trigger criteria are required offline. Only D meson candidates that are `TIS` at the hardware trigger level are retained while $D^0 \to K^-K^+$ candidates are asked to be `TOS` on either `Hlt1TrackMVA` or `Hlt1TwoTrackMVA`. As regards the Cabibbo-favoured decays, the trigger requirements are chosen to avoid any possible asymmetry of the final state arising from L0 and Hlt1 and are listed in Tables 3.1 and 3.2 for the D^+ and D^+_s method, respectively. In $D^+ \to K^0_S\pi^+$ decays, only candidates with the bachelor pion selected by the `Hlt1TrackMVA` trigger are considered. That pion is referred to as π^+_{trig}. In the case of the $D^+ \to K^-\pi^+\pi^+$ decay, one of the two pions selected by the `Hlt1TrackMVA` trigger is also identified as π^+_{trig}. If both pions are selected, π^+_{trig} is randomly chosen.

All the selected candidates from all the decay modes are processed using the `DecayTreeFitter` [107] (DTF) package. This method is particularly useful for candidates involving multiple decay vertices and performs a fit to the full decay chain with the possibility of additional contraints. It allows for the simultaneous extraction of decay time, position and momentum parameters and their uncertainties and correlations for

Decay	L0 requirement Hlt1 requirement
$D^0 \to K^-K^+$	D^{*+} `L0Global_TIS` D^0 `Hlt1 two/single-track TOS`
$D^0 \to K^-\pi^+$	D^{*+} `L0Global_TIS` K^- `Hlt1 single-track TOS`
$D^+ \to K^-\pi^+\pi^+_{trig}$	D^+ `L0Global_TIS` π^+_{trig} `Hlt1 single-track TOS AND` K^- `Hlt1 single-track TOS`
$D^+ \to K^0_S\pi^+_{trig}$	D^+ `L0Global_TIS` π^+_{trig} `Hlt1 single-track TOS`

Table 3.1: Trigger (L0 and Hlt1) requirements for the D^+ method. Single track corresponds to the `Hlt1TrackMVA` line, two track corresponds to the `Hlt1TwoTrackMVA` line.

Decay	L0 requirement Hlt1 requirement
$D^0 \to K^-K^+$	D^{*+} `L0Global_TIS` D^0 `Hlt1 two/single-track TOS`
$D^0 \to K^-\pi^+$	D^{*+} `L0Global_TIS` K^- `Hlt1 single-track TOS`
$D_s^+ \to K^-K^+\pi^+$	D_s^+ `L0Global_TIS` ϕ `Hlt1 two/single-track TOS`
$D_s^+ \to K^0_S K^+$	D_s^+ `L0Global_TIS` K^+ `Hlt1 single-track TOS`

Table 3.2: Trigger (L0 and Hlt1) requirements for the D_s^+ method. Single track corresponds to the `Hlt1TrackMVA` line, two track corresponds to the `Hlt1TwoTrackMVA` line.

all particles. For all the modes, the origin vertex of the reconstructed charm meson is constrained to the position of the primary vertex, and the momentum-scale calibrations[3] are applied. In case of $D^+_{(s)} \to K^0_S h^+$, the mass of the reconstructed K^0_S is constrained to its nominal value. Events where fit fails are discarded. In the following analysis only refitted quantities are used, unless it is differently stated.

In case of D^{*+} decays, large detection asymmetries of the soft pion are present. This is due to the fact that low-momentum particles with a certain charge and values of p_x

[3]Biased estimate of the magnetic field affects the measurement of particle momentum which can be corrected using resonances such as $J/\psi \to \mu^-\mu^+$ [108].

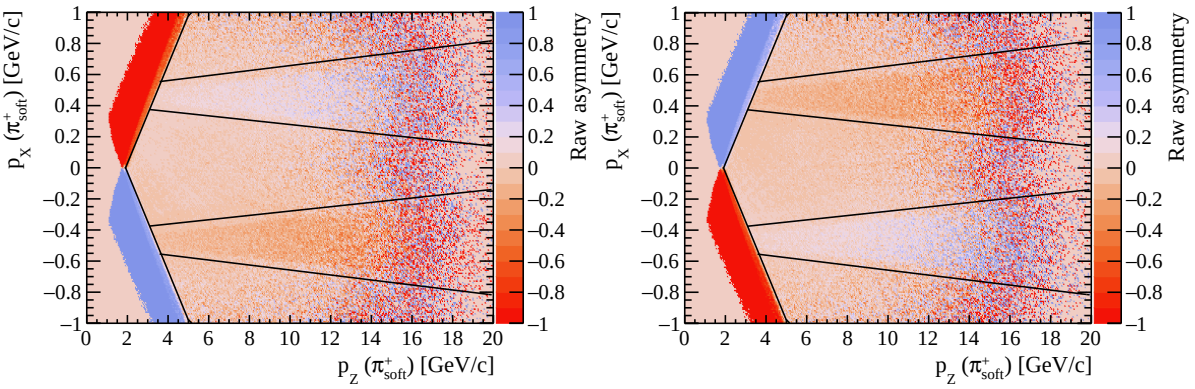

Figure 3.1: Distribution of the raw asymmetry in the (p_x, p_z) plane of the soft pion, separately for (left) magnet-down, (right) magnet-up polarity for $D^{*+} \to D^0(\to K^-K^+)\pi^+$ candidates reconstructed in 2016 data, as an example. The black lines show the boundaries of the large-asymmetry regions excluded by the fiducial cuts. Similar distributions are observed for $D^{*+} \to D^0(\to K^-\pi^+)\pi^+$ candidates.

and p_z are deviated by the magnetic field outside the detector acceptance, while the same does not happen for particles with equal p_x and p_z values but opposite charge. To exclude this kinematic regions the π^+_{soft} is required to be within the fiducial region defined by

$$\begin{aligned} |p_x| < 0.317 \cdot (p_z - 1910) \text{ and } [(|p_y/p_z| > 0.014) \\ \text{or } [((|p_y/p_z| < 0.014) \text{ and } (|p_x| < 418 - 0.01397 \cdot p_z)) \\ \text{or } (|p_x| > 497 + 0.01605 \cdot p_z)]], \end{aligned} \tag{3.19}$$

with p_x and p_z being in units MeV/c. A graphical representation of the fiducial requirements, together with the distribution of raw asymmetry as function of the soft pion p_x, p_z quantities is shown in Figure 3.1.

Secondary D^0 or $D^+_{(s)}$ mesons produced in the decay of beauty hadron are suppressed by requiring that the impact parameter (IP) is smaller than 50 μm. As discussed in Section 3.9.1, the requirement on the IP reduces the contamination from secondary charm to few percent.

D^{*+} candidates are selected by requiring the mass of the reconstructed D^0 to be in the range $[1844, 1887]\,\text{MeV}/c^2$. Combinatorial background due to the association of a D^0 candidate with a wrong soft pion is reduced by randomly removing all the candidates but one when more of them are present in the same event. This requirement removes about 10% (7%) and 5.5% (4%) of the candidates in $D^0 \to K^-K^+$ and $D^0 \to K^-\pi^+$ in 2015 and 2016 (2017 and 2018) data taking period, respectively. The different value between the different data taking periods arises from the different cut on the p_{T} of the

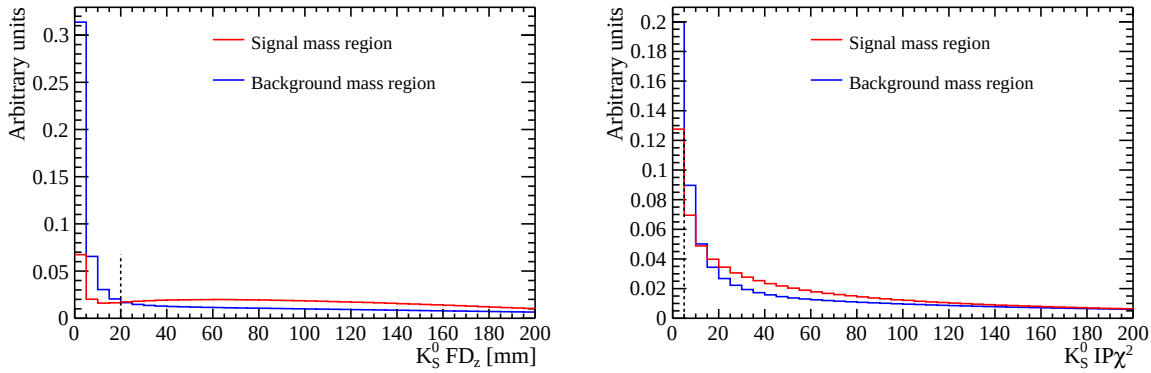

Figure 3.2: Normalized distribution of the K^0_S (left) flight distance and (right) impact parameter χ^2 for $D^+ \to K^0_S\pi^+$ candidates in the (red) signal region defined as ($|m(\pi^-\pi^+) - m_{K^0_S}| < 10$ MeV/c^2) and ($|m(K^0_S\pi^+) - m_{D^+}| < 20$ MeV/c^2), and in the (blue) background region defined as its complementary. The dashed black line shows the cut applied to improve signal purity. Similar distributions are observed for $D^+_s \to K^0_S K^+$ candidates. Only 2016 magnet-down data are shown, as an example.

soft pion in the Hlt2 line (Table 3.62). Multiple candidates are removed also in $D^+_{(s)}$ decays. Their fraction is smaller than 1%.

In $D^+_{(s)}$ decays containing a K^0_S in the final state, background due to three-body decays is reduced by requiring the reconstructed invariant mass[4] of the two pions forming the K^0_S candidate to be within 10 MeV/c^2 of the nominal K^0_S mass [31], have a flight distance larger than 20 mm along the z axis, and have the χ^2 on the IP larger than 5, as shown in Figure 3.2.

Regions at the edges of the p, p_T and η distributions of each particle are removed to be sure to have the same range between the different decay modes where it appears. These cuts are applied to the $D^+_{(s)}$, the π^+_{trig}, the K^-, the π^+, the K^0_S (or $K^-\pi^{+5}$) and to the D^0. Their aim is to "harmonize" the variables before the weighting procedure described in Section 3.5, discarding the events that would have been assigned a weight with value zero or infinite. $D^0 \to K^-K^+$ candidates are further selected by requiring DLL$_{K\pi} > 5$ on the kaons in the final state to reduce the misidentified background. A summary of all the offline requirements applied to $D^0 \to K^-K^+$ candidates is reported in Table 3.3.

To simplify the strategy and avoid correlations between the sub-samples in the two

[4]Clearly, the DTF constraint on the K^0_S mass is not applied for the calculation of this variable.

[5]Since the D^+ and the π^+_{trig} must have the same kinematic distribution between the $D^+ \to K^-\pi^+\pi^+_{trig}$ and $D^+ \to K^0_S\pi^+_{trig}$ decay modes, the kinematics of the K^0_S and of the pair $K^-\pi^+$ will also be forced to match.

Particle	Variable	Requirement
D^{*+}	Mass	$[2004.5, 2020]\,\mathrm{MeV}/c^2$
D^0	Mass	$[1844, 1887]\,\mathrm{MeV}/c^2$
	IP	< 50 μm
	p_T	$[2, 10]$ GeV/c
	η	$[2.1, 4.5]$
K^- (K^+)	$\mathrm{DLL}_{K\pi}$	> 5
π^+_{soft}	Fiducial cuts (Eq. 3.19)	yes

Table 3.3: Offline selection for $D^0 \to K^-K^+$ candidates.

methods, the $D^0 \to K^-\pi^+$ sample is randomly split in two. One half is used in the D^+ method while the second one in the D_s^+. Given the large amout of $D^0 \to K^-\pi^+$ decays collected, this operation is not limiting from the point of view of the final accuracy achievable on $\mathcal{A}^{CP}(K^-K^+)$. However, due to the sharing of the $D^0 \to K^-K^+$ sample, a correlation between the two $\mathcal{A}^{CP}(K^-K^+)$ measurements exists and it is properly treated as discussed in Section 3.7. Additional channel- and method-specific requirements are discussed in the following sections.

3.3.1 Offline selection for the D^+ method

The selection strategy for $D^0 \to K^-\pi^+$, $D^+ \to K^-\pi^+\pi^+_{trig}$ and $D^+ \to K^0_\mathrm{S}\pi^+_{trig}$ decays consists in the application of several criteria aimed at reducing backgrounds. $D^0 \to K^-\pi^+$ candidates are further selected by requiring $\mathrm{DLL}_{K\pi} > 5 (< -5)$ on the kaon (pion) in the final state to reduce the misidentified background. The same requirements are applied on the K^- and π^+ in $D^+ \to K^-\pi^+\pi^+_{trig}$ decays.

$D^+ \to K^0_\mathrm{S}\pi^+_{trig}$ candidates are contaminated by the presence of background decays like $D^+_{(s)} \to K^0_\mathrm{S}K^+$, $\Lambda_c^+ \to K^0_\mathrm{S}p$ and $\Lambda_c^+ \to \Lambda(\to p\pi^-)\pi^+$ as shown in Figure 3.3 by bands in the distributions of the $K^0_\mathrm{S}\pi^+_{trig}$ mass as a function of the momentum imbalance between the K^0_S meson and π^+_{trig}, defined as $[p(K^0_\mathrm{S}) - p(\pi^+_{trig})]/[p(K^0_\mathrm{S}) + p(\pi^+_{trig})]$. Superimposed on the data distributions are the expected dependencies that are calculated analytically in Section 3.16.2. The $D_s^+ \to K^0_\mathrm{S}K^+$ is a peaking background for the $D^+ \to K^0_\mathrm{S}\pi^+_{trig}$ candidates and is reduced by requiring $\mathrm{DLL}_{K\pi} < -5$ on the π^+_{trig}. The same cut is applied on the π^+_{trig} in $D^+ \to K^-\pi^+\pi^+_{trig}$ decays. $\Lambda_c^+ \to K^0_\mathrm{S}p$ background is reduced by requiring $\mathrm{DLL}_{p\pi} < 0$ on the π^+_{trig}. The same cut is applied on the π^+_{trig} in $D^+ \to K^-\pi^+\pi^+_{trig}$ decays. The misidentification of a proton from the Λ decay (in the $\Lambda_c^+ \to \Lambda\pi^+$ decay) as a daughter of the K^0_S is also visible in Figure 3.4 and is suppressed by requiring $|[p(\pi^-) - p(\pi^+)]/[p(\pi^-) + p(\pi^+)]| < 0.7$.

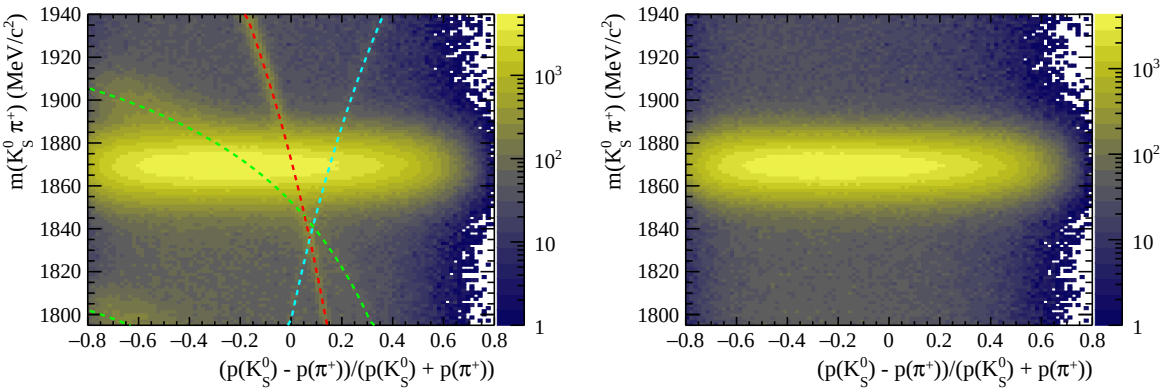

Figure 3.3: Distribution of $K^0_S\pi^+_{trig}$ mass as a function of the momentum imbalance for $D^+ \to K^0_S\pi^+_{trig}$ candidates (left) before and (right) after the particle-identification requirements on the π^+_{trig} and on the daughters of the K^0_S are applied. The expected distribution dependencies, in the hypothesis of infinite mass resolution, of (green-dashed line) $D^+_{(s)} \to K^0_S K^+$, (red-dashed line) $\Lambda^+_c \to K^0_S p$ and (blue-dashed line) $\Lambda^+_c \to \Lambda(\to p\pi^-)\pi^+$ misidentified decays are overlaid. The magnet-down 2016 data are shown, as an example.

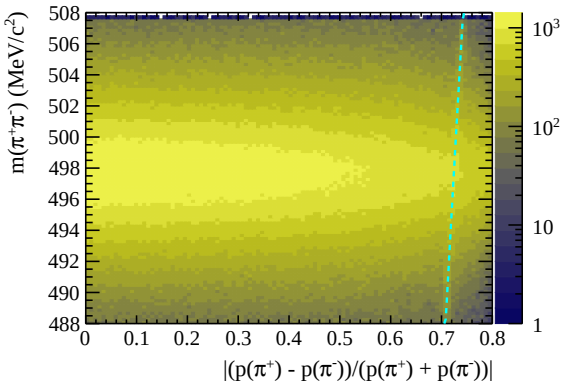

Figure 3.4: Distribution of $\pi^-\pi^+$ reconstructed invariant mass as a function of the absolute value of the momentum imbalance for K^0_S candidates in $D^+ \to K^0_S\pi^+_{trig}$ decays before the particle-identification requirements on the daughters of the K^0_S are applied, with overlaid the expected distribution, in the hypothesis of infinite mass resolution, of (blue-dashed line) $\Lambda \to p\pi^-$ misidentified decays coming from Λ^+_c decays. The magnet-down 2016 data are shown, as an example.

A summary of all the offline requirements applied in the D^+ method is reported in Tables 3.4 to 3.6.

Particle	Variable	Requirement
D^{*+}	Mass	$[2004.5, 2020]\,\mathrm{MeV}/c^2$
D^0	Mass	$[1844, 1887]\,\mathrm{MeV}/c^2$
	IP	< 50 µm
	p_T	$[2, 10]$ GeV/c
	η	$[2.1, 4.5]$
π^+_{soft}	Fiducial cuts (Eq. 3.19)	yes
K^-	$\mathrm{DLL}_{K\pi}$	> 5
	p	> 5 GeV/c
	p_T	$[1.5, 6]$ GeV/c
	η	$[2, 4.5]$
π^+	$\mathrm{DLL}_{K\pi}$	< -5
	p	> 5 GeV/c
	p_T	$[0.8, 4]$ GeV/c
	η	$[2, 4.5]$

Table 3.4: Offline selection for $D^0 \to K^-\pi^+$ candidates in the D^+ approach.

Particle	Variable	Requirement
D^+	Mass	$[1795, 1945]\,\mathrm{MeV}/c^2$
	IP	< 50 μm
	p_T	$[3.5, 10]$ GeV/c
	η	$[2, 4.5]$
K^-	$\mathrm{DLL}_{K\pi}$	> 5
	p	> 5 GeV/c
	p_T	$[1.5, 6]$ GeV/c
	η	$[2, 4.5]$
π^+	$\mathrm{DLL}_{K\pi}$	< -5
	p	> 5 GeV/c
	p_T	$[0.8, 4]$ GeV/c
	η	$[2, 4.5]$
π^+_{trig}	$\mathrm{DLL}_{K\pi}$	< -5
	$\mathrm{DLL}_{p\pi}$	< 0
	p_T	$[1.5, 8]$ GeV/c
	η	$[2, 4.5]$
$K^-\pi^+$	p	> 10 GeV/c
	p_T	> 2 GeV/c

Table 3.5: Offline selection for $D^+ \to K^-\pi^+\pi^+_{trig}$ candidates.

Particle	Variable	Requirement
D^+	Mass	$[1795, 1940]\,\mathrm{MeV}/c^2$
	IP	< 50 μm
	p_T	$[3.5, 10]$ GeV/c
	η	$[2, 4.5]$
K^0_S	$\lvert m(\pi^+\pi^-) - m^\mathrm{PDG}_{K^0_\mathrm{S}}\rvert$	$< 10\,\mathrm{MeV}/c^2$
	Flight distance along z	> 20 mm
	IP χ^2	> 5
	$\lvert[p(\pi^-) - p(\pi^+)]/[p(\pi^-) + p(\pi^+)]\rvert$	< 0.7
	p	> 10 GeV/c
	p_T	> 2 GeV/c
π^+_{trig}	$\mathrm{DLL}_{K\pi}$	< -5
	$\mathrm{DLL}_{p\pi}$	< 0
	p_T	$[1.5, 8]$ GeV/c
	η	$[2, 4.5]$

Table 3.6: Offline selection for $D^+ \to K^0_\mathrm{S}\pi^+_{trig}$ candidates.

3.3.2 Offline selection for the D_s^+ method

Similar to the D^+ method, the $D^0 \to K^-\pi^+$, $D_s^+ \to \phi\pi^+$ and $D_s^+ \to K_S^0 K^+$ candidates are selected with requirements aimed at suppressing physical backgrounds.

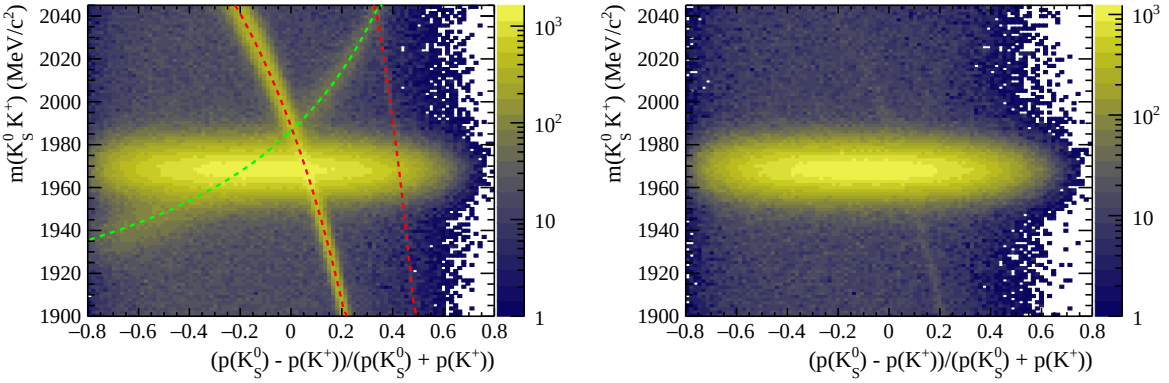

Figure 3.5: Distribution of $K_S^0 K^+$ mass as a function of the momentum imbalance for $D_{(s)}^+ \to K_S^0 K^+$ candidates (left) before and (right) after the particle-identification requirement on the bachelor kaon are applied. The expected distribution dependencies, in the hypothesis of infinite mass resolution, of (green-dashed line) $D^+ \to K_S^0\pi^+$ and (red-dashed line) $\Lambda_c^+ \to K_S^0 p$ and $\Xi_c^+ \to K_S^0 p$ misidentified decays are overlaid. The magnet-down 2016 data are shown.

As shown in Figure 3.5, $D_s^+ \to K_S^0 K^+$ candidates are contaminated by the presence of background decays, namely the $D^+ \to K_S^0\pi^+$, $\Lambda_c^+ \to K_S^0 p$ and $\Xi_c^+ \to K_S^0 p$ decays, where the companion hadron is misidentified as a kaon. These are suppressed by requiring $\mathrm{DLL}_{K\pi} > 15$ and $\mathrm{DLL}_{pK} < 0$ on the K^+, respectively. As one can notice from Figure 3.5 (right), a small fraction of $\Lambda_c^+ \to K_S^0 p$ decays survive these PID requirements. It is estimated to be $\sim 8.7 \cdot 10^{-4}$ around the D_s^+ mass peak and therefore assumed to have negligible impact on $\mathcal{A}^{CP}(K^-K^+)$. The same cuts are applied on the K^- in $D^0 \to K^-\pi^+$ decay. Candidates $D^0 \to K^-\pi^+$ are further selected by requiring $\mathrm{DLL}_{K\pi} < -5$ on the pion in the final state to reduce the misidentified background. The same requirement is applied on the π^+ in $D_s^+ \to \phi\pi^+$ decays. Finally, candidates $D_s^+ \to K^-K^+\pi^+$ are filtered by requiring the K^-K^+ mass to be within 5 MeV/c^2 of the nominal ϕ mass [31], as shown in Figure 3.6.
A summary of all the offline requirements applied in the D_s^+ method is reported in Tables 3.7 to 3.9.

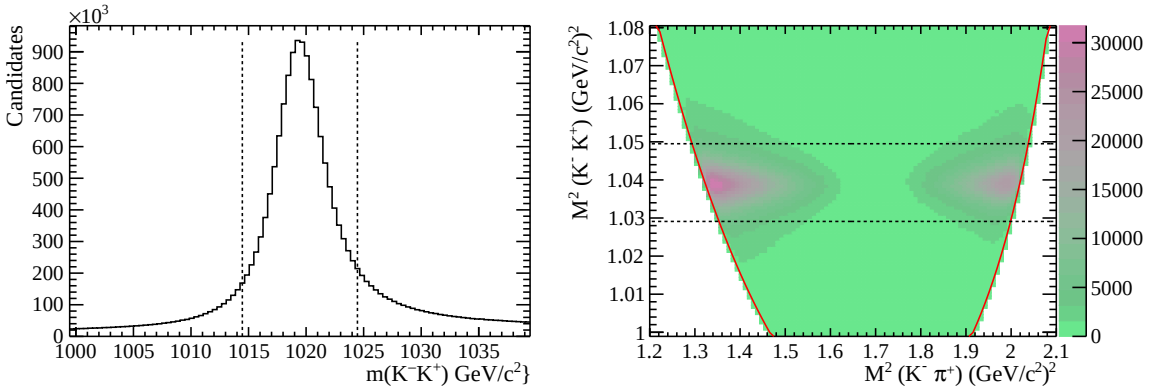

Figure 3.6: (Left) invariant mass distribution of K^-K^+ pair and (right) Dalitz plot for $D_s^+ \to K^-K^+\pi^+$ candidates in the ϕ mass region. The dashed black lines show the cuts applied. The red line represents the kinematic limit for the decay of a D_s^+ meson into $K^-K^+\pi^+$ final state. Only 2016 magnet-down data are shown, as an example.

Particle	Variable	Requirement
D^{*+}	Mass	$[2004.5, 2020]\,\mathrm{MeV}/c^2$
D^0	Mass	$[1844, 1887]\,\mathrm{MeV}/c^2$
	IP	< 50 µm
	p_T	$[2, 10]$ GeV/c
	η	$[2.1, 4.5]$
π^+_{soft}	Fiducial cuts (Eq. 3.19)	yes
K^-	$\mathrm{DLL}_{K\pi}$	> 15
	$\mathrm{DLL}_{p\pi}$- $\mathrm{DLL}_{K\pi}$	< 0
	p	> 5 GeV/c
	p_T	$[1.5, 8]$ GeV/c
	η	$[2, 4.5]$
π^+	$\mathrm{DLL}_{K\pi}$	< -5
	p	> 5 GeV/c
	p_T	$[0.8, 8]$ GeV/c
	η	$[2, 4.5]$

Table 3.7: Offline selection for $D^0 \to K^-\pi^+$ candidates in the D_s^+ approach.

Particle	Variable	Requirement
D_s^+	Mass	$[1900, 2045]\,\text{MeV}/c^2$
	IP	< 50 μm
	p_T	$[3, 12]$ GeV/c
	η	$[2, 4.5]$
ϕ	$\lvert m(K^+K^-) - m_\phi^\text{PDG}\rvert$	$< 5\,\text{MeV}/c^2$
π^+	$\text{DLL}_{K\pi}$	< -5
	p	> 5 GeV/c
	p_T	$[0.8, 8]$ GeV/c
	η	$[2, 4.5]$

Table 3.8: Offline selection for $D_s^+ \to \phi\pi^+$ candidates.

Particle	Variable	Requirement
D_s^+	Mass	$[1900, 2045]\,\text{MeV}/c^2$
	IP	< 50 μm
	p_T	$[3, 12]$ GeV/c
	η	$[2, 4.5]$
K_S^0	$\lvert m(\pi^+\pi^-) - m_{K_\text{S}^0}^\text{PDG}\rvert$	$< 10\,\text{MeV}/c^2$
	Flight distance along z	> 20 mm
	IP χ^2	> 5
K^+	$\text{DLL}_{K\pi}$	> 15
	$\text{DLL}_{p\pi}$- $\text{DLL}_{K\pi}$	< 0
	p	> 5 GeV/c
	p_T	$[0.8, 8]$ GeV/c
	η	$[2, 4.5]$

Table 3.9: Offline selection for $D_s^+ \to K_\text{S}^0 K^+$ candidates.

3.4 Determination of the raw asymmetries

The raw asymmetries for the signal and control decay modes are estimated from a simultaneous least-squares fit to the mass distributions of the selected positive (+) and negative (−) mesons candidates. For each sample, the function to fit to the data is given by

$$F^{\pm}_{\rm tot}(m|\vec{\alpha^{\pm}},\vec{\beta^{\pm}}) = N_{\rm sig}\,\frac{1\pm A_{\rm sig}}{2}\,F^{\pm}_{\rm sig}(m,\vec{\alpha^{\pm}}) + N_{\rm bkg}\,\frac{1\pm A_{\rm bkg}}{2}\,F^{\pm}_{\rm bkg}(m,\vec{\beta^{\pm}}), \tag{3.20}$$

where N and A represent the yield and the raw asymmetry of the various components respectively, $F_{\rm sig}$ and $F_{\rm bkg}$ are normalized to unity and $\vec{\alpha}$ and $\vec{\beta}$ are vectors of free parameters. Details about the functions used to describe signal and background decays are presented in Sections 3.4.1 and 3.4.2. The general strategy is to determine all shape parameters directly from the data. Fits are performed separately for each magnet polarity and data-taking years. This choice is driven by the desire of having a better control of the nuisance detection asymmetries. In fact, as a consequence of the detector left-right asymmetry, different detection asymmetries are expected when using the magnet with opposite polarities. Moreover, minor upgrades of the LHCb detector and of its trigger conditions among the years can also have an impact on detection asymmetries. The fit procedure has been validated with pseudoexperiments as discussed in Section 3.9.3 where systematic uncertainties due to the inaccuracy of the fit models have also been evaluated. The raw asymmetries of all signals are shifted by unknown offsets, different for each decay mode, sampled uniformly between -1% and 1%, such that the results remain blind until the analysis procedure is finalized and approved. In the following the raw asymmetries that are blind are indicated with the label $A^{\rm blind}$. $D^+ \to K^-\pi^+\pi^+_{trig}$ and $D^+_s \to \phi\pi^+$ ($D^+ \to K^0_{\rm S}\pi^+_{trig}$ and $D^+_s \to K^0_{\rm S}K^+$) modes share the same shift. In this way the *CP* asymmetries obtained with the D^+ and D^+_s methods have the same offset and can be compared and then combined. The offsets used in the blinding of the raw asymmetries are reported in Section 3.12.

3.4.1 Fit to the $D^+_{(s)}$ samples

The function describing $D^+_{(s)}$ decay with a $K^0_{\rm S}$ in the final state is the sum of a Gaussian (G) and a Johnson S_U function (J):

$$F^{\pm}_{D^+_{(s)}{\rm 2body}}(m) = f_J\,J(m|\mu^{\pm},\sigma^{\pm}_J,\nu_J,\tau_J) \tag{3.21}$$

$$+(1-f_J)\,G(m|\mu^{\pm},\sigma_G). \tag{3.22}$$

The Johnson S_U distribution is defined by its mean (μ), its standard deviation (σ), its skewness (ν) and its kurtosis (τ) as [109]

$$J(m) = \frac{e^{-r^2/2}}{2\pi\,w\,\sigma\,\tau\,\sqrt{z^2+1}}, \tag{3.23}$$

where

$$r = -\nu + \frac{\text{asinh}(z)}{\tau}, \quad z = \frac{m-\mu}{w\,\sigma} + \sqrt{e^{\tau^2}}\sinh(\nu\tau), \quad w = \frac{e^{\tau^2}-1}{2\sqrt{e^{\tau^2}\cosh(2\nu\tau)+1}}. \tag{3.24}$$

A sum of two Gaussians ($G_{1,2}$) and a Johnson S_U function (J) is used to describe the mass distribution for the $D^+ \to K^-\pi^+\pi^+_{trig}$ and $D^+_s \to \phi\pi^+$ modes

$$F^{\pm}_{D^+_{(s)}\text{3body}}(m) = f_J\, J(m|\mu^{\pm}_J, \sigma^{\pm}_J, \nu_J, \tau_J) \tag{3.25}$$

$$+(1-f_J)\big[f_{G_1}\, G_1(m|\mu^{\pm}_{G_1}, \sigma^{\pm}_{G_1}) \tag{3.26}$$

$$+(1-f_{G_1})\, G_2(m|\mu^{\pm}_{G_2}, \sigma^{\pm}_{G_2})\big]. \tag{3.27}$$

The mean and the widths of the signal functions are allowed to vary between $D^+_{(s)}$ and $D^-_{(s)}$ candidates, *i.e.* $\mu^{\pm}_{G_i(J)} = \mu_{G_i(J)} \pm \Delta\mu_{G_i(J)}$ and $\sigma^{\pm}_{G_i(J)} = \sigma_{G_i(J)} \pm \Delta\sigma_{G_i(J)}$. This choice is motivated by the so-called "curvature bias", due to the misalignment of the tracking layers of the detector, and causing an offset between the the momenta measured for particles with opposite charge, also in terms of resolution. In principle, this effect is also corrected with the momentum-scale calibration embedded in the DTF. However, the performance of this method is not perfect and different parameter values between positive and negative distributions have been found when fitting independently the positive and negative tagged sample.

The combinatorial background is modeled by an exponential function:

$$F^{\pm}_{\text{bkg}}(m) = e^{-\lambda^{\pm} m}, \tag{3.28}$$

where λ is free to float between positive and negative distributions due to the possible presence of non-peaking backgrounds introduced in Section 3.3.

3.4.2 Fit to the D^{*+} samples

The raw asymmetries are measured by means of fits to the $m(D^0\pi)$ invariant-mass spectra, defined as

$$m(D^0\pi) \equiv \sqrt{m^2_{D^0} + m^2_\pi + 2\sqrt{m^2_{D^0} + |\vec{p}_{D^0}|^2}\sqrt{m^2_\pi + |\vec{p}_\pi|^2} - 2\,\vec{p}_{D^0}\,\vec{p}_\pi}. \tag{3.29}$$

This equation does not rely on any mass hypotheses on the D^0 daughters and it is calculated using the known D^0 mass [31]. This choice is justified by the tight cut appied to the invariant mass of the D^0 and allows for a better resolution on the D^{*+} signal. However, backgrounds that do not peak in the D^0 mass distribution become peaking in

$m(D^0\pi)$ and are studied in Section 3.9.2. The signal component is parametrised with the following function for D^{*+} and D^{*-} decays

$$\begin{aligned} F^{\pm}_{\text{sig}}(m) = \Theta(m - m_{\text{trsh.}})\Big[& f_J J(m; \mu^{\pm}_J, \sigma_J, \nu_J, \tau_J) \\ & + (1 - f_J)\big[f_1 G_1(m; \mu^{\pm}_1, \sigma_1) \\ & + (1 - f_1)\big[f_2 G_2(m; \mu^{\pm}_2, \sigma_2) \\ & + (1 - f_2) G_3(m; \mu^{\pm}_3, \sigma_3)\big]\big]\Big], \end{aligned} \tag{3.30}$$

where Θ stands for the Heaviside function, $m_{\text{trsh.}} = 2004.4\,\text{MeV}/c^2$, $G_{1,2,3}$ are Gaussian function and J is the Johnson S_U function [109]. The value $m_{\text{trsh.}}$ corresponds to the minimum possible value of $\text{m}(D^0\pi)$ and it is fixed in the fits. All the other parameters entering Eq. 3.30 are left free to be adjusted. Also in this case, the means of the signal functions are allowed to vary between D^{*+} and D^{*-} candidates, *i.e.* $\mu^{\pm}_i = \mu_i \pm \Delta\mu_{G_i(J)}$, as motivated by the different parameter values found when fitting independently the positive and negative tagged sample.

The background pdf shares the same parameters between D^{*+} and D^{*-} decays. It is given by an empirical formula describing the combinatorial background of a true D^0 meson paired with a random π^+_{soft} coming from the primary vertex:

$$F_{\text{bkg}}(m) = \Theta(m - m_{\text{trsh.}})(m - m_{D^0} - m_\pi)^a e^{-b(m - m_{D^0} - m_\pi)}, \tag{3.31}$$

where a and b are free parameters in fits.

3.4.3 Fit results in the D^+ method

In Figures 3.7 and 3.8 (top) the invariant mass distributions with the fit projections overlaid are shown for the 2016 magnet-down sample, as an example. Figures 3.7 and 3.8 (bottom) represent the raw asymmetries calculated as $(N^+ - N^-)/(N^+ + N^-)$ for the number of candidates in each bin of the invariant mass histograms as a function of the invariant mass with the fit results overlaid. Here, the irregular shapes of the distributions result from the different parameters between the positive and negative mass spectra and are caused by the aforementioned curvature bias. In addition, Figures 3.7 and 3.8 (bottom) offer the possibility to check if the integrated asymmetry is accurately measured. As one can notice by looking at the residual distributions at the bottom of the plots, raw asymmetries are well described by the fits. Similar results can be observed for different year and magnet polarity configuration.

The results of the fits to the selected data without the weighting procedure applied are reported in Table 3.10 together with the total signal yields. Unblind results are also shown in Figure 3.63. In general, it is possible to notice that different raw asymmetry values are found among the several subsamples for each decay mode. This behaviour

is justified by the left-right asymmetry of the LHCb detector and by the evolution of its running conditions, as anticipated at the beginning of the section. In particular, results obtained from data set of opposite magnet polarity are not compatible between each others. However, in the case of the $D^+ \to K^0_S\pi^+_{trig}$ and $D^0 \to K^-K^+$ decay modes, compatibility among subsamples of the same magnet-polarity data set is found. This is justified by the combination of two effects: the low-statistic of the collected decay samples and the fact that in these decay channels the raw asymmetry is expected to be smaller than the ones measured in the $D^+ \to K^-\pi^+\pi^+_{trig}$ and $D^0 \to K^-\pi^+$ decay samples, as only the detection asymmetry of one particle, the pion (π^+_{trig} or π^+_{soft}), contributes.

The values of the signal and background parameters obtained when fitting the 2016 magnet-down sample are also reported in Tables 3.11 to 3.14, as an example. Similar results can be observed for different year and magnet polarity configuration.

	$D^+ \to K^0_S\pi^+_{trig}$	$D^+ \to K^-\pi^+\pi^+_{trig}$	$D^0 \to K^-\pi^+$	$D^0 \to K^-K^+$
tot. yields	$6 \cdot 10^6$	$188 \cdot 10^6$	$58 \cdot 10^6$	$37 \cdot 10^6$
	$A^{\text{blind}}_{\text{unweighted}}$ $[10^{-4}]$	$A^{\text{blind}}_{\text{unweighted}}$ $[10^{-4}]$	$A^{\text{blind}}_{\text{unweighted}}$ $[10^{-4}]$	$A^{\text{blind}}_{\text{unweighted}}$ $[10^{-4}]$
15 Dw	37.1 ± 23.5	-41.3 ± 4.6	-111.8 ± 7.7	15.1 ± 9.9
16 Dw	55.7 ± 10.4	-25.2 ± 2.0	-130.4 ± 3.5	-7.8 ± 4.4
17 Dw	53.3 ± 10.1	-21.0 ± 1.9	-115.0 ± 3.3	-21.3 ± 4.4
18 Dw	64.2 ± 9.9	-29.3 ± 1.9	-122.9 ± 3.3	-14.0 ± 4.3
15 Up	-51.5 ± 28.9	-70.7 ± 5.8	-274.3 ± 9.5	-150.1 ± 12.2
16 Up	-30.2 ± 11.2	-82.2 ± 2.3	-273.8 ± 4.2	-169.0 ± 4.6
17 Up	-22.5 ± 10.2	-92.2 ± 2.0	-292.0 ± 3.4	-160.8 ± 4.5
18 Up	-24.6 ± 9.6	-82.9 ± 1.8	-289.1 ± 3.1	-168.7 ± 4.2

Table 3.10: Raw asymmetries (A) obtained from fits to the $D^+ \to K^0_S\pi^+_{trig}$, $D^+ \to K^-\pi^+\pi^+_{trig}$, $D^0 \to K^-\pi^+$ and $D^0 \to K^-K^+$ samples when the kinematic weights are not applied, separately for the different data-taking years and polarity.

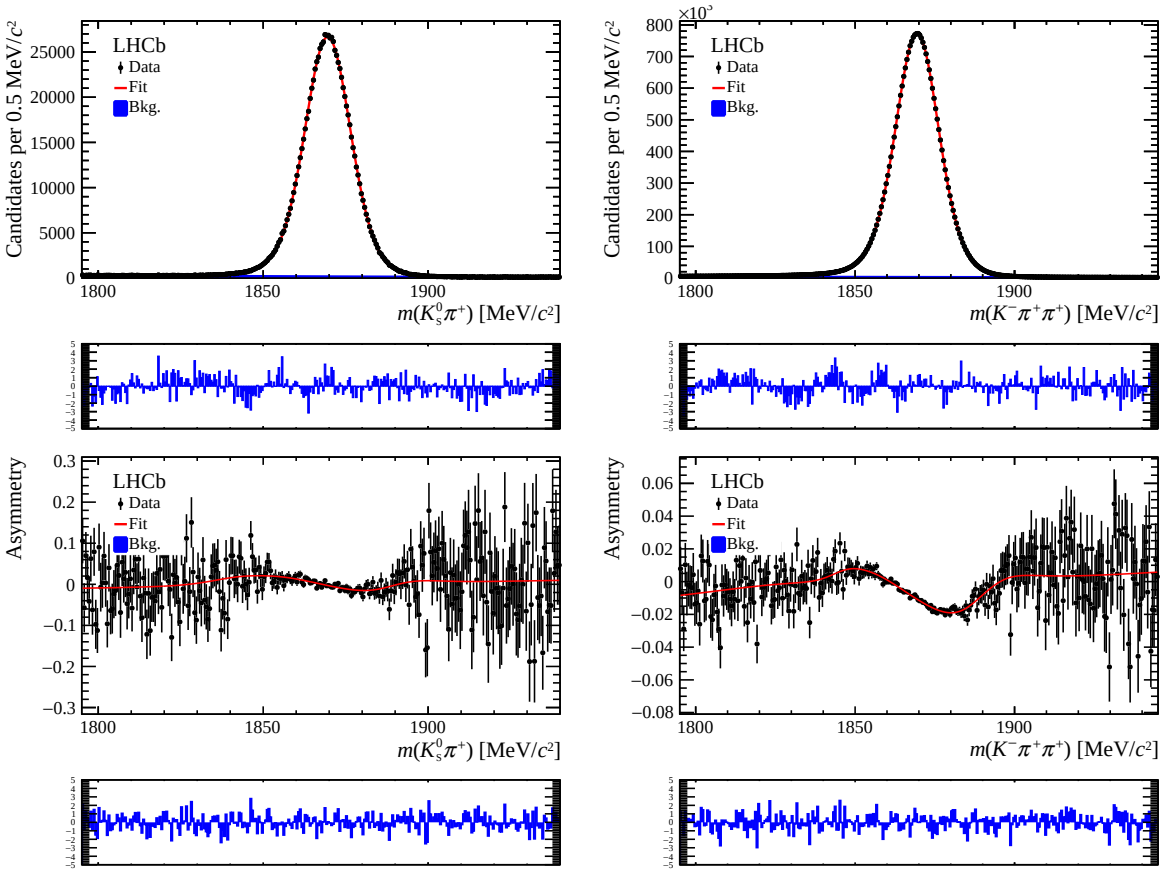

Figure 3.7: (top) Invariant mass distributions of $K^0_S\pi^+$ and $K^-\pi^+\pi^+$ modes for $D^\pm$ candidates reconstructed in 2016 magnet-down data, with fits results overlaid. (bottom) Distribution of the raw asymmetry as a function of the invariant mass. For each plot, the bottom panel shows distribution of the pulls between data and fit result. Similar results can be observed for different year and magnet polarity configuration.

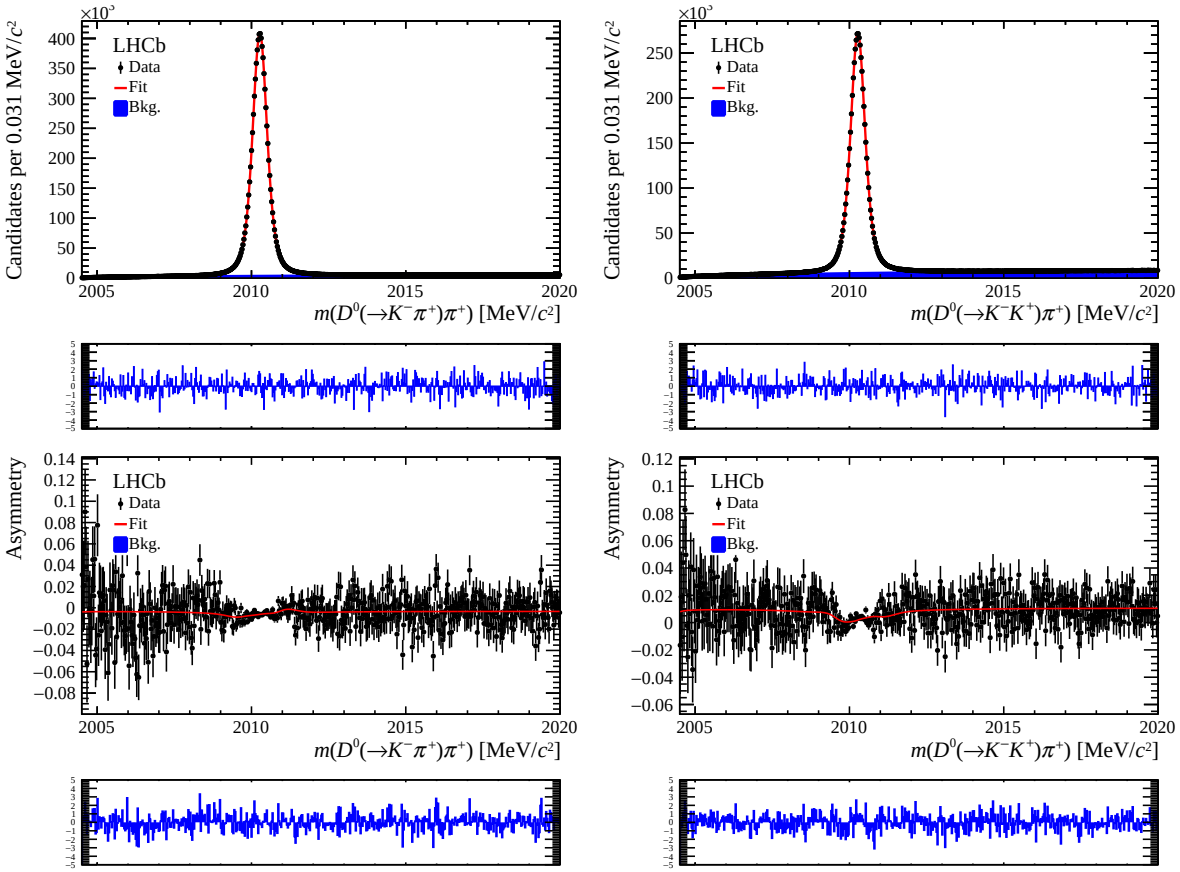

Figure 3.8: (top) Invariant mass distributions of $D^0\pi^+_{soft}$ modes for $D^{*\pm}$ candidates reconstructed in 2016 magnet-down data in the D^+ method, with fits results overlaid. (bottom) Distribution of the raw asymmetry as a function of the invariant mass. For each plot, the bottom panel shows distribution of the pulls between data and fit result. Similar results can be observed for different year and magnet polarity configuration.

Fit parameter	Value	Unity
A_{bkg}	-0.0019 ± 0.0060	
$A_{\text{sig}}^{\text{blind}}$	0.0056 ± 0.0010	
ν_J	-0.559 ± 0.054	
τ_J	0.401 ± 0.015	
N_{bkg}	53939.00 ± 384.65	
N_{sig}	970999.00 ± 1032.00	
λ	-0.00839 ± 0.00012	$[\text{MeV}/c^2]^{-1}$
$\Delta\lambda$	0.00013 ± 0.00012	$[\text{MeV}/c^2]^{-1}$
f_J	0.411 ± 0.018	
μ_J	3879.5700 ± 0.0099	MeV/c^2
σ_J	10.22 ± 0.13	MeV/c^2
σ_G	6.317 ± 0.031	MeV/c^2
$\Delta\mu$	-0.0785 ± 0.0081	MeV/c^2
$\Delta\sigma_J$	0.059 ± 0.019	MeV/c^2

Table 3.11: Shape parameters from the fit to the 2016 magnet-down $D^+ \to K^0_{\text{S}}\pi^+$ sample. Similar results can be observed for different year and magnet polarity configuration.

Fit parameter	Value	Unity
A_{bkg}	-0.0046 ± 0.0025	
$A_{\text{sig}}^{\text{blind}}$	-0.00252 ± 0.00020	
ν_J	-0.959 ± 0.036	
τ_J	0.854 ± 0.012	
N_{bkg}	941815.00 ± 6316.80	
N_{sig}	28149506.00 ± 8192.10	
λ	-0.005750 ± 0.000095	$[\text{MeV}/c^2]^{-1}$
$\Delta\lambda$	0.000121 ± 0.000033	$[\text{MeV}/c^2]^{-1}$
f_J	0.1452 ± 0.0044	
f_{G_1}	0.399 ± 0.025	
μ_J	3876.07 ± 0.46	MeV/c^2
μ_{G_1}	3878.57 ± 0.29	MeV/c^2
μ_{G_2}	3879.770 ± 0.038	MeV/c^2
σ_J	22.16 ± 0.53	MeV/c^2
σ_{G_1}	8.508 ± 0.051	MeV/c^2
σ_{G_2}	5.898 ± 0.038	MeV/c^2
$\Delta\mu_J$	-0.114 ± 0.039	MeV/c^2
$\Delta\mu_{G_1}$	-0.060 ± 0.018	MeV/c^2
$\Delta\mu_{G_2}$	-0.0519 ± 0.0071	MeV/c^2
$\Delta\sigma_J$	0.164 ± 0.046	MeV/c^2
$\Delta\sigma_{G_1}$	0.0211 ± 0.0094	MeV/c^2
$\Delta\sigma_{G_2}$	0.0051 ± 0.0032	MeV/c^2

Table 3.12: Shape parameters from the fit to the 2016 magnet-down $D^+ \to K^-\pi^+\pi^+$ sample. Similar results can be observed for different year and magnet polarity configuration.

Fit parameter	Value	Unity
A_{bkg}	-0.00337 ± 0.00086	
$A_{\text{sig}}^{\text{blind}}$	-0.01304 ± 0.00035	
ν_J	0.294 ± 0.012	
τ_J	1.415 ± 0.040	
N_{bkg}	1853402.00 ± 9853.70	
N_{sig}	8882905.00 ± 10204.00	
a	0.5611 ± 0.0049	
b	0.0158 ± 0.0012	$[\,\text{MeV}/c^2]^{-1}$
f_{G_1}	0.363 ± 0.027	
f_{G_2}	0.835 ± 0.012	
f_J	0.2073 ± 0.0093	
μ_{G_1}	2010.26908 ± 0.00100	MeV/c^2
μ_{G_2}	2010.2981 ± 0.0051	MeV/c^2
μ_{G_3}	2010.405 ± 0.023	MeV/c^2
μ_J	2010.404 ± 0.024	MeV/c^2
$\Delta\mu_{G_1}$	0.00027 ± 0.00041	MeV/c^2
$\Delta\mu_{G_2}$	-0.00008 ± 0.00050	MeV/c^2
$\Delta\mu_{G_3}$	0.0036 ± 0.0022	MeV/c^2
$\Delta\mu_J$	0.0007 ± 0.0010	MeV/c^2
σ_{G_1}	0.1776 ± 0.0024	MeV/c^2
σ_{G_2}	0.2688 ± 0.0046	MeV/c^2
σ_{G_3}	0.452 ± 0.012	MeV/c^2
σ_J	2.10 ± 0.19	MeV/c^2

Table 3.13: Shape parameters from the fit to the 2016 magnet-down $D^0 \to K^-\pi^+$ sample in the D^+ method. Similar results can be observed for different year and magnet polarity configuration.

Fit parameter	Value	Unity
A_{bkg}	0.01069 ± 0.00066	
$A_{\text{sig}}^{\text{blind}}$	-0.00078 ± 0.00044	
ν_J	0.211 ± 0.014	
τ_J	1.780 ± 0.080	
N_{bkg}	2962348.00 ± 14703.00	
N_{sig}	5951597.00 ± 14805.00	
a	0.5553 ± 0.0037	
b	0.01372 ± 0.00081	$[\text{MeV}/c^2]^{-1}$
f_{G_1}	0.280 ± 0.038	
f_{G_2}	0.790 ± 0.014	
f_J	0.232 ± 0.017	
μ_{G_1}	2010.2808 ± 0.0047	MeV/c^2
μ_{G_2}	2010.2852 ± 0.0025	MeV/c^2
μ_{G_3}	2010.3286 ± 0.0094	MeV/c^2
μ_J	2010.613 ± 0.089	MeV/c^2
$\Delta\mu_{G_1}$	0.00026 ± 0.00065	MeV/c^2
$\Delta\mu_{G_2}$	-0.00015 ± 0.00064	MeV/c^2
$\Delta\mu_{G_3}$	-0.0048 ± 0.0026	MeV/c^2
$\Delta\mu_J$	0.0060 ± 0.0020	MeV/c^2
σ_{G_1}	0.1676 ± 0.0054	MeV/c^2
σ_{G_2}	0.2628 ± 0.0071	MeV/c^2
σ_{G_3}	0.457 ± 0.017	MeV/c^2
σ_J	5.12 ± 1.32	MeV/c^2

Table 3.14: Shape parameters from the fit to the 2016 magnet-down $D^0 \to K^-K^+$ sample. Similar results can be observed for different year and magnet polarity configuration.

3.4.4 Fit results in the D_s^+ method

In Figures 3.9 and 3.10 (top) the invariant mass distributions with the fit projections overlaid are shown for the 2016 magnet-down sample, as an example. Figures 3.9 and 3.10 (bottom) represent the raw asymmetries as a function of the invariant mass with the fit results overlaid. Here, similarly to the D^+ method, the irregular shapes of the distributions are due to the curvature bias. In addition, residual distributions at the bottom of the plots demonstrate that raw asymmetries are well described by the fits. Similar results can be observed for different year and magnet polarity configuration.

The results of the fits to the selected data without the weighting procedure applied are reported in Table 3.10 together with the total signal yields. Unblind results are instead shown in Figure 3.64. As for the D^+ method, also in this case different raw asymmetry values are found among the several subsamples for each decay mode. Larger discrepancy are found between samples with opposite magnet polarity while compatibility among subsamples of the same magnet-polarity data set is observed in $D_s^+ \to K_S^0 K^+$, $D_s^+ \to \phi\pi^+$ and $D^0 \to K^- K^+$ decay modes. This is justified by the combination of two effects: the low-statistic of the collected decay samples and the fact that in these decay channels the raw asymmetry is expected to be smaller than the one measured in the $D^0 \to K^-\pi^+$ decay sample, as only the detection asymmetry of one particle (the K^+, the π^+ or the π^+_{soft}) contributes.

The values of the signal and background parameters obtained when fitting the 2016 magnet-down sample are reported in Tables 3.14 and 3.16 to 3.18, as an example. Similar results can be observed for different year and magnet polarity configuration.

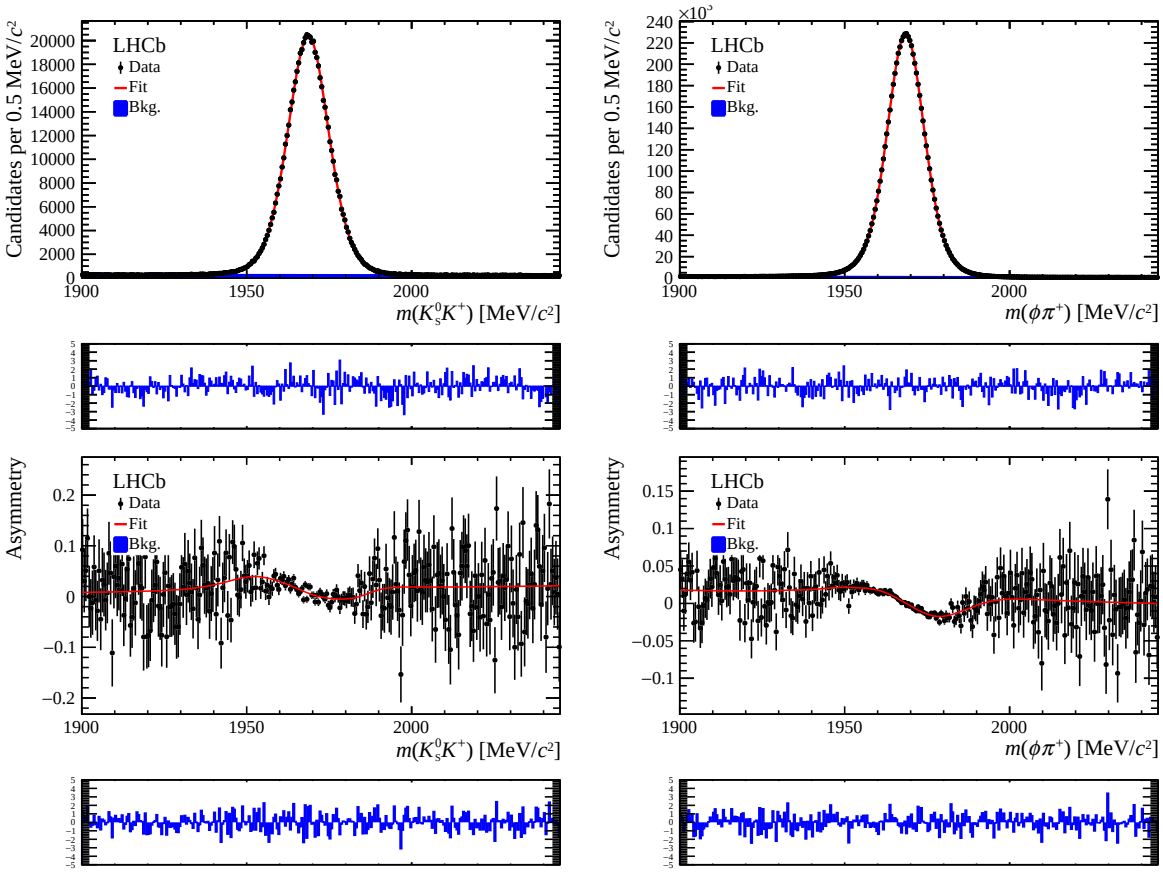

Figure 3.9: (top) Invariant mass distributions of the $K^0_S K^+$, $K^-K^+\pi^+$ modes for $D_s^\pm$ candidates reconstructed in 2016 magnet-down data, with fit results overlaid. (bottom) Distribution of the raw asymmetry as a function of the invariant mass. For each plot, the bottom panel shows the distribution of the pulls between data and fit projection. Similar results can be observed for different year and magnet polarity configuration.

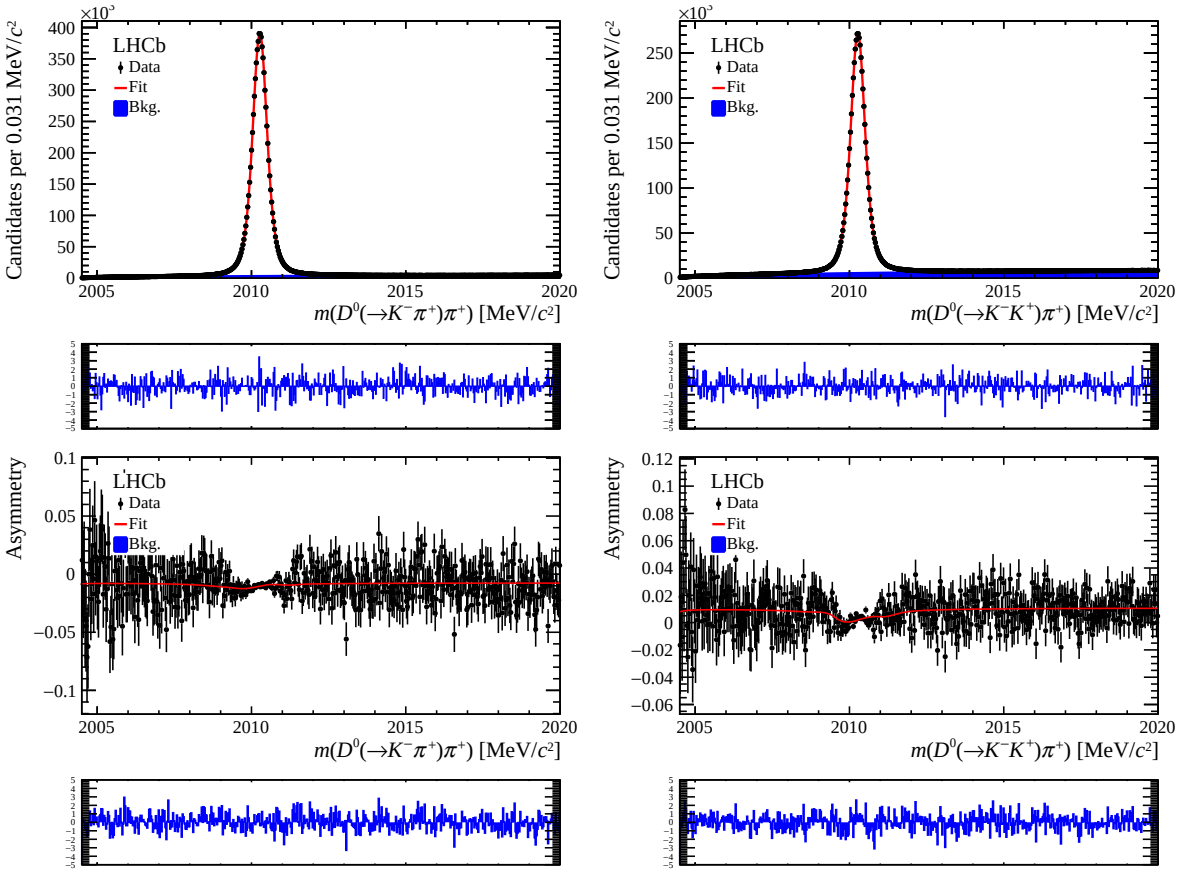

Figure 3.10: (top) Invariant mass distributions of the $D^0\pi^+_{soft}$ modes for $D^{*\pm}$ candidates reconstructed in 2016 magnet-down data in the D_s^+ method, with fit results overlaid. (bottom) Distribution of the raw asymmetry as a function of the invariant mass. For each plot, the bottom panel shows the distribution of the pulls between data and fit projection. Similar results can be observed for different year and magnet polarity configuration.

tot. yields	$5 \cdot 10^6$	$43 \cdot 10^6$	$56 \cdot 10^6$	$37 \cdot 10^6$
	$D_s^+ \to K_S^0 K^+$	$D_s^+ \to \phi\pi^+$	$D^0 \to K^-\pi^+$	$D^0 \to K^-K^+$
	$D_s^+ \to K_S^0 K^+$	$D_s^+ \to \phi\pi^+$	$D^0 \to K^-\pi^+$	$D^0 \to K^-K^+$
	$A^{\text{blind}}_{\text{unweighted}}$ $[10^{-4}]$	$A^{\text{blind}}_{\text{unweighted}}$ $[10^{-4}]$	$A^{\text{blind}}_{\text{unweighted}}$ $[10^{-4}]$	$A^{\text{blind}}_{\text{unweighted}}$ $[10^{-4}]$
15 Dw	154.3 ± 27.8	56.2 ± 8.8	-142.1 ± 9.7	15.1 ± 9.9
16 Dw	168.9 ± 12.8	73.6 ± 4.0	-173.7 ± 4.2	-7.8 ± 4.4
17 Dw	131.1 ± 11.8	60.5 ± 3.8	-154.0 ± 3.5	-21.3 ± 4.4
18 Dw	159.2 ± 11.6	67.3 ± 3.7	-153.1 ± 3.2	-14.0 ± 4.3
15 Up	32.0 ± 34.8	4.6 ± 10.8	-261.0 ± 7.8	-150.1 ± 12.2
16 Up	65.2 ± 14.6	9.0 ± 4.2	-230.0 ± 3.6	-169.0 ± 4.6
17 Up	80.0 ± 12.0	9.7 ± 3.8	-270.7 ± 3.4	-160.8 ± 4.5
18 Up	72.2 ± 11.2	5.7 ± 3.6	-256.0 ± 3.3	-168.7 ± 4.2

Table 3.15: Raw asymmetries (A) obtained from fits to the $D_s^+ \to K_S^0 K^+$, $D_s^+ \to \phi\pi^+$, $D^0 \to K^-\pi^+$ and $D^0 \to K^-K^+$ samples when the kinematic weights are not applied, separately for the different data-taking years and polarity.

Fit parameter	Value	Unity
A_{bkg}	0.0144 ± 0.0049	
$A_{\text{sig}}^{\text{blind}}$	0.0169 ± 0.0013	
ν_J	-0.058 ± 0.010	
τ_J	0.621 ± 0.028	
N_{bkg}	69793.00 ± 462.75	
N_{sig}	656440.00 ± 894.88	
λ	-0.001396 ± 0.000096	$[\text{MeV}/c^2]^{-1}$
$\Delta\lambda$	0.000091 ± 0.000094	$[\text{MeV}/c^2]^{-1}$
f_J	0.530 ± 0.030	
μ_J	3978.870 ± 0.011	MeV/c^2
σ_J	8.17 ± 0.13	MeV/c^2
σ_G	6.342 ± 0.081	MeV/c^2
$\Delta\mu$	-0.0897 ± 0.0089	MeV/c^2
$\Delta\sigma_J$	0.060 ± 0.020	MeV/c^2

Table 3.16: Shape parameters from the fit to the 2016 magnet-down $D_s^+ \to K_S^0 K^+$ sample. Similar results can be observed for different year and magnet polarity configuration.

Fit parameter	Value	Unity
A_{bkg}	0.0099 ± 0.0032	
$A_{\text{sig}}^{\text{blind}}$	0.00736 ± 0.00040	
ν_J	-0.622 ± 0.030	
τ_J	0.702 ± 0.013	
N_{bkg}	268120.00 ± 1405.30	
N_{sig}	6805024.00 ± 2917.50	
λ	-0.006323 ± 0.000075	$[\text{MeV}/c^2]^{-1}$
$\Delta\lambda$	-0.000122 ± 0.000052	$[\text{MeV}/c^2]^{-1}$
f_J	0.205 ± 0.013	
f_{G_1}	0.409 ± 0.023	
μ_J	3979.67 ± 0.22	MeV/c^2
μ_{G_1}	3977.77 ± 0.21	MeV/c^2
μ_{G_2}	3978.670 ± 0.032	MeV/c^2
σ_J	11.40 ± 0.29	MeV/c^2
σ_{G_1}	6.883 ± 0.095	MeV/c^2
σ_{G_2}	4.733 ± 0.043	MeV/c^2
$\Delta\mu_J$	-0.111 ± 0.041	MeV/c^2
$\Delta\mu_{G_1}$	-0.056 ± 0.032	MeV/c^2
$\Delta\mu_{G_2}$	-0.077 ± 0.011	MeV/c^2
$\Delta\sigma_J$	0.064 ± 0.030	MeV/c^2
$\Delta\sigma_{G_1}$	0.006 ± 0.016	MeV/c^2
$\Delta\sigma_{G_2}$	-0.0006 ± 0.0056	MeV/c^2

Table 3.17: Shape parameters from the fit to the 2016 magnet-down $D_s^+ \to \phi\pi^+$ sample. Similar results can be observed for different year and magnet polarity configuration.

Fit parameter	Value	Unity
A_{bkg}	-0.00767 ± 0.00093	
$A_{\text{sig}}^{\text{blind}}$	-0.01737 ± 0.00036	
ν_J	0.270 ± 0.015	
τ_J	1.380 ± 0.056	
N_{bkg}	1599122.00 ± 10942.00	
N_{sig}	8498688.00 ± 11253.00	
a	0.5664 ± 0.0054	
b	0.0174 ± 0.0014	$[\,\text{MeV}/c^2]^{-1}$
f_{G_1}	0.393 ± 0.022	
f_{G_2}	0.833 ± 0.013	
f_J	0.184 ± 0.015	
μ_{G_1}	2010.2707 ± 0.0010	MeV/c^2
μ_{G_2}	2010.2907 ± 0.0049	MeV/c^2
μ_{G_3}	2010.366 ± 0.019	MeV/c^2
μ_J	2010.424 ± 0.033	MeV/c^2
$\Delta\mu_{G_1}$	0.00026 ± 0.00038	MeV/c^2
$\Delta\mu_{G_2}$	0.00032 ± 0.00053	MeV/c^2
$\Delta\mu_{G_3}$	-0.0006 ± 0.0028	MeV/c^2
$\Delta\mu_J$	0.0014 ± 0.0016	MeV/c^2
σ_{G_1}	0.1818 ± 0.0022	MeV/c^2
σ_{G_2}	0.2807 ± 0.0055	MeV/c^2
σ_{G_3}	0.479 ± 0.017	MeV/c^2
σ_J	2.12 ± 0.23	MeV/c^2

Table 3.18: Shape parameters from the fit to the 2016 magnet-down $D^0 \to K^-\pi^+$ sample in the D_s^+ method. Similar results can be observed for different year and magnet polarity configuration.

3.5 Kinematic reweighting

Production and detection asymmetries depend on the kinematic. For this reason decay channels must have the same kinematic distributions in order to cancel nuisance asymmetries between them. The procedure adopted to equalize the kinematic distributions is described in this section. The evaluation of the corresponding systematic uncertainty is reported in Section 3.9.4.

3.5.1 Weighting procedure in D^+ method

The determination of $\mathcal{A}^{CP}(K^-K^+)$ with the D^+ decays as control channels (Eq. 3.16) requires that

1. the D^0 kinematic distributions of the $D^0 \to K^-K^+$ sample agree with those of the $D^0 \to K^-\pi^+$ signal, to cancel the D^{*+} production asymmetry and π^+_{soft} detection asymmetry[6];

2. the K^- kinematic distributions of the $D^+ \to K^-\pi^+\pi^+_{trig}$ sample agree with those of the $D^0 \to K^-\pi^+$ signal, to cancel the kaon detection asymmetry;

3. the π^+ kinematic distributions of the $D^+ \to K^-\pi^+\pi^+_{trig}$ sample agree with those of the $D^0 \to K^-\pi^+$ signal, to cancel the pion detection asymmetry;

4. the D^+ kinematic distributions of the $D^+ \to K^-\pi^+\pi^+_{trig}$ sample agree with those of the $D^+ \to K^0_S\pi^+_{trig}$ signal, to cancel the D^+ production asymmetry;

5. the π^+_{trig} kinematic distributions of the $D^+ \to K^-\pi^+\pi^+_{trig}$ sample agree with those of the $D^+ \to K^0_S\pi^+_{trig}$ signal, to cancel the pion detection asymmetry.

Per-candidate weights are applied to all the decay channels and their values are obtained from the division of normalized kinematic distributions. The distribution at the numerator is called target distribution, since when weights are applied to the distribution at the denominator, the two distributions will match. Background-subtracted kinematic distributions of track candidates obtained with the *sPlot* technique [110] are used. The values of the weights are extracted defining normalized six- and three-dimensional (p_T, η and ϕ) track distributions. The six-dimensional binning scheme is used when the variables of two particles are considered. The binning schemes consist in uniform 10^6 and 40^3 bins

[6]The two decay samples $D^{*+} \to D^0\pi^+$ with $D^0 \to K^-K^+$ and $D^0 \to \pi^-\pi^+$ have exactly the same online and offline selection with the only exception of the D^0 daughters having different requirements on PID and kinematic variables. Once D^0 kinematics distributions are equalised between the two decay modes, the ones of the D^{*+} and of the π^+_{soft} are also equal by definition. The strategy of using the D^0 kinematics instead of the ones of the D^{*+} and π^+_{soft} is particularly helpful as it reduces the equalization problem from 6 to 3 dimensions.

for six- and three-dimensional weighting, respectively. For each distribution, the events with a weight greater than a value of 15 are rejected together with the corresponding candidates of the target distribution. This step allows to remove areas of phase-space that have a poor overlap between the samples and avoids large statistical fluctuations due to the application of weights with large value to few events. It deletes approximately 5%, 10%, 5% and 15% of the candidates in $D^0 \to K^-K^+$, $D^0 \to K^-\pi^+$, $D^+ \to K^-\pi^+\pi^+_{trig}$ and $D^+ \to K^0_S\pi^+_{trig}$ samples, respectively. The process consists in an iterative weighting which converges when a reasonably good agreement is achieved in all the distributions (three iterations are sufficient). The procedure is explained in the following lines.

1. Compute weights from the six-dimensional (D^+,π^+_{trig}) distribution of the $D^+ \to K^-\pi^+\pi^+_{trig}$ decay to match the one of the $D^+ \to K^0_S\pi^+_{trig}$ decay. The weights are applied to the $D^+ \to K^-\pi^+\pi^+_{trig}$ sample.

2. Compute weights from the three-dimensional K^- distribution of the $D^+ \to K^-\pi^+\pi^+_{trig}$ sample to match the one of the $D^0 \to K^-\pi^+$ signal. The weights are applied to the $D^+ \to K^-\pi^+\pi^+_{trig}$ sample.

3. Compute weights from the three-dimensional π^+ distribution of the $D^0 \to K^-\pi^+$ sample to match the one of the $D^+ \to K^-\pi^+\pi^+_{trig}$ signal. The weights are applied to the $D^0 \to K^-\pi^+$ sample.

4. Compute weights from the six-dimensional (D^+,π^+_{trig}) distribution of the $D^+ \to K^0_S\pi^+_{trig}$ sample to match the one of the $D^+ \to K^-\pi^+\pi^+_{trig}$ signal. The weights are applied to the $D^+ \to K^0_S\pi^+_{trig}$ sample.

5. Compute weights from the three-dimensional D^0 distribution of the $D^0 \to K^-K^+$ sample to match the one of the $D^0 \to K^-\pi^+$ signal. The weights are applied to the $D^0 \to K^-K^+$ sample.

The weighting procedure is performed separately for data-taking year and magnet polarity to ensure a precise cancellation of the instrumental asymmetries. The kinematic distributions used as input of the weighting procedure with and without weights applied are shown for the magnet-down 2016 data in Figure 3.11, as an example. The (p_x, p_y, p_z) kinematic distributions are also shown for all the relevant particles in Figure 3.12 for the magnet-down 2016 data, as an example. As one can notice, imperfect agreement between the variable distributions is found with alternative kinematic variables and a thinner binning scheme. Larger discrepancies are found in the D^+ and π^+_{trig} (p_x, p_y, p_z) distributions, as a consequence of the large binning scheme used for the 6-dimensional weighting of the D^+ and π^+_{trig} particles (only 10 bins per dimension). However, the overall impact of these "local" discrepancies is expected to be small, as studied in Section 3.9.4. Weights distributions for the magnet-down 2016 sample are shown in Figure 3.13 for the

various decay modes, as an example. Similar results can be observed for different year and magnet polarity configuration.
The effective number of events of a weighted data-set (including background),

$$N_{\text{eff}} = \left(\sum_i w_i\right)^2 / \sum_i w_i^2,$$

roughly corresponds to the size of a hypothetical (unweighted) sample having the same statistical power of the weighted sample. The comparison between N_{eff} and the original sample size, N, quantifies the retention of statistical power due to the weighting procedure. The values for N_{eff}/N and N_{eff} are reported in Table 3.19. From the table, it is possible to notice that the impact of the weighting procedure on the statistical power of the decay samples is strong, in particular for the $D^+ \to K^0_S\pi^+_{trig}$, $D^+ \to K^-\pi^+\pi^+_{trig}$ and $D^0 \to K^-\pi^+$ decay modes. This is a direct consequence of the poor phase-space overlap between $D^+ \to K^0_S\pi^+_{trig}$ and $D^+ \to K^-\pi^+\pi^+_{trig}$ decay samples with an additional issue given by the fact that also phase-space overlap is required between $D^+ \to K^-\pi^+\pi^+_{trig}$ and $D^0 \to K^-\pi^+$ decay samples. Moreover, the $D^+ \to K^0_S\pi^+_{trig}$ decay sample is the one with lower effective yields and it is expected to limit the precision on the $\mathcal{A}^{CP}(K^-K^+)$ measurement.

	N_{eff}/N	N_{eff}
$D^0 \to K^-K^+$	75%	$28 \cdot 10^6$
$D^0 \to K^-\pi^+$	35%	$20 \cdot 10^6$
$D^+ \to K^-\pi^+\pi^+_{trig}$	25%	$47 \cdot 10^6$
$D^+ \to K^0_S\pi^+_{trig}$	25%	$2 \cdot 10^6$

Table 3.19: Values for the retention in statistical power due to the weighting procedure in the various decay samples.

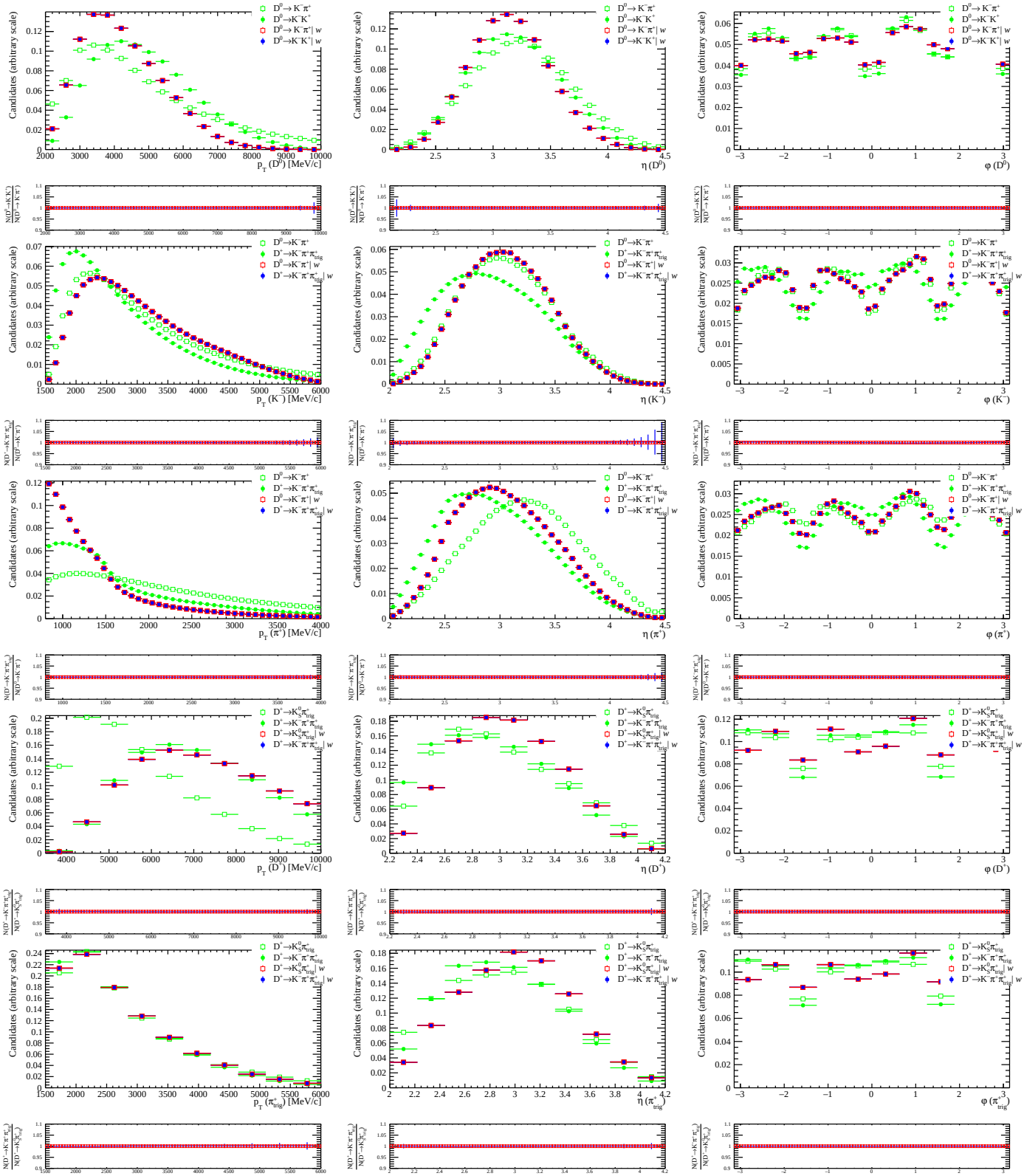

Figure 3.11: Comparison between normalized and background-subtracted (left) p_{T}, (center) η, (right) ϕ distributions of D^0, K^-, π^+, D^+ and π^+_{trig} candidates, before and after the kinematic weighting procedure applied. The binning of the distributions is the same used for the weights computation. For each plot, the bottom panel shows the ratio between the distributions after the weighting procedure. Magnet-down 2016 data are shown. Similar results can be observed for different year and magnet polarity configuration.

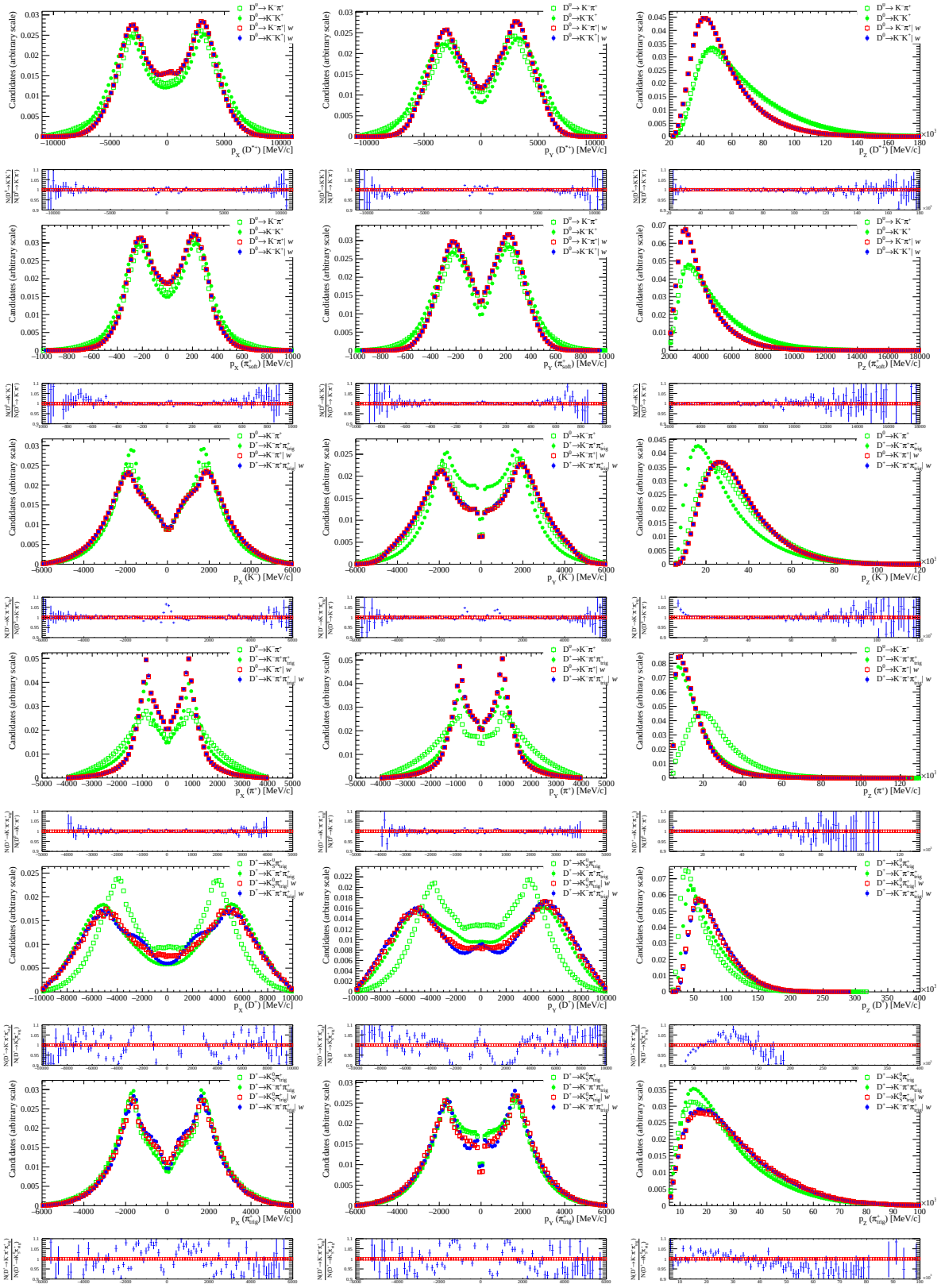

Figure 3.12: Comparison between normalized and background-subtracted (left) p_x, (center) p_y, (right) p_z distributions of D^{*+}, π^+_{soft}, K^-, π^+, D^+ and π^+_{trig} candidates, before and after the kinematic weighting procedure applied. For each plot, the bottom panel shows the ratio between the distributions after the weighting procedure. Magnet-down 2016 data are shown. Similar results can be observed for different year and magnet polarity configuration.

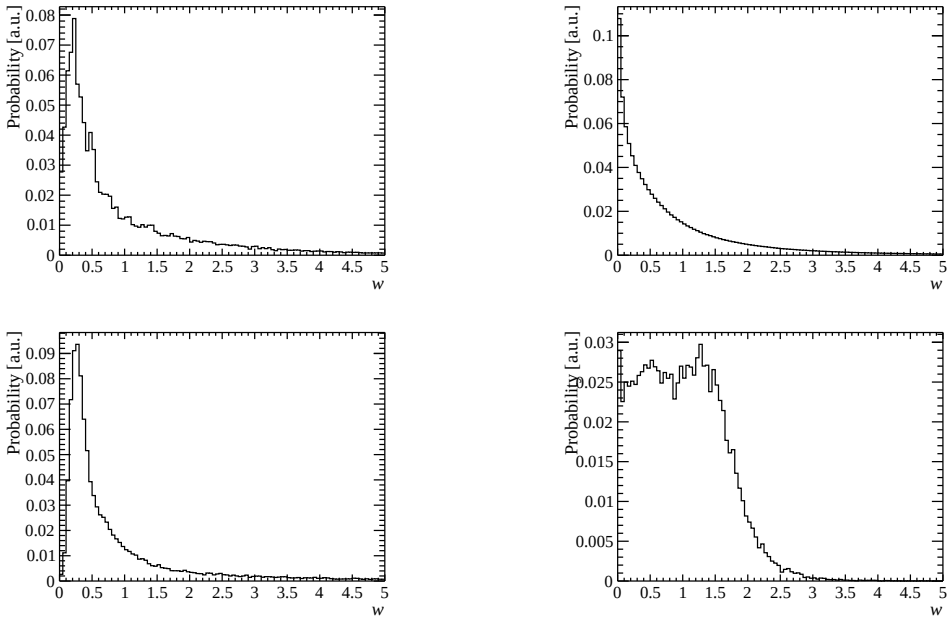

Figure 3.13: Distributions of weights applied to the (top left) $D^+ \to K^0_S \pi^+_{trig}$, (top right) $D^+ \to K^- \pi^+ \pi^+_{trig}$, (bottom left) $D^0 \to K^- \pi^+$ and (bottom right) $D^0 \to K^- K^+$ samples. Magnet-down 2016 data are shown. Similar results can be observed for different year and magnet polarity configuration.

3.5.2 Fit results on weighted samples in the D^+ method

In Figures 3.14 and 3.15 the invariant mass distributions of the weighted samples with the fit projections overlaid are shown for the 2016 magnet-down sample, as an example. Figures 3.14 and 3.15 also represent the raw asymmetries as a function of the invariant mass with the fit results overlaid. As one can notice, invariant mass distributions and raw asymmetries are well described by the fits. Similar results can be observed for different year and magnet polarity configuration.

The results of fits on the weighted samples are reported in Table 3.20. Unblind results are also shown in Figure 3.63. In general, significant changes are observed from the comparison with the results obtained without the weighting procedure (Table 3.10). These differences are somehow expected since the kinematic distributions of each particle deeply change after the application of the weights. Moreover, as anticipated by Table 3.19, it is possible to notice that the $\mathcal{A}^{CP}(K^-K^+)$ measurement is statistically limited by the $D^+ \to K^0_S\pi^+_{trig}$ decay control sample.

	$D^+ \to K^0_S\pi^+_{trig}$ $\vert^w$	$D^+ \to K^-\pi^+\pi^+_{trig}$ $\vert^w$	$D^0 \to K^-\pi^+$ $\vert^w$	$D^0 \to K^-K^+$ $\vert^w$
	A^{blind} $[10^{-4}]$	A^{blind} $[10^{-4}]$	A^{blind} $[10^{-4}]$	A^{blind} $[10^{-4}]$
15 Dw	34.4 ± 44.5	-25.9 ± 11.5	-96.0 ± 14.3	37.3 ± 12.3
16 Dw	71.1 ± 20.3	-7.8 ± 4.2	-128.6 ± 6.3	4.9 ± 5.2
17 Dw	48.2 ± 20.3	-6.5 ± 4.0	-116.6 ± 5.8	-9.5 ± 5.2
18 Dw	60.2 ± 19.8	-22.5 ± 3.9	-117.7 ± 5.7	-1.1 ± 5.1
15 Up	-6.1 ± 54.1	-92.4 ± 15.5	-299.0 ± 18.0	-155.1 ± 15.5
16 Up	-39.2 ± 22.1	-81.7 ± 4.8	-287.4 ± 8.3	-166.2 ± 5.7
17 Up	-37.3 ± 20.3	-99.3 ± 4.2	-308.9 ± 5.9	-167.1 ± 5.3
18 Up	-31.0 ± 19.1	-79.2 ± 3.8	-294.8 ± 5.5	-173.2 ± 4.9

Table 3.20: Raw asymmetries obtained from fits to the weighted $D^+ \to K^0_S\pi^+_{trig}$, $D^+ \to K^-\pi^+\pi^+_{trig}$, $D^0 \to K^-\pi^+$ and $D^0 \to K^-K^+$ samples, separately for the different data-taking years and polarities.

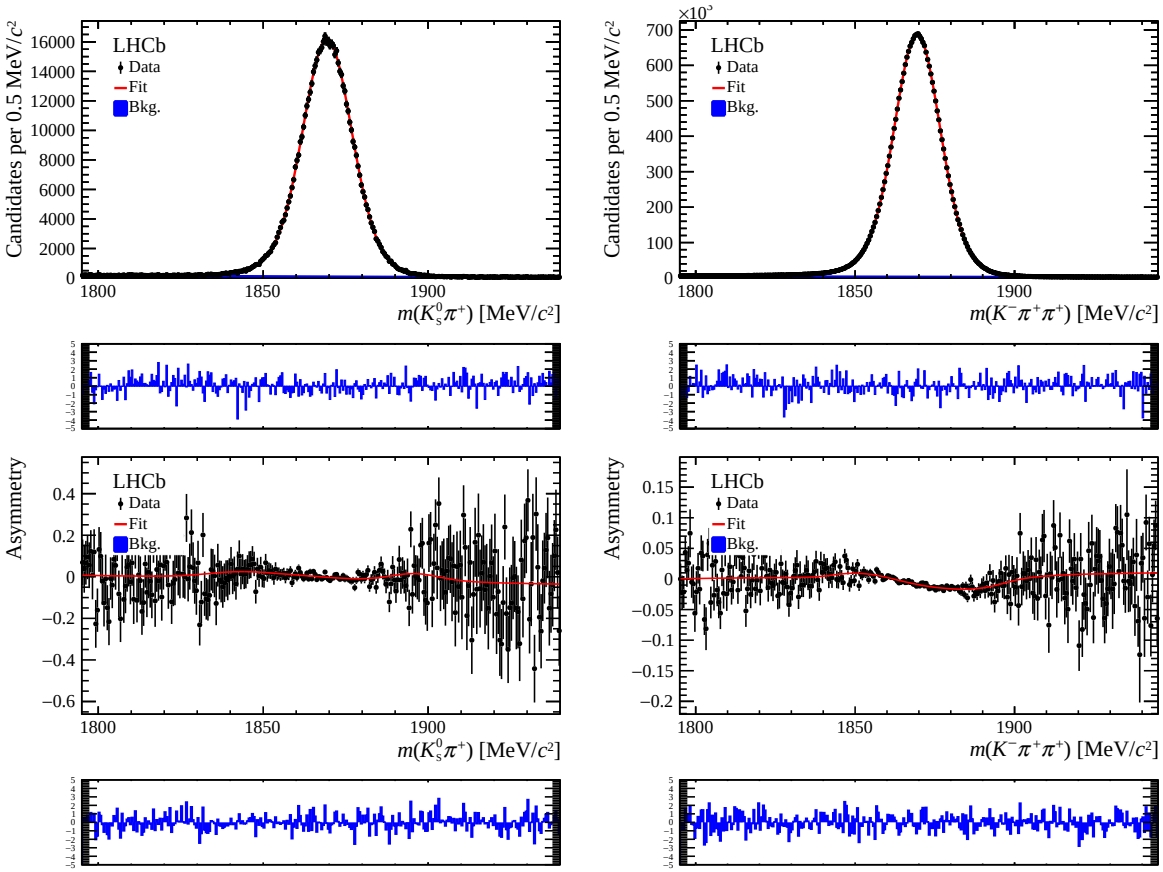

Figure 3.14: (top) Invariant mass distributions of $K^0_S\pi^+$ and $K^-\pi^+\pi^+$ modes for $D^\pm$ candidates reconstructed in 2016 magnet-down weighted data, with fits results overlaid. (bottom) Distribution of the raw asymmetry as a function of the invariant mass. For each plot, the bottom panel shows distributions of the pulls between data and fit results. Similar results can be observed for different year and magnet polarity configuration.

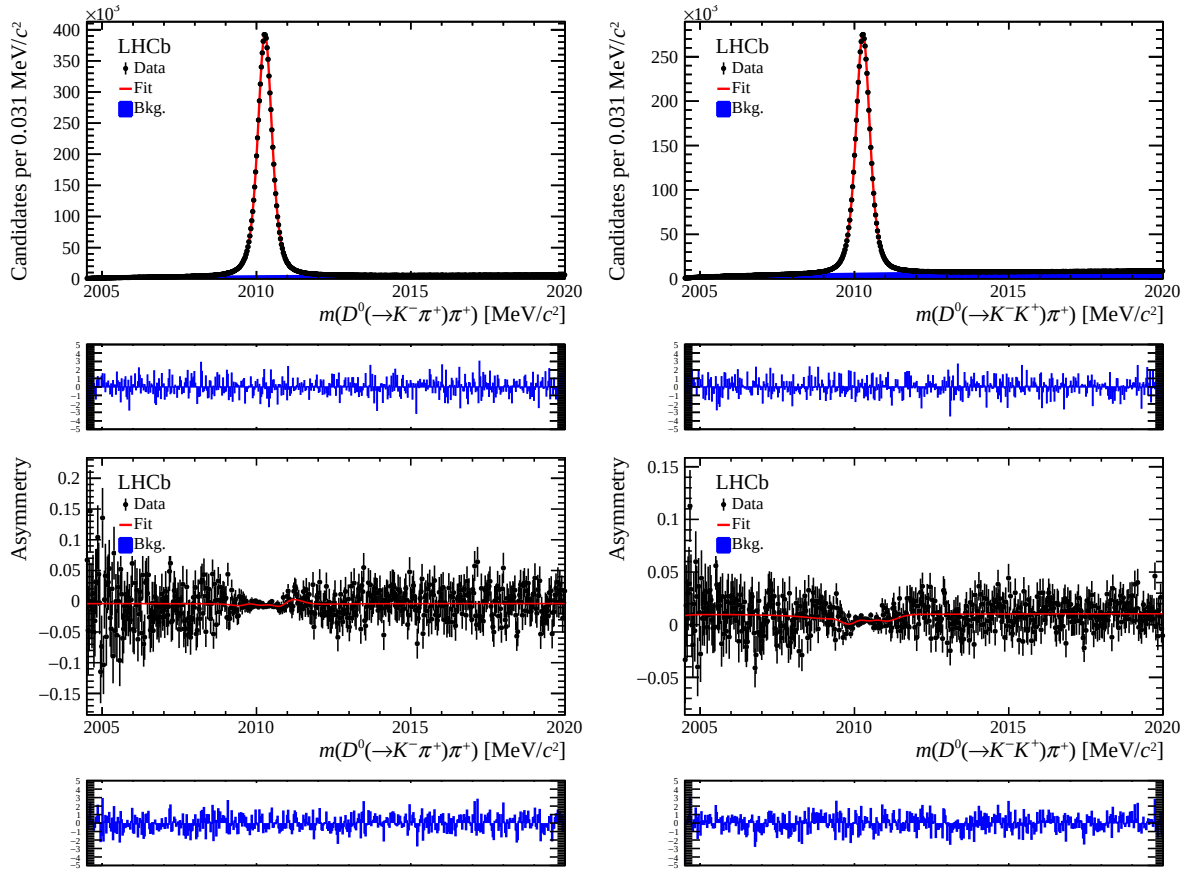

Figure 3.15: (top) Invariant mass distributions of $D^0(K^-K^+)\pi^+_{soft}$ modes for $D^{*\pm}$ candidates reconstructed in 2016 magnet-down weighted data in the D^+ method, with fits results overlaid. (bottom) Distribution of the raw asymmetry as a function of the invariant mass. For each plot, the bottom panel shows distributions of the pulls between data and fit results. Similar results can be observed for different year and magnet polarity configuration.

3.5.3 Weighting procedure in D_s^+ method

The determination of $\mathcal{A}^{CP}(K^-K^+)$ with the D_s^+ decays as control channels (Eq. 3.17) requires that:

1. the D^0 kinematic distributions of the $D^0 \to K^-K^+$ sample agree with those of the $D^0 \to K^-\pi^+$ signal, to cancel the D^{*+} production asymmetry and π^+_{soft} detection asymmetry;

2. the K^- kinematic distributions of the $D_s^+ \to K^0_S K^+$ sample agree with those of the $D^0 \to K^-\pi^+$ signal, to cancel the kaon detection asymmetry;

3. the π^+ kinematic distributions of the $D_s^+ \to \phi\pi^+$ sample agree with those of the $D^0 \to K^-\pi^+$ signal, to cancel the pion detection asymmetry;

4. the D_s^+ kinematic distributions of the $D_s^+ \to \phi\pi^+$ sample agree with those of the $D_s^+ \to K^0_S K^+$ signal, to cancel the D_s^+ production asymmetry.

Similar to the D^+ method, the value of the weights is extracted defining normalized three-dimensional (p_T, η and ϕ) tracks distributions as described in Section 3.5.1. The process consists in a iterative weighting, which converges when a reasonably good agreement is achieved in all the distributions (three iterations are sufficient). The procedure is described in the following lines.

1. Compute weights from the three-dimensional K^- distribution of the $D^0 \to K^-\pi^+$ sample to match the one of the $D_s^+ \to K^0_S K^+$ signal. The weights are applied to the $D^0 \to K^-\pi^+$ sample.

2. Compute weights from the three-dimensional D_s^+ distribution of the $D_s^+ \to \phi\pi^+$ sample to match the one of the $D_s^+ \to K^0_S K^+$ signal. The weights are applied to the $D_s^+ \to \phi\pi^+$ sample.

3. Compute weights from the three-dimensional π^+ distribution of the $D_s^+ \to \phi\pi^+$ sample to match the one of the $D^0 \to K^-\pi^+$ signal. The weights are applied to the $D_s^+ \to \phi\pi^+$ sample.

4. Compute weights from the three-dimensional D_s^+ distribution of the $D_s^+ \to K^0_S K^+$ sample to match the one of the $D_s^+ \to \phi\pi^+$ signal. The weights are applied to the $D_s^+ \to K^0_S K^+$ sample.

5. Compute weights from the three-dimensional D^0 distribution of the $D^0 \to K^-K^+$ sample to match the one of the $D^0 \to K^-\pi^+$ signal. The weights are applied to the $D^0 \to K^-K^+$ sample.

The weighting procedure is performed separately for data-taking year and magnet polarity to ensure a precise cancellation of the instrumental asymmetries. The kinematic distributions used as input of the weighting procedure with and without weights applied are shown for the magnet-down 2016 data in Figure 3.16, as an example. The (p_x, p_y, p_z) kinematic distributions are also shown for all the relevant particles in Figure 3.17 for the magnet-down 2016 data, as an example. Imperfect agreement between the variable distributions can be found with alternative kinematic variables and a thinner binning scheme. Discrepancies in the D_s^+ method are found to be smaller than the ones observed in the D^+ method. However, their impact is studied in Section 3.9.4. Weights distributions for the magnet-down 2016 sample are shown in Figure 3.18 for the various decay modes, as an example. Similar results can be observed for different year and magnet polarity configuration.

The comparison between N_{eff} and the original sample size, N, quantifies the retention of statistical power due to the weighting procedure. The values for N_{eff}/N and N_{eff} are reported in Table 3.21. Differently from the D^+ method, the impact of the weighting procedure on the statistical power of the decay samples is low as less stringent requirements are needed to match the various kinematic distributions. However, similarly to the D^+ method, the decay sample with a K^0_{S} in the final state, *i.e.* the $D_s^+ \to K^0_{\text{S}}K^+$ decay sample, has the lower effective yields and it is expected to limit the precision on the $\mathcal{A}^{CP}(K^-K^+)$ measurement. From the comparison between Tables 3.19 and 3.21 it is possible to understand that the D_s^+ method has better performances and it is expected to bring a better sensitivity to $\mathcal{A}^{CP}(K^-K^+)$. However, the achievable resolutions will differ only by a factor 20% and being dominated by two independent samples, the $D^+ \to K^0_{\text{S}}\pi^+_{trig}$ and $D_s^+ \to K^0_{\text{S}}K^+$ decay samples, the two measurements can be combined to further improve the precision on $\mathcal{A}^{CP}(K^-K^+)$.

	N_{eff}/N	N_{eff}
$D^0 \to K^-K^+$	75%	$28 \cdot 10^6$
$D^0 \to K^-\pi^+$	75%	$42 \cdot 10^6$
$D_s^+ \to \phi\pi^+$	55%	$24 \cdot 10^6$
$D_s^+ \to K^0_{\text{S}}K^+$	70%	$3 \cdot 10^6$

Table 3.21: Values for the retention in statistical power due to the weighting procedure in the various decay samples.

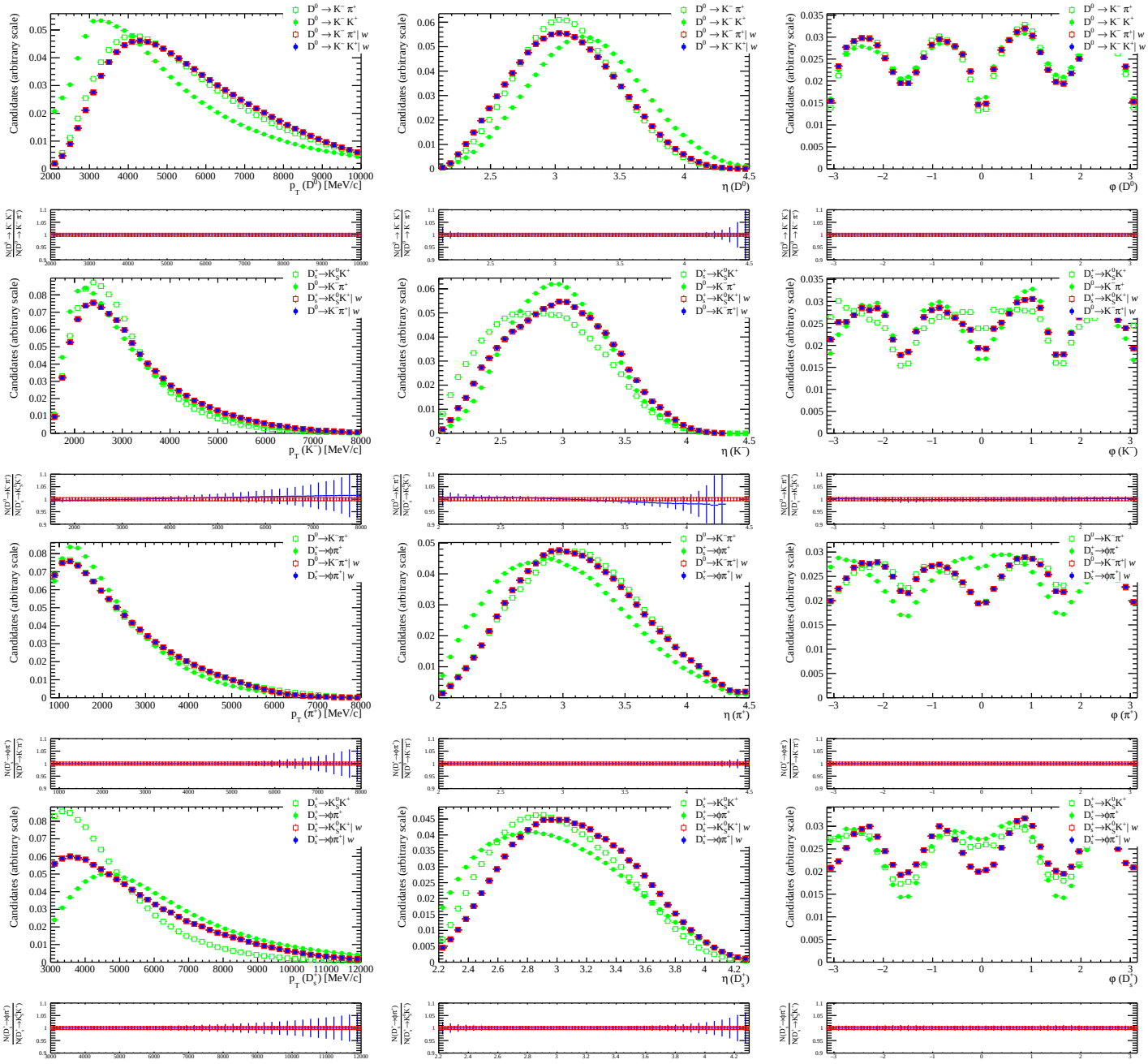

Figure 3.16: Comparison between normalized and background-subtracted (left) p_{T}, (center) η, (right) ϕ distributions of D^0, K^-, π^+ and D_s^+ candidates, before and after the kinematic weighting procedure applied. The binning of the distributions is the same used for the weights computation. For each plot, the bottom panel shows the ratio between the distributions after the weighting procedure. Magnet-down 2016 data are shown. Similar results can be observed for different year and magnet polarity configuration.

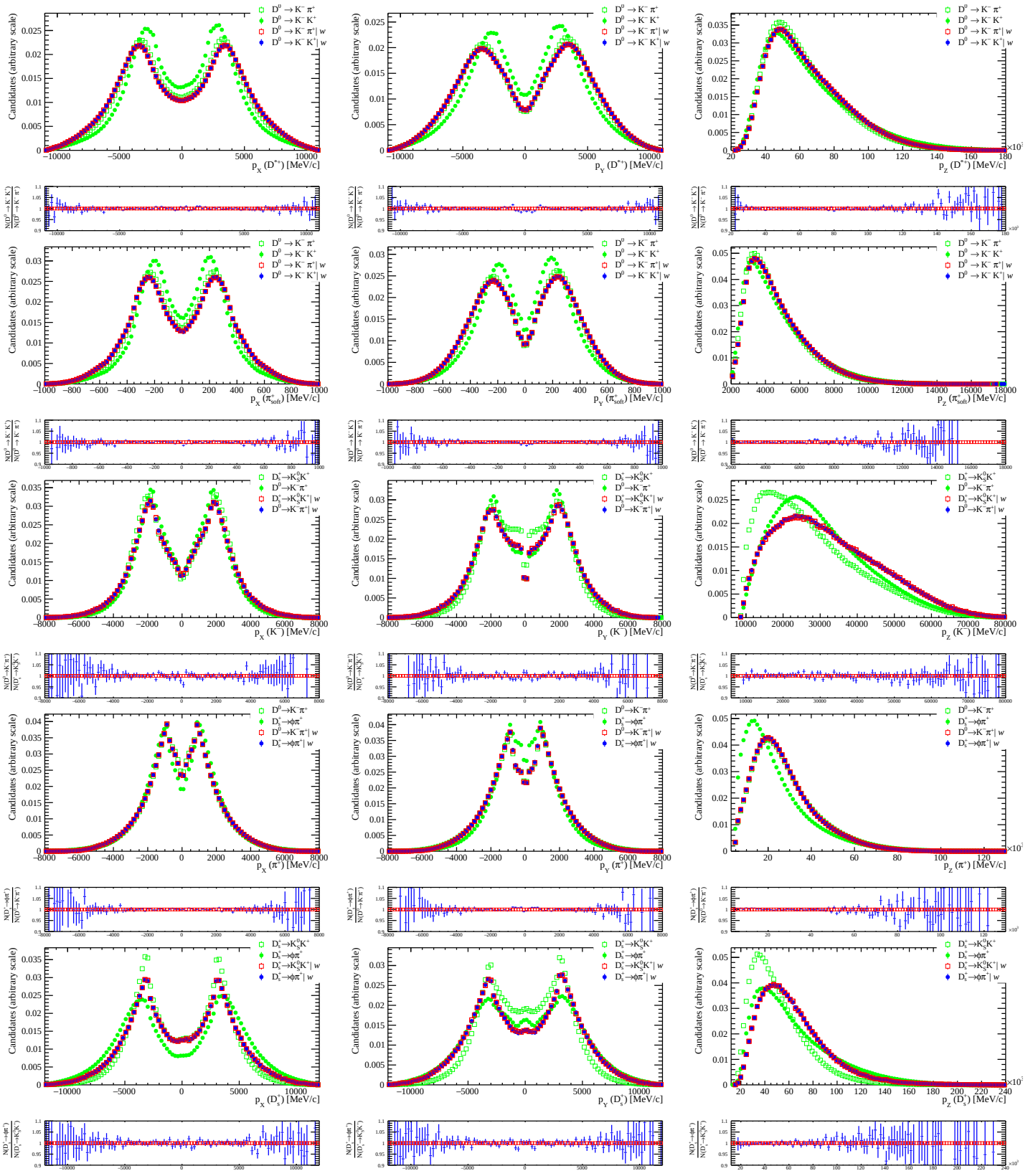

Figure 3.17: Comparison between normalized and background-subtracted (left) p_x, (center) p_y, (right) p_z distributions of D^0, K^-, π^+ and D_s^+ candidates, before and after the kinematic weighting procedure applied. For each plot, the bottom panel shows the ratio between the distributions after the weighting procedure. Magnet-down 2016 data are shown. Similar results can be observed for different year and magnet polarity configuration.

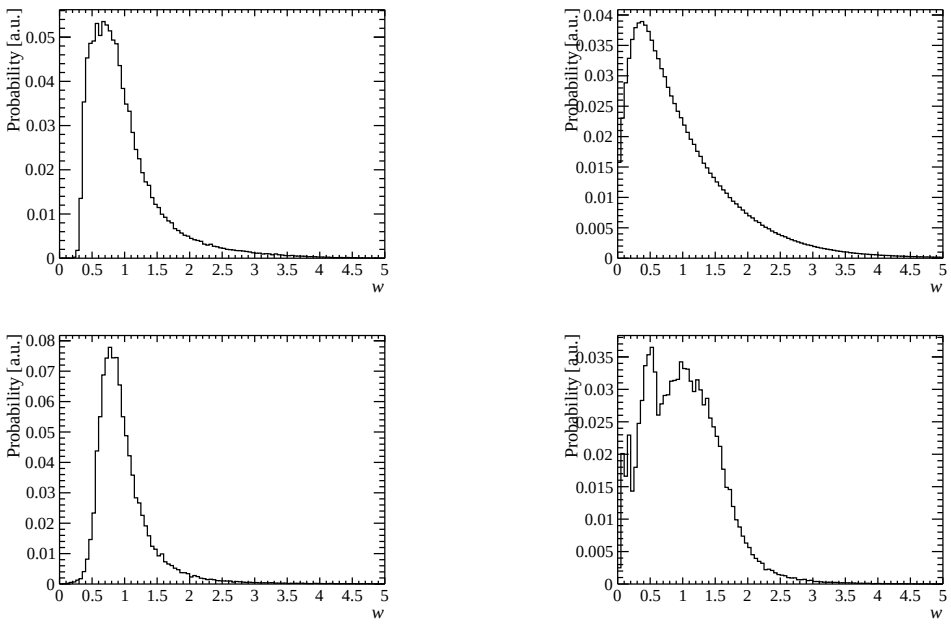

Figure 3.18: Distributions of weights applied to the (top left) $D_s^+ \to K_S^0 K^+$, (top right) $D_s^+ \to \phi\pi^+$, (bottom left) $D^0 \to K^-\pi^+$ and (bottom right) $D^0 \to K^-K^+$ samples. Magnet-down 2016 data are shown. Similar results can be observed for different year and magnet polarity configuration.

3.5.4 Fit results on weighted samples in the D_s^+ method

In Figures 3.19 and 3.20 the invariant mass distributions of the weighted samples with the fit projections overlaid are shown for the 2016 magnet-down sample, as an example. Figures 3.19 and 3.20 also represent the raw asymmetries as a function of the invariant mass with the fit results overlaid. As one can notice, invariant mass distributions and raw asymmetries are well described by the fits. Similar results can be observed for different year and magnet polarity configuration.

The results of fits on the weighted samples are reported in Table 3.22. Unblind results are also shown in Figure 3.64. Similarly to the D^+ method, significant changes are observed from the comparison with the results obtained without the weighting procedure (Table 3.15). However, these differences are smaller than the ones observed in the D^+ method. This can be justified considering that particles kinematic distributions do not heavily change after the application of the weights. Moreover, as anticipated by Table 3.21, it is possible to notice that the $\mathcal{A}^{CP}(K^-K^+)$ measurement is statistically limited by the $D_s^+ \to K_S^0 K^+$ decay control sample.

	$D_s^+ \to K_S^0 K^+ \,\vert^w$	$D_s^+ \to \phi\pi^+ \,\vert^w$	$D^0 \to K^-\pi^+ \,\vert^w$	$D^0 \to K^-K^+ \,\vert^w$
	A^{blind} $[10^{-4}]$	A^{blind} $[10^{-4}]$	A^{blind} $[10^{-4}]$	A^{blind} $[10^{-4}]$
15 Dw	137.1 ± 32.4	41.1 ± 14.5	-156.5 ± 10.3	1.1 ± 11.7
16 Dw	158.0 ± 15.2	73.0 ± 5.5	-189.2 ± 4.1	-13.1 ± 5.0
17 Dw	115.5 ± 14.1	53.4 ± 5.2	-154.8 ± 3.9	-29.8 ± 4.9
18 Dw	174.6 ± 13.9	58.3 ± 5.0	-163.9 ± 3.8	-19.7 ± 4.8
15 Up	32.2 ± 40.2	3.6 ± 19.9	-261.5 ± 13.5	-130.5 ± 14.9
16 Up	30.8 ± 17.3	8.4 ± 5.8	-224.8 ± 4.9	-157.8 ± 5.2
17 Up	76.0 ± 14.3	17.2 ± 5.3	-268.6 ± 4.0	-153.1 ± 5.0
18 Up	60.5 ± 13.4	8.8 ± 5.0	-246.0 ± 3.7	-153.5 ± 4.6

Table 3.22: Raw asymmetries obtained from fits to the weighted $D_s^+ \to K_S^0 K^+$, $D_s^+ \to \phi\pi^+$, $D^0 \to K^-\pi^+$ and $D^0 \to K^-K^+$ samples, separately for the different data-taking years and polarities.

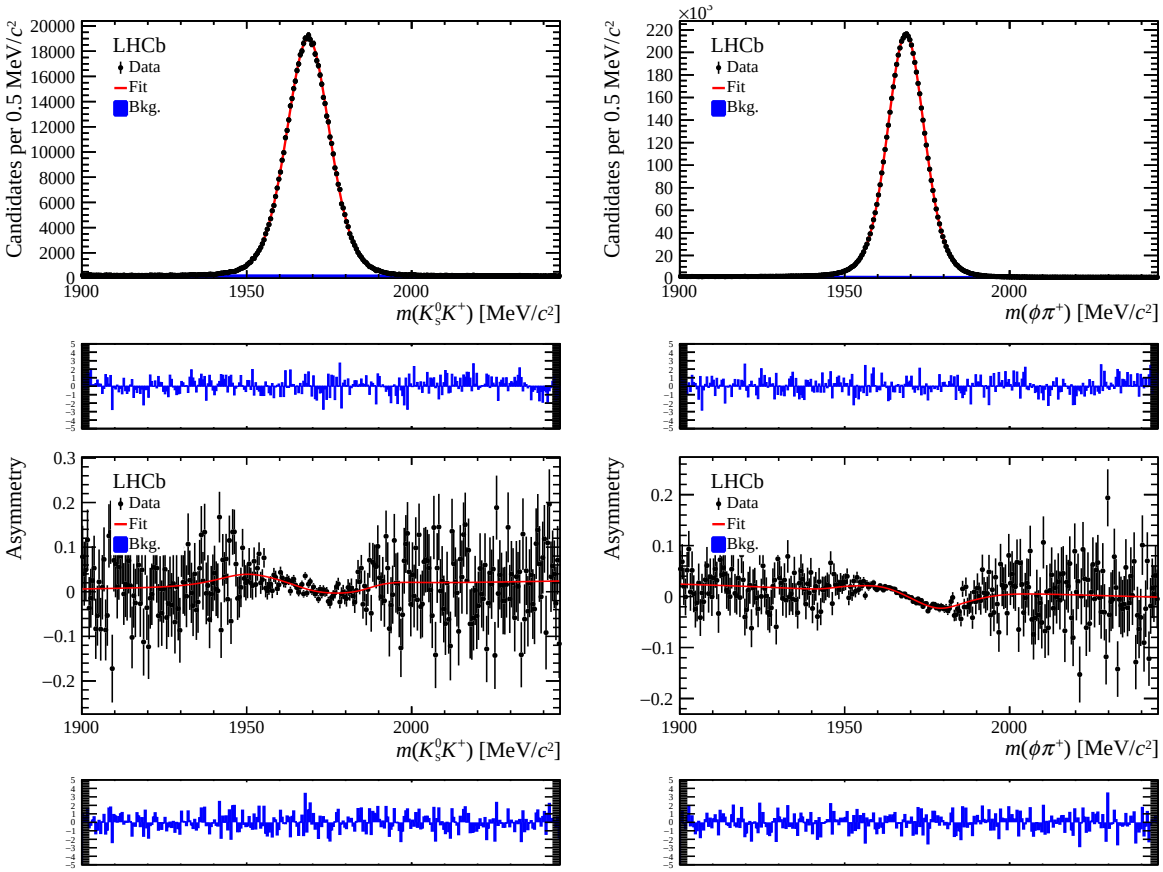

Figure 3.19: (top) Invariant mass distributions of $K^0_S K^+$ and $K^-K^+\pi^+$ modes for $D_s^\pm$ candidates reconstructed in 2016 magnet-down weighted data, with fits results overlaid. (bottom) Distribution of the raw asymmetry as a function of the invariant mass. For each plot, the bottom panel shows distributions of the pulls between data and fit results. Similar results can be observed for different year and magnet polarity configuration.

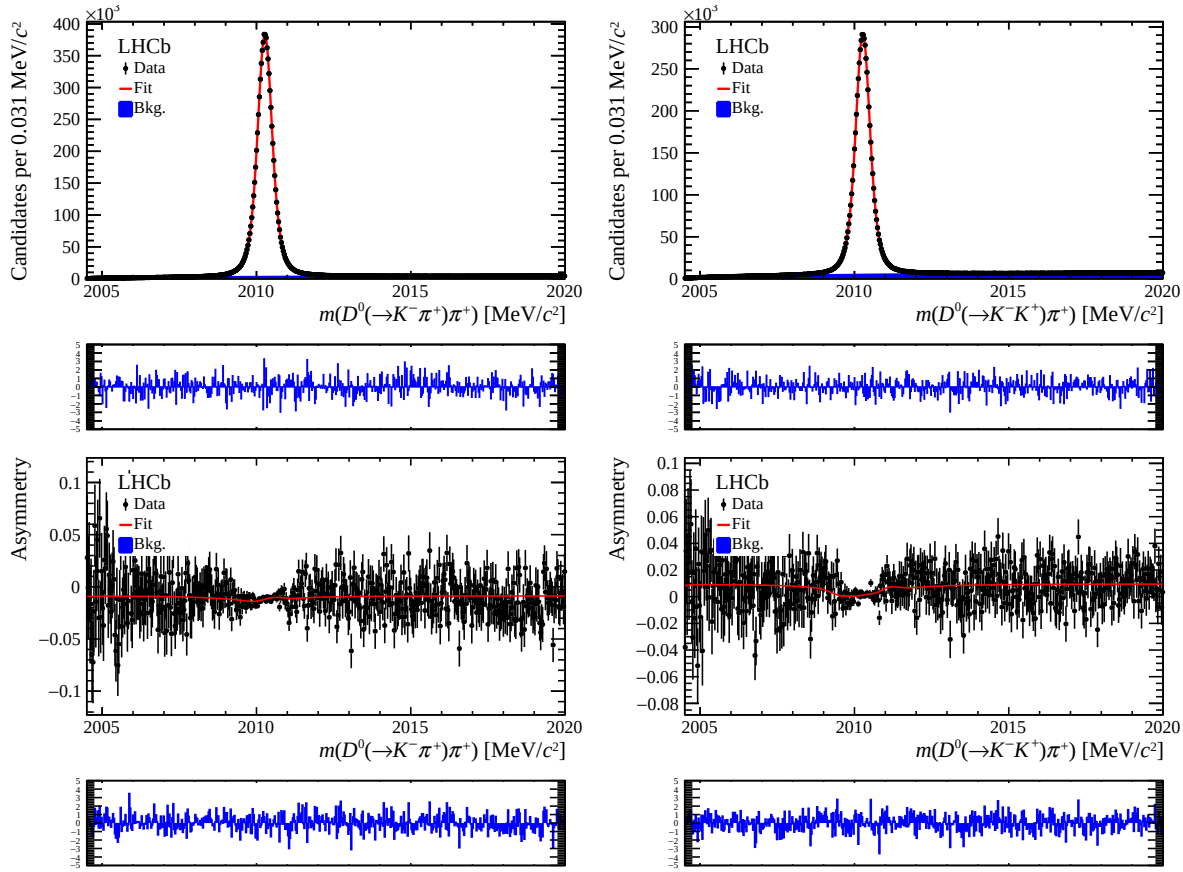

Figure 3.20: (top) Invariant mass distributions of $D^0(K^-\pi^+)\pi^+_{soft}$ and $D^0(K^-K^+)\pi^+_{soft}$ modes for $D^{*\pm}$ candidates reconstructed in 2016 magnet-down weighted data in the D^+_s method, with fits results overlaid. (bottom) Distribution of the raw asymmetry as a function of the invariant mass. For each plot, the bottom panel shows distributions of the pulls between data and fit results. Similar results can be observed for different year and magnet polarity configuration.

3.6 Neutral kaon asymmetry

An asymmetry in the detection of $K^0_S \to \pi^+\pi^-$ decays arises from the combined effect of *CP* violation and mixing in the neutral kaon system, and the different interaction rates of K^0 and $\overline{K}^0$ mesons with the detector material (regeneration). The asymmetry can be estimated using a combination of the material map of LHCb together with the knowledge of the mixing and scattering amplitudes of the neutral kaon system. As reported in Ref. [111], considering the interaction cross section χ ($\bar{\chi}$) of a K^0 ($\overline{K}^0$) with the matter, the time evolution of a neutral kaon is described by the solution of the Schödinger equation

$$i\frac{\partial}{\partial t}\begin{pmatrix}|K^0(t)\rangle\\|\overline{K}^0(t)\rangle\end{pmatrix} = (\mathbf{M} - \mathbf{i/2\Gamma} + \boldsymbol{\chi})\begin{pmatrix}|K^0(t)\rangle\\|\overline{K}^0(t)\rangle\end{pmatrix}, \tag{3.32}$$

where $\mathbf{M}$ and $\mathbf{\Gamma}$ are hermitian matrices already introduced in Section 1.3.1 describing mixing and decay of K^0 and $\overline{K}^0$ mesons in vacuum, *i.e.*

$$(\mathbf{M} - \mathbf{i/2\Gamma}) = \begin{pmatrix}M & M_{12}\\M^*_{12} & M\end{pmatrix} - i/2\begin{pmatrix}\Gamma & \Gamma_{12}\\\Gamma^*_{12} & \Gamma\end{pmatrix}, \tag{3.33}$$

and the matrix

$$\boldsymbol{\chi} = \begin{pmatrix}\chi & 0\\0 & \bar{\chi}\end{pmatrix} \tag{3.34}$$

describes the interaction of kaons with the matter. The time evolution in matter of an arbitrary neutral kaon state ψ in the K^0_L and K^0_S basis is given by the following equations:

$$|\psi(t)\rangle = \alpha_L(t)|K^0_L\rangle + \alpha_S(t)|K^0_S\rangle \text{ with} \tag{3.35}$$

$$\alpha_L(t) = e^{-i\Sigma t}\left[\alpha_L(0)\cos\Omega t - i\frac{\alpha_L(0)\Delta\lambda + \alpha_S(0)\Delta\chi}{2\Omega}\sin\Omega t\right], \tag{3.36}$$

$$\alpha_S(t) = e^{-i\Sigma t}\left[\alpha_S(0)\cos\Omega t - i\frac{\alpha_S(0)\Delta\lambda - \alpha_L(0)\Delta\chi}{2\Omega}\sin\Omega t\right], \tag{3.37}$$

where $\alpha_{L,S}(0)$ are the amplitude coefficients of K^0_S and K^0_L at production being $\alpha_L(0) = \alpha_S(0) = \sqrt{(1+|\epsilon|^2)}/\sqrt{2}/(1+\epsilon)$ for a pure K^0 and $\alpha_L(0) = -\alpha_S(0) = \sqrt{(1+|\epsilon|^2)}/\sqrt{2}/(1-\epsilon)$ for a pure $\overline{K}^0$ where $|\epsilon| = (2.228 \pm 0.011)\cdot 10^{-3}$ and $\arg(\epsilon) = \phi_\pm = (43.52 \pm 0.05)$ are the *CP* violation parameters in the kaon system, observed with $K^0_L \to \pi^-\pi^+$ decays [31]. The complex constants $\Omega \equiv \frac{1}{2}\sqrt{\Delta\lambda^2 + \Delta\chi^2}$ and $\Sigma \equiv \frac{1}{2}(\lambda_L + \lambda_S + \chi + \bar{\chi})$ describe mixing and absorption. They are described as a function of the masses $m_{L,S}$ and decay widths $\Gamma_{L,S}$ of the K^0_L and K^0_S states with

$$\Delta\lambda = \lambda_L - \lambda_S = \Delta m - \frac{i}{2}\Delta\Gamma = (m_L - m_S) - \frac{i}{2}(\Gamma_L - \Gamma_S), \tag{3.38}$$

and as a function of the coefficient χ ($\bar{\chi}$) of the K^0 ($\overline{K}^0$) states by means of

$$\Delta\chi = \chi - \bar{\chi} = -\frac{2\pi N}{m}\Delta f = -\frac{2\pi N}{m}(f - \bar{f}), \tag{3.39}$$

where N is the scattering density of the material, m the kaon mass, and f and $\bar{f}$ are the forward scattering amplitudes. The imaginary part of Δf is related to the total cross section via the optical theorem, *i.e.*

$$\sigma_{\text{tot}} = \frac{4\pi}{p}\mathfrak{Im}(f), \tag{3.40}$$

where p is the momentum of the neutral kaon. Similarly to charged kaons, the K^0 and $\overline{K}^0$ interaction cross-section depends on the momentum p of neutral kaons and on the number of nucleons A in the target. It is taken from Ref. [112] as

$$\Delta\sigma(\overline{K}^0) = \sigma(\overline{K}^0) - \sigma(K^0) = \frac{23.2A^{0.758\pm0.003}}{(p[\,\text{GeV}/c])^{0.614}}\ \text{mb}. \tag{3.41}$$

The phase of Δf hs been determined in Refs. [112, 113] to be $\arg(\Delta f) = (-124.7 \pm 0.8)$. It can be easily found that the decay rate of an arbitrary state ψ to *CP*-even final state $(\pi^-\pi^+)$ is proportional to

$$|\alpha_S(t) + \epsilon\alpha_L(t)|^2. \tag{3.42}$$

Finally, the time-dependent contribution to the raw asymmetry can be then obtained from

$$A_{\text{det}}(\overline{K}^0)(t,\vec{p}) = \frac{\epsilon(t)\left[\Gamma(\overline{K}^0{}_{t=0} \to \pi^-\pi^+)(t,\vec{p}) - \Gamma(K^0{}_{t=0} \to \pi^-\pi^+)(t,\vec{p})\right]}{\epsilon(t)\left[\Gamma(\overline{K}^0{}_{t=0} \to \pi^-\pi^+)(t,\vec{p}) + \Gamma(K^0{}_{t=0} \to \pi^-\pi^+)(t,\vec{p})\right]} \tag{3.43}$$

where t represents the neutral kaon decay time, $\vec{p}$ the momentum of the kaon and the dependence from decay-time acceptance of the K^0_{S} meson $\epsilon(t)$ is eliminated. All parameters used in the calculation are given in Table 3.23.

To evaluate the neutral kaon asymmetry in the selected data sample, the method here proposed makes use of a parametric description of the interaction with the detector material (dominated by the RF foil and VELO sensors for long reconstructed tracks from K^0_{S}), that is necessary to calculate the $\Delta\chi$ term, for a given momentum of the kaon. The material in the LHCb detector is not homogeneously distributed, as its map is described with different material and vacuum and air in between. Therefore, the path of the particle is divided into sections, each one corresponding to a certain traversed material, and the amplitude coefficients $\alpha_{L,S}(t_i)$ are calculated iteratively for a decay time difference $t_i - t_{i-1}$ starting from the origin vertex of the K meson and ending at its decay vertex. $a \equiv A_{\text{det}}(\overline{K}^0)(t,\vec{p})$ is calculated for each K^0_{S} candidate considering the

Parameter	Value
Δm	$(0.5293 \pm 0.0009) \cdot 10^{10}\ \hbar\text{s}^{-1}$
$\tau_S \equiv 1/\Gamma_S$	$(0.8954 \pm 0.0004) \cdot 10^{-10}$ s
$\tau_L \equiv 1/\Gamma_L$	$(5.116 \pm 0.021) \cdot 10^{-8}$ s
m	(497.614 ± 0.024) MeV/c^2
$\Delta\sigma(\overline{K}^0)$	$23.2A^{0.758\pm0.003}(p[\text{GeV}/c])^{-0.614}$ mb
$\arg(\Delta f)$	(-124.7 ± 0.8)
$\lvert\epsilon\rvert$	$(2.228 \pm 0.011) \cdot 10^{-3}$
$\arg(\epsilon)$	$\phi_\pm = (43.52 \pm 0.05)$

Table 3.23: Values of the parameters used to describe the neutral kaon asymmetry [31, 112, 113].

possible initial states K^0 and $\overline{K}^0$. The expected time-integrated asymmetry contributing on the raw asymmetry is then given by

$$A_{\text{det}}^{\text{pred}}(\overline{K}^0) = \frac{1}{N_w}\sum_{j=1}^{N} a_j \cdot w_j, \tag{3.44}$$

where N is the number of K^0_{S} candidates in the sample, a_j is the expected asymmetry of candidate j according to Eq. 3.43 and w_j with $\sum_{j=1}^{N} w_j = N_w$ is the overall weight applied to the candidate, *i.e.* the product of the kinematic and background-subtraction weight. More detail on the method can be found in Ref. [114]. It is worth highlighting that this approach includes the significant contribution from regeneration on the material distribution. An example of $A_{\text{det}}(\overline{K}^0)$ calculated using a description of the LHCb material is shown in Figure 3.21, where the variation in the asymmetry as a function of K^0_{S} η is given by the different amount of material traversed by the particle. The method is validated in Section 3.6.1 while the systematic uncertainty for $A_{\text{det}}^{\text{pred}}(\overline{K}^0)$ is quoted in Section 3.6.2 with a novel data-driven method.

3.6.1 Validation using downstream decays

To verify whether the proposed description of the neutral kaon asymmetry holds, a sample of $D^+ \to K^0_{\text{S}}\pi^+$ is analysed in which the $K^0_{\text{S}} \to \pi^-\pi^+$ decay is reconstructed using two downstream tracks (DD). As the amount of material traversed (relevant for regeneration) and the average lifetime (relevant for mixing and *CP* violation) are both significantly higher for the DD sample than the signal sample (made of long tracks), this is an ideal way to validate the procedure and evaluate a systematic uncertainty of $A_{\text{det}}^{\text{pred}}(\overline{K}^0)$, up to a high precision. In fact, the K^0_{S} considered in the LL sample decay after about $0.1\tau_S$, *i.e.* 10% of the known K^0_{S} lifetime on average, in comparison to $0.8\tau_S$

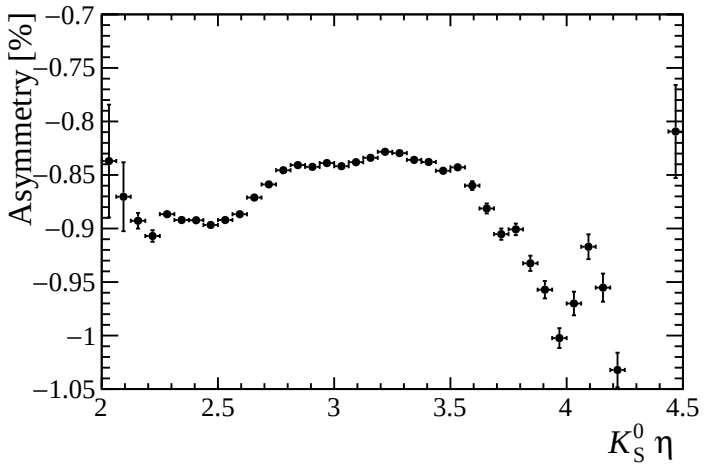

Figure 3.21: Predicted neutral-kaon asymmetry, including mixing, regeneration, and *CP* violation. Reconstructed kaons with downstream tracks in the 2018 magnet-up data and lifetime within the range $1.2 \leq t/\tau_{K^0_S} \leq 1.4$ are considered, as an example. Similar results can be observed for different year and magnet polarity configuration.

for the DD sample. As a consequence, the asymmetry in the LL sample is expected to be about 0.1%, while in the latter it should be one order of magnitude larger. As the reconstruction efficiency of downstream tracks is extremely low, the collected yields in the DD sample are less than 5% with respect to the LL sample. That's the reason why this sample is not used for the measurement of $\mathcal{A}^{CP}(K^-K^+)$ but exploited for this study.

By considering the differential behaviour of the raw asymmetry as a function of lifetime, the results from the model can be validated without the knowledge of the D^+ production asymmetry and π^+ detection asymmetry. This is achieved by applying a weighting procedure to equalise the D^+ kinematics of each K^0_S lifetime bin to one of them, arbitrarily chosen ($0.8 \leq t/\tau_S \leq 1.0$). Thus, the performed validation consists of a direct comparison of the results for $A^{\text{pred}}_{\text{det}}(\overline{K}^0)$ with the variation of the asymmetry observed as a function of lifetime. The validation is done using the data recorded with the `Hlt2CharmHadDp2KS0Pip_KS0DDTurbo` turbo line (see Table 3.66 in Section 3.16.1) in 2016, 2017 and 2018 data taking periods. On top of the online selection, only candidates with a minimum K^0_S lifetime of $0.2\tau_S$ are considered. The D^+ kinematics are constrained to $2.4 \leq \eta \leq 3.6$ and $p_{\text{T}} \geq 3.6\,\text{GeV}/c$ to remove areas of phase-space in which a high D^+ production asymmetry is expected. The K^0_S candidates must have a minimum p_{T} of $400\,\text{MeV}/c$, a requirement in place to reject background. After this offline selection, the sample is split into 11 bins of the K^0_S lifetime. An example of the resulting mass spectrum for the K^0_S and D^+ in one of the K^0_S lifetime bins is shown in Figure 3.22, as an example. As there is next to no $\pi^-\pi^+$ background present even in the lowest decay-time bin, a simple $\pi^-\pi^+$ mass window is used in the analysis of the candidates (indicated with

the vertical lines in the plot).

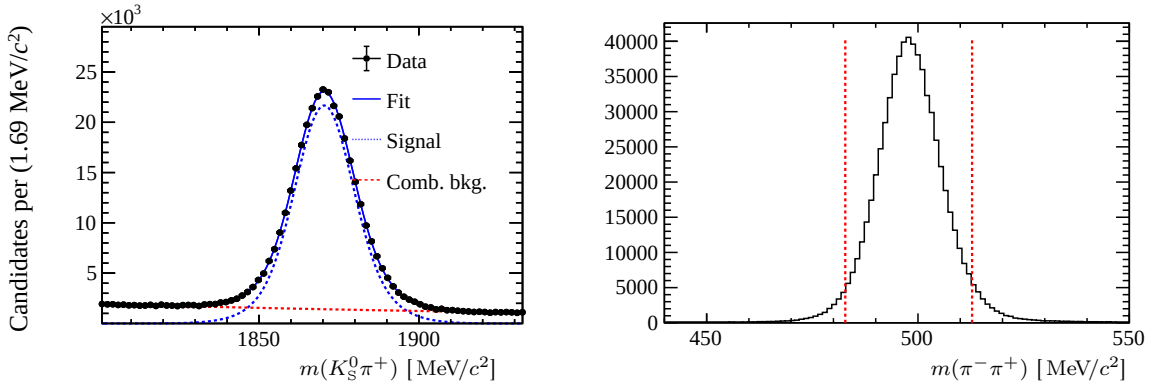

Figure 3.22: (left) Distribution of the $K^0_S\pi^+$ invariant mass for candidates with with $0.2 \leq t/\tau_S \leq 0.45$ in the 2018 magnet-down data set, as an example. The result of the binned maximum likelihood fit is shown as well. (right) Distribution of the $\pi^-\pi^+$ invariant mass, along with the mass range considered highlighted with vertical red lines, for candidates with $0.2 \leq t/\tau_S \leq 0.45$ in the 2018 magnet-down data set, as an example. Similar results can be observed for different year and magnet polarity configuration.

A small correlation is seen in the D^+ kinematics as a function of the K^0_S lifetime, as shown in Figure 3.23. While the influence of the production asymmetry is already limited by the minimum p_T of the D^+, this slight variation could affect this validation and for this reason, the reweigthing procedure previously described has been performed using the 2-dimensional (p_T, η) distributions. An example of the resulting changes of the raw asymmetries due to this weighting is shown in Figure 3.24. It is reassuring to see that the overall effect is small.

The raw asymmetries of these samples are determined with a simultaneous, binned maximum-likelihood fit to the $K^0_S\pi^+$ invariant-mass distributions. This procedure is repeated for each of the years, lifetime bins, and magnet polarities considered. The raw asymmetries from both magnet polarities are combined through the arithmetic mean, and a weighted average is used for the three years to combine all results per lifetime bin. The exact same procedure is applied for the predictions. To make sure that the nuisance asymmetry coming from the D^+ production and π^+ detection, constant over K^0_S decay time, are accounted for in the predictions, they are shifted by a constant. A comparison of these combined asymmetries between data and the predictions is shown in Figure 3.25. The overall agreement is good, with a p-value for the χ^2 of 39%, indicating that the results are statistically compatible with the predictions.

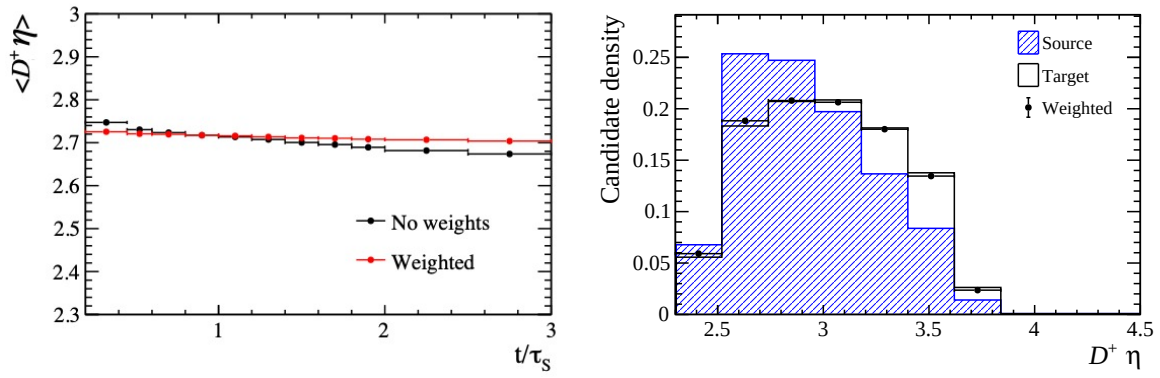

Figure 3.23: (left) The variation of the average D^+ meson's η as a function of the lifetime of the K^0_S (red) with and (black) without the per-candidate weights. (right) Underlying distribution of the D^+ meson's η. The "soruce" distribution is that of the candidates with a lifetime between 1.6 and 1.8 K^0_S lifetimes, while the target is the distribution for candidates in the $1.8 \leq t/\tau_S \leq 2.0$ lifetime bin. The "weighted" distribution is the result of assigning per-candidate weights to the source dataset. Only 2018 magnet-up data are shown, as an example. Similar results can be observed for different year and magnet polarity configuration.

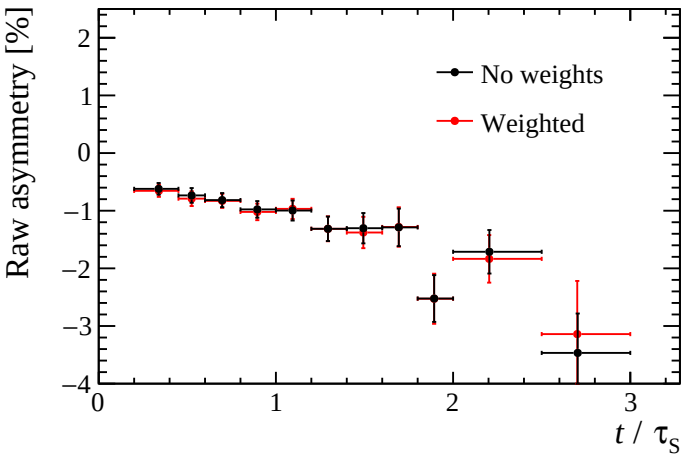

Figure 3.24: Raw asymmetries in $D^+ \to K^0_S\pi^+$ decays in the downstream reconstructed sample (red) with and (black) without per-candidate weights. 2018 data are shown, as an example. Similar results can be observed for different year and magnet polarity configuration.

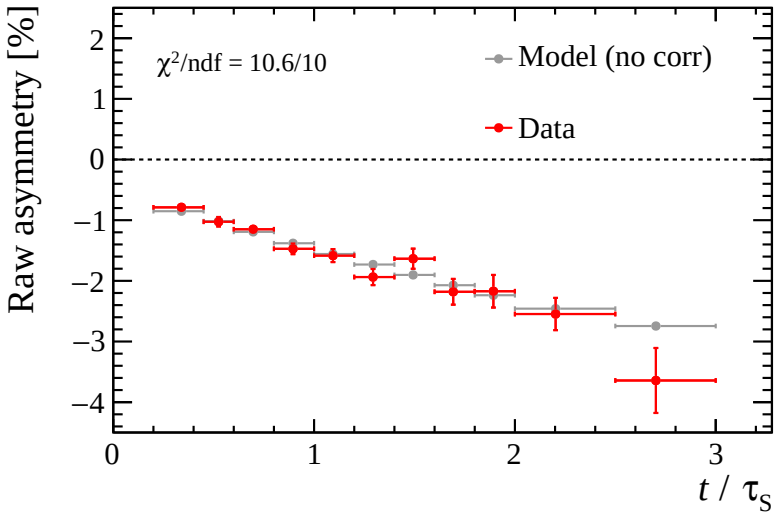

Figure 3.25: Raw asymmetries of $D^+ \to K^0_S\pi^+$ decays in the downstream reconstructed sample with per-candidate weights, after combining the data from all three years and magnet polarities. Also shown are the predictions from the procedure introduced in Ref. [114].

3.6.2 Systematic uncertainties

The prediction from the model is confirmed to describe well the differential behaviour of the neutral-kaon asymmetry. Therefore, shortcomings of the description, *e.g.* due to the negligence of higher-order interference effects, should be small. As such, an estimate is made from the data by adding an additional linear term in the raw asymmetry as a function of K^0_S lifetime:

$$A_{\text{raw}}(t) = A_{\text{nuisance}} + A^{\text{pred}}_{\text{det}}(t) + \delta A(t), \tag{3.45}$$

where $\delta A(t) = c \cdot t$ and c describes the (linear) departure from the predicted value and A_{nuisance} corresponds to constant production and detection asymmetries contributions. The parameter c is fitted through a χ^2 fit to the raw asymmetries of the DD sample used in the previous section. The resulting predictions with and without $\delta A(t)$ perturbation, and the data are shown in Figure 3.26. The improvement in the χ^2 is small considering the introduction of an extra degree of freedom. The value for the slope obtained is $(-9.6 \pm 7.5) \cdot 10^{-4}$, about 1.3 standard deviations away from zero. This value of c, along with its uncertainty are used to esxtimate the systematic uncertainty on the neutral-kaon correction for the signal sample. The average K^0_S decay times and amount of material traversed for the signal samples is much lower than the sample considered in the validation, as the K^0_S is required to have been reconstructed in the VELO. The

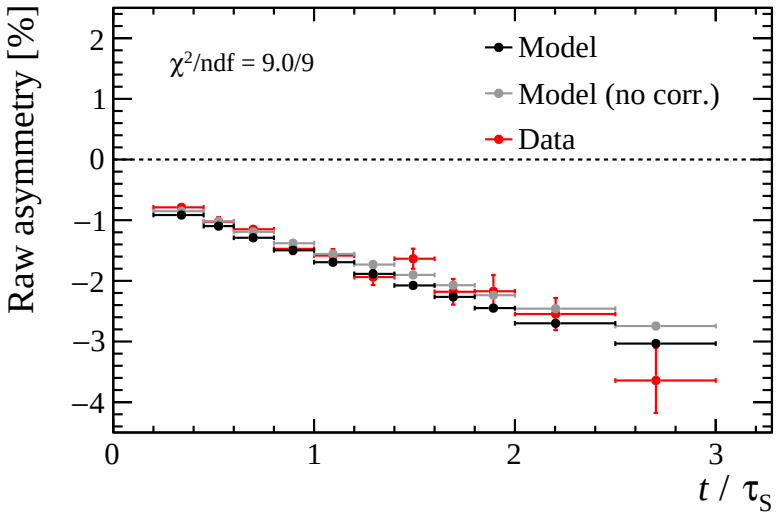

Figure 3.26: (red) Raw asymmetries, predictions (black) with and (grey) without the linear perturbation (same as shown in Figure 3.25).

distribution of K^0_S decay time is reported in Figure 3.27 for the $D^+ \to K^0_S\pi^+$ and $D^+_s \to K^0_S K^+$ decay samples. As one can notice, there is a substantial difference between the two average decay times. In particular, the one in the $D^+_s \to K^0_S K^+$ decay sample is about a factor 2 larger than the one found in the $D^+ \to K^0_S\pi^+_{trig}$ sample. This is due to the different kinematic requirements applied on the D^+ and the D^+_s decay samples, which directly affect the average momentum of the K^0_S while the flight-distance of the particle remains consistent between the two decay samples.

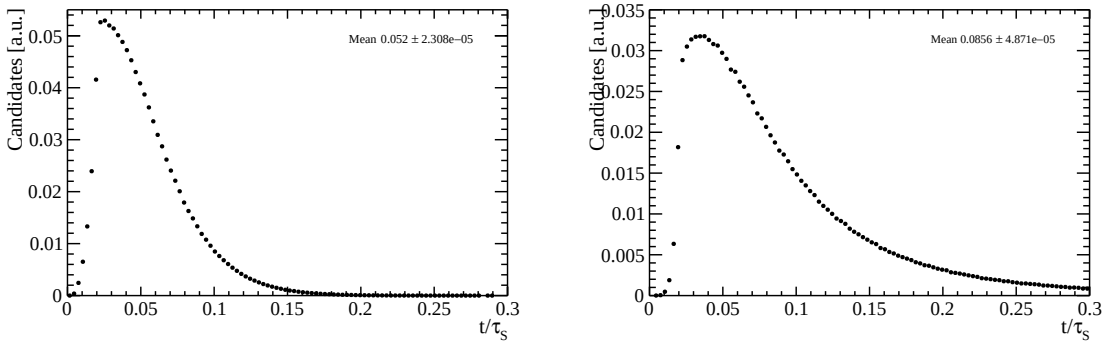

Figure 3.27: Background-subtracted decay time distributions for selected and kinematically weighted $K^0_S \to \pi^-\pi^+$ candidates in (left) $D^+ \to K^0_S\pi^+$ and (right) $D^+_s \to K^0_S K^+$ decay samples.

Table 3.24 reports the values of the neutral kaon asymmetry for each of the decay channels which contain a K^0_S meson. The first value reported, $A^{\rm pred}_{\rm det}$, corresponds to the value obtained from the model while the second value, $\delta A = c\langle t\rangle$, corresponds to the perturbation due to the added linear term in Eq. 3.45. The last term is the $A_{\rm det}(\overline{K}^0)$ correction used as direct input in Eqs. 3.16 and 3.17 having $A^{\rm pred}_{\rm det}$ as central value and the RMS of δA being its systematic uncertainty. The uncertainties between the two decay modes are dominated by the error on c and therefore they are fully correlated.

Decay mode	$A^{\rm pred}_{\rm det}(\overline{K}^0)$ $[10^{-4}]$	δA $[10^{-4}]$	$A_{\rm det}(\overline{K}^0)$ $[10^{-4}]$
$D^+ \to K^0_S\pi^+_{trig}$	-5.1	-0.5 ± 0.4	-5.1 ± 0.6
$D^+_s \to K^0_S K^+$	-8.5	-1.0 ± 0.8	-8.5 ± 1.3

Table 3.24: Neutral kaon asymmetries for the $D^+ \to K^0_S\pi^+_{trig}$ and $D^+_s \to K^0_S K^+$ decay samples. The first column corresponds to the values obtained from the detailed prediction, and the second column corresponds to the linear perturbation introduced in this section. The last column corresponds to the values used as input in this analysis, with $A^{\rm pred}_{\rm det}(\overline{K}^0)$ as central value and the RMS of δA its systematic uncertainty.

3.6.3 Cross-check: behaviour at low decay times

The presented estimate of the systematic uncertainty for $A_{\rm det}(\overline{K}^0)$ is based on the sample of downstream reconstructed K^0_S decays. As already noted, the typical K^0_S lifetimes considered in the main analysis are (much) lower than the lifetimes in the DD sample. As a cross-check, the statistical compatibility of the predictions with the additional linear perturbation, *i.e.* Eq. 3.45, is evaluated for a sample of long-long reconstructed K^0_S decays. To perform this check, the same procedure is repeated for the LL sample as for the DD sample, but now with lifetime bins concentrated at $t/\tau_S < 0.4$. The resulting comparison is shown in Figure 3.28. The data are well compatible with the perturbed predictions, as well as without the predictions without any linear perturbations. It is clear that the effect of the linear perturbation at these low decay times is limited, and this study only illustrates that no unexpected features are observed in the LL samples.

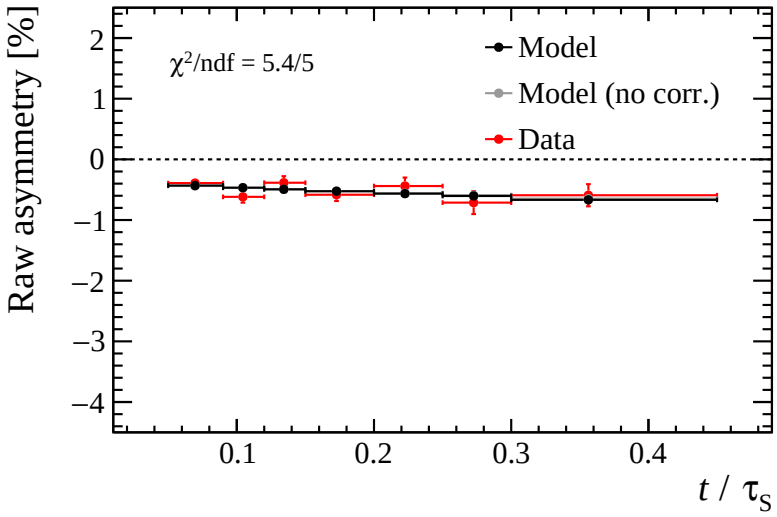

Figure 3.28: (red) Raw asymmetries of $D^+ \to K^0_S\pi^+$ decays, where the K^0_S is reconstructed using two long tracks, after combining the data from 2017 and 2018 and both magnet polarities. Also shown are the predictions, (grey) without and (black) with the slope fixed to that found in the DD sample.

3.7 Results: CP asymmetry in $D^0 \to K^-K^+$

For each data-taking year and polarity, the raw asymmetry of the weighted $D^0 \to K^-K^+$ decay is combined with the relevant raw asymmetries of the weighted Cabibbo favoured decays and corrected for the neutral kaon asymmetries to obtain the final result. The procedure is performed separately for each year and polarity, and then the results are averaged. As explained in Section 3.4, the two results are blinded using the same offset. The value of $\mathcal{A}^{CP}(K^-K^+)$ with the D^+ decay as control channels is obtained as

$$\begin{aligned}\mathcal{A}^{CP}(K^-K^+)|D^+ = A(K^-K^+) - A(K^-\pi^+) \\ + A(K^-\pi^+\pi^+) - [A(K^0_S\pi^+) - A_{\rm det}(\overline{K}^0)],\end{aligned}$$

while in the case of the D_s^+ decay, as

$$\begin{aligned}\mathcal{A}^{CP}(K^-K^+)|D_s^+ = A(K^-K^+) - A(K^-\pi^+) \\ + A(\phi\pi^+) - [A(K^0_S K^+) - A_{\rm det}(\overline{K}^0)],\end{aligned}$$

taking as input the values reported in Tables 3.20, 3.22 and 3.24. Graphical representations of the results and a comparison among them for the two methods are reported in Figure 3.29 and Figure 3.30. The results obtained with the two methods are correlated as they partially share the same data sets. To combine them, it is necessary to calculate correlation coefficients. As different $D^+_{(s)}$-meson decays are used as control samples and the $D^0 \to K^-\pi^+$ decay sample has been split in two, the correlation comes from the $D^0 \to K^-K^+$ (ρ_{KK}) decay sample, where the same events are used, but with different sets of weights. The correlation factor ρ_{KK} is calculated following

$$\text{cor}(A_1, A_2) = \frac{\sum_{i=1}^N u_i v_i}{\sqrt{\sum_{i=1}^N (u_i)^2}\sqrt{\sum_{i=1}^N (v_i)^2}}, \tag{3.46}$$

with $A_{1,2}$ being $A(K^-K^+)$ in the $D^+_{(s)}$ method and u_i and v_i are the two different weights applied to the i-th candidate of the $D^0 \to K^-K^+$ decay sample in the D^+ and the D_s^+ method, respectively, as demonstrated in Section 3.16.3.

The values obtained for ρ_{KK} are reported in Table 3.25. They are calculated for each subsample and result to be the same between positive and negative tagged candidates, but slightly different between the periods of data-taking. These differences come from different distributions of kinematic variables and weights between the subsamples and arise from different L0, Hlt1 and Hlt2 requirements applied in the online selection.

The total covariance is

$$\text{cov}(\mathcal{A}^{CP}|D^+, \mathcal{A}^{CP}|D_s^+) = \rho_{KK}\, \sigma^{D^+}_{A(KK)}\, \sigma^{D_s^+}_{A(KK)}, \tag{3.47}$$

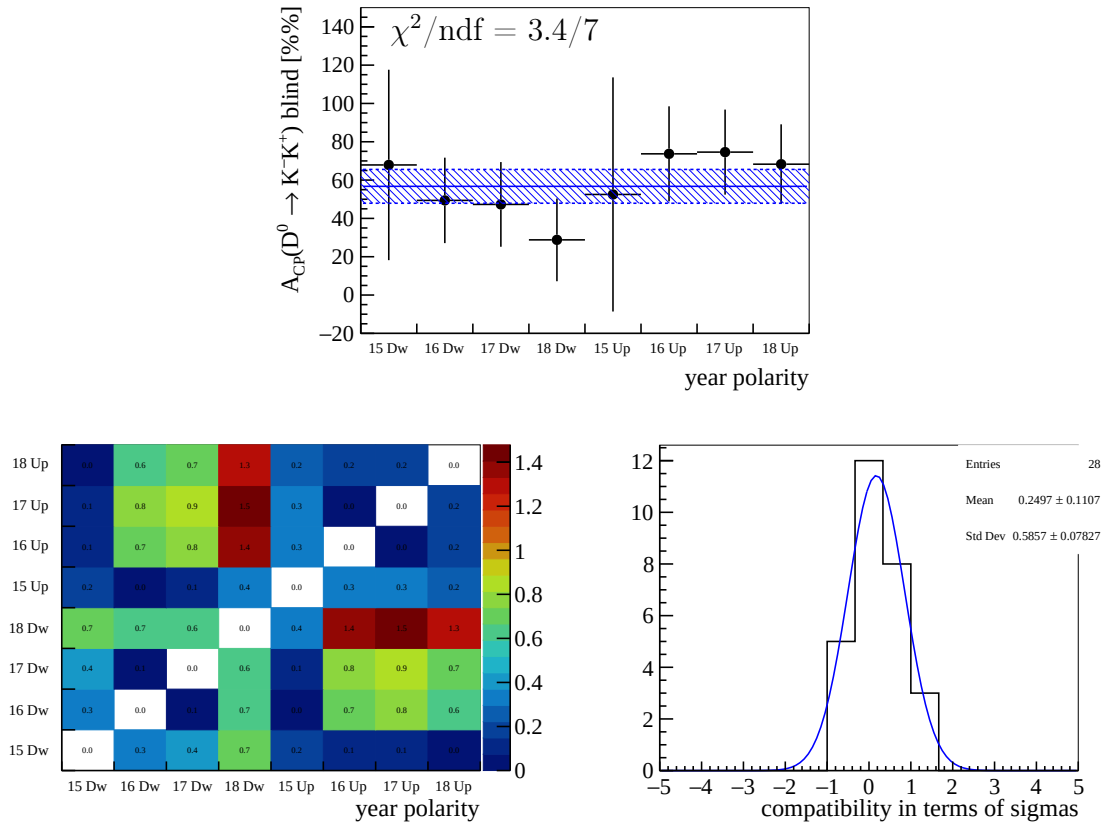

Figure 3.29: (top) Comparison between blind $\mathcal{A}^{CP}$ results in the D^+ method in different data-taking years and magnet polarities. The uncertainties are statistical only. The line together with the blue band represent the average between the results from the subsamples. (bottom) (left) Matrix representing the compatibility in terms of sigma between each pair i, j of subsamples given by absolute value of $(A_i - A_j)/\sqrt{\sigma^2(A_i) + \sigma^2(A_j)}$ and (right) its distribution.

where $\sigma^{D^+_{(s)}}_{A(KK)}$ are the statistical uncertainties on the raw asymmetries $A(K^-K^+)$ in the two methods. The total correlation coefficient $\rho^{\text{stat}}_{\mathcal{A}^{CP}}$, calculated dividing Eq. 3.47 by the $\mathcal{A}^{CP}$ statistical uncertainties, is reported in Table 3.26. A summary of the results, with the compatibility among the values obtained with the two methods are reported on the same table, separately for data-taking years and magnet polarities.

The weighted average among the various sub-samples results to be

$$\mathcal{A}^{CP}(K^-K^+)^{\text{blind}}|D^+ = (56.7 \pm 8.8) \cdot 10^{-4}, \tag{3.48}$$

$$\mathcal{A}^{CP}(K^-K^+)^{\text{blind}}|D^+_s = (45.9 \pm 6.7) \cdot 10^{-4}, \tag{3.49}$$

	ρ_{KK}
15 Dw	0.74
16 Dw	0.73
17 Dw	0.74
18 Dw	0.74
15 Up	0.74
16 Up	0.70
17 Up	0.74
18 Up	0.74

Table 3.25: Measurements of ρ_{KK}, separately for data-taking years and polarity.

	$\mathcal{A}^{CP\ \text{blind}}(D^+)$ $[10^{-4}]$	$\mathcal{A}^{CP\ \text{blind}}(D_s^+)$ $[10^{-4}]$	$\rho^{\text{stat}}_{\mathcal{A}^{CP}}$	compatibility
15 Dw	67.9 ± 49.7	53 ± 38.8	0.06	0.24
16 Dw	49.4 ± 22.3	82.6 ± 17.4	0.05	-1.20
17 Dw	47.3 ± 22.1	54.4 ± 16.2	0.05	-0.27
18 Dw	28.8 ± 21.6	19.4 ± 16	0.05	0.36
15 Up	52.5 ± 61.1	94 ± 49.2	0.06	-0.54
16 Up	73.7 ± 24.8	36.1 ± 19.7	0.04	1.21
17 Up	74.6 ± 22.2	48.2 ± 16.5	0.05	0.98
18 Up	68.3 ± 20.8	32.3 ± 15.4	0.05	1.43
w. avg	56.7± 8.8	45.9± 6.7	0.05	1.00

Table 3.26: Measurements of $\mathcal{A}^{CP}(K^-K^+)$ with D^+ and D_s^+ methods, separately for data-taking years and magnet polarities. In the last two columns are reported the total correlation coefficient and the compatibility in terms of sigmas given by $(A_{D^+} - A_{D_s^+})/\sqrt{\sigma^2(A_{D^+}) + \sigma^2(A_{D_s^+}) - 2\rho^{\text{stat}}_{\mathcal{A}^{CP}}\sigma(A_{D^+})\sigma(A_{D_s^+})}$.

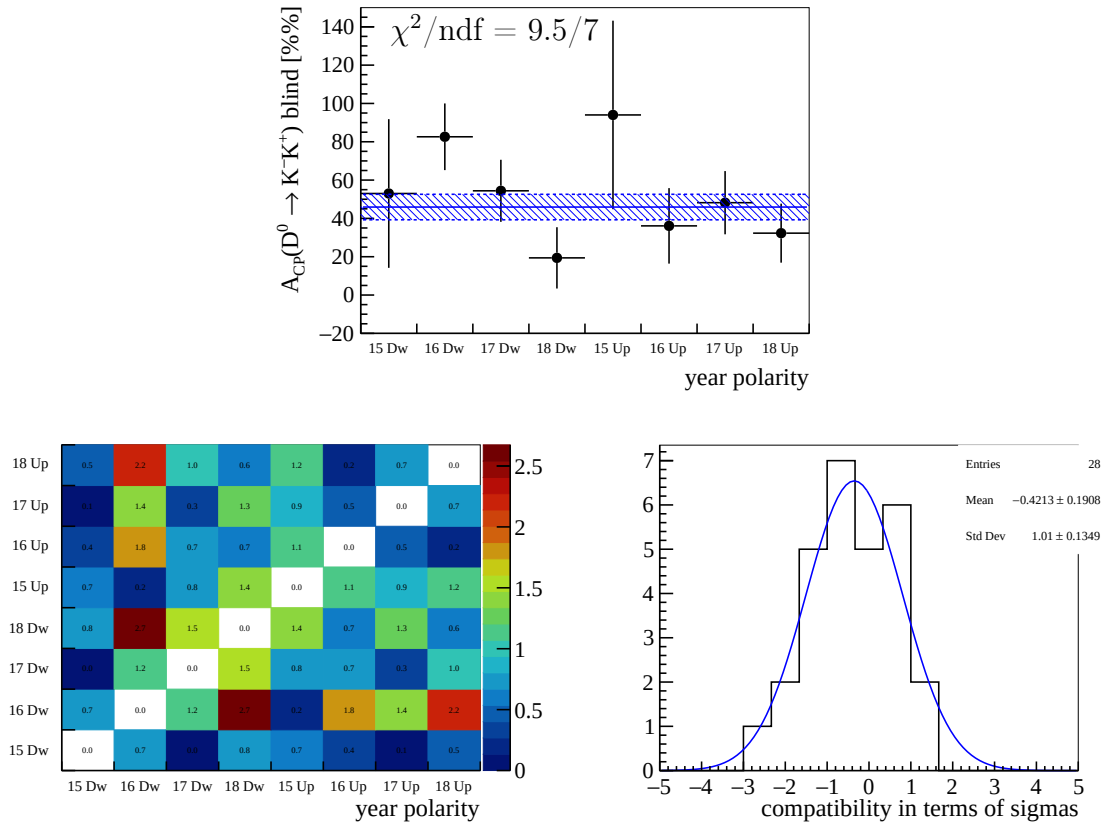

Figure 3.30: (top) Comparison between blind $\mathcal{A}^{CP}$ results in the D_s^+ method in different data-taking years and magnet polarities. The uncertainties are statistical only. The line together with the blue band represent the average between the results from the subsamples. (bottom) (left) Matrix representing the compatibility in terms of sigma between each pair i, j of subsamples given by absolute value of $(A_i - A_j)/\sqrt{\sigma^2(A_i) + \sigma^2(A_j)}$ and (right) its distribution.

where only the statistical uncertainty is reported. The correlation among the two results is taken to be the weighted average value between the various sub-samples, *i.e.* $\rho^{\text{stat}}_{\mathcal{A}^{CP}} = 0.05$. The two measurements result to be compatible between each others within one standard deviation. Given that completely independent control-channels are used to cancel out nuisance asymmetries, this agreement highlights the stability of the analysis.

3.7.1 Fitting results without kinematic weighting

For each data-taking year and polarity, preliminary values for $\mathcal{A}^{CP}(K^-K^+)$ are obtained combining the raw asymmetry of the $D^0 \to K^-K^+$ decay with the relevant raw asymmetries of the Cabibbo favoured decays. Those results are reported here only for illustrative purpose, to be compared with the weighted ones. The value of $\mathcal{A}^{CP}(K^-K^+)_{\text{unweighted}}$ with the D^+ decay as control channels is obtained as

$$\begin{aligned}\mathcal{A}^{CP}(K^-K^+)_{\text{unweighted}}|D^+ = A_{\text{unweighted}}(K^-K^+) - A_{\text{unweighted}}(K^-\pi^+) \\ + A_{\text{unweighted}}(K^-\pi^+\pi^+) - [A_{\text{unweighted}}(K^0_S\pi^+) - A_{\text{det}}^{\text{unweighted}}(\overline{K}^0)].\end{aligned}$$

while in the case of the D_s^+ decay, as

$$\begin{aligned}\mathcal{A}^{CP}(K^-K^+)_{\text{unweighted}}|D_s^+ = A_{\text{unweighted}}(K^-K^+) - A_{\text{unweighted}}(K^-\pi^+) \\ + A_{\text{unweighted}}(\phi\pi^+) - [A_{\text{unweighted}}(K^0_S K^+) - A_{\text{det}}^{\text{unweighted}}(\overline{K}^0)],\end{aligned}$$

taking as input the values reported in Tables 3.10 and 3.15, respectively. The value of $A_{\text{det}}(\overline{K}^0)^{\text{unweighted}}$ is measured to be $-7.8 \cdot 10^{-4}$ and $-10.0 \cdot 10^{-4}$ for the unweighted $D^+ \to K^0_S\pi^+_{trig}$ and $D_s^+ \to K^0_S K^+$ decay samples, respectively, following the procedure described in Section 3.6.

A summary of the results for the two methods is reported in Table 3.27 while graphical representations can be found in Figure 3.31. As expected, the compatibility among the various sub-samples is not excellent, indicating the necessity to apply a kinematic weighting procedure, for a better cancellation of the nuisance parameters. In particular, the D^+ method seems to have less consistency with respect to the D_s^+ method. This feature is justified by the large differences between the kinematic distributions before the application of the weights increasing the sensitivity to left-right detector asymmetries and changes in its running conditions over the time.

To evaluate the effect of the weighing procedure, the unweighted average among the various sub-samples results is reported

$$\mathcal{A}^{CP}(K^-K^+)^{\text{blind}}_{\text{unweighted}}|D^+ = (36.9 \pm 4.6) \cdot 10^{-4}, \tag{3.50}$$

$$\mathcal{A}^{CP}(K^-K^+)^{\text{blind}}_{\text{unweighted}}|D_s^+ = (33.5 \pm 5.5) \cdot 10^{-4}. \tag{3.51}$$

where only the statistical uncertainty is reported. It is evident as the kinematic weighting procedure has a relevant impact on the final results, it consists in a absolute difference of about $20 \cdot 10^{-4}$ and $12 \cdot 10^{-4}$, and a compatibility in terms of standard deviations of 2.6 and 3.2 assuming the maximum correlation possible, for D^+ and D_s^+ methods, respectively.

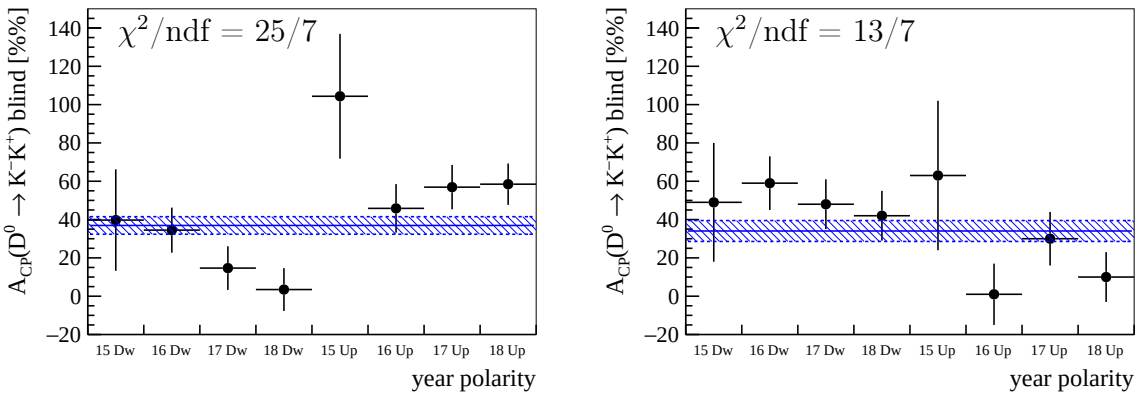

Figure 3.31: Comparison between blind $\mathcal{A}^{CP}{}_{\text{unweighted}}$ results in the (left) D^+ and (right) D_s^+ method in different data-taking years and magnet polarities. The uncertainties are statistical only. The line together with the blue band represent the average between the results from the subsamples.

	$\mathcal{A}^{CP\,\text{blind}}{}_{\text{unweighted}}(D^+)$ $[10^{-4}]$	$\mathcal{A}^{CP\,\text{blind}}{}_{\text{unweighted}}(D_s^+)$ $[10^{-4}]$
15 Dw	39.7 ± 26.5	49.0 ± 31.3
16 Dw	34.5 ± 11.8	59.1 ± 14.3
17 Dw	14.7 ± 11.4	48.1 ± 13.4
18 Dw	3.5 ± 11.2	41.9 ± 13.2
15 Up	104.4 ± 32.6	62.6 ± 39.1
16 Up	45.8 ± 12.7	1.3 ± 16.1
17 Up	56.9 ± 11.7	30.0 ± 13.6
18 Up	58.5 ± 10.8	10.2 ± 12.7
w. avg	36.9 ± 4.6	33.5 ± 5.5

Table 3.27: Measurements of $\mathcal{A}^{CP}(K^-K^+)_{\text{unweighted}}$ with D^+ and D_s^+ methods, separately for data-taking years and magnet polarities.

3.8 Validation with Monte Carlo samples

The compatibility between the results obtained with the D^+- and D_s^+- methods represents a valid check of the robustness of the analysis strategy. A further cross-check is made to validate the strategy: the whole analysis (selection and weighting) is performed on a set of simulated samples with increased statistic with respect to that of data. In particular, $D^+ \to K^0_S \pi^+_{trig}$ and $D_s^+ \to K^0_S K^+$ decay samples are produced using the maximum number of generated events possible[7] while the other decay mode are produced in order to obtain a number of events comparable to that of data. Because of the very large number of events needed, Particle Gun (pGun) simulation is used for this study. In the LHCb simulation framework, pGun productions correspond to events where only the signal particles are generated starting from a pre-sampled kinematic distribution from Pythia 8 [115]. In general, the primary vertex resolution is measured by means of the reconstructed tracks in the event. In the case of a pGun production, an ad-hoc smearing is applied to the true primary vertex position to emulate the presence of the underlying event. This kind of simulations are 50-100 times faster than a standard full simulation. As a drawback, since the underlying even is not simulated, they poorly reproduce variables affected by local occupancy, such as PID variables or tracking performances. However, detection asymmetries are simulated while production asymmetries can be easily injected. In the LHCb simulation framework, each simulated event is generated requiring the presence of a certain decay mode together with a set of requirements, such as all the reconstructible particles are within the LHCb acceptance or that certain kinematic thresholds are satisfied, *e.g.* to anticipate the cuts applied later in the Hlt1 and Hlt2 selection. Each decay together with the generation-level cuts identify the so-called "Event Type". The list of the current available Event Types can be found at the public page `http://lhcbdoc.web.cern.ch/lhcbdoc/decfiles/`. The Event Types used in this validation study together with the number of generated events and the number of the observed yields after selection[8] are reported in Table 3.28. In order to increase the generation efficiency, the neutral kaon is directly generated as a K^0_S decaying in two pion, *i.e.* the K^0 mixing and its detection asymmetry are not simulated. All the needed samples for the 2016, 2017 and 2018 data taking years, magnet-up and -down, have been produced.

No *CP* asymmetry is injected in the $D^0 \to K^-K^+$ simulated sample, so the expected value of $\mathcal{A}^{CP}(K^-K^+)$ measured on simulation is zero. The original and weighted distributions of the magnet-down 2016 sample are shown in Figures 3.32 and 3.33, as an example. As one can notice, these distributions are similar to the ones observed in data (Figures 3.11 and 3.16). The raw asymmetries for the D^+ and D_s^+ methods are reported

[7] Within the LHCb collaboration there are rules that determine the maximum amount of events generated and saved on disk. In the case more events are needed a special approval for that MC production is required.

[8] The selection is the one applied to data reported in Section 3.3, including Hlt1 and Hlt2 requirements.

in Tables 3.29 and 3.30, respectively. It is possible to observe that the results for the 2016 significantly differ from the ones measured in the 2017 and 2018 samples. This difference is expected as the configuration of the simulation of the LHCb detector deeply changes between 2016 and 2017 while it remains essentially the same between 2017 and 2018. In particular, internal LHCb studies report that the parametric estimation of the errors on the VELO hits for the 2017 and 2018 simulated samples is wrong, bringing to significant biases on detection efficiencies determined from MC. Anyway, given the missing underlying event, the results are not expected to be compatible with those observed on the data.

The values for the correlation coefficients ρ_{KK} and $\rho_{K\pi}$ are reported in Table 3.31. A summary of the results obtained in this study, with the total correlation coefficient $\rho_{\mathcal{A}^{CP}}$ and the compatibility among the values obtained with the two methods, separately for data-taking years and magnet polarities, are reported in Table 3.32.

A value of $\mathcal{A}^{CP}(K^-K^+)|D^+ = (-5.3 \pm 3.2) \cdot 10^{-4}$ is measured with the D^+ method and $\mathcal{A}^{CP}(K^-K^+)|D_s^+ = (-1.7 \pm 3.0) \cdot 10^{-4}$ with the D_s^+ method with a total correlation equal to $\rho^{\rm MC}_{\mathcal{A}^{CP}} = 0.27$. Results are in good agreement between themselves at the level of 0.96 sigma, and both compatible with zero. The combined value is $\mathcal{A}^{CP}(K^-K^+) = (-3.3 \pm 2.5) \cdot 10^{-4}$. The analysis strategy is therefore validated on simulation, at least at the level of precision allowed by the statistics of the simulated sample.

Event Type	Nickname	Generated events	Selected events
24163904	Dst_D0pi,KK=TightCut,3	$5{\cdot}10^8$	$4.4{\cdot}10^7$
24163903	Dst_D0pi,Kpi=TightCut,3	$5{\cdot}10^9$	$1.7{\cdot}10^8$
21103011	D+_K-pi+pi+=res,TightCut,ACPKKCuts	$2.6{\cdot}10^9$	$1.2{\cdot}10^8$
21103101	D+_Kspi+=phsp TightCut ACPKKCuts	$3{\cdot}10^9$	$2.1{\cdot}10^8$
23263023	Ds+_K-K+pi+=res,TightCut,ACPKKCuts	$1.1{\cdot}10^9$	$4.9{\cdot}10^7$
23103111	Ds+_KsK+=phsp,TightCut,ACPKKCuts	$3{\cdot}10^9$	$8.3{\cdot}10^7$

Table 3.28: Details of the pGun production.

	$D^+ \to K^0_S\pi^+_{trig}\ \vert^w$	$D^+ \to K^-\pi^+\pi^+_{trig}\ \vert^w$	$D^0 \to K^-\pi^+\ \vert^w$	$D^0 \to K^-K^+\ \vert^w$
	$A\ [10^{-4}]$	$A\ [10^{-4}]$	$A\ [10^{-4}]$	$A\ [10^{-4}]$
16 Dw	7.2 ± 3.7	-25.1 ± 3.8	16.3 ± 3.7	41.9 ± 4.5
17 Dw	-48.6 ± 4.3	-84.2 ± 3.8	5.1 ± 3.8	34.4 ± 4.5
18 Dw	-49.4 ± 3.8	-86.2 ± 3.7	3.8 ± 3.9	42.9 ± 4.3
16 Up	-0.3 ± 3.7	-46.0 ± 3.7	-75.9 ± 3.6	-39.9 ± 4.1
17 Up	53.7 ± 4.0	12.3 ± 3.8	-74.3 ± 3.8	-43.3 ± 4.3
18 Up	53.4 ± 3.9	16.4 ± 3.7	-73.6 ± 3.8	-37.2 ± 4.7

Table 3.29: Raw asymmetries resulting from the observed yields in the weighted pGun $D^+ \to K^0_S\pi^+_{trig}$, $D^+ \to K^-\pi^+\pi^+_{trig}$, $D^0 \to K^-\pi^+$ and $D^0 \to K^-K^+$ samples, separately for the different data-taking years and polarities.

	$D^+_s \to K^0_S K^+\ \vert^w$	$D^+_s \to \phi\pi^+\ \vert^w$	$D^0 \to K^-\pi^+\ \vert^w$	$D^0 \to K^-K^+\ \vert^w$
	$A\ [10^{-4}]$	$A\ [10^{-4}]$	$A\ [10^{-4}]$	$A\ [10^{-4}]$
16 Dw	47.6 ± 4.6	12.2 ± 4.6	-5.7 ± 1.9	33.7 ± 3.9
17 Dw	-31.1 ± 3.3	-97.4 ± 5.0	-13.4 ± 2.0	29.5 ± 3.9
18 Dw	-33.9 ± 3.4	-89.4 ± 4.9	-11.1 ± 2.1	41.8 ± 3.8
16 Up	26.4 ± 3.2	-1.9 ± 4.9	-65.8 ± 1.9	-35.6 ± 3.6
17 Up	113.4 ± 3.3	96.7 ± 5.0	-59.4 ± 2.0	-38.0 ± 3.8
18 Up	114.5 ± 3.4	97.4 ± 5.0	-56.9 ± 2.0	-33.6 ± 4.2

Table 3.30: Raw asymmetries resulting from the observed yields in the weighted pGun $D^+_s \to K^0_S K^+$, $D^+_s \to \phi\pi^+$, $D^0 \to K^-\pi^+$ and $D^0 \to K^-K^+$ samples, separately for the different data-taking years and polarities.

	ρ_{KK}	$\rho_{K\pi}$
16 Dw	0.74	0.42
17 Dw	0.75	0.42
18 Dw	0.75	0.42
16 Up	0.74	0.42
17 Up	0.75	0.42
18 Up	0.75	0.42

Table 3.31: Measurements of ρ_{KK} and $\rho_{K\pi}$ on pGun samples, separately for data-taking years and polarity.

	$\mathcal{A}^{CP}$ (D^+) $[10^{-4}]$	$\mathcal{A}^{CP}$ (D_s^+) $[10^{-4}]$	$\rho_{\mathcal{A}^{CP}}$	compatibility
16 Dw	-6.7 ± 7.8	4 ± 7.8	0.26	1.13
17 Dw	-6.4 ± 8.2	-23.5 ± 7.4	0.27	1.81
18 Dw	2.4 ± 7.8	-2.6 ± 7.4	0.27	0.54
16 Up	-9.7 ± 7.6	1.8 ± 7.1	0.26	1.28
17 Up	-10.4 ± 8	4.7 ± 7.3	0.26	1.62
18 Up	-0.5 ± 8.1	6.1 ± 7.6	0.29	0.71
w. avg	-5.3 ± 3.2	-1.7 ± 3.0	0.27	0.96

Table 3.32: Measurements of $\mathcal{A}^{CP}(K^-K^+)$ with D^+ and D_s^+ methods on pGun samples, separately for data-taking years and magnet polarities. In the last two columns are reported the total correlation coefficient and the compatibility in terms of sigmas.

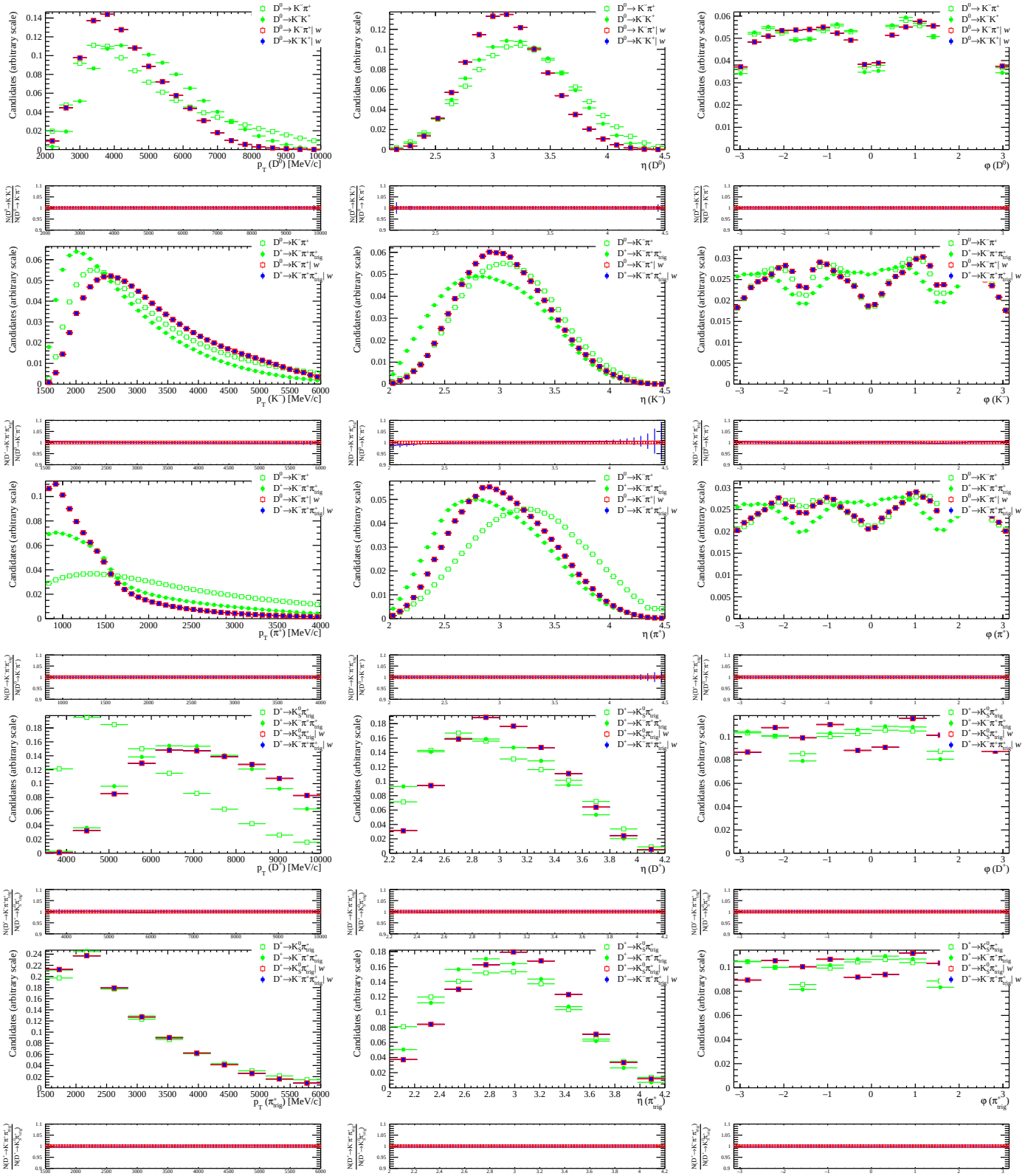

Figure 3.32: Comparison between normalized kinematic distributions of D^0, K^-, π^+, D^+ and π^+_{trig} MC candidates, before and after the kinematic weighting. The binning of the distributions is the same used for the weights computation. For each plot, the bottom panel shows the ratio between the distributions after the kinematic weighting. Only magnet-down 2016 data are shown. Similar results can be observed for different year and magnet polarity configuration.

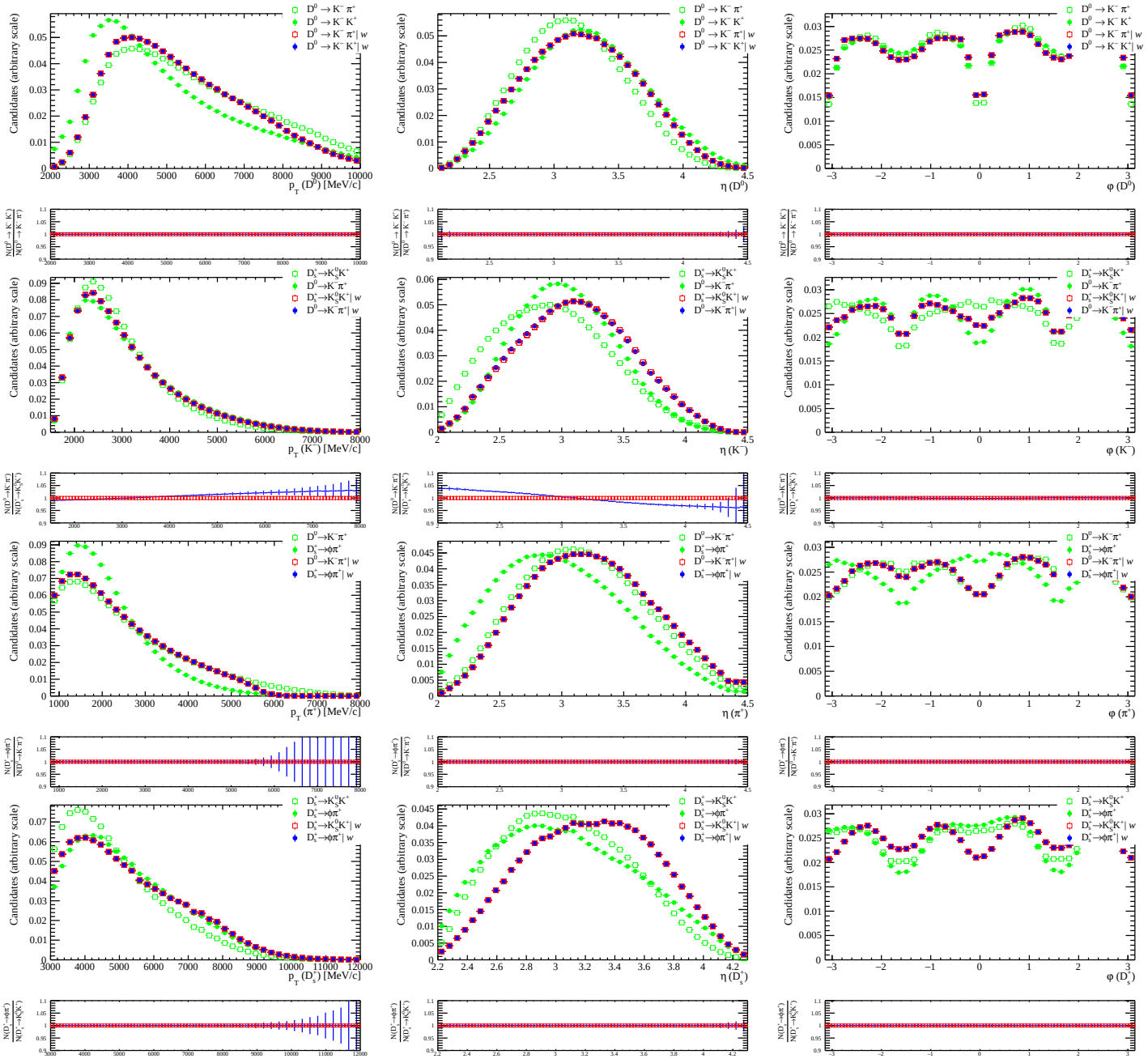

Figure 3.33: Comparison between normalized kinematic distributions of D^0, K^-, π^+ and D_s^+ MC candidates, before and after the kinematic weighting. The binning of the distributions is the same used for the weights computation. For each plot, the bottom panel shows the ratio between the distributions after the kinematic weighting. Only magnet-down 2016 data are shown. Similar results can be observed for different year and magnet polarity configuration.

3.8.1 Additional checks on $A_{\rm det}(K^-\pi^+)$

The aim of this section is to check on pGun data that the detection asymmetry $A_{\rm det}(f)$ of a certain final state $f = p_1, .., p_n$ corresponds to $\sum_{i=1}^{n} A_{\rm det}(p_i)$ up to a certain precision, *i.e.* the detection efficiencies are factorizable. This would also demonstrate that the detection asymmetry of each particle is independent from the other particles in the same final state as required by the strategy of this analysis to be valid (see Eqs. 3.16 and 3.17). In particular, the $D^+ \to K^-\pi^+\pi^+_{trig}$ and $D^0 \to K^-\pi^+$ decays have been considered by checking at what level of precision the relation $A_{\rm det}(K^-\pi^+) = A_{\rm det}(K^-) + A_{\rm det}(\pi^+)$ holds.

In this exercise, the `TupleToolMCTruth` algorithm of `DaVinci`[9] within the LHCb analysis framework has been exploited to obtain the information of each generated particle being reconstructed or not and then retrieve the detection efficiency of one or m particles, defined as

$$\varepsilon(p_1...p_m) = \frac{N(p_1|\text{Reconstructed}\,\&\,...\,\&\,p_m|\text{Reconstructed})}{N(\text{generated events})}. \tag{3.52}$$

The charge-dependent detection efficiencies of K^- and π^+ as a function of the particle momenta together with their detection asymmetries are shown in Figure 3.34 for $D^+ \to K^-\pi^+\pi^+_{trig}$ and $D^0 \to K^-\pi^+$ decay samples. For each particle, the detection asymmetry as a function of the momenta results to be compatible between the two subsamples demonstrating that, at this level of precision, it depends only on the kinematics of the particle and not on the decay.

In Table 3.33, the detection asymmetries for kaon and pion separately, and for the combined $K^-\pi^+$ pair are reported together with the algebrical sum $A_{\rm det}(K^-) + A_{\rm det}(\pi^+)$ for each sample. $A_{\rm det}(K^-\pi^+)$ results to be compatible with $A_{\rm det}(K^-) + A_{\rm det}(\pi^+)$ up to a precision of $4 \cdot 10^{-5}$ given by the combination between the two samples.

	$D^+ \to K^-\pi^+\pi^+_{trig}$	$D^0 \to K^-\pi^+$
$A_{\rm det}(K^-)\,[10^{-4}]$	(-36.4 ± 0.4)	(-31.5 ± 0.3)
$A_{\rm det}(\pi^+)\,[10^{-4}]$	(0.1 ± 0.4)	(0.5 ± 0.3)
$A_{\rm det}(K^-\pi^+)\,[10^{-4}]$	(-35.7 ± 0.4)	(-30.8 ± 0.3)
$A_{\rm det}(K^-) + A_{\rm det}(\pi^+)\,[10^{-4}]$	(-36.3 ± 0.5)	(-31.0 ± 0.4)

Table 3.33: Kaon and pion detection asymmetries together with the detection asymmetry of the $K^-\pi^+$ pair and their sum measured in $D^+ \to K^-\pi^+\pi^+_{trig}$ and $D^0 \to K^-\pi^+$ decay samples.

To take into account the different kinematics between the $D^+ \to K^-\pi^+\pi^+_{trig}$ and $D^0 \to K^-\pi^+$ decay modes, the 3-dimensional $(p_{\rm T}, \eta, \phi)$ distributions of kaon and pion

[9] `DaVinci` is the physics analysis software for the LHCb experiment, based on the Gaudi framework [116].

are equalised. The final results for $A_{\rm det}(K^-)$ and $A_{\rm det}(\pi^+)$ together with $A_{\rm det}(K^-\pi^+)$ are reported in Table 3.34. All the measurements are found compatible between the two different decay modes. Therefore, up to the level of precision of the simulation, the assumption $A_{\rm det}(K^-\pi^+) = A_{\rm det}(K^-) + A_{\rm det}(\pi^+)$ together with the weighting procedure is validated.

	$D^+ \to K^-\pi^+\pi^+_{trig}$	$D^0 \to K^-\pi^+$	compatibility
$A_{\rm det}(K^-)\|^w\,[10^{-4}]$	(-31.7 ± 0.5)	(-31.4 ± 0.3)	0.51
$A_{\rm det}(\pi^+)\|^w\,[10^{-4}]$	(0.0 ± 0.5)	(0.4 ± 0.3)	0.69
$A_{\rm det}(K^-\pi^+)\|^w\,[10^{-4}]$	(-31.3 ± 0.6)	(-30.7 ± 0.3)	0.89

Table 3.34: Kaon and pion detection asymmetries together with the detection asymmetry of the $K^-\pi^+$ pair measured in $D^+ \to K^-\pi^+\pi^+_{trig}$ and $D^0 \to K^-\pi^+$ decay samples after the application of kinematic weights. In the last column is reported the compatibility in terms of sigmas.

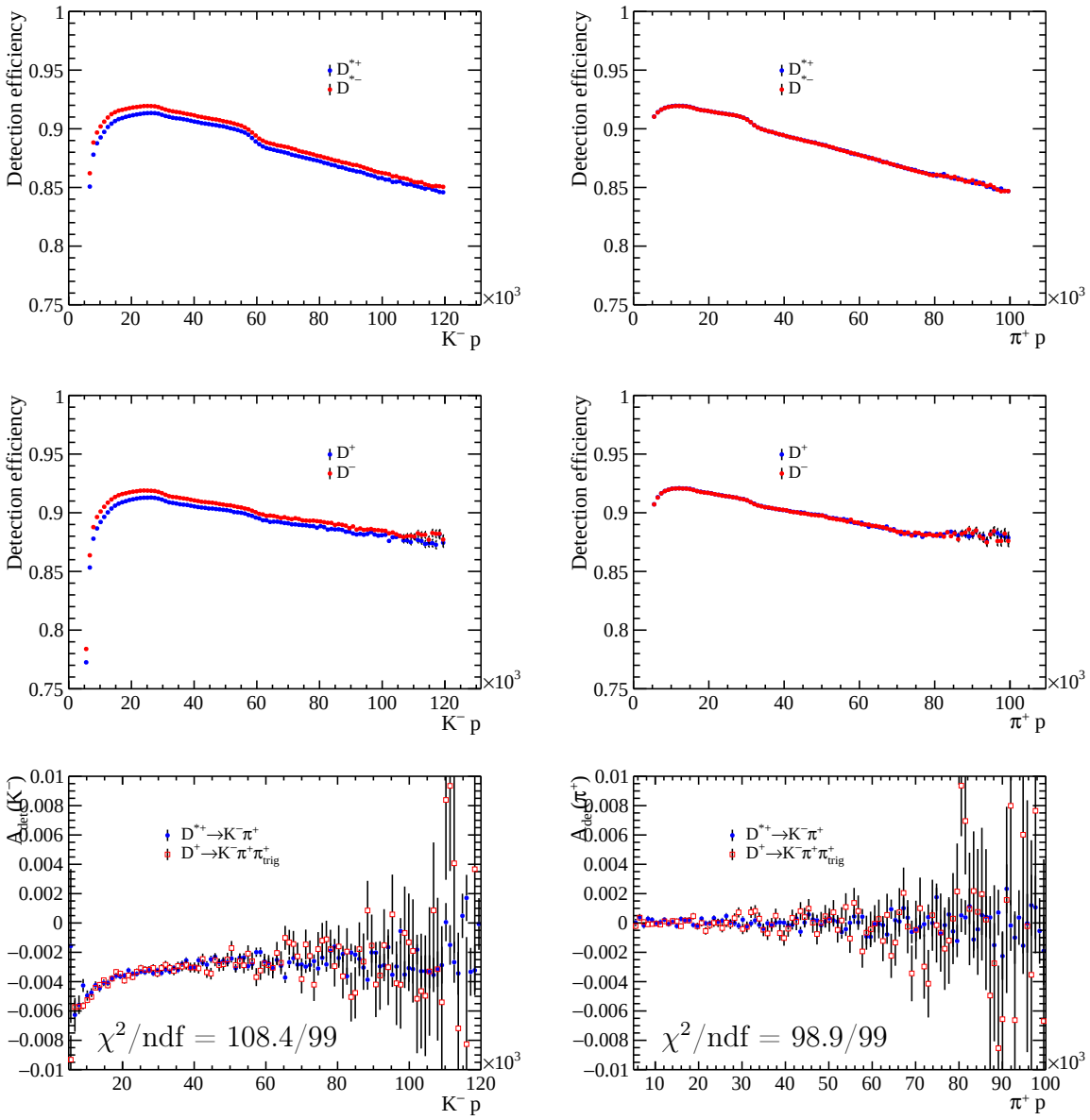

Figure 3.34: Charge-dependent detection efficiencies for (left) kaons and (right) pions for (first row) $D^+ \to K^-\pi^+\pi^+_{trig}$ and (second row) $D^0 \to K^-\pi^+$ decay samples. Last row: comparison between two different decay modes, (red) $D^+ \to K^-\pi^+\pi^+_{trig}$ and (blue) $D^0 \to K^-\pi^+$, of the detection asymmetries for (left) kaons and (right) pions.

3.8.2 Production asymmetries in MC samples

In the Monte Carlo data samples used for the validation of $\mathcal{A}^{CP}(K^-K^+)$, the D^{*+} and $D^+_{(s)}$ production asymmetries are not simulated. However, using values measured by LHCb, it is possible to add to the pGun data sample a kinematic dependent production asymmetry. The inclusive D^+ and D^+_s production asymmetries from pp interactions have been measured by LHCb [106, 117] to be

$$A_{\text{prod}}(D^+) = (-0.96 \pm 0.26 \pm 0.18)\%,$$
$$A_{\text{prod}}(D^+_s) = (-0.52 \pm 0.13 \pm 0.10)\%,$$

evidencing a non-zero production asymmetry. A dependence of $A_{\text{prod}}(p_{\text{T}}, \eta)$ is added to the Monte Carlo data sample from a 2-dimensional function

$$A_{\text{prod}} = a \cdot \eta + b \cdot p_{\text{T}} + c \tag{3.53}$$

represented in Figure 3.35 where the coefficients a, b and c are fitted from the LHCb A_{prod} (D^+_s) measurements and are found to be $a = (-0.069)\%$, $b = (0.0087)\%(\text{ GeV}/c)^{-1}$ and $c = (-0.36)\%$.

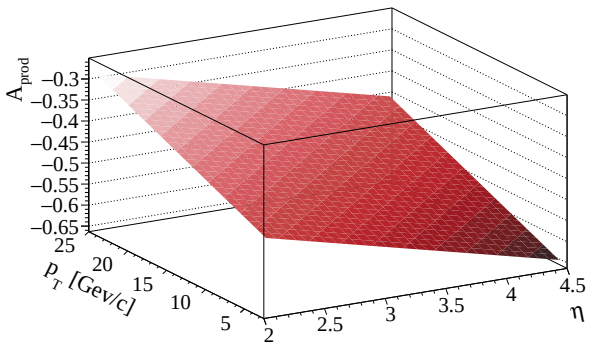

Figure 3.35: $A_{\text{prod}}(p_{\text{T}}, \eta)$ model used as input to simulated data.

The production asymmetries added to the pGun MC data are reported in Table 3.35, where the statistical errors are two order of magnitudes below the last digit reported. To validate the cancellation of the production asymmetries in the differences between the raw asymmetries, the full analysis is applied and the imperfect cancellation of the production asymmetries ΔA_{prod}, has been estimated. As the same function $A_{\text{prod}}(p_{\text{T}}, \eta)$ is applied to each pair of D meson with different decay modes, residues from the difference of the two production asymmetries can only arise from imperfect matching of the kinematic distributions. The values are reported in Table 3.36 and are found to be $\mathcal{O}(10^{-6})$.

decay	A_{prod}
D^+ method	
$D^+ \to K^0_S \pi^+_{trig}$	$-50.73 \cdot 10^{-4}$
$D^+ \to K^- \pi^+ \pi^+_{trig}$	$-50.70 \cdot 10^{-4}$
$D^0 \to K^- \pi^+$	$-53.40 \cdot 10^{-4}$
$D^0 \to K^- K^+$	$-53.40 \cdot 10^{-4}$
D^+_s method	
$D^+_s \to K^0_S K^+$	$-53.69 \cdot 10^{-4}$
$D^+_s \to \phi \pi^+$	$-53.68 \cdot 10^{-4}$
$D^0 \to K^- \pi^+$	$-53.09 \cdot 10^{-4}$
$D^0 \to K^- K^+$	$-53.09 \cdot 10^{-4}$

Table 3.35: Production asymmetries calculated following the $A_{\text{prod}}(p_{\text{T}}, \eta)$ model for each D meson in each decay samples for the D^+ and D^+_s method.

$\Delta A_{\text{prod}}(D^+)$ $[10^{-4}]$	$\Delta A_{\text{prod}}(D^{*+})\|D^+$
0.03	< 0.01

$\Delta A_{\text{prod}}(D^+_s)$	$\Delta A_{\text{prod}}(D^{*+})\|D^+_s$
0.01	< 0.01

Table 3.36: Difference between the D meson production asymmetries ΔA_{prod} in the D^+ and D^+_s method.

3.8.3 $\mathcal{A}^{CP}(K^-K^+)$ in MC samples

In the pGun data samples used for the validation, the amount of generated $D^0 \to K^-K^+$ and $\overline{D}^0 \to K^-K^+$ decays is the same, *i.e.* the value of $\mathcal{A}^{CP}(K^-K^+)$ is fixed to zero. In the following, we injected several values for $\mathcal{A}^{CP}(K^-K^+)$ in the $D^0 \to K^-K^+$ sample, namely 1%, 2% and 3%. After the application of the weighting procedure in the D^+ and D_s^+ methods, the raw asymmetries are measured in each decay mode and the measurements of $\mathcal{A}^{CP}(K^-K^+)$ are done. The measured values for $\mathcal{A}^{CP}(K^-K^+)$ together with the *CP* asymmetries injected in the $D^0 \to K^-K^+$ samples are reported in Table 3.37. Since the data samples remain the same, the resulting pseudomeasurements of $\mathcal{A}^{CP}(K^-K^+)$ are fully correlated and driven by the same fluctuation observed in Table 3.32. Finally, the measured and injected values for $\mathcal{A}^{CP}(K^-K^+)$ are found to be compatible between each others and between the D^+ and D_s^+ method.

$\mathcal{A}^{CP}(K^-K^+)$ input value	$\mathcal{A}^{CP}(K^-K^+)\|D^+$	$\mathcal{A}^{CP}(K^-K^+)\|D_s^+$
1%	$(94.8 \pm 3.2) \cdot 10^{-4}$	$(98.3 \pm 3.0) \cdot 10^{-4}$
2%	$(194.8 \pm 3.2) \cdot 10^{-4}$	$(198.3 \pm 3.0) \cdot 10^{-4}$
3%	$(294.8 \pm 3.2) \cdot 10^{-4}$	$(298.3 \pm 3.0) \cdot 10^{-4}$

Table 3.37: *CP* asymmetries injected in the $D^0 \to K^-K^+$ samples and the one measured with the D^+ and D_s^+ method.

3.9 Systematic uncertainties

The systematic uncertainty in the neutral kaon asymmetry has been already evaluated in Section 3.6.2 with a novel data-driven method. In this section, additional systematic uncertainties are quoted considering possible contributions due to the presence of D^{*+}, D^+ or D_s^+ mesons from b-hadron decays (Section 3.9.1), the presence of peaking backgrounds (Section 3.9.2), the mismodeling in the shapes used to fit the raw asymmetries (Section 3.9.3), the inaccuracy in the kinematic weighting (Section 3.9.4) and the neglected contribution from charged kaon detection asymmetries in the $D_s^+ \to \phi\pi^+$ decays (Section 3.9.5).

Moreover, consistency checks are performed in Section 3.10 to support the analysis procedure and investigate possible unexpected biases by comparing results obtained in subsamples selected according to criteria that are not expected to affect the measurement. Table 3.38 reports a summary of all the systematic uncertainties, whose determination is explained in details in the following sections.

Source	$\mathcal{A}^{CP}(K^-K^+)\|D^+$	$\mathcal{A}^{CP}(K^-K^+)\|D_s^+$	ρ
Neutral kaon asym.	0.6	1.3	1.00
Secondary decays	0.6	0.3	/
Peaking backgrounds	0.3	0.4	0.74
Fit model	1.1	1.0	0.05
Kinematic diff.	0.8	0.4	/
Charged kaon asym.	/	1.0	/
Total systematic	1.6	2.0	0.28
Statistical	8.8	6.7	0.05

Table 3.38: Summary of the uncertainties in units of 10^{-4} on the measured quantities.

3.9.1 Contamination from secondary decays

The requirement imposed on the impact parameter with respect to the PV of the charm meson candidates (IP < 50 μm) rejects most of the secondary decays. In each sample, a fraction f_{sec} of surviving secondary charm mesons is present. The raw asymmetry is then written as

$$A = A_{prompt} + f_{sec}\,(A_{sec} - A_{prompt})\,, \tag{3.54}$$

where A^{prompt} (A^{sec}) is the raw asymmetry of the decay when the D candidate is produced promptly (in secondary decays).

If this fraction is different between the various decay modes, an imperfect cancellation of the charm-meson production asymmetries can occur, generating a bias on $\mathcal{A}^{CP}(K^-K^+)$. Defining $\Delta^X_{sec} = f^X_{sec}\left(A^X_{sec} - A^X_{prompt}\right)$ for each decay mode X, the bias Δ_{sec} on $\mathcal{A}^{CP}(K^-K^+)$, on the basis of Eqs. 3.16 and 3.17, can be written as

$$\Delta_{sec}|D^+ = \Delta^{K^+K^-}_{sec} - \Delta^{K^-\pi^+}_{sec} + \Delta^{K^-\pi^+\pi^+_{trig}}_{sec} - \Delta^{K^0_S\pi^+_{trig}}_{sec}, \tag{3.55}$$

$$\Delta_{sec}|D^+_s = \Delta^{K^+K^-}_{sec} - \Delta^{K^-\pi^+}_{sec} + \Delta^{\phi\pi^+}_{sec} - \Delta^{K^0_S K^+}_{sec}, \tag{3.56}$$

for the D^+ and D^+_s method, respectively. For each D species (D^0, D^+_s, D^+), the difference $A^{\rm sec}_{\rm raw} - A^{\rm pr}_{\rm raw}$ is expected to be equal between two different decay modes. The term $\Delta^{K^-K^+}_{sec} - \Delta^{K^-\pi^+}_{sec}$ in Eqs. 3.55 and 3.56 can therefore be written as

$$\Delta^{K^-K^+}_{sec} - \Delta^{K^-\pi^+}_{sec} = \langle A^{D^0,{\rm sec}}_{\rm raw} - A^{D^0,{\rm pr}}_{\rm raw}\rangle (f^{K^-K^+}_{\rm sec} - f^{K^-\pi^+}_{\rm sec}), \tag{3.57}$$

where $\langle A^{D^0,{\rm sec}}_{\rm raw} - A^{D^0,{\rm pr}}_{\rm raw}\rangle$ is the weighted average of $A^{\rm sec}_{\rm raw} - A^{\rm pr}_{\rm raw}$ measured in $D^0 \to K^+K^-$ and $D^0 \to K^-\pi$ modes. A similar assumption holds for the D^+ and D^+_s modes.

The bias is evaluated by measuring $f_{\rm sec}$ and the prompt and secondary raw asymmetries for each decay mode. The IP distribution of simulated secondary decays, normalised to combinatorial background-subtracted data in the region IP $\in [150, 300]$ μm, is used to determine the number of secondary and prompt decays in data in the baseline region IP < 50 μm. This is done separately for each tag, in order to determine also the asymmetries of prompt and secondary decays. The combinatorial background subtraction is performed by means of signal and sideband regions defined as reported in Table 3.39. Relative weights between signal and background regions are obtained through fits to the invariant mass distribution as described in Section 3.4. Kinematic weighting is performed on data samples according to the baseline procedure described in Section 3.5, to cancel detection and production asymmetries.

Several samples of secondary decays are produced with pGun simulation starting from B^0, B^+ and B^0_s meson decays. The samples are then weighted to correctly match the expected relative ratios between those produced from B^0, B^+ and B^0_s, according to the numbers reported in Tables 3.40 and 3.41. To get a better agreement between

Decay mode	Mass	Signal range [MeV/c^2]	Sideband [MeV/c^2]
$D^0 \to K^+K^-$	$m(D^0\pi)$	$2006.5 - 2012$	$2015 - 2019$
$D^0 \to K^-\pi^+$	$m(D^0\pi)$	(same)	(same)
$D_s^+ \to \phi\pi^+$	$m(K^-K^+\pi^+)$	$1923 - 2003$	$2015 - 2045$
$D_s^+ \to K_S^0K^+$	$m(K_S^0K^+)$	(same)	(same)
$D^+ \to K^-\pi^+\pi^+_{trig}$	$m(K^-\pi^+\pi^+)$	$1820 - 1915$	$1920 - 1935$
$D^+ \to K_S^0\pi^+_{trig}$	$m(K_S^0\pi^+)$	(same)	(same)

Table 3.39: Signal and sideband ranges of the invariant mass used for each decay modes.

Charm meson	B mother	Cross section [μb]	$\mathcal{B}$ ($B \to DX$)
D^{*+}	B^0	86.6 ± 6.4	0.226 ± 0.007
	B^+	(same)	0.036 ± 0.007
D^+	B^0	(same)	0.369 ± 0.033
	B^+	(same)	0.124 ± 0.013
D_s^+	B^0	(same)	0.101 ± 0.020
	B^+	(same)	0.090 ± 0.014
	B_s^0	(same)$\cdot(0.122 \pm 0.006) \cdot 2$	0.930 ± 0.250

Table 3.40: B mother cross-sections and branching ratios of secondary decays produced [31]. Here, the cross-section of B_s^0 meson is estimated considering the measurement of $f_s/(f_u + f_d)$ being the production fractions of B_s^0 hadrons normalized to the sum of B^+ and B^0 fractions [118].

data and MC, a 3D weighting is applied on the $p_{\rm T}$, η and ϕ of the D candidates in MC to match the kinematics of the background-subtracted data sample in the region IP $> 100\,\mu$m. To take into account possible systematic effects on the determination of $f_{\rm sec}$, the study is repeated by using the normalisation region IP $\in [100, 200]\,\mu$m or by using simulated secondary decays where only B^+ decays are considered. For each decay mode, the maximum observed variation of $f_{\rm sec}$ is taken as uncertainty on this quantity. The results are shown in Figures 3.36 and 3.37 and reported in Table 3.42. The raw asymmetries have the same blinding shifts as those of the baseline analysis.

For each D species, the average $\langle A_{\rm raw}^{D^0,{\rm sec}} - A_{\rm raw}^{D^0,{\rm pr}} \rangle$ and the $f_{\rm sec}$ difference between the two decay modes are calculated, and the results are reported in Table 3.43. For each method, the total bias is computed according to Eqs. 3.55 and 3.56 and reported in the same table. The systematic uncertainty due to the neglected secondary fractions is assigned from the RMS of $\Delta_{\rm sec}$, corresponding to $0.6 \cdot 10^{-4}$ for the D^+ method and $0.3 \cdot 10^{-4}$ for the D_s^+ method. Assuming the only contribution of the D^0 decay modes,

Decay	B mother	N	Generator level efficiency	Weight
$D^0 \to K^-K^+$	B^0	$30 \cdot 10^6$	0.2544 ± 0.0001	1
	B^+	$30 \cdot 10^6$	0.2344 ± 0.0001	0.15
$D^0 \to K^-\pi^+$	B^0	$20 \cdot 10^6$	0.2772 ± 0.0001	1
	B^+	$20 \cdot 10^6$	0.2604 ± 0.0001	0.15
$D^+ \to K^-\pi^+\pi^+_{trig}$	B^0	$10 \cdot 10^6$	0.0654 ± 0.0000	1
	B^+	$10 \cdot 10^6$	0.0498 ± 0.0000	0.26
$D^+ \to K^0_S\pi^+_{trig}$	B^0	$10 \cdot 10^6$	0.0161 ± 0.0000	1
	B^+	$10 \cdot 10^6$	0.0129 ± 0.0000	0.27
$D^+_s \to \phi\pi^+$	B^0	$10 \cdot 10^6$	0.0767 ± 0.0000	0.45
	B^+	$10 \cdot 10^6$	0.0740 ± 0.0000	0.39
	B^0_s	$10 \cdot 10^6$	0.0762 ± 0.0000	1
$D^+_s \to K^0_S K^+$	B^0	$10 \cdot 10^6$	0.0452 ± 0.0000	0.45
	B^+	$10 \cdot 10^6$	0.0438 ± 0.0000	0.39
	B^0_s	$10 \cdot 10^6$	0.0447 ± 0.0000	1

Table 3.41: Weights applied to the pGun samples for secondary decays to take into account the different B mother cross-section, the branching ratios (reported in Table 3.40), the efficiencies of the generator-level cuts and the number of generated events N.

Method	Decay mode	f_{sec} [%]	$A_{\text{raw}}^{\text{sec blind}}$ $[10^{-4}]$	$A_{\text{raw}}^{\text{pr blind}}$ $[10^{-4}]$	$A_{\text{raw}}^{\text{sec}} - A_{\text{raw}}^{\text{pr}}$ $[10^{-4}]$
D^+	$D^0 \to K^+K^-$	4.25 ± 0.38	-96 ± 28	-80.8 ± 2.7	-15 ± 29
	$D^0 \to K^-\pi^+$	5.07 ± 0.41	-180 ± 37	-204.8 ± 3.3	25 ± 39
	$D^+ \to K^-\pi^+\pi^+_{trig}$	3.02 ± 0.14	58 ± 48	-51.5 ± 2.4	109 ± 50
	$D^+ \to K^0_S\pi^+_{trig}$	2.63 ± 0.30	63 ± 195	15 ± 10	48 ± 200
D^+_s	$D^0 \to K^+K^-$	4.56 ± 0.28	-93 ± 26	-84.1 ± 2.5	-9 ± 28
	$D^0 \to K^-\pi^+$	4.71 ± 0.26	-205 ± 31	-206.2 ± 2.3	1 ± 32
	$D^+_s \to \phi\pi^+$	5.84 ± 0.71	-13 ± 67	40.8 ± 4.7	-54 ± 71
	$D^+_s \to K^0_S K^+$	5.60 ± 0.44	86 ± 61	107.1 ± 7.3	-21 ± 65

Table 3.42: Raw prompt and secondary asymmetries and fractions of secondary decays for the full Run 2 sample, (top) D^+ method and (bottom) D^+_s method.

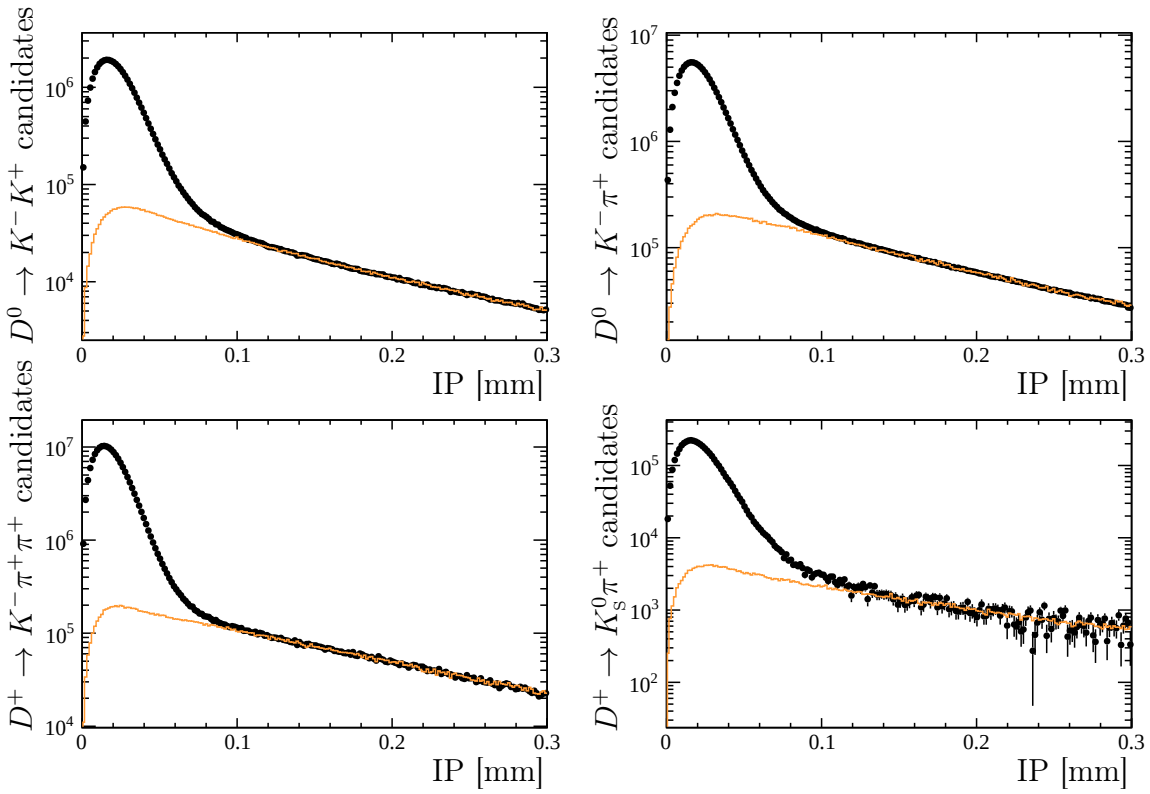

Figure 3.36: Distribution of the IP for the full Run 2 data sample, for (top left) $D^0 \to K^+K^-$, (top right) $D^0 \to K^-\pi^+$, (bottom left) $D^+ \to K^-\pi^+\pi^+_{trig}$ and (bottom right) $D^+ \to K^0_S\pi^+_{trig}$ decays (D^+ method). The distribution for secondary decays MC sample, normalised in the IP $> 150\,\mu$m region, is overlaid.

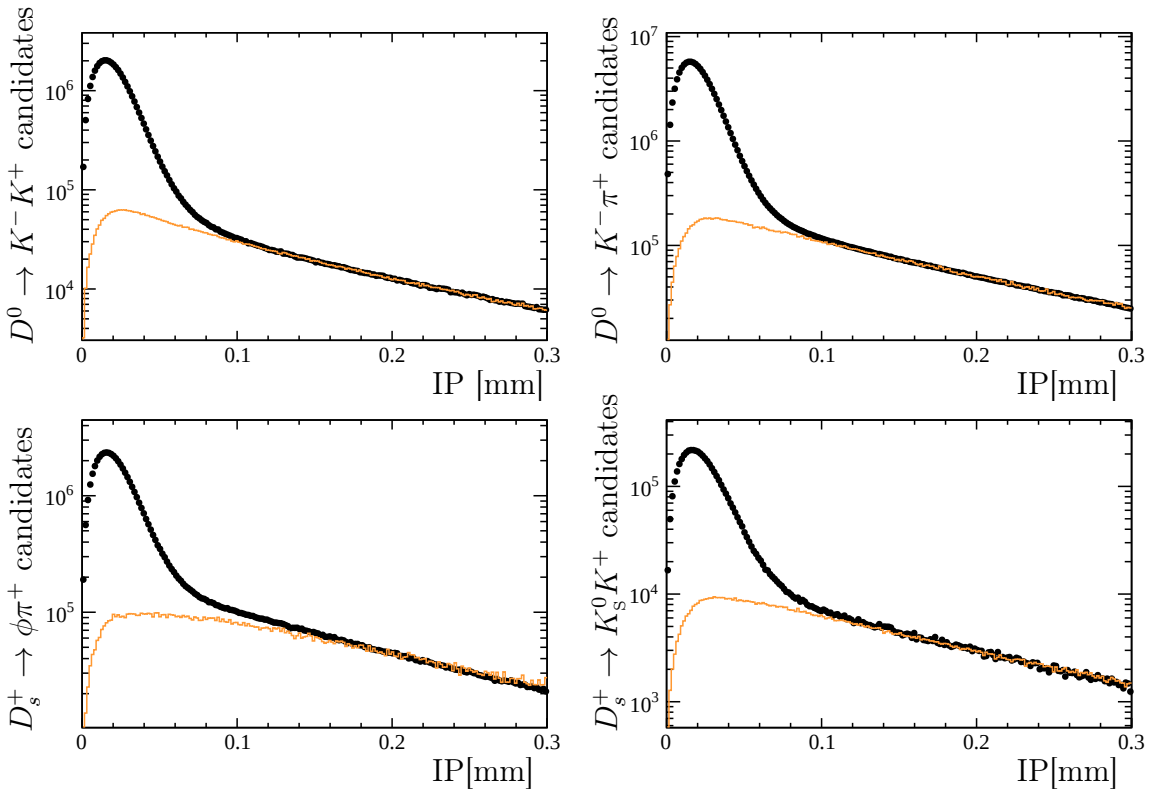

Figure 3.37: Distribution of the IP for the full Run 2 data sample, for (top left) $D^0 \to K^+K^-$, (top right) $D^0 \to K^-\pi^+$, (bottom left) $D_s^+ \to \phi\pi^+$ and (bottom right) $D_s^+ \to K_S^0K^+$ decays (D_s^+ method). The distribution for secondary decays MC sample, normalised in the IP $> 150\,\mu$m region, is overlaid.

Method	Decay mode	$\langle A_{\rm raw}^{\rm sec} - A_{\rm raw}^{\rm pr} \rangle$ $[10^{-4}]$	$\Delta f_{\rm sec}$ [%]	$\Delta_{\rm sec}$ $[10^{-4}]$
D^+	$D^0 \to K^+K^-$ $D^0 \to K^-\pi^-$	-1 ± 23	-0.83 ± 0.56	0.01 ± 0.19
	$D^+ \to K^-\pi^+\pi^+_{trig}$ $D^+ \to K^0_{\rm S}\pi^+_{trig}$	106 ± 48	0.39 ± 0.33	0.41 ± 0.40
				$\Delta_{\rm sec} = (0.42 \pm 0.44)$
D_s^+	$D^0 \to K^+K^-$ $D^0 \to K^-\pi^-$	-5 ± 21	-0.15 ± 0.38	0.01 ± 0.04
	$D_s^+ \to \phi\pi^+$ $D_s^+ \to K^0_{\rm S}K^+$	-36 ± 48	0.24 ± 0.83	-0.09 ± 0.32
				$\Delta_{\rm sec} = (-0.08 \pm 0.32)$

Table 3.43: Average of prompt-secondary asymmetry difference and $\Delta f_{\rm sec}$ for each D species, for (top) D^+ method and (bottom) D_s^+ method. The resulting partial biases are reported in the rightmost columns, along with the total bias for each method.

the correlation between the two uncertainties is negligible.

3.9.2 Presence of peaking background

The presence of mis-reconstructed $D^+_{(s)}$ meson has already been investigated in Section 3.3 where tight cuts are applied to suppress peaking-backgrounds and other backgrounds polluting the invariant-mass spectrum. Given the small fraction of these decays in the signal region, $\sim 10^{-4}$, and assuming a (conservative) value of 5% for the raw asymmetry of these backgrounds, the impact on $\mathcal{A}^{CP}(K^-K^+)$ is estimated to be smaller than 10^{-5} and therefore negligible.

As regards the D^{*+} reconstructed samples, partially- or mis-reconstructed D^0 meson decaying from a D^{*+} may peak in the $m(D^0\pi)$ invariant mass distribution and mimic the signal in the $D^0 \to K^-K^+$ and $D^0 \to K^-\pi^+$ channels. Precisely, peaking backgrounds (PB) in the $m(D^0\pi)$ invariant mass distribution are originated from the cut around the D^0 peak in the $m(p_1p_2)$ invariant mass distribution, with p_1 or p_2 being the misidentified particles, where they do not peak. In order to assess a related systematic uncertainty, the following strategy is adopted.

1. The fraction and asymmetry of each PB decay are measured by performing fits to the $m(p_1p_2)$ invariant mass spectra, considering all the events in the full $m(D^0\pi)$ invariant mass window 2004.5–2020 MeV/c^2 and using templates obtained from simulation.

2. The measured fraction and asymmetry of the PB are used as input for toy fits to the $m(D^0\pi)$ distribution, where the fits are performed with and without the PB components.

3. The RMS of the distribution of the difference between $\mathcal{A}^{CP}(K^-K^+)$ measured with and without the PB components is taken as systematic uncertainty.

For the $D^0 \to K^-\pi^+$ mode the following decays are considered as peaking background

- semileptonic $D^0 \to K^-\mu^+\nu_\mu$ and $D^0 \to K^-e^+\nu_e$ decays, with D^0 originating from $D^{*+} \to D^0\pi^+$, where the charged lepton is reconstructed as a pion and the neutrino is not reconstructed;

- $D^0 \to K^+K^-$ and $D^0 \to \pi^+\pi^-$ decays, with D^0 originating from $D^{*+} \to D^0\pi^+$, where a kaon (pion) is reconstructed as a pion (kaon);

- $D^0 \to \pi^+\pi^-\pi^0$ decay, with D^0 originating from $D^{*+} \to D^0\pi^+$, where a charged pion is reconstructed as kaon and the π^0 is not reconstructed.

For what concerns the $D^0 \to K^-K^+$ mode, the following decays are considered as peaking background

- semileptonic $D^0 \to K^-\mu^+\nu_\mu$ and $D^0 \to K^-e^+\nu_e$ decays, with D^0 originating from $D^{*+} \to D^0\pi$, where the charged lepton is reconstructed as a kaon and the neutrino is not reconstructed;
- $D^0 \to K^-\pi^+$ decay, with D^0 originating from $D^{*+} \to D^0\pi^+$, where the pion is reconstructed as a kaon;
- $D^0 \to K^-\pi^+\pi^0$ decay, with D^0 originating from $D^{*+} \to D^0\pi^+$, where the charged pion is reconstructed as a kaon and the π^0 is not reconstructed.

Other decays that must be taken into account when studying the $m(p_1p_2)$ distribution, even if they do not peak in the $m(D^0\pi)$ distribution (indeed they show a combinatorial-like shape), are

- $D_s^+ \to K^-K^+\pi^+$ where the pion plays the role of the soft pion ($D^0 \to K^+K^-$ mode);
- $D^+ \to K^-\pi^+\pi^+$ where one pion is reconstructed as a kaon, and the other pion plays the role of the soft pion ($D^0 \to K^+K^-$ mode);
- $\Lambda_c^+ \to K^-p\pi^+$ where the proton is reconstructed as a kaon, and the pion plays the role of the soft pion ($D^0 \to K^+K^-$ mode).

The distributions of the reconstructed-as-signal $D^0 \to K^-\pi^+$ invariant mass of the decays mentioned above, with the baseline selection applied (except for the cut on $m(p_1p_2)$), are shown in Figure 3.38. The distributions are obtained using the fast-simulation toolkit RapidSim [119] that reproduces phase-space decays of beauty and charm quark hadrons and allows for quick studies of the properties of signal and background decays. These distributions are normalised according to the branching ratio and the selection efficiency. The `PIDCalib` [120] tool is used to emulate the PID efficiency on the RapidSim samples. Similar plots are shown for the $D^0 \to K^-K^+$ mode in Figure 3.39. The list of the decays simulated with RapidSim, along with the number of events generated and surviving the selection, is reported in Table 3.44.

A fit is performed on data in order to measure the relative fractions of each PB. The fit is performed in the range $[1750, 2010]$ MeV/c^2 of the $m(p_1p_2)$ invariant-mass distribution, separately for year and magnet polarity. The signal model is given by the sum of three Gaussian functions with different means and standard deviations. Two Gaussians are convolved with a function parameterising the finale-state QED radiation. The values of the standard deviations are shared between the positively- and negatively-tagged samples, while the means are different. An exponential function is used to model the combinatorial background, while templates obtained from the RapidSim samples are used to model the PB components. For the $D^0 \to K^-\pi^+$ mode, a unique raw asymmetry parameter is considered in the fit for $D^0 \to \pi^+\pi^-$ and $D^0 \to \pi^+\pi^-\pi^0$ decays,

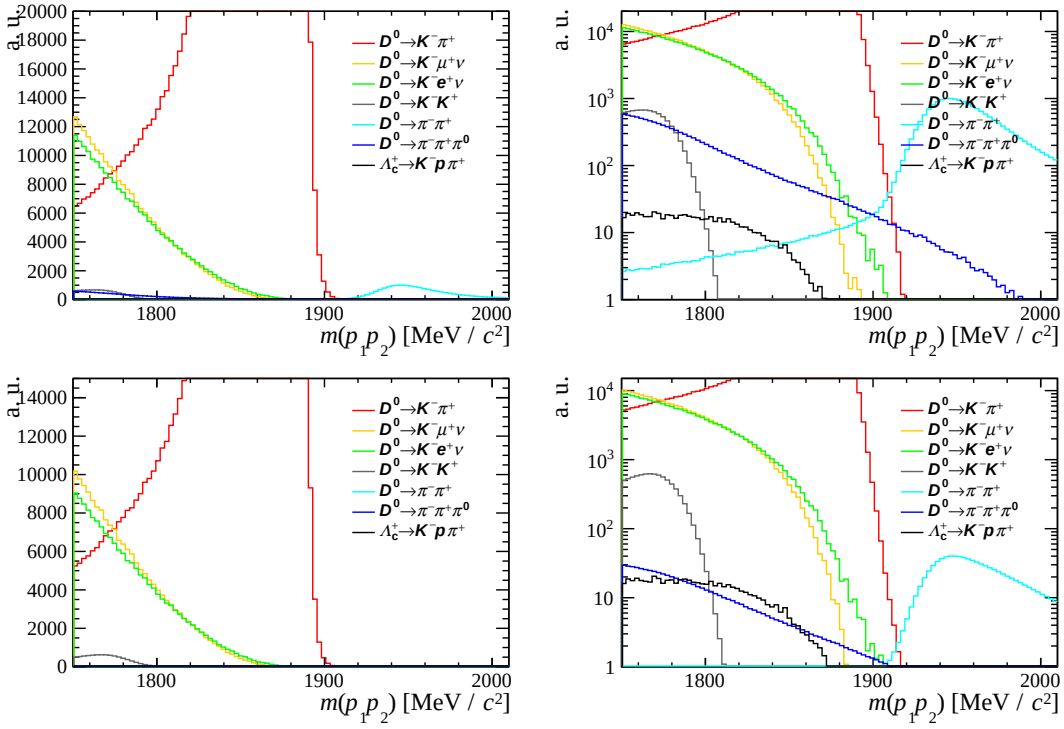

Figure 3.38: Distribution of the invariant mass $m(p_1p_2)$, where p_1 or p_2 are the misidentified particles, for the $D^0 \to K^-\pi^+$ mode, for (top) D^+ method and (bottom) D_s^+ method. Signal distribution (in red) is shown for comparison. The plots are shown in log scale on the right.

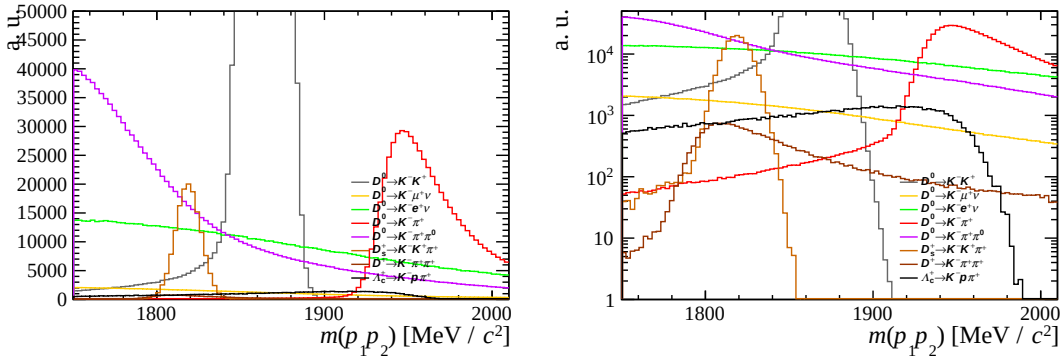

Figure 3.39: Distribution of the invariant mass $m(p_1p_2)$, where p_1 or p_2 are the misidentified particles, for the $D^0 \to K^-K^+$ mode. Signal distribution (in grey) is shown for comparison. The plots are shown in log scale on the right.

Decay	Generated events [10^9]	Selected events [10^3]		
		$D^0 \to K^-\pi^+$ (D_s^+ method)	$D^0 \to K^-\pi^+$ (D^+ method)	$D^0 \to K^+K^-$
$D^0 \to K^-\pi^+$	4	23200	28700	262
$D^0 \to K^-\mu^+\nu_\mu$	5	251	314	61.5
$D^0 \to K^-e^+\nu_e$	5	232	296	531
$D^0 \to K^-K^+$	1	23.4	30.0	12700
$D^0 \to \pi^+\pi^-$	1	9.75	134	-
$D^0 \to \pi^+\pi^-\pi^0$	3	2.34	22.3	-
$\Lambda_c^+ \to K^-p\pi^+$	3	0.797	0.784	42.3
$D^0 \to K^-\pi^+\pi^0$	3	-	-	104
$D_s^+ \to K^-K^+\pi^+$	3	-	-	74.0
$D^+ \to K^-\pi^+\pi^+$	3	-	-	2.55

Table 3.44: List of decays simulated with RapidSim, with number of generated and selected events.

and similarly in the $D^0 \to K^-K^+$ mode, for $D^0 \to K^-\pi^+$ and $D^0 \to K^-\pi^+\pi^0$ decays. In the $D^0 \to K^-K^+$ mode, the raw asymmetries of the semileptonic decays and $D^0 \to K^-\pi^+$ decay are a unique parameter in the fit, under the assumption that the detection asymmetries of leptons and pions are negligible with respect to that of kaons. Besides the listed PB decays, in the $D^0 \to K^-K^+$ mode one more component is needed to better describe data in the region below 1800 MeV/c^2, so a Gaussian shape is used to model this component, which has also its own raw asymmetry in the fit. Some studies performed by tightening the PID cuts show that these are real kaons, probably originating from inclusive K^-K^+X decays. Anyway, as it will be shown, they do not enter the signal region and they are needed only to increase the quality of the fit and have a better leverage on the determination of the other components.

The results of the fits are reported in Figures 3.40 and 3.41 for the 2018 magnet-down data sample, as example. The values of the raw asymmetries obtained from the fit to the 2018 magnet-down sample are reported in Table 3.45, as an example. Similar results are obtained with the samples of all the other years and magnet polarities. The fit results allow the fraction of PB to be extrapolated under the signal region $m(p_1p_2) \in [1844, 1887]$ MeV/c^2, whereas the raw asymmetries are assumed to be equal through the full mass range. For the $D^0 \to K^-K^+$ mode, the yield fractions of the PB relative to the signal in the signal window are about 1.3% or below, whereas for the $D^0 \to K^+\pi^-$ mode they are at most $8 \cdot 10^{-5}$.

To evaluate the effect of the PB components on the measurement of $\mathcal{A}^{CP}(K^-K^+)$, 1000 toys are performed (separately for each year and magnet polarity). A pseudo data-sample is generated according to the baseline fit model in $m(D^0\pi)$ distribution.

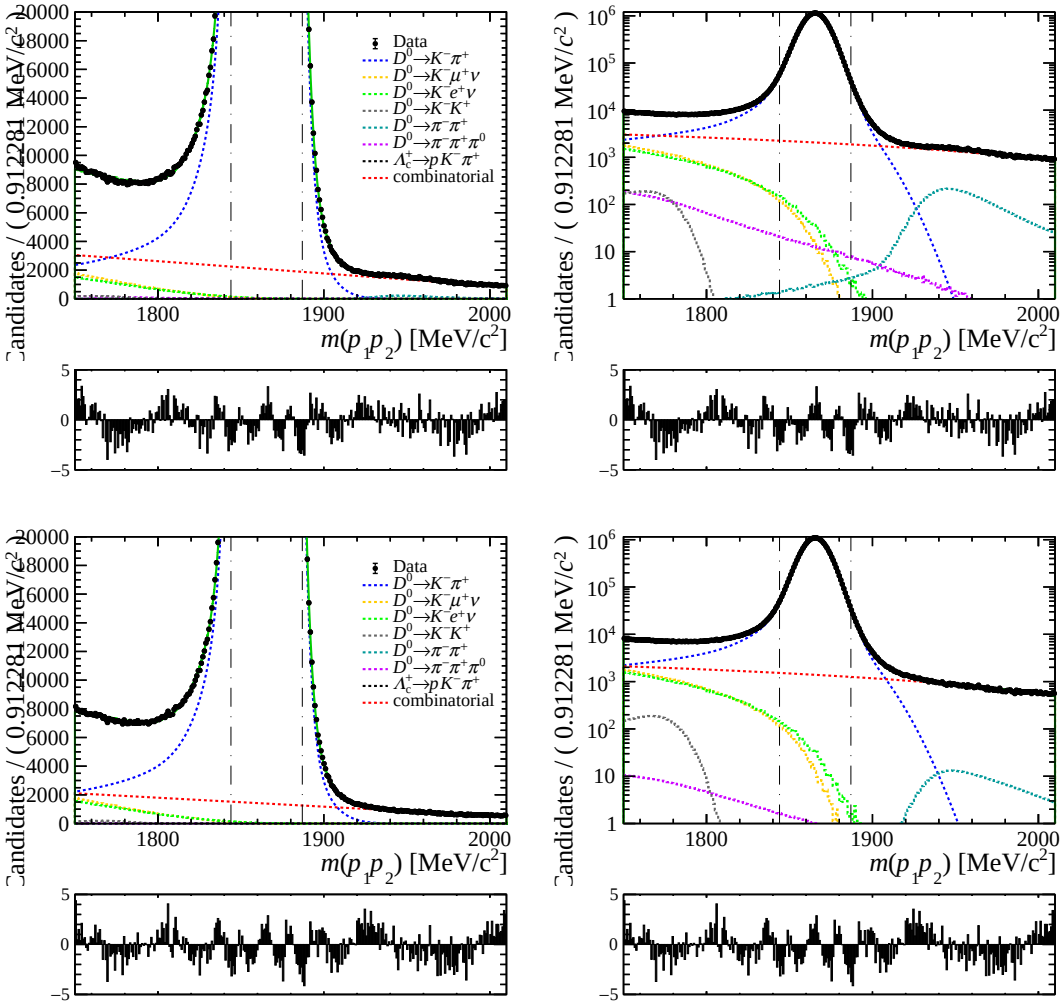

Figure 3.40: Fit to the full range of $m(p_1p_2)$ including the PB components for the $D^0 \to K^-\pi^+$ mode for (top) D^+ method and (bottom) D_s^+ method, 2018 magnet-down data sample. The plots are shown in log scale on the right. Two vertical dashed lines show the signal region of the baseline selection.

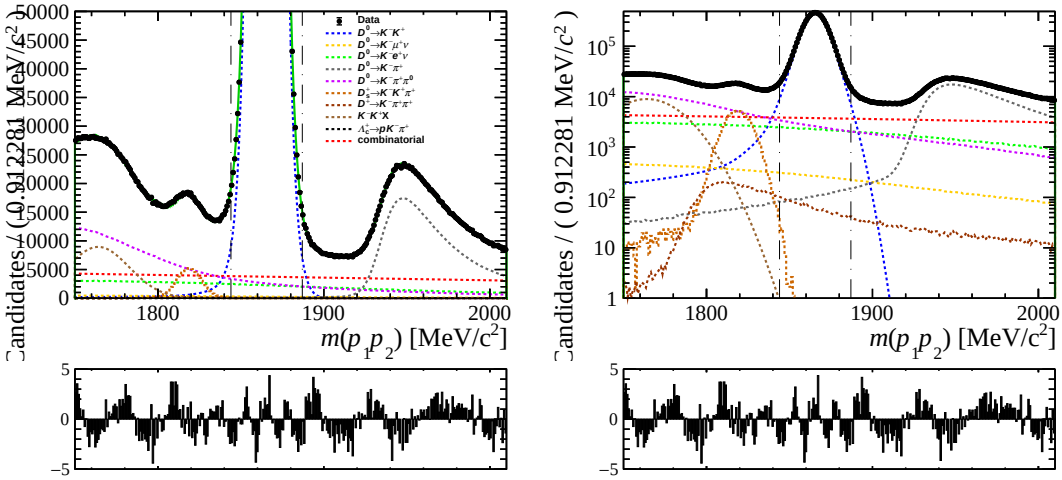

Figure 3.41: Fit to the full range of $m(p_1p_2)$ including the PB components for the $D^0 \to K^-K^+$, 2018 magnet-down data sample. The plots are shown in log scale on the right. Two vertical dashed lines show the signal region of the baseline selection.

Then a fit with baseline model and one with baseline model plus PB templates are performed. The $m(D^0\pi)$ templates of the PB components are shown in Figures 3.42 and 3.43, normalised according to the measured relative ratio. For each toy, the values of the asymmetries and relative ratios of the PB components are generated according to a multivariate gaussian that takes as input the values and their correlations measured in the fit to $m(p_1p_2)$, then they are fixed to the generated values in the fit. The decays $D^0 \to K^-K^+$ and $D^0 \to \pi^-\pi^+$ are dropped from this study in the $D^0 \to K^-\pi^+$ mode because their measured ratio relative to signal is below 10^{-6}. For each toy, the value of $\mathcal{A}^{CP}(K^-K^+)$ is computed by combining the results of all the years and magnet polarities, both for baseline, $\mathcal{A}^{CP}(K^-K^+)_{\rm base}$, and alternative fits, $\mathcal{A}^{CP}(K^-K^+)_{\rm alt}$. The RMS of the distributions of $\mathcal{A}^{CP}(K^-K^+)_{\rm alt} - \mathcal{A}^{CP}(K^-K^+)_{\rm base}$, shown in Figure 3.44, are taken as systematic uncertainties, namely $0.3 \cdot 10^{-4}$ and $0.4 \cdot 10^{-4}$ for D^+ and D_s^+ methods, respectively. Since these systematic uncertainties are dominated by the presence of peaking backgrounds in the $D^0 \to K^-K^+$ decay samples, their correlation is assumed to be equal to ρ_{KK}, *i.e.* $\rho_{\rm syst} = 0.74$.

Decay mode	Peaking background source	$A_{\text{raw}}[\%]$
$D^0 \to K^-K^+$	$D^0 \to K^-\pi^+$ $D^0 \to K^-\pi^+\pi^0$ $D^0 \to K^-\mu^+\nu_\mu$ $D^0 \to K^-e^+\nu_e$	-2.91 ± 0.20
$D^0 \to K^-\pi^+$ (D^+ method)	$D^0 \to K^-\mu^+\nu_\mu$ $D^0 \to K^-e^+\nu_e$	-10.8 ± 1.7
	$D^0 \to \pi^-\pi^+\pi^0$	-14.3 ± 5.5
$D^0 \to K^-\pi^+$ (D_s^+ method)	$D^0 \to K^-\mu^+\nu_\mu$ $D^0 \to K^-e^+\nu_e$	-5.0 ± 2.6
	$D^0 \to \pi^-\pi^+\pi^0$	-100 ± 129

Table 3.45: Raw asymmetries of the peaking background components obtained from the fit to the 2018 magnet-down sample.

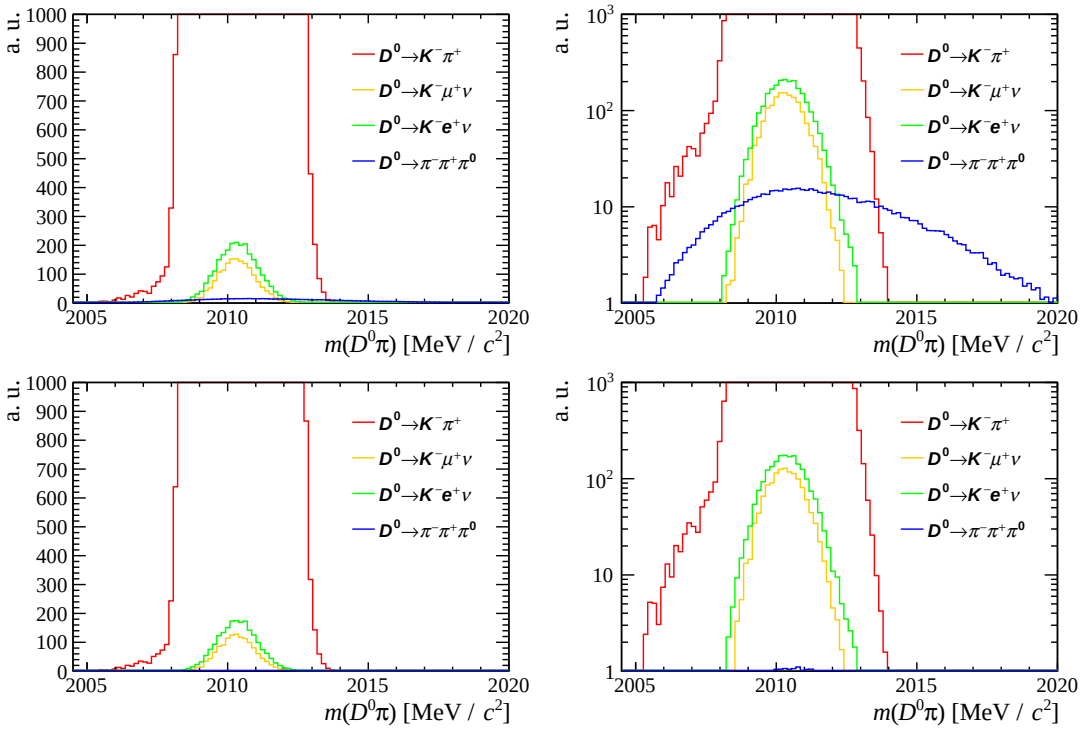

Figure 3.42: Distribution of $m(D^0\pi)$ for the $D^0 \to K^-\pi^+$ mode, for (top) D^+ method and (bottom) D_s^+ method. Signal distribution (in red) is shown for comparison. The plots are shown in log scale on the right.

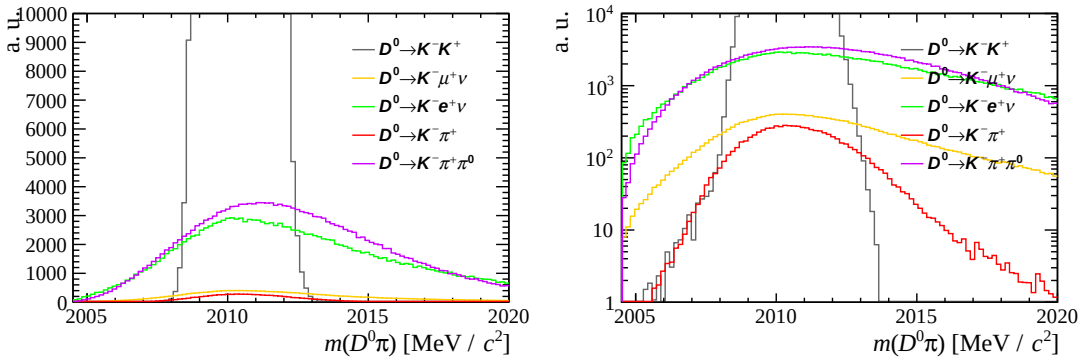

Figure 3.43: Distribution of $m(D^0\pi)$ for the $D^0 \to K^-K^+$ mode. Signal distribution (in grey) is shown for comparison. The plots are shown in log scale on the right.

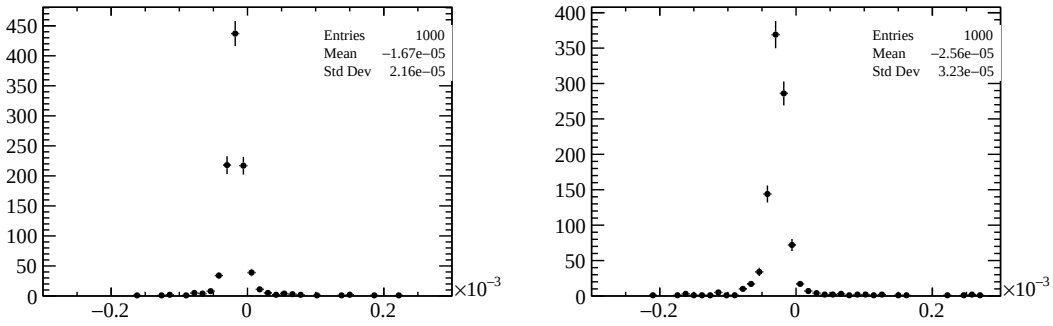

Figure 3.44: Distribution of $\mathcal{A}^{CP}(K^-K^+)_{\text{alt}} - \mathcal{A}^{CP}(K^-K^+)_{\text{base}}$ used to evaluate the systematic uncertainty associated to peaking background for (left) D^+ method and (right) D_s^+ method.

3.9.3 Inaccuracy of the fit model

The mass models described in Section 3.4 are used in the fits to determine the raw asymmetries and describe the data. The fit procedure is validated by looking at the pull distributions between the input value for $\mathcal{A}^{CP}(K^-K^+)$ and the one measured with the nominal fit model in 1000 pseudo-experiments where the events are generated according to the results of the fit to data. The results are summarised in Figure 3.45. The fit models behave correctly, showing no significant bias in the asymmetry and proper estimations of the uncertainties.

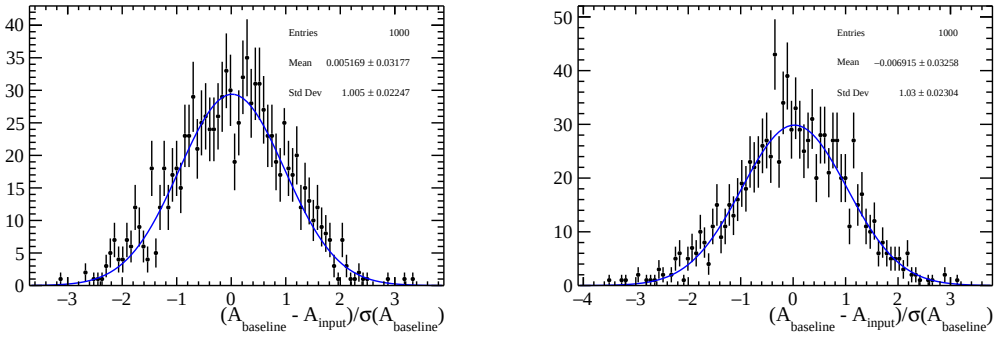

Figure 3.45: Pull distribution between input and measured $\mathcal{A}^{CP}$ asymmetry for 1000 pseudo-experiments generated and fitted with the baseline fit model for the (left) D^+ method and (right) D_s^+ method.

Alternative models, however, provide an equally good description of the data. The systematic uncertainties are evaluated studying the difference between the baseline results and the ones from the alternative fit models with 1000 pseudo-experiments. The procedure consists of generating a pseudo-experiment according to the results of the fit to data, and fitting this sample both with the nominal and alternative fit models. In the generation of the pseudo-experiment, kinematic weights are randomly extracted from their distributions (Figures 3.13 and 3.18) and applied to the events in order to correctly reproduce the measurement. This procedure is applied to each data-taking period sub-sample, and the resulting weighted average $\mathcal{A}^{CP}(K^-K^+)$ is considered. The difference between the value measured with the baseline ($\mathcal{A}^{CP}_{\rm base}$) and the alternative ($\mathcal{A}^{CP}_{\rm alt}$) model for each of the pseudo-experiments is used to assess a systematic uncertainty. The alternative models used are:

- **bkg$^{\pm}$**; background parameters free to float between positive and negative distributions.
- **lessGauss**; the signal is described with one fewer Gaussian function than the baseline.

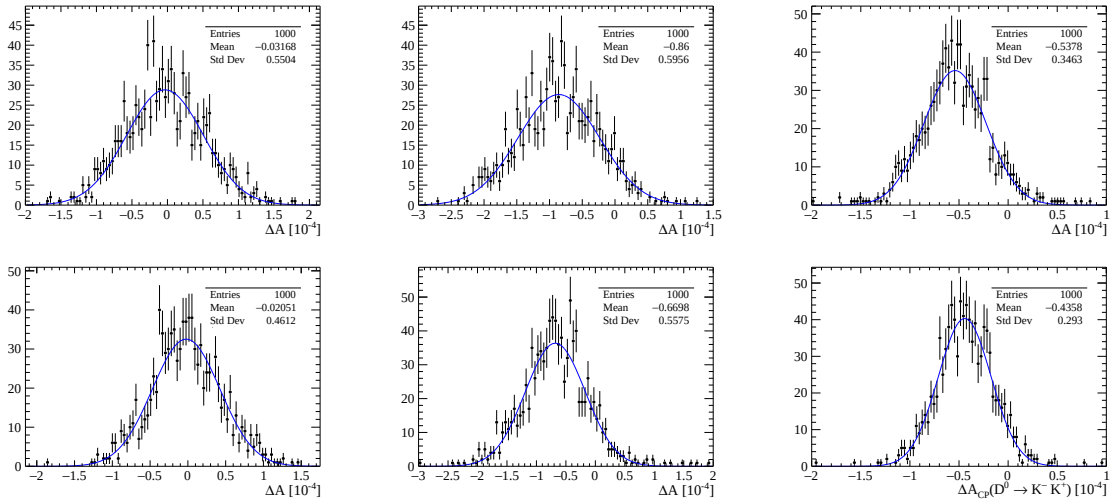

Figure 3.46: Distribution of $\mathcal{A}^{CP}_{\text{base}} - \mathcal{A}^{CP}_{\text{alt}}$ for 1000 pseudo-experiments when fitting with the (left) bkg$^{\pm}$, (center) lessGauss and (right) BifurGauss alternative model with the (top) D^+ approach and (bottom) D^+_s approach.

- **BifurGauss**; one of the Gaussian function has two parameters to describe the widths.

The distributions of $\mathcal{A}^{CP}_{\text{base}} - \mathcal{A}^{CP}_{\text{alt}}$ for the various fit models are shown in Figure 3.46 for the full Run 2 sample. As one can notice, biases between the fit models exists but they are small compared to the statistical uncertainty of the measurements.
A fit-model-independent approach relying on a simple background subtraction is also considered. It consists in defining signal and background regions in the invariant-mass spectrum as in Table 3.46, and correcting the yield measured in the signal region with the one observed in the background region. A factor scale is applied to this yield, evaluated with an exponential fit to the data in the background region. This approach is independent by any assumption on the fitting models and is based on the only conjecture that the raw asymmetry of the background component is constant over the invariant mass spectrum. The measured $\mathcal{A}^{CP}_{\text{alt}}$ together with the difference with the baseline results obtained from data (Table 3.26) are reported in Table 3.47 for the D^+ and D^+_s methods, where the errors are calculated assuming the maximum possible correlations between the baseline and model-independent results.

Table 3.48 reports the RMS of the $\mathcal{A}^{CP}_{\text{base}} - \mathcal{A}^{CP}_{\text{alt}}$ distributions from pseudo-experiments and the RMS of results of the fit-model-independent test. The maximum deviations are observed in the latter test and are taken as systematic uncertainties, namely $1.1 \cdot 10^{-4}$ and $1.0 \cdot 10^{-4}$ in the D^+ and D^+_s approach, respectively. Their correlation corrisponds to the statistical one observed in data, *i.e.* $\rho_{\text{syst}} = 0.05$.

Decay mode	Mass	Signal window [MeV/c^2]	Background window [MeV/c^2]
$D^0 \to K^-K^+$	$m(D^0\pi)$	$2009.4 - 2011.1$	$2016 - 2019$
$D^0 \to K^-\pi^+$	$m(D^0\pi)$	$2009.4 - 2011.1$	$2016 - 2019$
$D^+ \to K^-\pi^+\pi^+_{trig}$	$m(K^-\pi^+\pi^+)$	$1841.1 - 1896.0$	$1920 - 1935$
$D^+ \to K^0_S\pi^+_{trig}$	$m(K^0_S\pi^+)$	$1845.6 - 1893.1$	$1795 - 1815, 1915 - 1940$
$D^+_s \to \phi\pi^+$	$m(K^-K^+\pi^+)$	$1947.8 - 1988.8$	$2020 - 2045$
$D^+_s \to K^0_S K^+$	$m(K^0_S K^+)$	$1946.6 - 1990.5$	$1900 - 1915, 2020 - 2045$

Table 3.46: Signal and sideband ranges of the invariant mass used for each decay modes. The signal regions corresponds to ± 3 sigmas of the invariant mass resolution model.

$\mathcal{A}^{CP}(K^-K^+)$ method	$\mathcal{A}^{CP}_{\rm alt}$ $[10^{-4}]$	$\mathcal{A}^{CP}_{\rm base} - \mathcal{A}^{CP}_{\rm alt}$ $[10^{-4}]$
D^+	57.8 ± 8.8	1.0 ± 0.5
D^+_s	45.5 ± 6.6	-0.4 ± 0.9

Table 3.47: $\mathcal{A}^{CP}_{\rm alt}$ measured with the fit-model-independent approach together with the difference between the baseline results $\mathcal{A}^{CP}_{\rm base}$ and the latter with the D^+ and D^+_s method, obtained from data.

Fit Model	RMS$(\mathcal{A}^{CP}_{\rm base} - \mathcal{A}^{CP}_{\rm alt})$ $\vert D^+$ $[10^{-4}]$	RMS$(\mathcal{A}^{CP}_{\rm base} - \mathcal{A}^{CP}_{\rm alt})$ $\vert D^+_s$ $[10^{-4}]$
bkg$^\pm$	0.55	0.46
lessGauss	1.05	0.87
BifurGauss	0.64	0.53
Fit-model-independent	1.12	0.98

Table 3.48: RMS of the difference between the baseline results and the ones from the alternative models with the D^+ and D^+_s approach, obtained from MC toys and with the fit-model-independent test.

3.9.4 Residual kinematic differences

The weighting procedure discussed in Section 3.5 may be imperfect and kinematic differences between the various modes entering the determination of the *CP* asymmetries are still present after the weighting. It can be easily shown that the bias ΔA on the difference of raw asymmetries $A(a) - A(b)$ due to the normalized kinematic distributions $D_{a,b}(\vec{p})$ of samples a and b not being the same is

$$\Delta A = \int A_{P,D}(\vec{p}) \; [D_a(\vec{p}) - D_b(\vec{p})] \; d\vec{p}, \tag{3.58}$$

where $A_{P,D}(\vec{p})$ is the variation of the nuisance (production or detection) asymmetry as a function of momentum of the considered particle. Since it is not possible to access separately to A_P and A_D, the total raw asymmetry observed in the highest statistic samples are instead used in Eq. 3.58 to compute the biases on the measured asymmetries.

As an example, Figures 3.47 to 3.50 show the variation of the raw asymmetry of the highest statistic sample as a function of the particle momentum in the magnet-down 2016 sample. The figures also show the difference between the normalised momentum distributions of the weighted samples. Similar results can be observed for different year and magnet polarity configuration. The bias resulting from the imperfect agreement is computed by integrating Eq. 3.58 as a function of the momentum $\vec{p} = (p_x, p_y, p_z)$ of the various particles. The data sample is divided in 5 bins for each dimension and then integrated. The resulting ΔA values for all the relevant particles is reported in Table 3.49. The systematic is computed by summing in quadrature the biases estimated for each individual term. The final systematic uncertainties due to imperfect weighting are $0.8 \cdot 10^{-4}$ in the D^+ method and $0.4 \cdot 10^{-4}$ in the D_s^+ method. Given that the $D^0 \to K^-\pi^+$ decay sample is split in two sub-samples for the D^+ and D_s^+ method, the only contribution to the correlation between the two systematic uncertainties may arise from the $D^0 \to K^-K^+$ sample which is shared between the two methods. Then, considering that the systematic uncertainties due to the imperfect matching of the kinematic distributions in D^{*+} and π^+_{soft} are maximally correlated between the two methods, the correlation between the final systematic uncertainties is below 1% and therefore negligible.

Particle	$\Delta A[10^{-4}]\|D^+$
K^-	0.02 ± 0.02
π^+	0.02 ± 0.01
π^+_{trig}	0.25 ± 0.09
D^+	0.75 ± 0.11
D^{*+}	0.08 ± 0.01
π^+_{soft}	0.06 ± 0.01
Tot.	0.80 ± 0.14

Particle	$\Delta A[10^{-4}]\|D^+_s$
K^-	0.38 ± 0.03
π^+	0.06 ± 0.01
D^+_s	0.08 ± 0.04
D^{*+}	0.03 ± 0.01
π^+_{soft}	0.03 ± 0.02
Tot.	0.39 ± 0.05

Table 3.49: Systematic uncertainties due to the residual kinematic differences for the D^+ and D^+_s approaches.

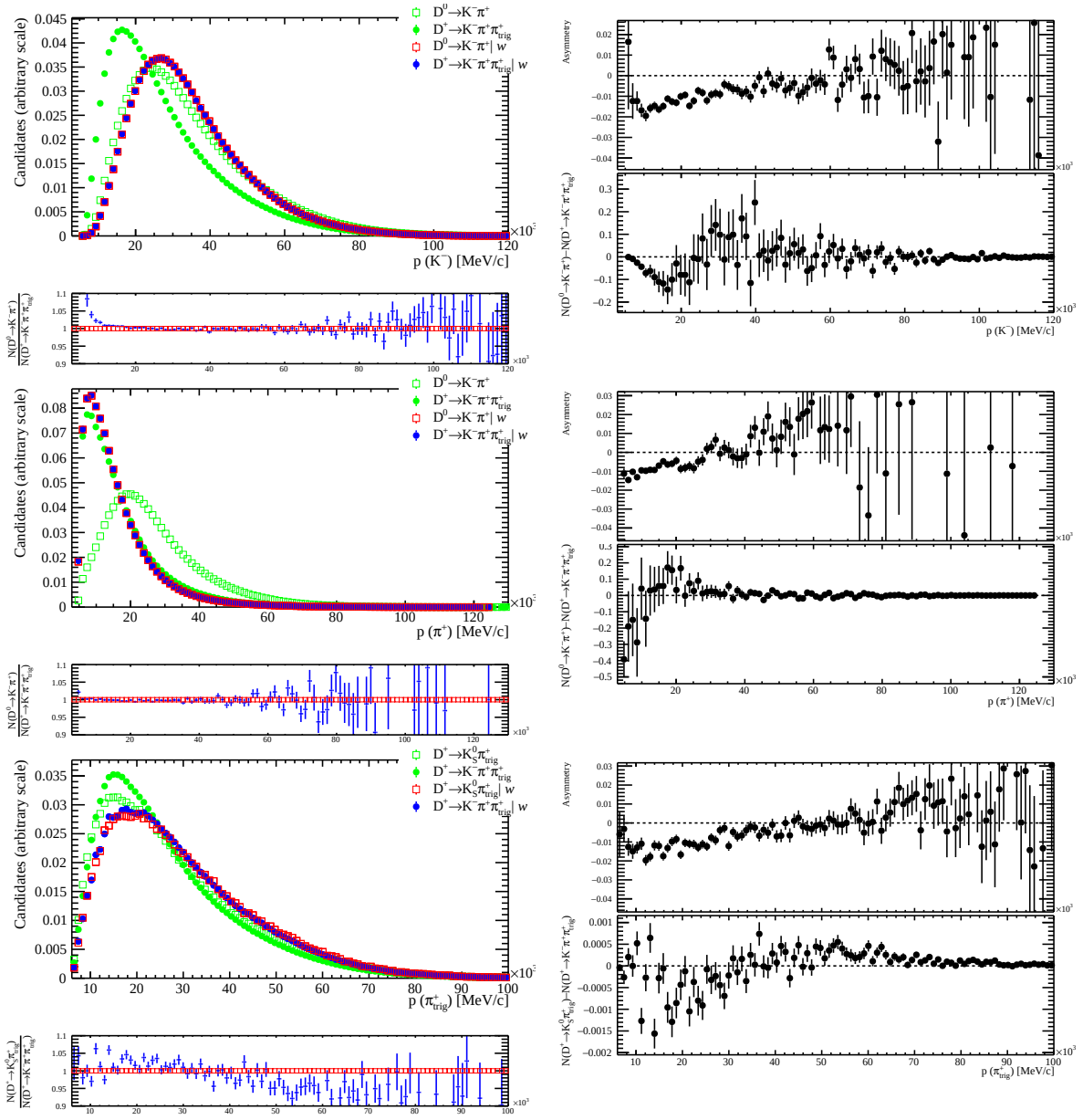

Figure 3.47: (left) Comparison between normalized and background-subtracted momentum distribution of K^-,π^+ and π^+_{trig} candidates from the D^{*+} and D^+ decay samples, before and after the kinematic weighting. (right) Raw asymmetry as a function of the momentum distributions of K^-, π^+ and π^+_{trig} candidates from the $D^+ \to K^-\pi^+\pi^+_{trig}$ decay sample where the bottom plots are the difference between the weighted distributions. Magnet-down 2016 data are shown. Similar results can be observed for different year and magnet polarity configuration.

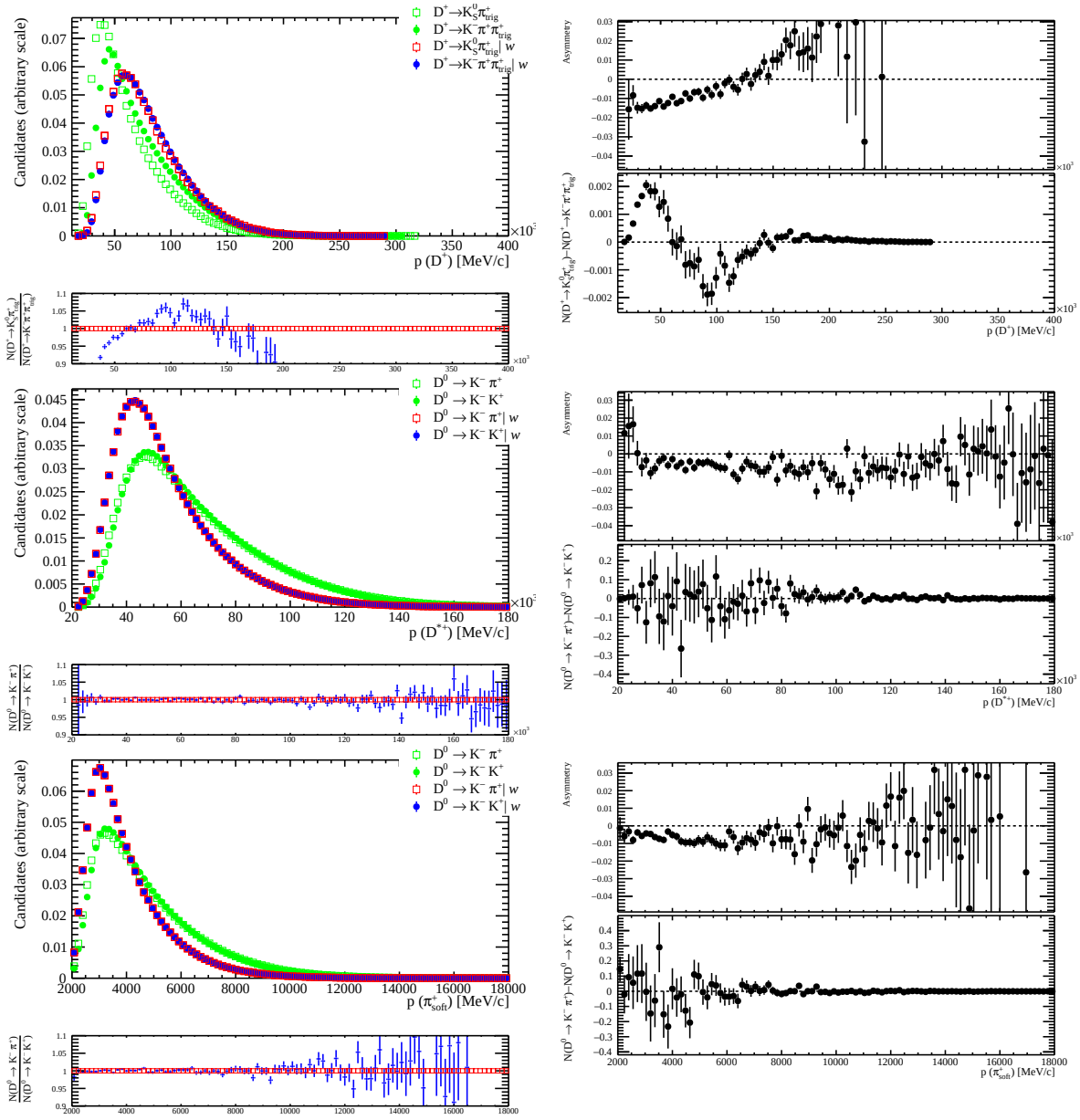

Figure 3.48: (left) Comparison between normalized and background-subtracted momentum distribution of D^+, D^{*+} and π^+_{soft} candidates from the D^{*+} and D^+ decay samples, before and after the kinematic weighting. (right) Raw asymmetry as a function of the momentum distributions of D^+, D^{*+} and π^+_{soft} candidates from the $D^+ \to K^-\pi^+\pi^+_{trig}$ and $D^0 \to K^-\pi^+$ decay samples where the bottom plots are the difference between the weighted distributions. Magnet-down 2016 data are shown. Similar results can be observed for different year and magnet polarity configuration.

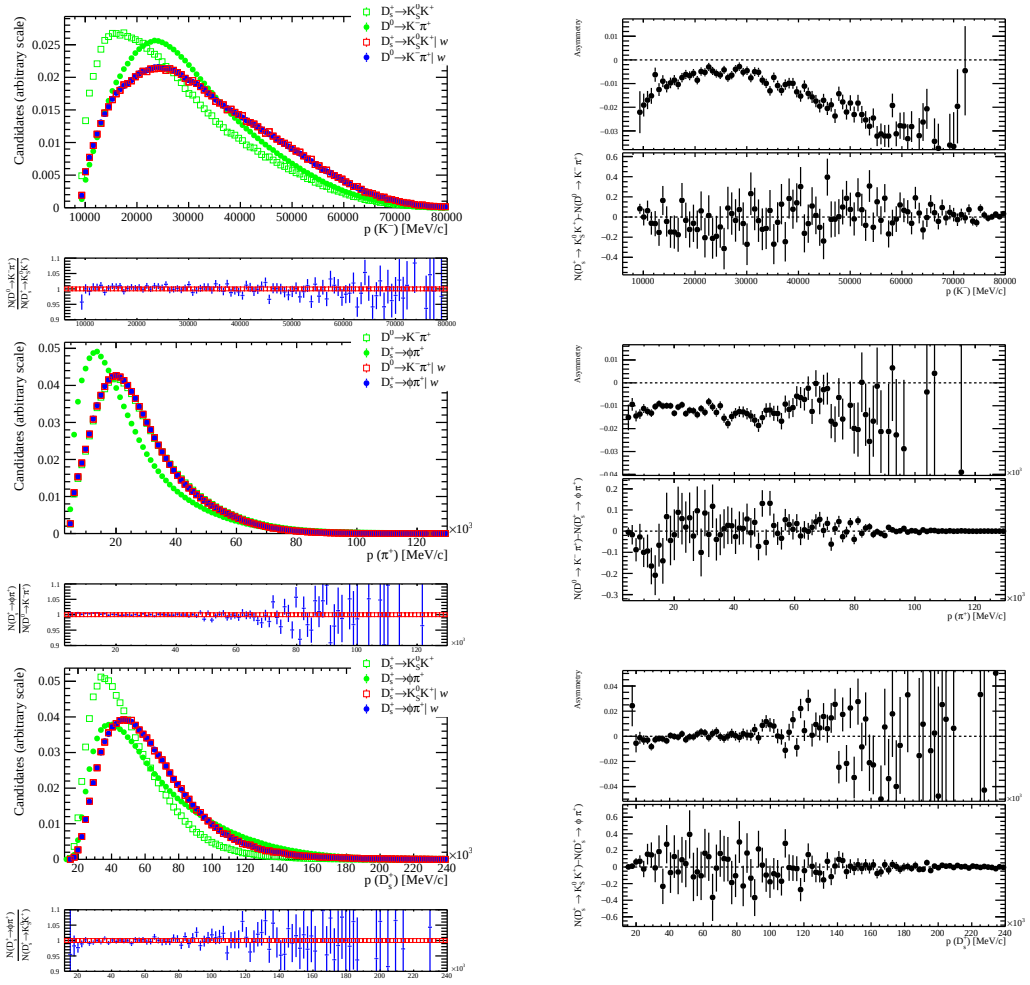

Figure 3.49: (left) Comparison between normalized and background-subtracted momentum distribution of K^-, π^+ and D_s^+ candidates from the D^{*+} and D_s^+ decay samples, before and after the kinematic weighting. (right) Raw asymmetry as a function of the momentum distributions of K^-, π^+ and D_s^+ candidates from the $D^0 \to K^-\pi^+$ and $D_s^+ \to \phi\pi^+$ decay samples where the bottom plots are the difference between the weighted distributions. Magnet-down 2016 data are shown. Similar results can be observed for different year and magnet polarity configuration.

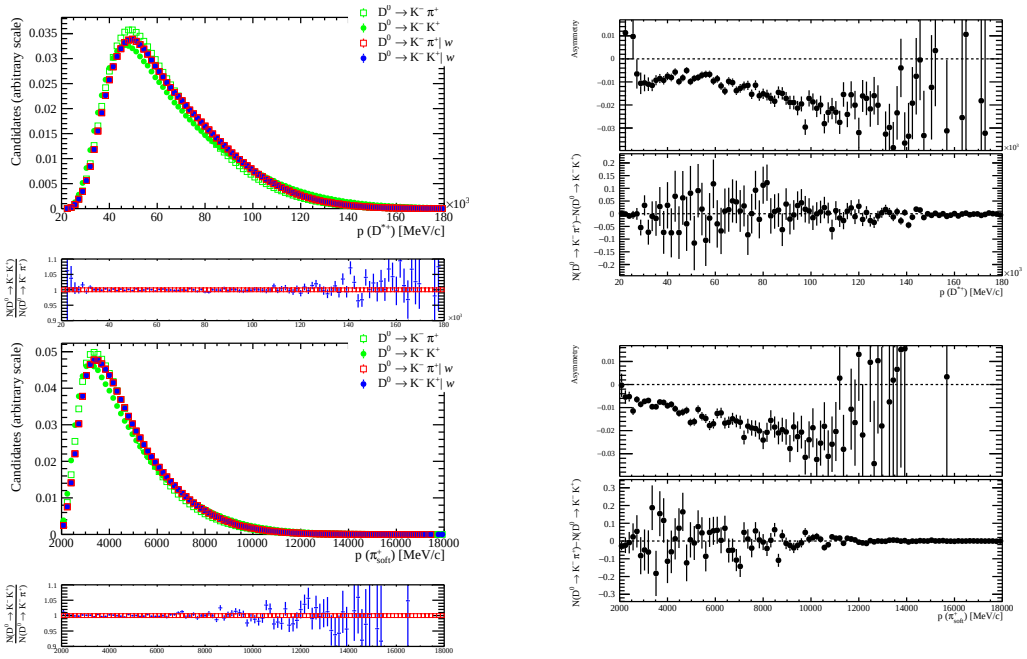

Figure 3.50: (left) Comparison between normalized and background-subtracted momentum distribution of D^{*+} and π^+_{soft} candidates from the D^{*+} ecay samples, before and after the kinematic weighting. (right) Raw asymmetry as a function of the momentum distributions of D^{*+} and π^+_{soft} candidates from the $D^0 \to K^-\pi^+$ decay samples where the bottom plots are the difference between the weighted distributions. Magnet-down 2016 data are shown. Similar results can be observed for different year and magnet polarity configuration.

3.9.5 Charged kaon asymmetry in $D_s^+ \to K^-K^+\pi^+$ decay

The ϕ detection asymmetry in the $D_s^+ \to \phi\pi^+$ decay channel is zero by definition due to the symmetric final state. However, the non-resonant component of the $D_s^+ \to K^-K^+\pi^+$ decay may induce a kaon detection asymmetry due to the different kinematic of the K^+ (K^-) decaying from D_s^+ (D_s^-), referred as same-charge kaon, and the K^+ (K^-) decaying from D_s^- (D_s^+), referred as opposite-charge kaon, as seen in Figure 3.51. This asymmetry does not cancel with the method described in the previous sections and it needs to be quoted. Since the detection asymmetry of a charged kaon depends mainly on its momentum, it is possible to get an estimation from

$$A_{\rm det}(K^-K^+) = \int dp_1 dp_2 \; [A_K(p_1) - A_K(p_2)] \; D(p_1, p_2), \tag{3.59}$$

where $A_K = A_{\rm det}(K^+) = -A_{\rm det}(K^-)$, the labels 1 and 2 indicate the kaon with same and opposite charge as the D_s^+ candidate, respectively, and $D(p_1, p_2)$ their 2-dimensional momentum distribution.

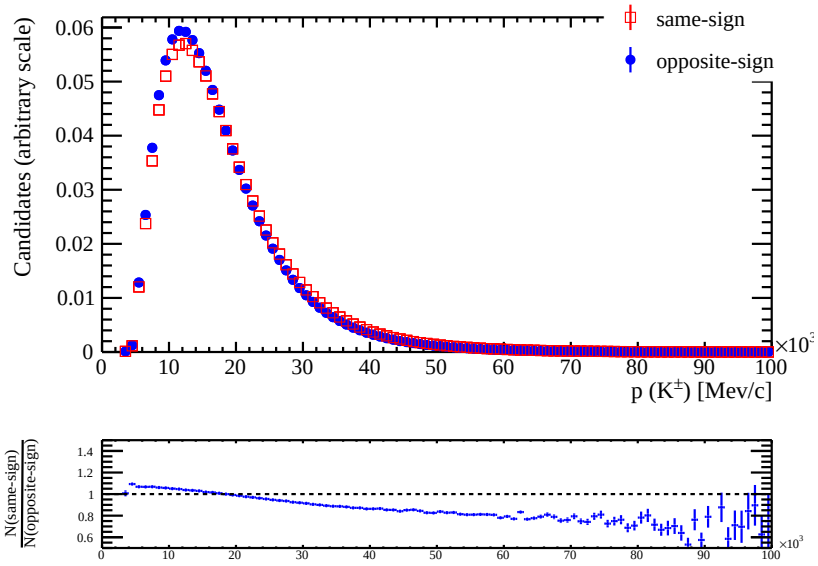

Figure 3.51: Comparison between normalized and background-subtracted momentum distributions of kaons with (red) same and (blue) opposite charge as the D_s^+ candidate for $D_s^+ \to \phi\pi^+$ weighted sample. The bottom panel shows the ratio between the distributions of the same-charge and opposite-charge kaons.

The value of $A_{\rm det}(K^-K^+)$ is quantified from Eq. 3.59 by using as input the charged-kaon detection asymmetry as a function of the kaon momentum as determined from a large simulated sample of pGun $D^+ \to K^-\pi^+\pi^+$ decays (Figure 3.52). The resulting value is $A_{\rm det}(K^-K^+) = (-0.96 \pm 0.19) \cdot 10^{-4}$ and its RMS, corresponding to $1.0 \cdot 10^{-4}$,

is assigned as systematic uncertainty for the neglected differences between K^- and K^+ kinematics.

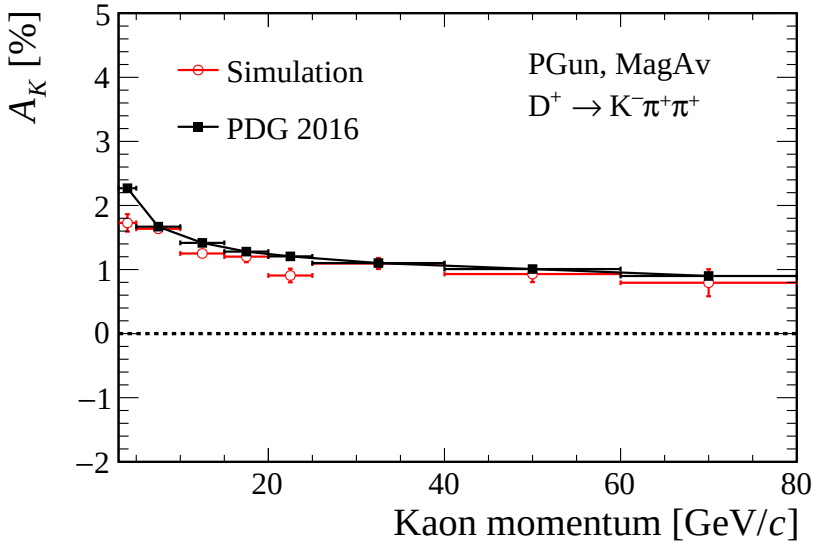

Figure 3.52: Detection asymmetry of a charged kaon (A_K) as a function of its momentum, as determined from simulated $D^+ \to K^-\pi^+\pi^+$ decays, in comparison with the prediction from the tabulated PDG cross-sections. The red curve is used in the computation of the systematic uncertainty. Reproduced from Ref. [121].

3.10 Consistency checks

Consistency checks are performed in the following to rule out possible systematic uncertainties not accounted for in the analysis. The checks are performed using the entire data sample of $D^0 \to K^-\pi^+$ decays for D^+ and the D_s^+ methods. This enhance the precision of the tests as each of them is independent between the two methods. For this reason as reference the baseline results have been recalculated. They are

$$\mathcal{A}^{CP}(K^-K^+)^{\text{blind}}|D^+ = (57.5 \pm 8.7) \times 10^{-4}, \tag{3.60}$$
$$\mathcal{A}^{CP}(K^-K^+)^{\text{blind}}|D_s^+ = (44.3 \pm 6.6) \times 10^{-4}, \tag{3.61}$$

where only the statistical uncertainty is considered.

3.10.1 $\mathcal{A}^{CP}(K^-K^+)$ dependencies

$\mathcal{A}^{CP}(K^-K^+)$ is an observable which must not depend on the running conditions, kinematics and topological variables of the involved decays. Dependencies are inspected dividing the data set into statistically independent subsets according to the data-taking run block (Figure 3.53), Hlt1 TCK (Figure 3.54), the $D^0 \to K^-K^+$ Hlt1 trigger categories (Figure 3.55), the D^0 decay-time (Figure 3.56), the D^0 transverse momentum (Figure 3.57), the D^0 pseudo-rapidity (Figure 3.58), the IPχ^2 of the control channel daughters (Figure 3.59), the $K^0_{\rm S}$ decay-time (Figure 3.60) and the $K^0_{\rm S}$ pseudo-rapidity (Figure 3.61). Samples that do not contain the examined variable are randomly split. All the test are performed using the default sets of kinematic weights excepts when splitting the samples according to the D^0 $p_{\rm T}$, the D^0 η, the IPχ^2 of the control channel daughters and the $K^0_{\rm S}$ η where subsample-specific weights are computed. In order to calculate the average between the results, the maximum correlation is taken into account between the measurements from non-independent data samples. The observed variations in results are consistent with statistical fluctuations; the resulting p value is distributed uniformly between 0 and 1 as shown in Figure 3.62.

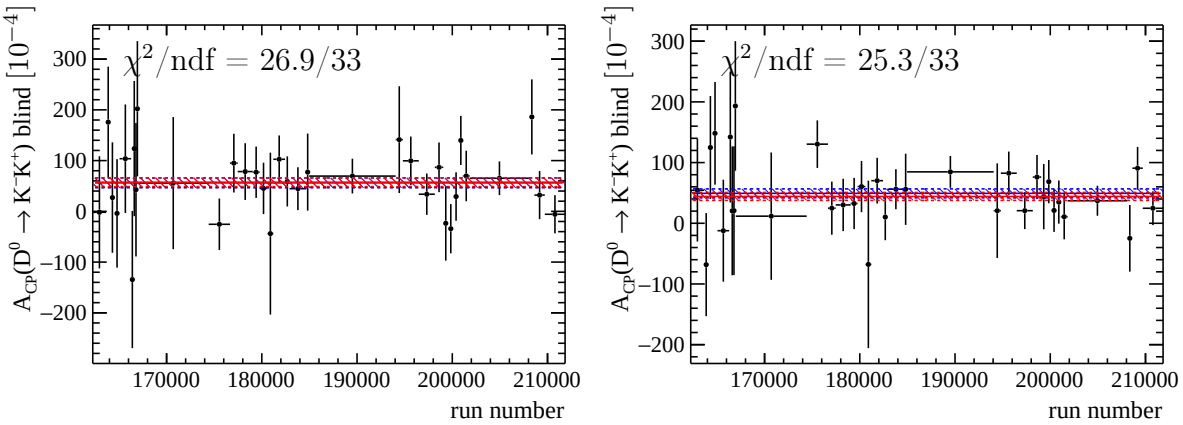

Figure 3.53: Comparison between blind $\mathcal{A}^{CP}(K^-K^+)$ results in the (left) D^+ and (right) D_s^+ method in different run blocks. The uncertainties are statistical only. The average between the results from the subsamples (blue band) is consistent with the result obtained from the integrated sample (red band).

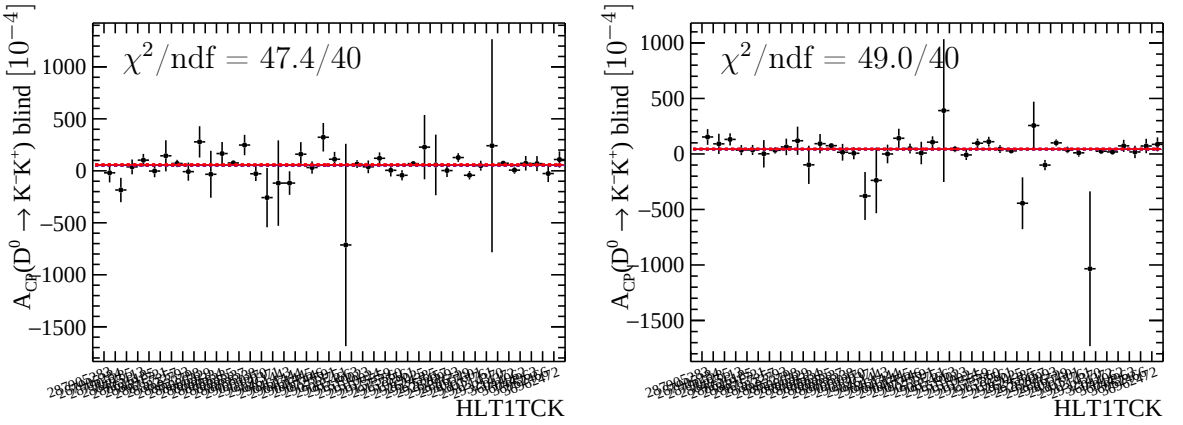

Figure 3.54: Comparison between blind $\mathcal{A}^{CP}(K^-K^+)$ results in the (left) D^+ and (right) D_s^+ method in different Hlt1 TCKs. The uncertainties are statistical only. The average between the results from the subsamples (blue band) is consistent with the result obtained from the integrated sample (red band).

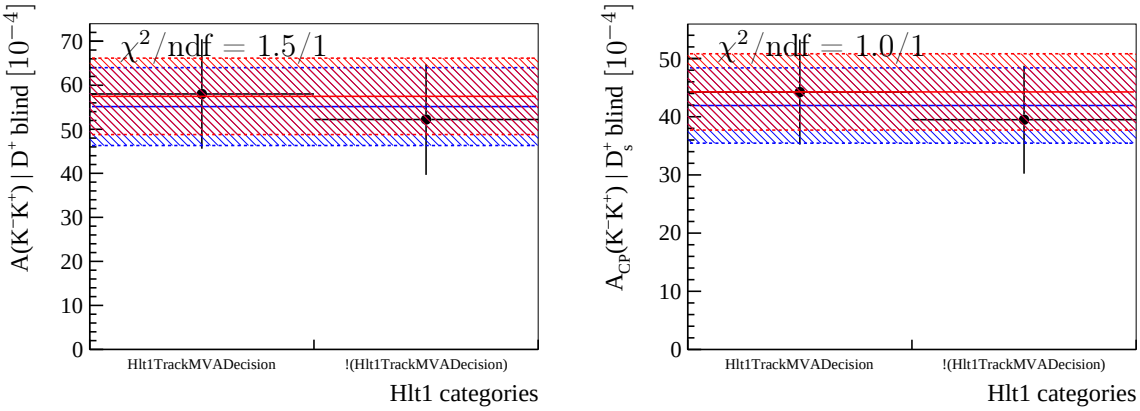

Figure 3.55: Comparison between blind $\mathcal{A}^{CP}(K^-K^+)$ results in the (left) D^+ and (right) D_s^+ method in different $D^0 \to K^-K^+$ Hlt1 categories. The uncertainties are statistical only. The average between the results from the subsamples (blue band) is consistent with the result obtained from the integrated sample (red band).

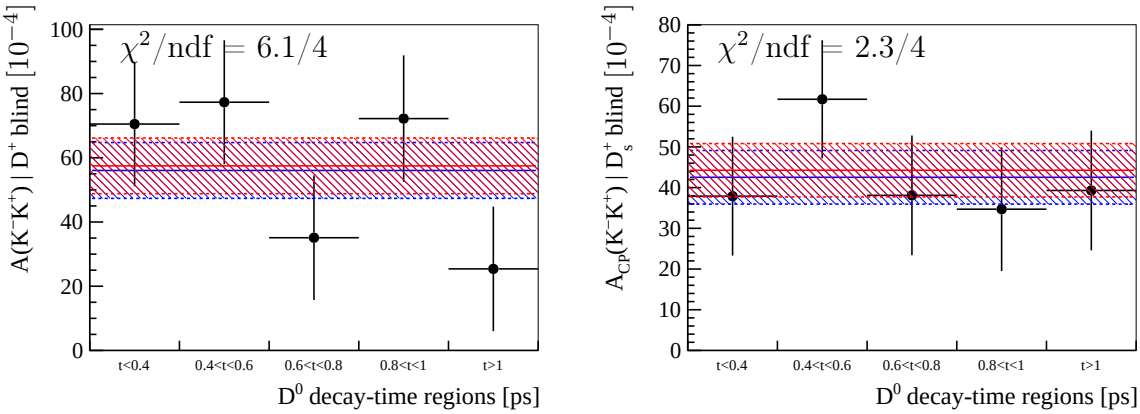

Figure 3.56: Comparison between blind $\mathcal{A}^{CP}(K^-K^+)$ results in the (left) D^+ and (right) D_s^+ method in different D^0 decay-time regions. The uncertainties are statistical only. The average between the results from the subsamples (blue band) is consistent with the result obtained from the integrated sample (red band).

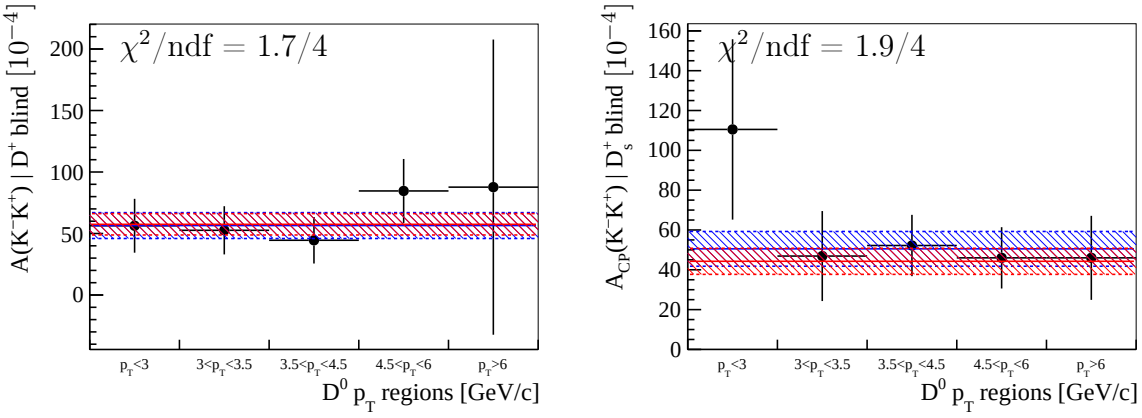

Figure 3.57: Comparison between blind $\mathcal{A}^{CP}(K^-K^+)$ results in the (left) D^+ and (right) D_s^+ method in different D^0 p_{T} regions. The uncertainties are statistical only. The average between the results from the subsamples (blue band) is consistent with the result obtained from the integrated sample (red band).

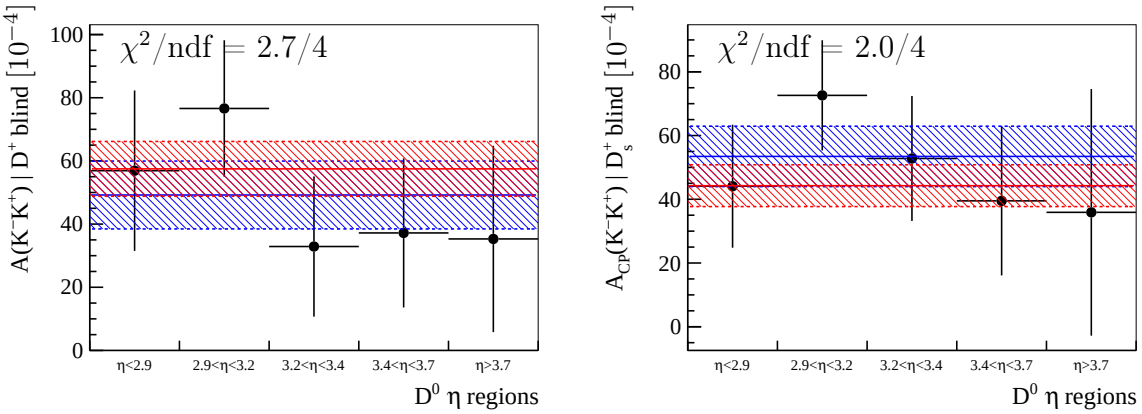

Figure 3.58: Comparison between blind $\mathcal{A}^{CP}(K^-K^+)$ results in the (left) D^+ and (right) D_s^+ method in different D^0 η regions. The uncertainties are statistical only. The average between the results from the subsamples (blue band) is consistent with the result obtained from the integrated sample (red band).

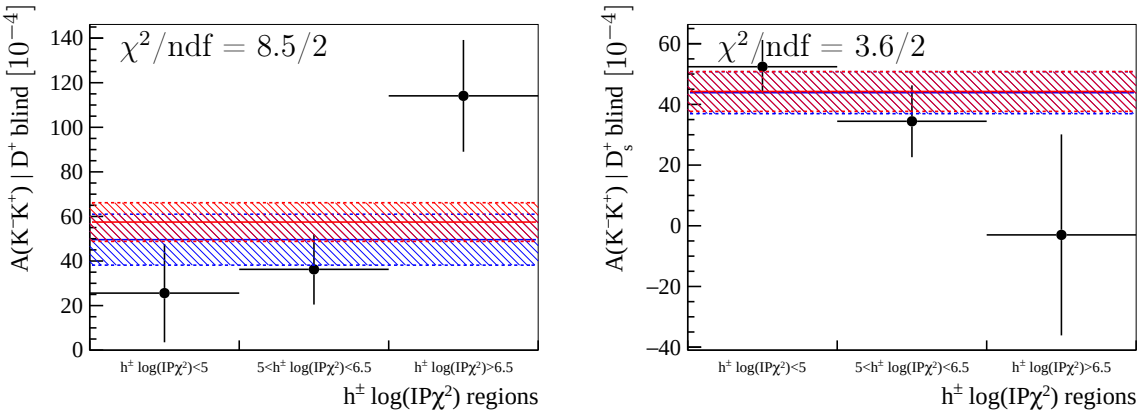

Figure 3.59: Comparison between blind $\mathcal{A}^{CP}(K^-K^+)$ results in the (left) D^+ and (right) D_s^+ method in different IPχ^2 regions of the daughters K^-, π^+ and π^+_{trig} of the control channels in the D^+ method and of the daughters K^- and π^+ of the control channels in the D_s^+ method. The uncertainties are statistical only. The average between the results from the subsamples (blue band) is consistent with the result obtained from the integrated sample (red band).

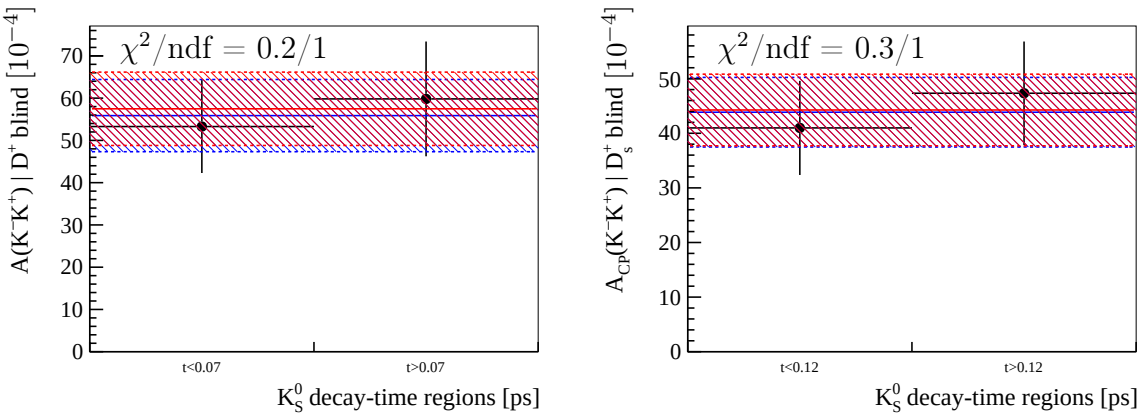

Figure 3.60: Comparison between blind $\mathcal{A}^{CP}(K^-K^+)$ results in the (left) D^+ and (right) D_s^+ method in different K^0_S decay-time regions. The uncertainties are statistical only. The average between the results from the subsamples (blue band) is consistent with the result obtained from the integrated sample (red band).

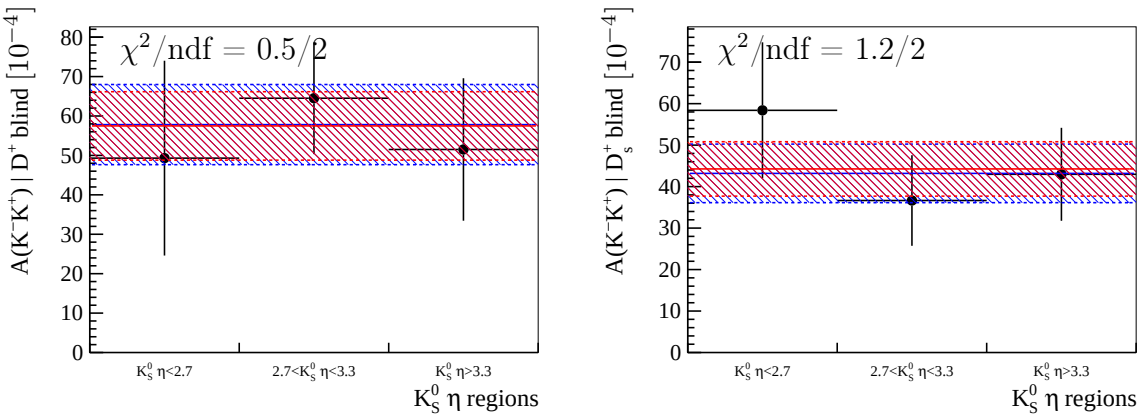

Figure 3.61: Comparison between blind $\mathcal{A}^{CP}(K^-K^+)$ results in the (left) D^+ and (right) D_s^+ method in different K^0_S η regions. The uncertainties are statistical only. The average between the results from the subsamples (blue band) is consistent with the result obtained from the integrated sample (red band).

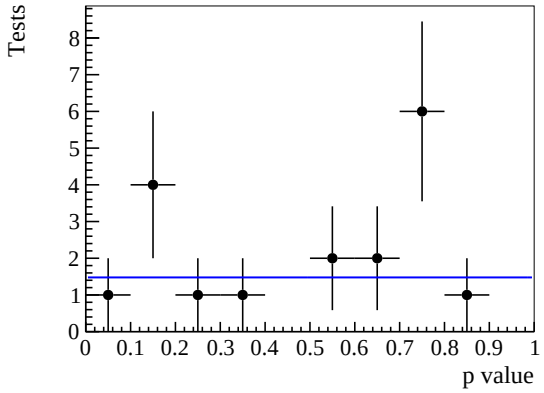

Figure 3.62: Distribution of the p values resulting from the consistency checks on $\mathcal{A}^{CP}(K^-K^+)$ measured in subsamples of the data. The blue line represents the expected uniform distribution.

3.10.2 $\mathcal{A}^{CP}(K^-K^+)$ and PID selection

To check any possible bias due to a not perfect cancellation of PID asymmetries[10], the effect of alternative PID selection criteria is investigated. Requirements $\mathrm{DLL}_{K\pi}(\pi) < x$ AND $\mathrm{DLL}_{K\pi}(K) > y$ with $x = \{-5, 0, 5\}$ and $y = \{5, 10, 15\}$ are applied to the daughters K^-, π^+ and π^+_{trig} of the control channels in the D^+ method and of the daughters K^- and π^+ of the control channels in the D^+_s method. The various requirements x, y as well as the results obtained, the correlation with the results in Eqs. 3.60 and 3.61 and the resulting compatibility in terms of sigmas are reported in Tables 3.50 and 3.51 for the D^+ and the D^+_s method, respectively. All the measurements obtained in the sub-samples are found to be compatible, indicating a good cancellation of the PID asymmetries between the various channels.

$\mathrm{DLL}_{K\pi}(\pi) < x$ AND $\mathrm{DLL}_{K\pi}(K) > y$	$\mathcal{A}^{CP}(K^-K^+)$ $^{\text{blind}}(D^+)$ $[10^{-4}]$	$\rho^{\text{stat}}_{\mathcal{A}^{CP}}$	compatibility
$x = 5, y = 5$	55.1 $\pm$7.7	0.88	0.58
$x = 5, y = 10$	55.9 $\pm$7.8	0.87	0.37
$x = 5, y = 15$	56.8 $\pm$7.9	0.87	0.16
$x = 0, y = 5$	53.7 $\pm$7.9	0.89	0.95
$x = 0, y = 10$	54.9 $\pm$7.9	0.89	0.65
$x = 0, y = 15$	57 $\pm$7.8	0.87	0.11
$x = -5, y = 5$	52.2 $\pm$8.2	0.92	1.55
$x = -5, y = 10$	56.3 $\pm$7.8	0.88	0.29
$x = -5, y = 15$	57.3 $\pm$8.2	0.91	0.05

Table 3.50: Measurements of $\mathcal{A}^{CP}(K^-K^+)$ with different PID requirements on the daughters K^-, π^+ and π^+_{trig} of the control channels in the D^+ method. In the last two columns are reported the correlation coefficient with the results with the baseline selection, and the compatibility in terms of sigmas.

[10]The PID asymmetry of a particle is formally included in its detection asymmetry and is defined as

$$A_{\mathrm{PID}}(h^+) \equiv \frac{\varepsilon_{\mathrm{PID}}(h^+) - \varepsilon_{\mathrm{PID}}(h^-)}{\varepsilon_{\mathrm{PID}}(h^+) + \varepsilon_{\mathrm{PID}}(h^-)}, \tag{3.62}$$

with $\varepsilon_{\mathrm{PID}}(h^+)$ ($\varepsilon_{\mathrm{PID}}(h^-)$) being the efficiency of the PID requirements applied to the positively (negatively) charged hadron h.

$\mathrm{DLL}_{K\pi}(\pi) < x$ AND $\mathrm{DLL}_{K\pi}(K) > y$	$\mathcal{A}^{CP}(K^-K^+)$ $^{\text{blind}}(D_s^+)$ $[10^{-4}]$	$\rho^{\text{stat}}_{\mathcal{A}^{CP}}$	compatibility
$x = 5, y = 5$	43.1 ±6.2	0.78	0.27
$x = 5, y = 10$	43.8 ±6.5	0.87	0.14
$x = 5, y = 15$	43.2 ±6.7	0.97	0.65
$x = 0, y = 5$	42.9 ±6.1	0.8	0.34
$x = 0, y = 10$	47.5 ±6.3	0.81	0.81
$x = 0, y = 15$	44.2 ±6.7	0.97	0.04
$x = -5, y = 5$	44.2 ±6	0.81	0.02
$x = -5, y = 10$	44.6 ±6.3	0.89	0.11
$x = -5, y = 15$	44.9 ±6.6	0.98	0.48

Table 3.51: Measurements of $\mathcal{A}^{CP}(K^-K^+)$ with different PID requirements on the daughters K^- and π^+ of the control channels in the D_s^+ method. In the last two columns are reported the correlation coefficient with the results with the baseline selection, and the compatibility in terms of sigmas.

3.10.3 $\mathcal{A}^{CP}(K^-K^+)$ and Hlt1 trigger

Tests presented in this section aim at checking a possible bias on $\mathcal{A}^{CP}(K^-K^+)$ due to non-factorization of the Hlt1 trigger asymmetries[11] in the D^+ method (see Table 3.1).

$\mathcal{A}^{CP}(K^-K^+)$ with different Hlt1 requirements

The measurement of $\mathcal{A}^{CP}(K^-K^+)$ has been repeated for both the D^+ and D_s^+ methods with different Hlt1 selections with respect to those in Tables 3.1 and 3.2 to check the the cancellation of the Hlt1 trigger asymmetries between the $D^+ \to K^-\pi^+\pi^+_{trig}$ and $D^0 \to K^-\pi^+$ decays. The alternative Hlt1 requirements are reported in Tables 3.52 and 3.53 and the results are

$$\mathcal{A}^{CP}(K^-K^+)^{\text{blind}}|D^+ = [50.16 \pm 12.05] \cdot 10^{-4}, \tag{3.64}$$

$$\mathcal{A}^{CP}(K^-K^+)^{\text{blind}}|D_s^+ = [44.60 \pm 6.68] \cdot 10^{-4}. \tag{3.65}$$

It is worth to underline that the comparison, as reported in the introduction of Section 3.10, has to be done with Eq. 3.60 and Eq. 3.61. In the case of the D^+ method, the degradation in precision is relevant as the alternative trigger requirements increase the uncertainty from $8.7 \cdot 10^{-4}$ to $12.0 \cdot 10^{-4}$ and it is possible to exclude only a large effect. Conversely, in the case of the D_s^+ method, the test is more powerful, as it is possible to check effect of the factorization at the level of $1.26 \cdot 10^{-4}$, corresponding to the square root of the squared difference between the uncertainties of the baseline and alternative measurements. The difference between the two D_s^+ results is $0.34 \cdot 10^{-4}$, indicating no evidence of problem with trigger effects. In summary, the compatibility with the baseline results is 0.9 and 0.2 standard deviations for D^+ and D_s^+ methods, respectively.

Test using the $D^+ \to K^-\pi^+\pi^+_{trig}$ and $D^0 \to K^-\pi^+$ decays

The test here presented consists in dividing the $D^+ \to K^-\pi^+\pi^+_{trig}$ and the $D^0 \to K^-\pi^+$ samples in three subsamples (A, B, C), where different Hlt1 requirements have been applied, namely `Hlt1TrackMVA_TOS` on the kaon (sample A), `Hlt1TrackMVA_TOS` on the pion (sample B) and `Hlt1TrackMVA_TOS` on the kaon and pion (sample C). In the $D^+ \to K^-\pi^+\pi^+_{trig}$ sample the requirement `Hlt1TrackMVA_TOS` on the π^+_{trig} is always applied. The raw asymmetries measured in each samples after the weighting procedure are

[11] The trigger asymmetry of a particle is formally included in its detection asymmetry and is defined as

$$A_{\text{trig}}(h^+) \equiv \frac{\varepsilon_{\text{trig}}(h^+) - \varepsilon_{\text{trig}}(h^-)}{\varepsilon_{\text{trig}}(h^+) + \varepsilon_{\text{trig}}(h^-)}, \tag{3.63}$$

with $\varepsilon_{\text{trig}}(h^+)$ ($\varepsilon_{\text{trig}}(h^-)$) being the efficiency of the trigger requirements applied to the positively (negatively) charged hadron h.

Decay	Hlt1 requirement
$D^0 \to K^-K^+$	D^0 Hlt1 two/single-track TOS
$D^0 \to K^-\pi^+$	K^- Hlt1 single-track TOS AND π^+ Hlt1 single-track TOS
$D^+ \to K^-\pi^+\pi^+_{trig}$	π^+_{trig} Hlt1 single-track TOS AND K^- Hlt1 single-track TOS AND π^+ Hlt1 single-track TOS
$D^+ \to K^0_S\pi^+_{trig}$	π^+_{trig} Hlt1 single-track TOS

Table 3.52: Alternative Hlt1 requirements for the D^+ method. Single track corresponds to the Hlt1TrackMVA line, two track corresponds to the Hlt1TwoTrackMVA line.

Decay	Hlt1 requirement
$D^0 \to K^-K^+$	D^0 Hlt1 two/single-track TOS
$D^0 \to K^-\pi^+$	K^- Hlt1 single-track TOS AND π^+ Hlt1 single-track TOS
$D^+_s \to K^-K^+\pi^+$	π^+ Hlt1 single-track TOS
$D^+_s \to K^0_S K^+$	K^+ Hlt1 single-track TOS

Table 3.53: Alternative Hlt1 requirements for the D^+_s method. Single track corresponds to the Hlt1TrackMVA line, two track corresponds to the Hlt1TwoTrackMVA line.

reported in Tables 3.54 and 3.55 for $D^+ \to K^-\pi^+\pi^+_{trig}$ and $D^0 \to K^-\pi^+$ decays, respectively, where correlation coefficient between the various subsamples are also indicated. The various raw asymmetries show differences below $4 \cdot 10^{-4}$, indicating that when two Hlt1 requirements are present, as in the sample C, the raw asymmetries are different from the sample A and B, where only one Hlt1 trigger asymmetry is present. Given the different trigger requirements, it is worth underlining that those quantities are not expected to be precisely zero. This corresponds to the following condition $A_{\rm trig}(K^-\pi^+) \neq A_{\rm trig}(K^-)$ and $A_{\rm trig}(K^-\pi^+) \neq A_{\rm trig}(\pi^+)$, where $A_{\rm trig}(K^-\pi^+) = A_{\rm trig}(K^-) + A_{\rm trig}(\pi^+)$, given the small values of the asymmetries. However, to check cancellation mechanism in the baseline analysis, it is useful to introduce the measurement of the quantity $\Delta A = A(D^+ \to K^-\pi^+\pi^+_{trig}) - A(D^0 \to K^-\pi^+)$. This evaluation is performed in each pair of subsamples with the same trigger selection. All the subsamples are weighted to have identical kinematic distributions of K^- and π^+ between A, B and C samples and between the $D^+ \to K^-\pi^+\pi^+_{trig}$ and $D^0 \to K^-\pi^+$ decay samples. Then, it is checked if ΔA is the same between the various measurements. The value of ΔA corresponds to the sum of the following asymmetries, $A_{\rm det}(\pi^+_{trig}) - A_{\rm det}(\pi^+_{soft}) + A_{\rm prod}(D^+) - A_{\rm prod}(D^{*+})$ where, given that the A, B and C samples have different combination of trigger asym-

metries, with potential different correlations, any effect induced by the non-factorization would result in differences between the ΔA measurements. Measurement of ΔA are reported in Table 3.56. It is possible to check the effects of different trigger combinations calculating the differences $\Delta A(X) - \Delta A(Y)$, where $X, Y = A, B, C$. For example, $\Delta A(A)$ relies on the cancellation of the $A_{\text{trig}-3-\text{body}}(K^-) - A_{\text{trig}-2-\text{body}}(K^-)$ checking a possible correlation effects between the K^- and π^+_{trig} in the three body decays, *i.e.* $\epsilon_{\text{trig}}(K^-, \pi^+_{trig}) \neq \epsilon_{\text{trig}}(K^-) \cdot \epsilon_{\text{trig}}(\pi^+_{trig})$. The same applies to the other combination. The values of differences between the various ΔA are

$$\Delta A(A) - \Delta A(B) = [-0.67 \pm 1.70] \cdot 10^{-4}, \tag{3.66}$$
$$\Delta A(C) - \Delta A(B) = [-2.91 \pm 1.37] \cdot 10^{-4}, \tag{3.67}$$
$$\Delta A(A) - \Delta A(C) = [2.24 \pm 1.56] \cdot 10^{-4}, \tag{3.68}$$

while compatibility in terms of standard deviations are reported in the following table.

	$\Delta A(A)$	$\Delta A(B)$	$\Delta A(C)$
$\Delta A(A)$		0.39	1.44
$\Delta A(B)$			2.12
$\Delta A(C)$			

Given the reweighing procedure, all the differences must be equal to zero, if the triggers efficiencies factorize. The measurements of the various ΔA are found to be compatible between each others by less than 2.1 standard deviations, without showing any effects at the precision level of $1.5 \cdot 10^{-4}$.

$D^+ \to K^-\pi^+\pi^+_{trig}$		
$A(A)^{\text{blind}}[10^{-4}]$	$A(B)^{\text{blind}}[10^{-4}]$	$A(C)^{\text{blind}}[10^{-4}]$
-36.37 ± 1.53	-33.56 ± 1.62	-39.12 ± 1.86

Table 3.54: Results of the raw asymmetries in the $D^+ \to K^-\pi^+\pi^+_{trig}$ sample after the equalization of K^- and π^+ kinematics in the different subsamples. Correlation between the measurements are found to be $\rho_{AB} = 0.70$, $\rho_{AC} = 0.81$ and $\rho_{BC} = 0.83$.

Test using the $D^+_s \to \phi\pi^+$ decays

An additional null-test is performed with the $D^+_s \to \phi\pi^+$ decays. The data sample is divided in four subsamples (A, B, C, D), where different Hlt1 requirements have been applied, namely `Hlt1TrackMVA_TOS` on the same-sign kaon K^+ with respect to the π^+ (sample A), `Hlt1TrackMVA_TOS` on the K^+ and π^+ (sample B), `Hlt1TrackMVA_TOS` on

$D^0 \to K^-\pi^+$		
$A(A)^{\text{blind}}[10^{-4}]$	$A(B)^{\text{blind}}[10^{-4}]$	$A(C)^{\text{blind}}[10^{-4}]$
-196.03 ± 1.28	-193.89 ± 1.45	-196.54 ± 1.69

Table 3.55: Results of the raw asymmetries in the $D^0 \to K^-\pi^+$ sample after the equalization of K^- and π^+ kinematics in the different subsamples. Correlation between the measurements are found to be $\rho_{AB} = 0.63$, $\rho_{AC} = 0.75$ and $\rho_{BC} = 0.85$.

$\Delta A[10^{-4}]$		
A	B	C
159.66 ± 1.99	160.33 ± 2.18	157.42 ± 2.52

Table 3.56: Results of $A(D^+ \to K^-\pi^+\pi^+_{trig}) - A(D^0 \to K^-\pi^+)$ in the different set of subsamples.

the opposite-sign kaon K^- with respect to the π^+ (sample C), and `Hlt1TrackMVA_TOS` on the K^- and π^+ (sample D). After the trigger requirements the four data samples show different kinematic distributions. For this reason, a three-dimensional kinematic weighing in $(p_{\text{T}}, \eta, \phi)$ of each track is used, where the weighing variables of the K^+, the K^- and the π^+ of the sample A, B, C and D are matched between each others. To better understand the sign of the asymmetries involved in the various subsamples, it is worth to remind the definition of the raw asymmetry

$$A = \frac{N(D_s^+) - N(D_s^-)}{N(D_s^+) + N(D_s^-)}. \tag{3.69}$$

The raw asymmetries of each sample can be written as

$$A(A) = A_{\text{trig}}(K^+) + A_{\text{R}}, \tag{3.70}$$
$$A(B) = A_{\text{trig}}(K^+) + A_{\text{trig}}(\pi^+) + \delta_+ + A_{\text{R}}, \tag{3.71}$$
$$A(C) = A_{\text{trig}}(K^-) + A_{\text{R}}, \tag{3.72}$$
$$A(D) = A_{\text{trig}}(K^-) + A_{\text{trig}}(\pi^+) + \delta_- + A_{\text{R}}, \tag{3.73}$$

where A_{trig} quantifies the asymmetry arising from the online trigger selection and A_{R} contains the remaining nuisance asymmetries $A_{\text{prod}} + A_{\text{det}}$. The parameter $\delta_\pm$ evaluates how much the factorization of the trigger asymmetries is valid for the same-sign $(+)$ and opposite-sign asymmetries $(-)$. It is possible to demonstrate that $\delta_\pm$, under reasonable assumptions have the same sign of the $A_{\text{trig}}(K^\pm)$, and opposite sign between them. Thus, is possible to define $\delta = (\delta_+ - \delta_-)/2$ as the average effect on the asymmetries due to possible efficiencies correlation between same-sign and opposite-sign tracks. It is also

reasonable to assume that the effect could be larger for same-sign tracks with respect to the opposite-sign ones that in the majority of the cases are reconstructed in different regions of the detector. The values of $A_{\rm trig}(K^-)$, $A_{\rm trig}(\pi^+)$ and δ are given by

$$A_{\rm trig}(K^-) = \frac{A(C) - A(A)}{2}, \tag{3.74}$$

$$A_{\rm trig}(\pi^+) = \frac{[A(B) - A(A)] + [A(D) - A(C)]}{2}, \tag{3.75}$$

$$\delta = \frac{[A(B) - A(A)] - [A(D) - A(C)]}{2}. \tag{3.76}$$

The raw asymmetries obtained in each subsample are reported in Table 3.57 together with the correlation coefficients between the various subsamples. The measurements give

$$A_{\rm trig}(K^-) = [-3.55 \pm 2.12] \cdot 10^{-4}, \tag{3.77}$$

$$A_{\rm trig}(\pi^+) = [0.35 \pm 1.65] \cdot 10^{-4}, \tag{3.78}$$

$$\delta = [1.02 \pm 1.27] \cdot 10^{-4}, \tag{3.79}$$

showing no evidence for asymmetries arising from the online trigger selection. The value of δ is consistent with zero with a precision of $1.3 \cdot 10^{-4}$.

$D_s^+ \to \phi\pi^+$			
$A(A)^{\rm blind}[10^{-4}]$	$A(B)^{\rm blind}[10^{-4}]$	$A(C)^{\rm blind}[10^{-4}]$	$A(D)^{\rm blind}[10^{-4}]$
52.63 ± 4.47	54.00 ± 4.59	45.53 ± 4.68	44.86 ± 4.86

Table 3.57: Results of the raw asymmetries in the $D_s^+ \to \phi\pi^+$ sample in the different subsamples. Correlation between the measurements are found to be $\rho_{AB} = 0.90$, $\rho_{AC} = 0.57$, $\rho_{AD} = 0.56$, $\rho_{BC} = 0.56$, $\rho_{BD} = 0.60$ and $\rho_{CD} = 0.90$.

3.11 Combination for $\mathcal{A}^{CP}(K^-K^+)$

The results for $\mathcal{A}^{CP}(K^-K^+)$ in the D^+- and D_s^+-method

$$\mathcal{A}^{CP}(K^-K^+)^{\text{blind}}|D^+ = [56.7 \pm 8.8\,(\text{stat}) \pm 1.6\,(\text{syst})] \cdot 10^{-4}, \tag{3.80}$$

$$\mathcal{A}^{CP}(K^-K^+)^{\text{blind}}|D_s^+ = [45.9 \pm 6.7\,(\text{stat}) \pm 2.0\,(\text{syst})] \cdot 10^{-4}, \tag{3.81}$$

where the statistical and systematic uncertainties are correlated with $\rho_{\text{stat}} = 0.05$ and $\rho_{\text{syst}} = 0.28$, respectively, as reported in Table 3.38. The two measurements are found to be compatible between each others within one standard deviation and therefore they can be combined. The combination using the BLUE approach [122] yields

$$\mathcal{A}^{CP}(K^-K^+)^{\text{blind}} = [49.9 \pm 5.4\,(\text{stat}) \pm 1.6\,(\text{syst})] \cdot 10^{-4}, \tag{3.82}$$

while the overall correlation coefficient between the two measurements results to be $\rho_{\mathcal{A}^{CP}} = 0.06$.

3.12 Unblinding of $\mathcal{A}^{CP}(K^-K^+)$

As explained in Section 3.4, the raw asymmetries of all signals are shifted by offsets A^{offset}, different for each decay mode but equal between $D^+ \to K^-\pi^+\pi^+_{trig}$ and $D^+_s \to \phi\pi^+$ ($D^+ \to K^0_S\pi^+_{trig}$ and $D^+_s \to K^0_S K^+$) in order to obtain the same overall offset between the *CP* asymmetries measured with the D^+ and D^+_s methods. The values of A^{offset} are reported in Table 3.58 for each decay mode. The real raw asymmetries A are given by $A^{\text{blind}} + A^{\text{offset}}$ and, following Eqs. 3.16 and 3.17, the true $\mathcal{A}^{CP}(K^-K^+)$ values are given by summing -0.00431103 to the blind values. Therefore, the results are

$$\mathcal{A}^{CP}(K^-K^+)|D^+ = [13.6 \pm 8.8\,(\text{stat}) \pm 1.6\,(\text{syst})] \cdot 10^{-4},$$
$$\mathcal{A}^{CP}(K^-K^+)|D^+_s = [2.8 \pm 6.7\,(\text{stat}) \pm 2.0\,(\text{syst})] \cdot 10^{-4},$$

with their combination given by

$$\mathcal{A}^{CP}(K^-K^+) = [6.8 \pm 5.4\,(\text{stat}) \pm 1.6\,(\text{syst})] \cdot 10^{-4}. \tag{3.83}$$

	$D^+ \to K^0_S\pi^+_{trig}$ $D^+_s \to K^0_S K^+$	$D^+ \to K^-\pi^+\pi^+_{trig}$ $D^+_s \to \phi\pi^+$	$D^0 \to K^-\pi^+$	$D^0 \to K^-K^+$
A^{offset}	-0.00660803	-0.00656796	0.00684662	0.00249552

Table 3.58: Offsets applied to the raw asymmetries of each decay mode.

The unblind values of the raw asymmetries measured in the various decay samples are also reported in Figures 3.63 and 3.64 for the D^+ and D^+_s method, respectively.

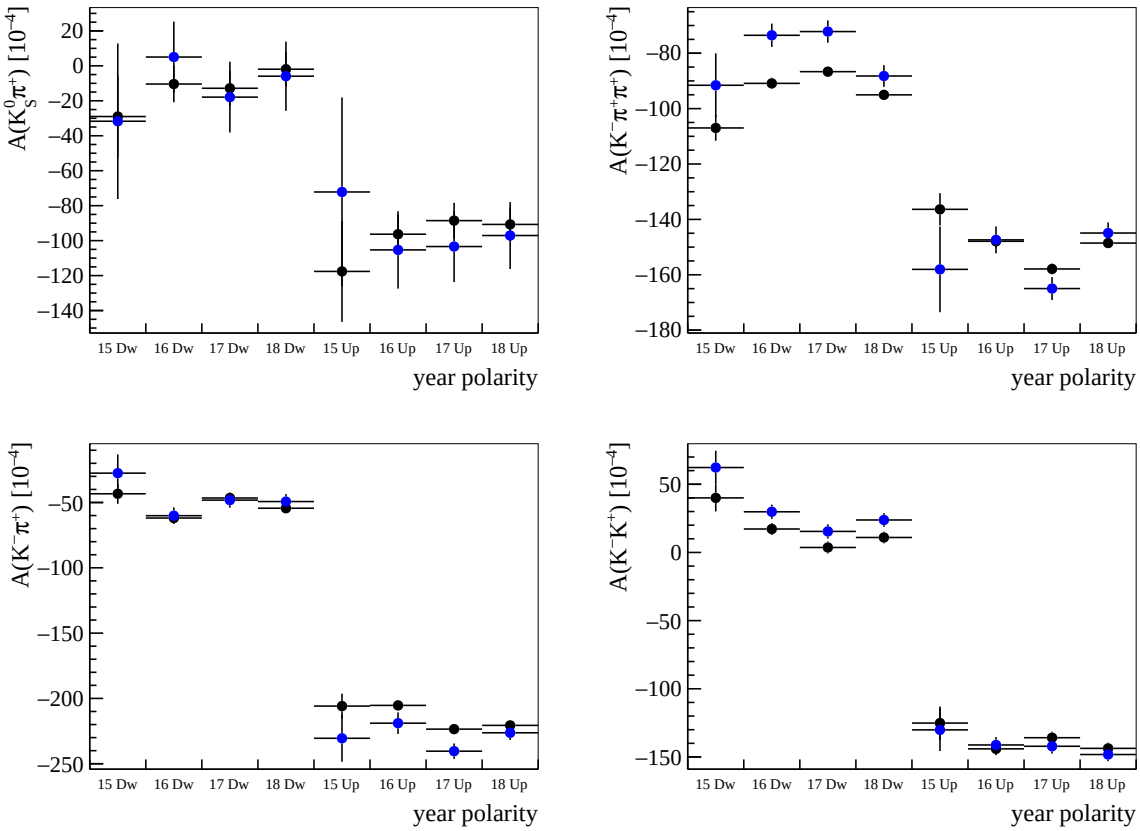

Figure 3.63: Comparison between unblind raw asymmetries measured in the D^+ method in different data-taking years and magnet polarities (blue) with and (black) without per-candidate kinematic weights applied.

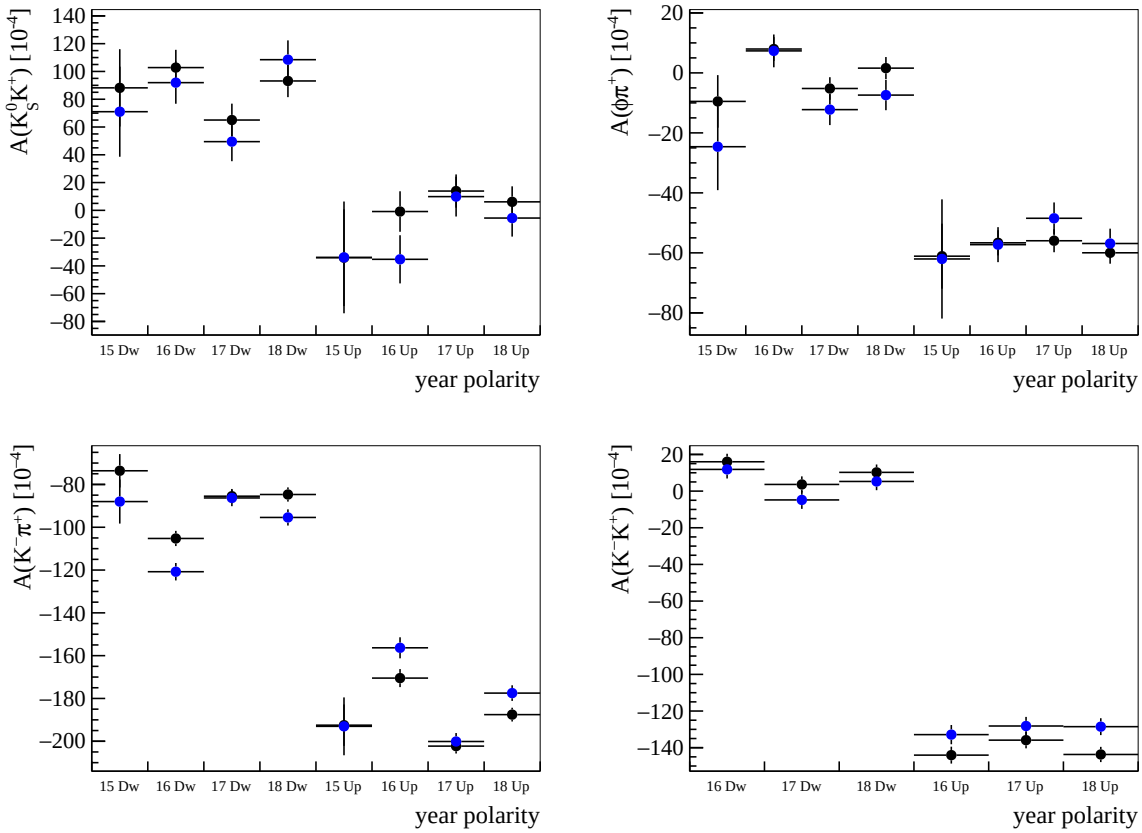

Figure 3.64: Comparison between unblind raw asymmetries measured in the D_s^+ method in different data-taking years and magnet polarities (blue) with and (black) without per-candidate kinematic weights applied.

3.13 Average lifetimes

As explained in Section 1.5.1, the time-integrated *CP* asymmetry is not only sensitive to the *CP* violation in the decay, but there is also a time-dependent contribution arising from *CP* violation in mixing and in the interference between mixing and decay amplitudes. This contribution depends on the average decay time of the D^0 meson, as described by Eq. 1.66. For this reason, it is necessary to study the average decay time of the signal events in each decay mode to allow interpretation in terms of direct and indirect *CP* violation. The average decay time for the selected and kinematically weighted events is determined using the background-subtraction technique realized defining the signal and sideband regions as reported in Table 3.39 and with the nominal fit to the $m(D^0\pi^+_{soft})$ reported in Section 3.4. The background-subtracted distributions obtained for all the collected candidates during Run 2 are shown in Figure 3.65. The average decay-times are directly computed from the distributions and are equal to

$$\langle t_{KK}\rangle^{\text{raw}}|D^+ = (0.752784 \pm 0.000097)\ \text{ps}, \tag{3.84}$$

$$\langle t_{KK}\rangle^{\text{raw}}|D_s^+ = (0.708770 \pm 0.000088)\ \text{ps}, \tag{3.85}$$

for the D^+ and D_s^+ method, respectively.

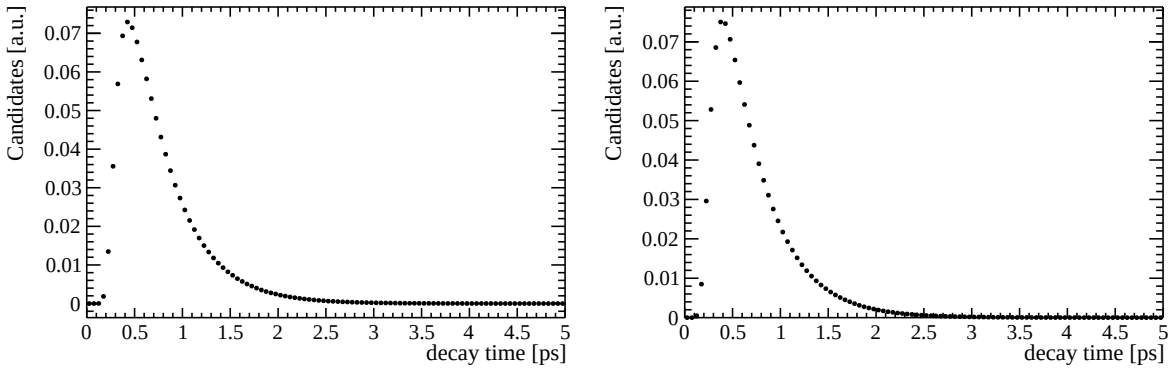

Figure 3.65: Background-subtracted decay time distributions for selected and kinematically weighted $D^0 \to K^-K^+$ decay candidates in the (left) D^+ method and (righ) D_s^+ method.

The presence of secondary D^0 affects the average lifetime according to the equation

$$\langle t_{KK}\rangle^{\text{raw}} = (1 - f_{\text{sec}})\langle t_{KK}\rangle + f_{\text{sec}}\langle t_{KK}\rangle^{\text{sec}}, \tag{3.86}$$

$$\langle t_{KK}\rangle = \frac{\langle t_{KK}\rangle^{\text{raw}} - f_{\text{sec}}\langle t_{KK}\rangle^{\text{sec}}}{1 - f_{\text{sec}}}. \tag{3.87}$$

where $\langle t_{KK}\rangle$ is the actual average decay time of the prompt decays and $\langle t_{KK}\rangle^{\text{sec}}$ is the average decay time of the secondary decays. The value of f_{sec} for the D^+ and D_s^+

methods are measured on the full Run 2 sample according to the procedure described in Section 3.9.1 where systematic uncertainties are also accounted for. The results are

$$f_{\text{sec}}|D^+ = [4.25 \pm 0.38]\% \text{ and } f_{\text{sec}}|D_s^+ = [4.56 \pm 0.28]\%,$$

in the D^+ and D_s^+ method, respectively. The values of $\langle t_{KK} \rangle^{\text{sec}}$ are evaluated by means of the secondary decays simulated with Particle Gun used in Section 3.9.1 where selection criteria and kinematic weights are applied to match with the data in $\text{IP}(D) > 100\,\mu\text{m}$ region. The decay-time distributions of the simulated samples are shown in Figure 3.66 and their average values correspond to

$$\langle t_{KK} \rangle^{\text{sec}} = (1.23148 \pm 0.00055) \text{ ps and } \langle t_{KK} \rangle^{\text{sec}} = (1.16781 \pm 0.00052) \text{ ps}$$

in the D^+ and D_s^+ method, respectively.

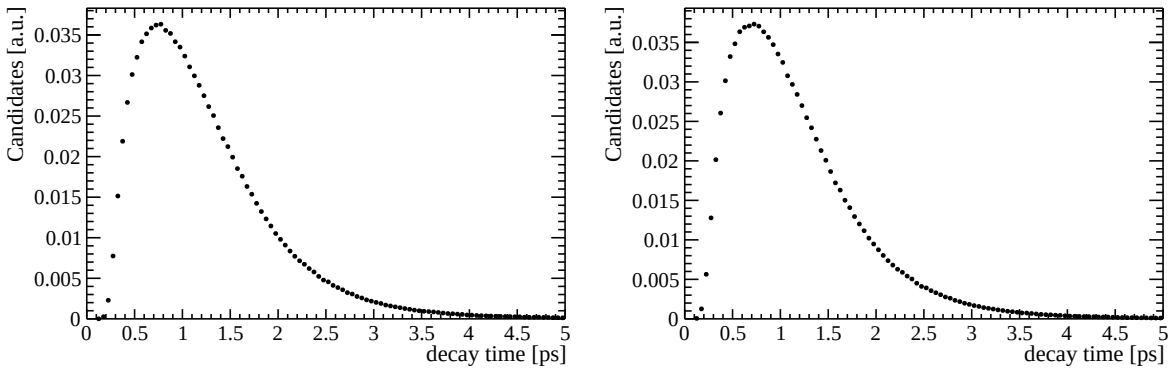

Figure 3.66: Decay time distributions obtained for the simulated secondary $D^0 \to K^-K^+$ decays in the (left) D^+ method and (righ) D_s^+ method.

Finally, the corrected average decay-times for the $D^0 \to K^-K^+$ decay candidates are found to be

$$\langle t_{KK} \rangle|D^+ = (0.7315 \pm 0.0020) \text{ ps}, \tag{3.88}$$
$$\langle t_{KK} \rangle|D_s^+ = (0.6868 \pm 0.0014) \text{ ps}, \tag{3.89}$$

for the D^+ and D_s^+ method, respectively.

To evaluate the relative decay time, the nominal D^0 lifetime $\tau_{hh} = \tau_{K\pi} = (0.4101 \pm 0.0015)$ ps [31] is used, bringing to

$$\langle t_{KK} \rangle/\tau|D^+ = (1.7838 \pm 0.0081), \tag{3.90}$$
$$\langle t_{KK} \rangle/\tau|D_s^+ = (1.6748 \pm 0.0071), \tag{3.91}$$

for the D^+ and D_s^+ method, respectively.

3.14 Run 1 and Run 2 combination for $a^{\rm d}_{\pi\pi}$ and $a^{\rm d}_{KK}$

The combination aims at determining the direct *CP* violation parameters, $a^{\rm d}_{\pi\pi}$ and $a^{\rm d}_{KK}$, as defined in Section 3.1, from the time-integrated and time-dependent measurements of *CP* violation in D^0 decays. The strategy to combine Run 1 and Run 2 measurements is to build a joint multivariate Gaussian p.d.f, defined as

$$g\left(\overrightarrow{m}, \overrightarrow{\lambda}, \overrightarrow{\sigma^2}\right) = \frac{1}{\sqrt{(2\pi)^n \left|\Sigma\right|}} \exp\left(-\frac{1}{2}\left(\overrightarrow{m} - \overrightarrow{\lambda}\right)^T \Sigma^{-1} \left(\overrightarrow{m} - \overrightarrow{\lambda}\right)\right), \tag{3.92}$$

where λ_i correspond to the true values of the observables, m_i and σ_i are their measurements and related errors as reported in Table 3.59, and Σ is the covariance matrix of all the measurements. In this combination, ΔY is assumed to be universal, *i.e.* $\Delta Y_{KK} \equiv \Delta Y_{\pi\pi}$. The true values of $\mathcal{A}^{CP}(K^-K^+)$ and ΔA_{CP} enter in the p.d.f. as function of the parameters ΔY, $\langle t \rangle_{hh}$, and τ_{D^0} (named x_i from here on), and of the direct *CP* violation asymmetries a^d_{KK} and $a^d_{\pi\pi}$, namely

$$\mathcal{A}^{CP}(K^-K^+) = a^d_{KK} + \frac{\langle t \rangle_{KK}}{\tau_{D^0}} \cdot \Delta Y, \tag{3.93}$$

$$\Delta A_{CP} = a^d_{KK} + \frac{\langle t \rangle_{KK}}{\tau_{D^0}} \cdot \Delta Y - a^d_{\pi\pi} - \frac{\langle t \rangle_{\pi\pi}}{\tau_{D^0}} \cdot \Delta Y. \tag{3.94}$$

The covariance matrix Σ contains contributions from the statistical and systematic uncertainties as reported in the various analyses. The Run 1 and Run 2 statistical and systematic errors are uncorrelated. In π-tagged and μ-tagged Run 1 data sample, the correlations between $\langle t \rangle_{\Delta A_{CP}}$ and $\langle t \rangle_{\mathcal{A}^{CP}(K^-K^+)}$ are assumed to be the maximum possible. In Run 2, the correlations between ΔA_{CP} π-tagged and $\mathcal{A}^{CP}(K^-K^+)$ are determined to be 0.06 and 0.08 for D^+ and D^+_s method, respectively. The correlation between $\langle t \rangle_{\Delta A_{CP}}$ and $\langle t \rangle_{\mathcal{A}^{CP}(K^-K^+)}$ are calculated to be 0.52 and 0.56 for D^+ and D^+_s method, respectively, while the correlation between the average times for the two methods is 0.74. The correlations between ΔY and the measurements of $\mathcal{A}^{CP}(K^-K^+)$ and ΔA_{CP} are found to be negligible, as explained in Section 3.16.4. The considered correlations are reported in Table 3.60 and Table 3.61.

The log-likelihood function is built taking the logarithm of the joint p.d.f. without the additive terms that do not depend on the parameters

$$\log L(x_i, a^d_{KK}, a^d_{\pi\pi}) = -\frac{1}{2}\left(\overrightarrow{m} - \overrightarrow{\lambda}(x_i, a^d_{KK}, a^d_{\pi\pi})\right)^T \Sigma^{-1} \left(\overrightarrow{m} - \overrightarrow{\lambda}(x_i, a^d_{KK}, a^d_{\pi\pi})\right). \tag{3.95}$$

The maximum of the log-likelihood function is obtained by finding the values of the parameters ($\hat{x}_i$,$\hat{a}^d_{KK}$,$\hat{a}^d_{\pi\pi}$) that minimize the following function

$$\chi^2(x_i, a^d_{KK}, a^d_{\pi\pi}) = \left(\overrightarrow{m} - \overrightarrow{\lambda}(x_i, a^d_{KK}, a^d_{\pi\pi})\right)^T \Sigma^{-1} \left(\overrightarrow{m} - \overrightarrow{\lambda}(x_i, a^d_{KK}, a^d_{\pi\pi})\right). \tag{3.96}$$

Measurement	Data sample	$m_i \pm \sigma_i$	Reference
$\mathcal{A}^{CP}(K^-K^+)$	π-tagged Run 1	$(14 \pm 15 \pm 10) \cdot 10^{-4}$	[64]
$\mathcal{A}^{CP}(K^-K^+)$	μ-tagged Run 1	$(-6 \pm 15 \pm 10) \cdot 10^{-4}$	[63]
$\mathcal{A}^{CP}(K^-K^+)$	π-tagged D^+-method Run 2	$(13.6 \pm 8.8 \pm 1.6) \cdot 10^{-4}$	this analysis
$\mathcal{A}^{CP}(K^-K^+)$	π-tagged D_s^+-method Run 2	$(2.8 \pm 6.7 \pm 2.0) \cdot 10^{-4}$	this analysis
ΔA_{CP}	π-tagged Run 1	$(-10 \pm 8 \pm 3) \cdot 10^{-4}$	[75]
ΔA_{CP}	μ-tagged Run 1	$(14 \pm 16 \pm 8) \cdot 10^{-4}$	[63]
ΔA_{CP}	π-tagged Run 2	$(-18.2 \pm 3.2 \pm 0.9) \cdot 10^{-4}$	[1]
ΔA_{CP}	μ-tagged Run 2	$(-9 \pm 8 \pm 5) \cdot 10^{-4}$	[1]
τ_{D^0}	-	$(4.101 \pm 0.015) \cdot 10^{-13}$ s	[31]
$\langle t \rangle_{KK}$	ΔA_{CP} π-tagged Run 1	$(8.827 \pm 0.058) \cdot 10^{-13}$ s	[123]
$\langle t \rangle_{\pi\pi}$	ΔA_{CP} π-tagged Run 1	$(8.354 \pm 0.054) \cdot 10^{-13}$ s	[123]
$\langle t \rangle_{KK}$	ΔA_{CP} μ-tagged Run 1	$(4.437 \pm 0.003) \cdot 10^{-13}$ s	[63]
$\langle t \rangle_{\pi\pi}$	ΔA_{CP} μ-tagged Run 1	$(4.379 \pm 0.005) \cdot 10^{-13}$ s	[63]
$\langle t \rangle_{KK}$	$\mathcal{A}^{CP}(K^-K^+)$ π-tagged Run 1	$(9.180 \pm 0.069) \cdot 10^{-13}$ s	[64]
$\langle t \rangle_{KK}$	$\mathcal{A}^{CP}(K^-K^+)$ μ-tagged Run 1	$(4.310 \pm 0.006) \cdot 10^{-13}$	[63]
$\langle t \rangle_{KK}$	ΔA_{CP} π-tagged Run 2	$(6.946 \pm 0.001) \cdot 10^{-13}$ s	[124]
$\langle t \rangle_{\pi\pi}$	ΔA_{CP} π-tagged Run 2	$(6.407 \pm 0.002) \cdot 10^{-13}$ s	[124]
$\langle t \rangle_{KK}$	ΔA_{CP} μ-tagged Run 2	$(4.918 \pm 0.002) \cdot 10^{-13}$ s	[124]
$\langle t \rangle_{\pi\pi}$	ΔA_{CP} μ-tagged Run 2	$(4.931 \pm 0.003) \cdot 10^{-13}$ s	[124]
$\langle t \rangle_{KK}$	$\mathcal{A}^{CP}(K^-K^+)$ D^+-method Run 2	$(7.315 \pm 0.020) \cdot 10^{-13}$ s	this analysis
$\langle t \rangle_{KK}$	$\mathcal{A}^{CP}(K^-K^+)$ D_s^+-method Run 2	$(6.868 \pm 0.014) \cdot 10^{-13}$ s	this analysis
ΔY	Run 1+Run 2	$(-1.04 \pm 1.12 \pm 0.33) \cdot 10^{-4}$	[46, 125–127]

Table 3.59: Run 1 and Run 2 measurements used in the combination. The statistical uncertainty is reported as first while the systematic one as latter. If only one error is reported it includes both the uncertainties.

Those values are the least squares estimators of the unknown parameters. The combined results are

$$a^d_{KK} = (7.7 \pm 5.7) \cdot 10^{-4}, \tag{3.97}$$

$$a^d_{\pi\pi} = (23.2 \pm 6.1) \cdot 10^{-4}, \tag{3.98}$$

with a correlation value corresponding to $\rho(a^d_{KK}, a^d_{\pi\pi}) = 0.88$. The values differ from zero for 1.4 and 3.8 standard deviations, respectively. This corresponds to an evidence for direct *CP* violation in the $D^0 \to \pi^-\pi^+$ decay. Figure 3.67 presents the 2-dimensional contour plot for a^d_{KK} and $a^d_{\pi\pi}$ from LHCb measurements using the contribution of the presented analysis and compared with the results obtained from the combination of Run 1 only measurements.

Run 1 measurement	Run 1 measurement $\mathcal{A}^{CP}(K^-K^+)$ π-tagged	ΔA_{CP} π-tagged	$\mathcal{A}^{CP}(K^-K^+)$ μ-tagged	ΔA_{CP} μ-tagged
$\mathcal{A}^{CP}(K^-K^+)$ π-tagged	(1,1)	(0.24,0)	(0.36,1)	
ΔA_{CP} π-tagged		(1,1)		
$\mathcal{A}^{CP}(K^-K^+)$ μ-tagged			(1,1)	(0.23,0.40)
ΔA_{CP} μ-tagged				(1,1)
Run 2 measurement	$\mathcal{A}^{CP}(K^-K^+)$ D^+-method	$\mathcal{A}^{CP}(K^-K^+)$ D_s^+-method	ΔA_{CP} π-tagged	ΔA_{CP} μ-tagged
$\mathcal{A}^{CP}(K^-K^+)$ D^+-method	(1,1)	(0.05,0.28)	(0.06,0)	
$\mathcal{A}^{CP}(K^-K^+)$ D_s^+-method		(1,1)	(0.08,0)	
ΔA_{CP} π-tagged			(1,1)	
ΔA_{CP} μ-tagged				(1,1)

Table 3.60: Correlation matrix for the statistical and systematic uncertainties ($\sigma_{\rm stat}$,$\sigma_{\rm syst}$) between the measurements in Run 1 and Run 2. The values are taken from the papers and analysis notes cited in Table 3.59.

Run 1 measurement	Run 1 measurement $\langle t\rangle_{\Delta A_{CP}}$ π-tagged	$\langle t\rangle_{\mathcal{A}^{CP}(K^-K^+)}$ π-tagged	$\langle t\rangle_{\Delta A_{CP}}$ μ-tagged	$\langle t\rangle_{\mathcal{A}^{CP}(K^-K^+)}$ μ-tagged
$\langle t\rangle_{\Delta A_{CP}}$ π-tagged	1	0.84		
$\langle t\rangle_{\mathcal{A}^{CP}(K^-K^+)}$ π-tagged		1		
$\langle t\rangle_{\Delta A_{CP}}$ μ-tagged			1	0.50
$\langle t\rangle_{\mathcal{A}^{CP}(K^-K^+)}$ μ-tagged				1
Run 2 measurement	$\langle t\rangle_{\mathcal{A}^{CP}(K^-K^+)}$ D^+-method	$\langle t\rangle_{\mathcal{A}^{CP}(K^-K^+)}$ D_s^+-method	$\langle t\rangle_{\Delta A_{CP}}$ π-tagged	
$\langle t\rangle_{\mathcal{A}^{CP}(K^-K^+)}$ D^+-method	1	0.74	0.52	
$\langle t\rangle_{\mathcal{A}^{CP}(K^-K^+)}$ D_s^+-method		1	0.56	
$\langle t\rangle_{\Delta A_{CP}}$ π-tagged			1	

Table 3.61: Correlation matrix for the uncertainties between the average time measurements in $D^0 \to K^-K^+$ in Run 1 and Run 2.

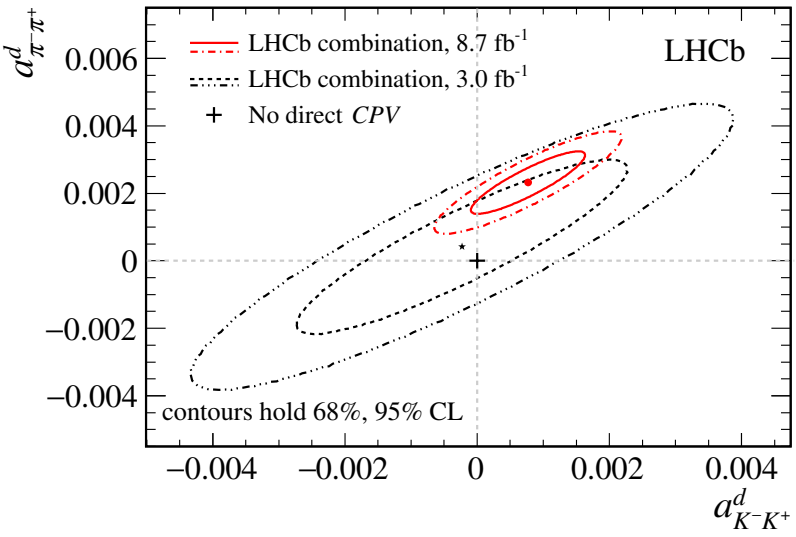

Figure 3.67: a^d_{KK} vs $a^d_{\pi\pi}$ contour plot from Run 1 vs Run 1+2 LHCb measurements. The Run 1 combination uses a value of $\Delta Y = (1.30 \pm 2.97) \cdot 10^{-4}$ corresponding to the Run 1 average [126, 127].

3.15 Conclusions

The *CP* asymmetries in Cabibbo suppressed $D^0 \to K^-K^+$ decays are measured using promptly produced D^{*+} decays reconstructed in the *pp*-collision data collected by LHCb during 2015-2018, and corresponding to approximately $5.7\,\text{fb}^{-1}$ of integrated luminosity. Two independent approaches, *i.e.* the D^+ method and the D_s^+ method, are used to subtract nuisance asymmetry given by detector effects. The results are

$$\mathcal{A}^{CP}(K^-K^+)|D^+ = (13.6 \pm 8.8\,(\text{stat}) \pm 1.6\,(\text{syst})) \cdot 10^{-4},$$
$$\mathcal{A}^{CP}(K^-K^+)|D_s^+ = (2.8 \pm 6.7\,(\text{stat}) \pm 2.0\,(\text{syst})) \cdot 10^{-4},$$

for the D^+ and the D_s^+ method, respectively. They are the world's most precise measurements of this quantity to date. The statistical uncertainties are correlated by a coefficient $\rho_{\text{stat}} = 0.05$, while the systematical one by $\rho_{\text{syst}} = 0.28$. The total correlation coefficient is $\rho_{\mathcal{A}^{CP}} = 0.06$. Their combination is measured to be

$$\mathcal{A}^{CP}(K^-K^+) = (6.8 \pm 5.4\,(\text{stat}) \pm 1.6\,(\text{syst})) \cdot 10^{-4}.$$

The measurements are also correlated with the ΔA_{CP} measurement using promptly produced D^{*+} collected by LHCb during Run 2 [1] with a coefficient ρ_{stat}=0.06 (0.08) for D^+ (D_s^+) method. The results are combined with all the LHCb measurements for $\mathcal{A}^{CP}(K^-K^+)$, ΔA_{CP}, and ΔY to obtain the direct *CP* parameters a^d_{KK} and $a^d_{\pi\pi}$. The combined results are

$$a^d_{KK} = (7.7 \pm 5.7) \cdot 10^{-4},$$
$$a^d_{\pi\pi} = (23.2 \pm 6.1) \cdot 10^{-4},$$

with a correlation value corresponding to $\rho(a^d_{KK}, a^d_{\pi\pi}) = 0.88$. The values differ from zero for 1.4 and 3.8 standard deviations, respectively. In particular, $a^d_{\pi\pi}$ shows an evidence for direct *CP* violation in $D^0 \to \pi^-\pi^+$ decays.

3.16 Additional material

3.16.1 Hlt2 requirements

Particle	Variable	Requirement
D^{*+}	$m(D^0\pi^+_{soft}) - m(h^-h'^+) - m(\pi^+_{soft})$	$[-9.57018, 20.42982]\,\text{MeV}/c^2$
	Vertex χ^2/ndf	< 25
D^0	$m(h^-h'^+)$	$[1715, 2015]\,\text{MeV}/c^2$
	Vertex χ^2/ndf	< 10
	Flight-distance χ^2	> 25
	Direction angle (a.k.a. acosDIRA)	$< 17.3\,\text{mrad}$
	p_T	$> 1\,\text{GeV}/c$
	p_T 1 out of 2 daughters	$> 1\,\text{GeV}/c$
h^- or h'^+	$\text{DLL}_{K\pi}$	< 5 (π) or > 5 (K)
	Impact-parameter χ^2	> 4
	p_T	$> 800\,\text{MeV}/c$
	p	$> 5\,\text{GeV}/c$
	Track χ^2/ndf	< 3
π^+_{soft}	p_T	$> 100\,\text{MeV}/c^{(a)}$, $> 200\,\text{MeV}/c^{(b)}$
	p	$1\,\text{GeV}/c$
	Track χ^2/ndf	< 3

Table 3.62: Hlt2 requirements used to select $D^{*+} \to D^0\,(\to h^-h'^+)\pi^+_{soft}$ decays. (a) refers to the 2015 and 2016 data-taking years while (b) refers to the 2017 and 2018 ones.

Particle	Variable	Requirement
$D^+_{(s)}$	Mass	$[1789, 2049]\,\text{MeV}/c^2$
	Flight-distance χ^2	> 30
	Decay time	$> 0.25\,\text{ps}$
	Vertex χ^2/ndf	< 10
	Direction angle (a.k.a. acosDIRA)	$< 17.3\,\text{mrad}$
	p_T	$> 2.0\,\text{GeV}/c$
K^0_S	$\lvert m(\pi^+\pi^-) - m^\text{PDG}_{K^0_\text{S}}\rvert$	$< 35\,\text{MeV}/c^2$
	Decay time (wrt the PV)	$> 0.5\,\text{ps}$
	z coordinate of the decay vertex	$[-100, 500]\,\text{mm}$
	Vertex-fit χ^2/ndf	< 30
Bachelor h^+	$\text{DLL}_{K\pi}$	< 5 (π) or > 5 (K)
	Impact-parameter χ^2	> 36
	p_T	$> 200\,\text{MeV}/c$
	Track χ^2/ndf	< 3
K^0_S decay-products	Track χ^2/ndf	< 3
	Impact-parameter χ^2	> 36
	Track type	long

Table 3.63: Hlt2 requirements used to select $D^+_{(s)} \to K^0_\text{S} h^+$ decays.

Particle	Variable	Requirement
D^+	Mass	$[1779, 1949]\,\text{MeV}/c^2$
	Flight-distance χ^2	> 150
	Decay time	$> 0.4\,\text{ps}$
	Vertex χ^2/ndf	< 6
	Direction angle (a.k.a. acosDIRA)	$< 10.0\,\text{mrad}$
	p_T 2 out of 3 daughters	$> 400\,\text{MeV}/c$
	p_T 1 out of 3 daughters	$> 1\,\text{GeV}/c$
	Minimal IPχ^2 2 out of 3 daughters	> 10
	Minimal IPχ^2 1 out of 3 daughters	> 50
	sum of p_T of daughters	$> 3.0\,\text{GeV}/c$
K^-	Impact-parameter χ^2	> 4
	$\text{DLL}_{K\pi}$	> 5
	Track χ^2/ndf	< 3
	p_T	$> 250\,\text{MeV}/c$
$\pi^\pm$	$\text{DLL}_{K\pi}$	< 5
	Impact-parameter χ^2	> 4
	Track χ^2/ndf	< 3
	p_T	$> 250\,\text{MeV}/c$

Table 3.64: Hlt2 requirements used to select $D^+ \to K^-\pi^+\pi^+$ decays.

Particle	Variable	Requirement
D_s^+	Mass	$[1889, 2049]\,\text{MeV}/c^2$
	Flight-distance χ^2	> 100
	Decay time	$> 0.2\,\text{ps}$
	Vertex χ^2/ndf	< 6
	Direction angle (a.k.a. acosDIRA)	$< 14.1\,\text{mrad}$
	p_T 2 out of 3 daughters	$> 400\,\text{MeV}/c$
	p_T 1 out of 3 daughters	$> 1\,\text{GeV}/c$
	Minimal IPχ^2 2 out of 3 daughters	> 10
	Minimal IPχ^2 1 out of 3 daughters	> 50
	sum of p_T of daughters	$> 3.0\,\text{GeV}/c$
$K^\pm$	Impact-parameter χ^2	> 4
	$\text{DLL}_{K\pi}$	> 5
	Track χ^2/ndf	< 3
	p_T	$> 250\,\text{MeV}/c$
π^+	$\text{DLL}_{K\pi}$	< 5
	Impact-parameter χ^2	> 4
	Track χ^2/ndf	< 3
	p_T	$> 250\,\text{MeV}/c$

Table 3.65: Hlt2 requirements used to select $D_s^+ \to K^-K^+\pi^+$ decays.

Particle	Variable	Requirement
$D^+_{(s)}$	Mass	$[1789, 2049]\,\text{MeV}/c^2$
	Flight-distance χ^2	> 30
	Decay time	$> 0.25\,\text{ps}$
	Vertex χ^2/ndf	< 10
	Direction angle (a.k.a. acosDIRA)	$< 17.3\,\text{mrad}$
	p_T	$> 2.0\,\text{GeV}/c$
K^0_S	$\lvert m(\pi^+\pi^-) - m^\text{PDG}_{K^0_\text{S}}\rvert$	$< 64\,\text{MeV}/c^2$
	Decay time (wrt the PV)	$> 0.5\,\text{ps}$
	Distance along z from the PV	$> 400\,\text{mm}$
	z coordinate of the decay vertex	$[300, 2275]\,\text{mm}$
	Vertex-fit χ^2/ndf	< 30
Bachelor h^+	$\text{DLL}_{K\pi}$	< 5 (π) or > 5 (K)
	Impact-parameter χ^2	> 36
	p_T	$> 200\,\text{MeV}/c$
	Track χ^2/ndf	< 3
K^0_S decay-products	Track χ^2/ndf	< 4
	p	$> 3\,\text{GeV}/c$
	p_T	$> 175\,\text{MeV}/c$
	Track type	downstream

Table 3.66: Hlt2 requirements used to select $D^+_{(s)} \to K^0_\text{S} h^+$ decays where the K^0_S is reconstructed from downstream tracks.

3.16.2 Kinematic separation of $D^+ \to K^0_S h^+$ and $K^0_S \to \pi^-\pi^+$ decays

The invariant mass of two particles X and Y of mass m_X and m_Y and momenta $\vec{p}_X$ and $\vec{p}_Y$ is defined as

$$M^2_{XY} = \left(\sqrt{p^2_X + m^2_X} + \sqrt{p^2_Y + m^2_Y}\right)^2 - (\vec{p}_X + \vec{p}_Y)^2. \tag{3.99}$$

If the two particles originate from the two-body decay of a common mother P of mass m_0, then $M_{12} = m_0$. If, instead, one wrongly assigns the masses to the outgoing particles, the resulting invariant mass

$$M^2_{12} = \left(\sqrt{p^2_X + m^2_1} + \sqrt{p^2_Y + m^2_2}\right)^2 - (\vec{p}_X + \vec{p}_Y)^2, \tag{3.100}$$

where the mass m_1 (m_2) is assigned to the particle with momentum $\vec{p}_X$ ($\vec{p}_Y$), is shifted with respect to m_0 as

$$M^2_{12} = m^2_0 - \Delta M^2, \tag{3.101}$$

with

$$\begin{aligned}
\Delta M^2 &= M^2_{XY} - M^2_{12} \\
&= (m^2_X - m^2_1) + (m^2_Y - m^2_2) \\
&\quad + 2p_X p_Y \left(\sqrt{1 + \left(\frac{m_X}{p_X}\right)^2}\sqrt{1 + \left(\frac{m_Y}{p_Y}\right)^2} - \sqrt{1 + \left(\frac{m_1}{p_X}\right)^2}\sqrt{1 + \left(\frac{m_2}{p_Y}\right)^2}\right) \\
&\approx (m^2_X - m^2_1) + (m^2_Y - m^2_2) \\
&\quad + p_X p_Y \left[\left(\frac{m_X}{p_X}\right)^2 + \left(\frac{m_Y}{p_Y}\right)^2 - \left(\frac{m_1}{p_X}\right)^2 - \left(\frac{m_2}{p_Y}\right)^2\right] \\
&= (m^2_X - m^2_1)(1 + p_Y/p_X) + (m^2_Y - m^2_2)(1 + p_X/p_Y) \\
&= \frac{2}{1+\beta}(m^2_X - m^2_1) + \frac{2}{1-\beta}(m^2_Y - m^2_2),
\end{aligned} \tag{3.102}$$

where the approximation holds the first order in (m/p) and the momentum imbalance β is further defined as

$$\beta = \frac{p_X - p_Y}{p_X + p_Y}. \tag{3.103}$$

The above expression, for a $P^\pm \to X^0 Y^\pm$ decay, when using a $D^+_{(s)}$ meson, a neutral kaon and a charged pion or kaon as arbitrary mass assignments for the initial and the

final state particles (*i.e.* a $D^+_{(s)} \to K^0_{\rm S}\, h^+$ decay), becomes:

$$M^2(D^+_{(s)} \to K^0_S h'^+) \approx m^2_{D^+_{(s)}} - \frac{2}{1-\beta}(m^2_{h'} - m^2_h), \tag{3.104}$$

$$M^2(\Lambda^+_c \to K^0_S p) \approx m^2_{\Lambda^+_c} - \frac{2}{1-\beta}(m^2_p - m^2_h), \tag{3.105}$$

$$M^2(\Xi^+_c \to K^0_S p) \approx m^2_{\Xi^+_c} - \frac{2}{1-\beta}(m^2_p - m^2_h), \tag{3.106}$$

$$M^2(\Lambda^+_c \to \Lambda^0 h^+) \approx m^2_{\Lambda^+_c} - \frac{2}{1+\beta}(m^2_\Lambda - m^2_{K^0_S}). \tag{3.107}$$

For a $P^0 \to X^+Y^-$ decay, when using a neutral kaon and a pair of charged pions as arbitrary mass assignments for the initial and the final state particles (*i.e.* a $K^0_S \to \pi^-\pi^+$ decay), it becomes:

$$M^2(\Lambda \to p\pi^-) \approx m^2_\Lambda - \frac{2}{1\pm\beta}(m^2_p - m^2_\pi). \tag{3.108}$$

The above relations are graphically shown in Figures 3.3 to 3.5.

3.16.3 Correlation between raw asymmetries

Consider to select N events and to apply two different sets of weights, $\{u_1, .., u_N\}$ and $\{v_1, .., v_N\}$, in which pairs of values having the same index are correlated, estimators of number of events are given by

$$\hat{\mu} = \sum_{i=1}^{N} u_i, \quad \hat{\nu} = \sum_{i=1}^{N} v_i, \tag{3.109}$$

while an estimator of the covariance between $\hat{\mu}$ and $\hat{\nu}$ is given by [128]

$$\mathrm{cov}(\hat{\mu}, \hat{\nu}) = \sum_{i=1}^{N} u_i v_i. \tag{3.110}$$

Considering two different asymmetries, defined as

$$A_1 = \frac{\hat{\mu}^+ - \hat{\mu}^-}{N}, \quad A_2 = \frac{\hat{\nu}^+ - \hat{\nu}^-}{N}, \tag{3.111}$$

where $\hat{\mu}^{\pm} = \sum_{i=1}^{n} u_i^{\pm}$ and $\hat{\nu}^{\pm} = \sum_{i=1}^{n} v_i^{\pm}$ are the sum of the weights applied to the positive and negative tagged candidates, the covariance is determined to be

$$\mathrm{cov}(A_1, A_2) = \frac{1}{N^2}\left[\mathrm{cov}(\hat{\mu}^+, \hat{\nu}^+) + \mathrm{cov}(\hat{\mu}^-, \hat{\nu}^-) - \mathrm{cov}(\hat{\mu}^+, \hat{\nu}^-) - \mathrm{cov}(\hat{\mu}^-, \hat{\nu}^+)\right]. \tag{3.112}$$

As the tagged positive and negative data samples are statistically independent, the terms $\mathrm{cov}(\hat{\mu}^+, \hat{\nu}^-)$ and $\mathrm{cov}(\hat{\mu}^-, \hat{\nu}^+)$ are zero and the covariance is given by

$$\mathrm{cov}(A_1, A_2) = \frac{\sum_{i=1}^{N} u_i v_i}{N^2}. \tag{3.113}$$

The correlation coefficient results to be

$$\mathrm{cor}(A_1, A_2) = \frac{\mathrm{cov}(A_1, A_2)}{\sqrt{\mathrm{Var}\,(A_1)} \cdot \sqrt{\mathrm{Var}\,(A_2)}} = \frac{\sum_{i=1}^{N} u_i v_i}{\sqrt{\sum_{i=1}^{N} (u_i)^2}\sqrt{\sum_{i=1}^{N} (v_i)^2}}, \tag{3.114}$$

where $\mathrm{Var}\,(A_1) = \mathrm{Var}\,(\hat{\mu})\,/N^2$ with $\mathrm{Var}\,(\hat{\mu}) = \sum_{i=1}^{N} (u_i)^2$, and similarly for $\mathrm{Var}\,(A_2)$.

3.16.4 Correlation between ΔY and $D^0 \to h^-\ h^+$ raw asymmetry

The statistical correlation between ΔY and the measurements $\mathcal{A}^{CP}(K^-K^+)$ and ΔA_{CP} can be estimated using the results for the $D^0 \to K^-K^+$ and $D^0 \to \pi^-\pi^+$ raw asymmetry as a function of the decay time obtained in Run 2 with the prompt sample [46] and reproduced in Figure 3.68. In this sample, the nuisance contributions of production and

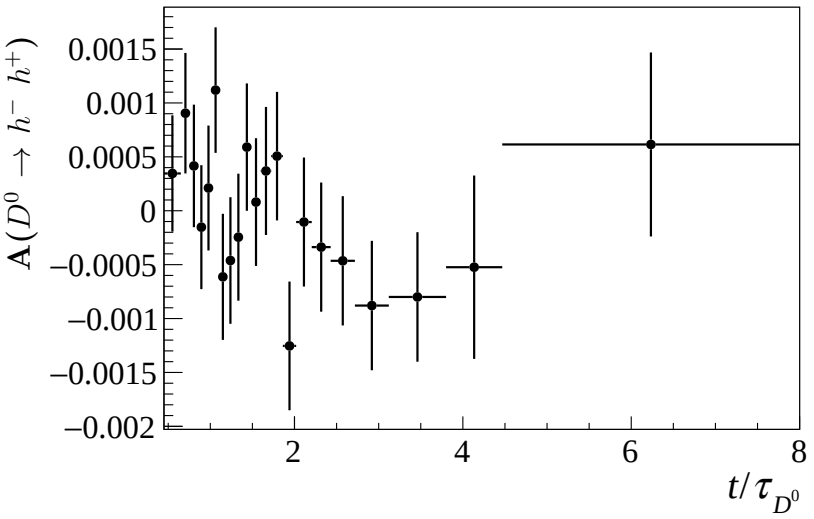

Figure 3.68: Raw asymmetry as a function of decay time for $D^0 \to K^-K^+$ and $D^0 \to \pi^-\pi^+$ candidates.

detection asymmetries are equalized among all the bins of decay time by means of a kinematic weighting procedure. Then, the raw asymmetry as a function of decay time $A_{hh}(t)$ in $D^0 \to h^-h^+$ decays, with $h = K$ or π, can be written as

$$A_{hh}(t) = c + \frac{t}{\tau}\Delta Y_{hh}, \tag{3.115}$$

where c represents a constant value and ΔY_{hh} the slope of the function $A_{hh}(t)$, describing possible time-dependent *CP* violation. Similarly, the average time-integrated raw asymmetry $A_{hh} \equiv \langle A_{hh}(t) \rangle$ is given by

$$A_{hh} = c + \frac{\langle t \rangle}{\tau}\Delta Y_{hh}, \tag{3.116}$$

with $\langle t \rangle / \tau$ being the average decay-time. Polinomial fits to the distribution with two and one parameters return the values of c, ΔY_{hh} and A_{hh}, respectively. They are

$$\begin{aligned} c &= 0.000317153 \pm 0.000245959 \\ \Delta Y_{hh} &= -0.000193803 \pm 0.000119554, \\ &\text{with } \rho(c, \Delta Y_{hh}) = -0.84625, \text{ and} \\ A_{hh} &= -0.0000202576 \pm 0.000131044. \end{aligned} \tag{3.117}$$

The value of $\langle t \rangle / \tau$ can also be calculated from $(A_{hh} - c)/\Delta Y_{hh}$ resulting to be 1.74. From Eq. 3.116,the convariance between A_{hh} and ΔY_{hh} is given by

$$COV(A_{hh}, \Delta Y_{hh}) = \rho(c, \Delta Y_{hh})\, \sigma_c\, \sigma_{\Delta Y_{hh}} + \frac{\langle t \rangle}{\tau} \sigma^2_{\Delta Y_{hh}}, \tag{3.118}$$

with a correlation factor corresponding to

$$\rho = \frac{COV(A_{hh}, \Delta Y_{hh})}{\sigma_{A_{hh}}\, \sigma_{\Delta Y_{hh}}}, \tag{3.119}$$

which is found to be of the order of 10^{-6}. Therefore, no correlation is assumed between the measurements of direct CP violation, $\mathcal{A}^{CP}(K^- K^+)$ and ΔA_{CP}, and ΔY.

Chapter 4

Performance studies for an Upgrade-II 4D VELO

4.1 Introduction

The proposed future upgrade of the LHCb experiment (Upgrade II) aims to maximise the heavy flavour physics capabilities running at the Hi-Lumi LHC [129]. To measure precisely effects from physics beyond the Standard Model in the sensitive, rare heavy-flavour decays, the overall data sample will increase to an equivalent of 300 fb^{-1} integrated luminosity by the end of Run 6. This goal will be achieved by increasing the maximum instantaneous luminosity to $1.5 \cdot 10^{34}$ cm^2s^{-1} for Run 5 and beyond, which is a factor 7.5 more than the already challenging operational conditions of the Upgrade I detector.

As explained in Section 2.8, the performance of the VELO is crucial to the success of the LHCb's heavy flavour physics programme [74]. The guiding principle for the design of this future detector is to maintain, or ideally improve, the excellent performance of the VELO Upgrade-I in terms of track and vertex resolution, efficiency, and signal purity for all the benchmark physics analyses.

In this chapter, preliminary results concerning the performance expected for a future VELO in the harsh scenario of Upgrade-II are presented. In particular, the development of a new environment containing a fast simulation of the VeloPix detector together with the track reconstruction algorithm is essential in order to have a solid starting point comparable with the official LHCb simulation. The independence from the complexity of the LHCb software framework is a necessary aspect of the fast simulation, in order to guarantee maximal flexibility in the design of the new VELO. This chapter is organized as follows. Section 4.2 explains the idea of the fast simulation and its workflow. Sections 4.3 to 4.5 report the implementation of the sensor response together with the clustering process and the pattern recognition algorithm. Finally, in Section 4.6 the performances are estimated and compared with the ones from the official LHCb simulation in Upgrade-

I conditions. Then, Section 4.7 is dedicated to the measurement of the performance parameters using the TimeSpot sensor and further geometrical improvements. Finally, a preliminary study regarding the use of a new pattern recognition algorithm, suited for FPGA and aimed to supersede the current one, is reported in Section 4.8. Section 4.9 contains the final consideration about the results achieved by the fast simulation.

4.2 Fast Simulation framework

The fast simulation framework aims at reproducing the official LHCb simulation for the VeloPix (VP) detector described in Ref. [130] in a less complex environment.

The official Monte Carlo (MC) simulations of events in LHCb proceed in three stages. The `Gauss` application [131] covers the generation of primary collisions and the transport of the emerging final states particles through the detector geometry using the `Geant4` toolkit. In all volumes which are flagged as sensitive, the entry and exit point of a traversing particle as well as the energy deposited by the particle are stored in a `MChit` object. In the `Boole` application, the `MChits` are processed and the response of detector and front-end electronics is simulated using sub-detector specific algorithms. The output of `Boole` are raw banks in the same format as those used in the DAQ system for real data. The `Brunel` application decodes the raw data and performs the event reconstruction including the clustering, the pattern recognition and track fit algorithms.

The fast simulation reproduces faithfully the VeloPix geometry as demonstrated in Figure 4.1 where fast simulation and official design are compared. Flexibility in the design has been also implemented in the code for the fast simulation, in particular different z positions are allowed together with the possibility to rotate each module by a certain angle, looking for an optimal design.

To obtain reliable results, the information on the MC particles generated in the `Gauss`+`Geant4` simulation stage is used as input for the fast simulation. All the particles, including the secondary ones produced in the interaction with the LHCb material, are considered. Indeed, two input methods are developed considering `MCparticles` or `MChits`. The first method consists in simulating the propagation in the 3-dimensional space and the passage through matter of charged particles. A simplified simulation of the passive material for the account of multiple scattering effects, concerning the RF foil and the VP modules, have been also considered. The deposit of charge in the VP sensitive volumes results in the creation of `MChits`. The second method instead uses as input directly the `MChit` information computed in the official `Gauss`+`Geant4` LHCb simulation. Consequently, it relies on a more accurate simulation of multiple scattering effects. Independently from the methods, once the charge is deposited in the VP active material from `MChits` information, the sensor response and the digitisation are simulated. Reconstruction algorithms such as the clustering process for the creation of reconstructed hits and the pattern recognition of approximately straight lines are then

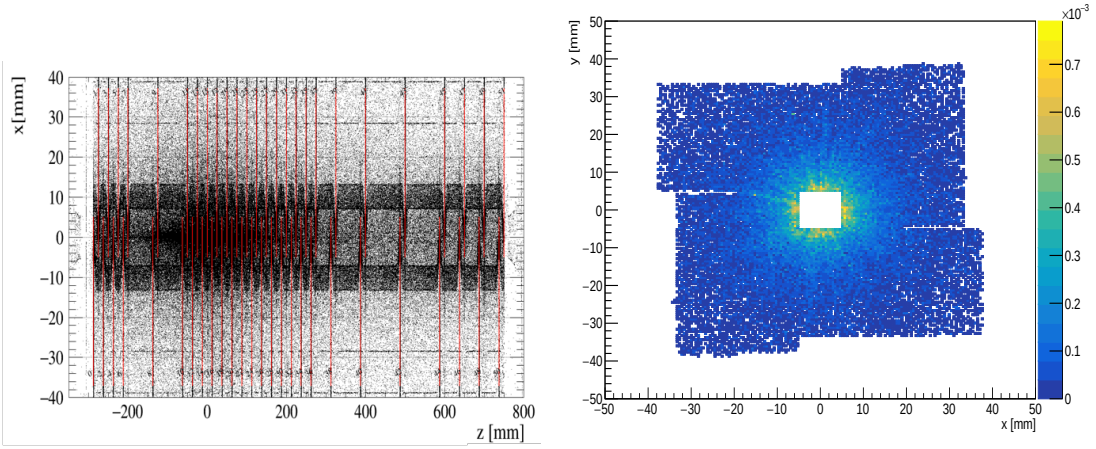

Figure 4.1: (left) Representation in the zx plane of the VeloPix detector by means of origin vertex positions of prompt and secondary particles as simulated in the official LHCb simulation. The region close to (0,0) identifies particles originated in the primary vertex, while secondary particles originated from the interaction with the RFfoil and the VELO material highlight the detector modules. The VeloPix modules, as modeled in the fast simulation, are represented with red lines. (right) Distribution of the active pixels in the (x, y) plane for all the modules.

run to obtain track candidates. Both methods are validated and described more in detail in the following.

4.3 MCparticles as input

In this approach, all the charged particles present in the Gauss+Geant4 simulation are considered, including the ones created in interactions with material. They are protons, kaons, pions, muons and electrons but also α particles and other charged nuclei. Each particle is propagated in the 3-dimensional space following

$$\begin{aligned} x(z) &= x_{OV} + p_x/p_z\,(z - z_{OV}), \\ y(z) &= y_{OV} + p_y/p_z\,(z - z_{OV}), \end{aligned} \tag{4.1}$$

with $\vec{p} = (p_x, p_y, p_z)$ being the generated momentum of the particle and $\overrightarrow{OV} = (x_{OV}, y_{OV}, z_{OV})$ its *origin vertex*. The trajectory of the particle is calculated until it decays into other particles or it is absorbed by material. This information is given by the *end vertex* position.

When a charged particle crosses a material, it is generally characterized by a loss of energy and a deflection from its incident direction. This is a consequence of inelastic

collisions with the atomic electrons and elastic scattering with nuclei. These effects are described in detail in Ref. [31] and simulated.

4.3.1 Charge deposit

The mean energy loss through ionization by a moderate relativistic ($0.1 \leq \beta\gamma \leq 1000$) heavy particle with charge z and velocity β in a medium with atomic number Z and mass number A is well described by the Bethe-Bloch equation

$$\left\langle -\frac{dE}{dx} \right\rangle = Kz^2 \frac{Z}{A} \frac{1}{\beta^2} \left[\frac{1}{2} \ln \frac{2m_e c^2 \beta^2 \gamma^2 W_{max}}{I^2} - \beta^2 - \frac{\delta(\beta\gamma)}{2} \right], \tag{4.2}$$

with dE/dx being the *mass stopping power* in units MeV g^{-1} cm^2 and

$$W_{max} = \frac{2m_e c^2 \beta^2 \gamma^2}{1 + 2\gamma m_e/M + (m_e/M)^2}, \tag{4.3}$$

while the others parameters are defined in Table 4.1. As shown in Figure 4.2, $\langle -dE/dx \rangle$ presents same dependencies for most materials, decreasing slowly with Z. At low velocity ($\beta\gamma \sim 0.1$), the projectile velocity is comparable to atomic electron "velocities" and the energy loss is governed by a factor $1/\beta^2$. For higher velocities relativistic effects take place and, after a point of minimum, called MIP (Minimum Ionizing Particle), a logarithmic rise begins. The last component in Eq. 4.2 is the *density correction*, due to the polarization of the atoms in the material once the particle crosses it. Polarized atoms act as shield for furthest atoms, reducing in this way the long range interaction of particles. This effect is larger for large $\beta\gamma$ values.

In this formulation, the mean energy loss rate $\langle -dE/dx \rangle$ does not depend on the thickness of the traversed material. However, being a statistical process, this value does not give a complete picture of this phenomenon. For detectors with moderate thickness x, the energy loss probability function $f(\Delta; \beta\gamma, x)$ is adequately described by the highly-skewed Landau (or Landau-Vavilov) distribution [132, 133]. The most probable energy-loss is

$$\Delta_p = \xi \left[\ln \frac{2mc^2 \beta^2 \gamma^2}{I} + \ln \frac{\xi}{I} + j - \beta^2 - \delta(\beta\gamma) \right], \tag{4.4}$$

where $\xi = \frac{K}{2} \frac{Z}{A} z^2 \frac{x}{\beta^2}$ (in MeV for x in gcm^{-2}) and $j = 0.200$ [134]. While $\langle -dE/dx \rangle$ is independent from thickness, Δ_p/x scales as $a \ln x + b$. The energy loss probability distribution is asymmetric. The mean and the value with higher probability do not correspond and the full width at half maximum (FWHM) of the Landau-Vavilov function is about 4ξ for detectors of moderate thickness. The function $f(\Delta; x)$ is represented in Figure 4.3 for pions of 500 MeV traversing layers of different thickness.

Symbol	Definition	Value or (usual) units
$m_e c^2$	electron mass $\times$ c^2	0.5109989461 (31) MeV
r_e	classical electron radius	
	$e^2/4\pi\epsilon_0 m_e c^2$	2.8179403227(19) fm
α	fine structure constant	
	$e^2/4\pi\epsilon_0\hbar c$	1/137.035999139(31)
N_A	Avogadro's number	$6.022140857(74)\cdot 10^{23}$ mol-1
ρ	density	g cm^{-3}
x	mass per unit area	g cm^{-2}
M	incident particle mass	MeV/c^2
E	incident particle energy γMc^2	MeV
W	energetic transfer to an electron in a single collision	MeV
W_{max}	maximum possible energy transfer to an electron in a single collision	MeV
z	charge number of incident particle	
Z	atomic number of absorber	
A	atomic mass of absorber	g mol^{-1}
K	$4\pi N_A r_e^2 m_e c^2$ (coefficient for dE/dx)	0.307075 MeV mol^{-1} cm^2
I	mean exitation energy	eV
$\delta(\beta\gamma)$	density effect correction to ionization energy loss	
X_0	radiation length	g cm^{-3}
$(4\alpha r_e^2 N_A)^{-1}$	(coefficient for X_0)	716.408 g cm^{-3}

Table 4.1: Summary of variables used in this section. The kinematic variables β and γ have their usual relativistic meanings.

In the current simulation, the energy loss of each charged particle traversing a sensitive silicon layer of 200 μm is sampled from a Landau distribution parametrized through Δ_p and ξ in the ROOT data analysis framework[1].

4.3.2 Multiple Scattering

A charged particle traversing a medium is deflected by many small-angle scatters. Most of these deflections are due to Coulomb scattering from nuclei as described by the Rutherford cross section. For many small-angle scatters the net scattering and displacement

[1] https://root.cern.ch/doc/master/QuantFuncMathCore_8cxx_source.html#l00189

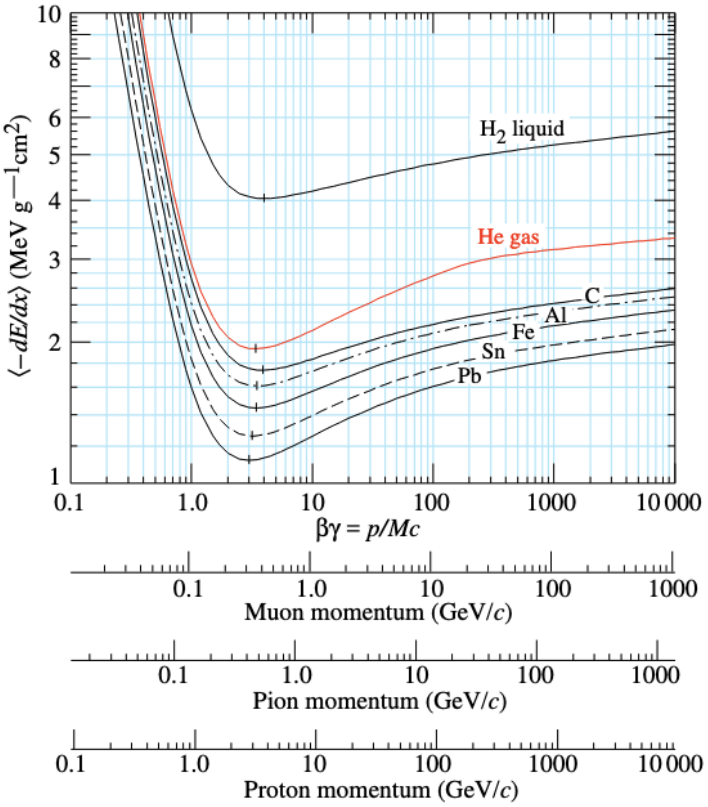

Figure 4.2: Mean energy loss rate in liquid (bubble chamber) hydrogen, gaseous helium, carbon, aluminum, iron, tin, and lead. Radiative effects, relevant for low momenta muons and pions in high-Z absorbers, are not included.

distributions are Gaussian via the central limit theorem. Less frequent "hard" scatters produce non-Gaussian tails. These Coulomb scattering distributions are well-represented by the theory of Molière [135]. If one define

$$\theta_0 = \theta_{plane}^{RMS} = \frac{1}{\sqrt{2}}\theta_{space}^{RMS}, \tag{4.5}$$

then it is sufficient for many applications to use a Gaussian approximation for the central 98% of the projected angular distribution, with an RMS width given by Lynch & Dahl [136]

$$\theta_0 = \frac{13.6\,\text{MeV}}{\beta cp} z \sqrt{\frac{x}{X_0}} \left[1 + 0.038 \ln\left(\frac{xz^2}{X_0\beta^2}\right)\right]. \tag{4.6}$$

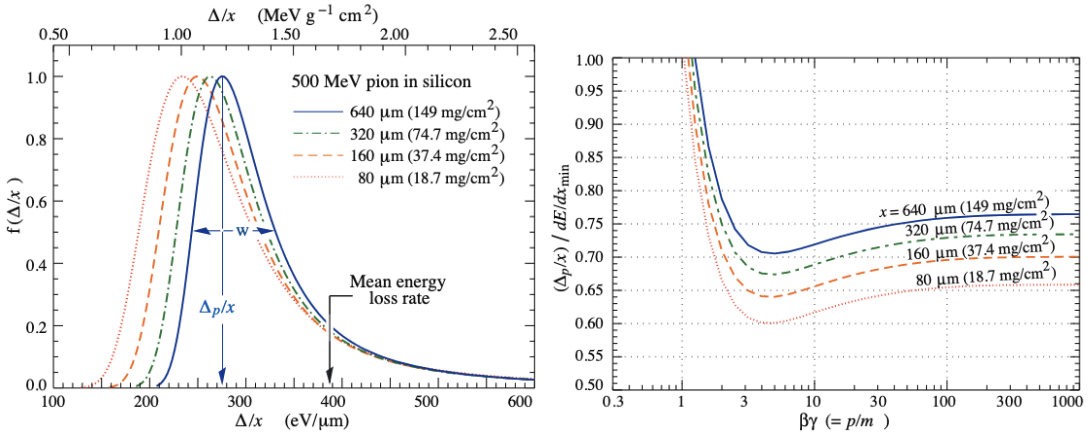

Figure 4.3: (left) Energy loss probability distribution in silicon for 500 MeV pions normalized to unity at the most probable value (Δ_p/x). W represents the FWHM. (right) most probable value of energy-loss scaled to the mass stopping power at the minimum in terms of $\beta\gamma$.

Here p, βc, and z are the momentum, velocity, and charge number of the incident particle, and x/X_0 is the thickness of the scattering medium in radiation lengths given by

$$X_0 \approx \frac{A(4\alpha r_e^2 N_A)^{-1}}{Z(Z+1)\ln(287)/\sqrt{Z}}. \tag{4.7}$$

In addition to the angular deviation θ_{plane}, multiple Coulomb scattering is also described with other quantities such as s_{plane}, Ψ_{plane} and y_{plane}, graphically represented in Figure 4.4. In particular

$$\Psi_{plane}^{RMS} = \frac{1}{\sqrt{3}}\theta_{plane}^{RMS} = \frac{1}{\sqrt{3}}\theta_0, \tag{4.8}$$

$$y_{plane}^{RMS} = \frac{1}{\sqrt{3}}x\theta_{plane}^{RMS} = \frac{1}{\sqrt{3}}x\theta_0, \tag{4.9}$$

with $y = x\Psi$ and y and θ having the correlation coefficient $\rho_{y\theta} = \sqrt{3}/2 \approx 0.87$. For Monte Carlo generation of a joint $(y_{plane}, \theta_{plane})$ distribution it is convenient to work with independent Gaussian random variables z_1 and z_2, with zero mean and unitary variance, and then set

$$\begin{aligned} y_{plane} &= z_1 x\theta_0(1-\rho_{y\theta}^2)^{1/2}/\sqrt{3} + z_2\rho_{y\theta}x\theta_0/\sqrt{3}, \\ &= z_1 x\theta_0/\sqrt{12} + z_2 x\theta_0/2, \\ \theta_{plane} &= z_2\theta_0. \end{aligned} \tag{4.10}$$

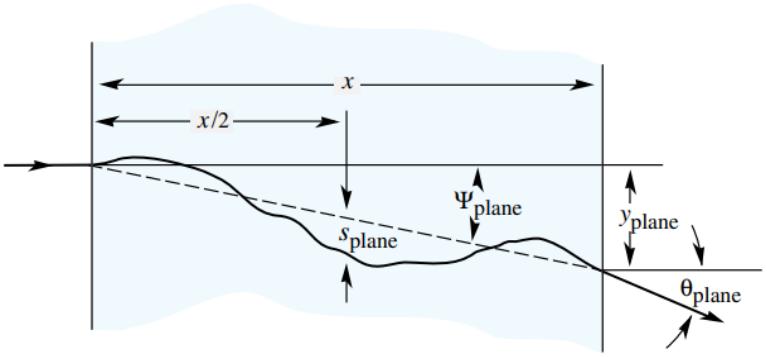

Figure 4.4: Schematic representation of deviations through small angles of incident particle passing through a medium of thickness x.

Note that the second term for y plane equals $x\theta_{plane}/2$ and represents the displacement that would have occurred had the deflection θ_{plane} all occurred at the single point $x/2$.

In the current simulation, Multiple Scattering effects are accounted for in the interaction with the RF foil and the VP modules following the previous instruction for $(y_{plane}, \theta_{plane})$ in the independent planes xz and yz. As a consequence, a translation of the origin vertex position $\overrightarrow{OV} \to \overrightarrow{OV'}$ joined with a rotation of the momenta $\vec{p} \to \vec{p'}$ is applied, modifying the equation describing the propagation of the particle through space (Eq. 4.1). Here, the RF foil is approximated as an aluminium cylinder with radius 5 mm and width 350 µm. While each module is simulated as a silicon layer 800 µm thick. The comparison between the geometries developed in the official LHCb simulation and in the fast simulation is shown Figures 4.5 and 4.6. As one can notice, they correspond to a huge simplification of the real geometry. The idea of having thicker modules than in reality arises from the necessity to compensate the missing RF foil material surrounding each module (see Figure 4.1) which is not reproduced in the cylindrical modelisation. However, although these geometries are clearly imperfect, they result to be sufficient for a reasonable evaluation of the performances as reported in Section 4.6.

Since tracks originating from secondary vertices with large impact parameters are the principal signature of beauty and charm hadrons decaying in LHCb, the impact parameter resolution is an excellent benchmark performance number for a new detector. The impact parameter resolution is well described to first order by the following expression.

$$\begin{aligned}\sigma_{IP}^2 &= \sigma_{MS}^2 + \sigma_{extrap}^2, \\ &= \frac{r_1^2}{p_T}\left(0.0136\,\text{GeV}/c\sqrt{\frac{x}{X_0}}\left(1+0.038\ln\frac{x}{X_0}\right)\right)^2 + \left(\frac{\Delta_{02}^2\sigma_1^2\Delta_{01}^2\sigma_2^2}{\Delta_{12}^2}\right).\end{aligned} \tag{4.11}$$

This formula gives an indication of the driving factors behind the design. Indeed, the first term arises from multiple scattering effects and is proportional to $1/p_{\mathrm{T}}$ of the track,

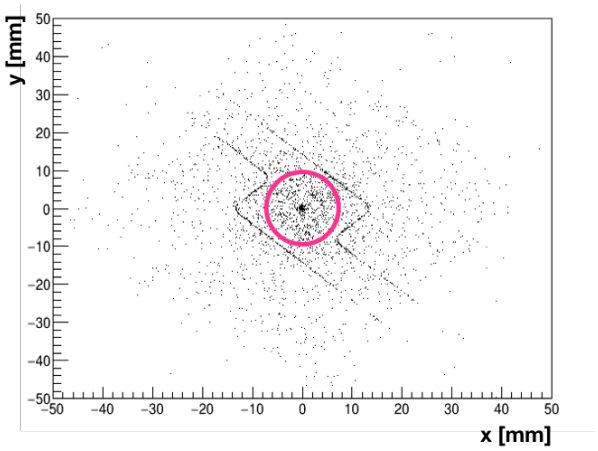

Figure 4.5: RF foil representation by means of origin vertex positions of secondary particles as simulated in the official LHCb simulation (black dots) with its geometrical representation in the fast simulation (red cylinder) overlaid.

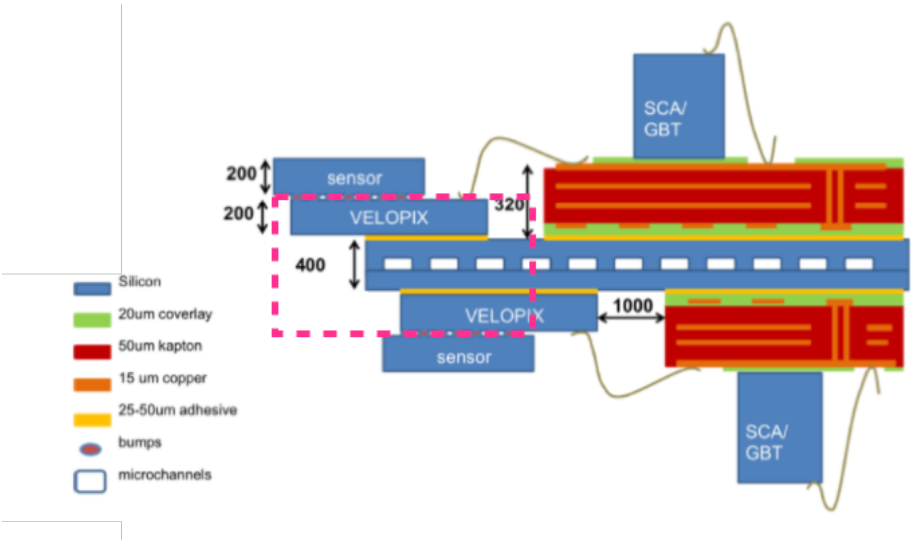

Figure 4.6: Transverse profile of a VP module with its geometrical representation in the fast simulation (red dashed rectangle) overlaid.

while the second term is a constant contribution depending on geometrical factors. Here, r_1 is the radius of the first measured point on the track; x/X_0 is the fractional radiation length before the second measured point, which includes the foil, any dead area of silicon traversed, and the material of the first measured point; σ_1 and σ_2 are the errors on the first and second measurement points, respectively; and Δ_{ij} represents the distance between i and j, where i and j can be 0 (the vertex), 1 (the first measured point), or 2 (the second

measured point). The presence of the r_1^2 term indicates that the first measured point should be as close to the interaction point as possible, which is achieved by designing the minimum possible inner dimensions, reducing the size of the guard rings, and having as many stations as possible. The presence of the $\sqrt{x/X_0}$ term shows on the other hand, the importance of reducing the material budget, *i.e.* decreasing the number of stations, having the stations as thin as possible, or diminishing the material contribution of the RF foil. The final term σ^2_{extrap} illustrates the importance of maintaining the best possible precision, especially for tracks with high momentum where contributions from multiple scattering can be neglected..

The dependence of the impact parameter resolution as a function of $1/p_{\mathrm{T}}$ is therefore an important variable to investigate the impact of the material budged of the detector. In particular, it is important to check that the simulated multiple scattering effects are consistent with the one obtained in the official LHCb simulation. Figure 4.7 reports $\sigma(IP_x)$ as a function of $1/p_{\mathrm{T}}$ as measured in the fast simulation and compared with the official results. As one can notice, the impact parameter resolution is well reproduced.

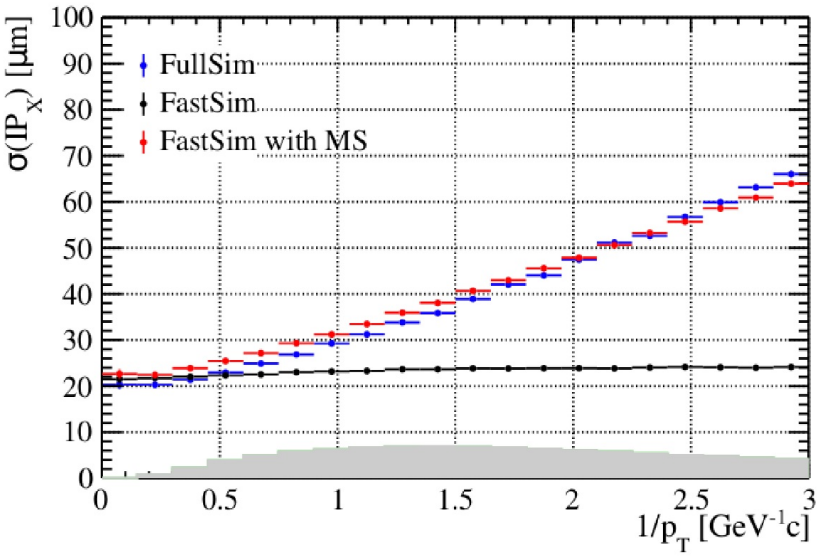

Figure 4.7: Resolution on the impact parameter along the x axis as a function of $1/p_T$ in the (blue) official LHCb simulation and in the fast simulation (red) with and (black) without the Multiple Scattering effects applied to the particles.

4.3.3 Pros and cons

The simulation framework working with `MCparticles` is very flexible since any parameter concerning the design of the detector can be modified quickly. However, one can observe that *origin* and *end* vertices of the particles in input may depend on the geometry used

for the LHCb detector in the Gauss+Geant4 simulation, in the case they are produced in material interactions or absorbed. For this reason, it can be better used for studies involving only promptly produced particles where the dependence from the geometry is negligible. As an example, it can be used for the optimization of the z positions for a 4D real time device using FPGA implementing the algorithm described in Section 4.8. Anyway, if the geometry of the fast simulation is perfectly aligned with the official one then reliable results are obtained. In fact, MCparticles contains all the particles including the secondary ones, generated from the interaction with the material described in the Geant4 LHCb simulation, such as the RF foil. Secondary particles are about the 28% of the charged particles produced in a pp collision and are particularly important in order to correctly reproduce tracking performances. In fact, being low momentum particles of no physics interest, they contribute to increase the occupancy of the modules worsening the combinatorial problem that the reconstruction algorithm has to break down.

Considerable effort has gone into making the description of the simulation of LHCb, in particular the RF foil, in order to have a complete description of the effects arising from the interaction with passive material. For this reason, MChits coming directly from the official Gauss+Geant4 simulation stage has to be preferred as input for the fast simulation.

4.4 MChits as input

In this approach, MChits coming from the official Gauss+Geant4 simulation or from the previous method using MCParticles are used as input. The energy lost by the particle traversing the VP material is transformed in deposited charge in the relevant pixels and digitized realizing a bitmap for each module that will be used in the reconstruction step. The simulation of the VP sensor response is inherited from Boole/v40r4 [130] and described in the following.

4.4.1 Sensor response

For each MChit, the number of electron-hole pairs n released in the sensor is calculated according to

$$n = \Delta E / W, \tag{4.12}$$

where ΔE is the deposited energy (obtained from MChit) and $W = 3.6$ eV is the average energy required to produce an electron-hole pair in Silicon.

In order to simulate spatial fluctuations of the deposited charge within the sensor, the trajectory between entry and exit point of the MChit is divided into equally sized intervals with a length given by StepSize $= 5$ µm, as shown in Figure 4.8. The most

probable number of electrons deposited within one interval, n_{mp}, is given by

$$n_{\text{mp}} = \texttt{ChargeUniform} \cdot \texttt{StepSize}, \tag{4.13}$$

with `ChargeUniform` = 70 electrons/ µm. In the first pass, the number of electrons n_i assigned to each interval i is sampled from a Gaussian distribution with mean n_{mp} and standard deviation $\sigma = \sqrt{n_{\text{mp}}}$. If the total amount of charges $\sum_i n_i$ allocated by this method is less than n, an additional amount of charge, sampled from a $1/n^2$ distribution (with a lower cut-off given by the parameter `MinChargeTail` = 10 electrons) is added to one of the intervals, randomly chosen. This step is repeated until $\sum_i n_i > n$. Finally, the charges n_i, assigned to the intervals are scaled such as their sum matches n. Figure 4.9 (left) shows the distribution of the charge deposited per interval.

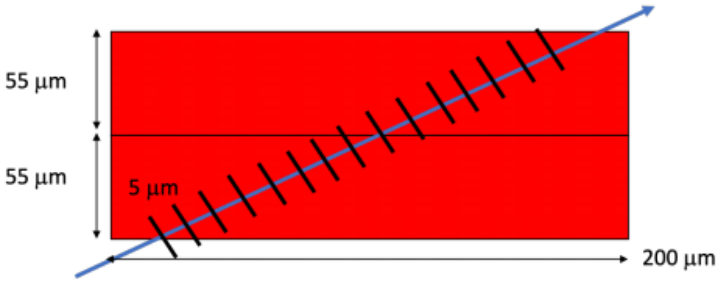

Figure 4.8: Schematic view of the passage of a particle through two adjacent pixels in the VP sensor.

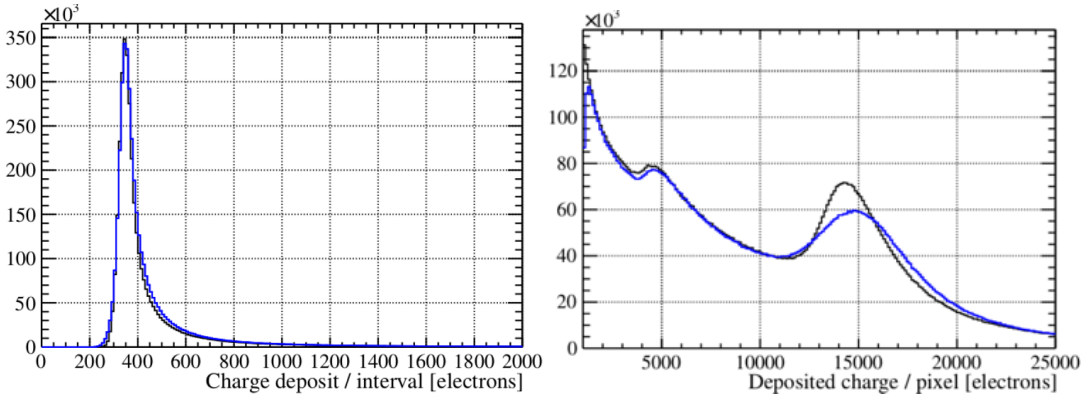

Figure 4.9: Charge deposit in terms of number of electrons produced by the passage of a particle (left) in a interval of 5 µm and (right) in a pixel. The (black) fast simulation with `MCParticles` as input is compared with the (blue) official LHCb simulation. Similar results are obtained with `MCHits` as input.

Next, the drift and diffusion of the charge carriers are simulated. For this purpose the charges n_i are sub-divided into five "lumps". For each of these "lumps", random

uncorrelated diffusion steps Δx, Δy are sampled from a Gaussian distribution with standard deviation $\sigma = D\sqrt{\Delta z}$, where Δz is the distance of the centre of interval i to the front side (*i.e.* the pixel implant side) of the sensor. For the diffusion coefficient D, the following expression is used

$$D\sqrt{\frac{2k_BTd}{qV_{\text{bias}}}}, \tag{4.14}$$

where k_B is the Boltzmann constant, T is the temperature parameter (-20° C), V_{bias} is the applied bias voltage (105 V) and d the sensor thickness (200 µm). Eq. 4.14 assumes that diffusion coefficient D and mobility μ are related by the Einstein relation $D = \mu k_BT/q$, and that the electric field is uniform and given by V_{bias}/d, which is a reasonable approximation.

In the simulation, the VP modules are represented as 2-dimensional histograms where each pixel represents a bin of size 55×55 µm ^{2} reproducing the sensitive area of the sensors. During the simulation of an event, the contributions of all the `MChits` are used to "fill" the modules with a certain amount of charge which is deposited in a certain pixel, every time the generated (x, y) positions fall into its region. The distribution of the charge accumulated in one pixel after the passage of a particle is shown in Figure 4.9. In this figure, it is possible to observe a pronounced peak at about 15 000 electrons, corresponding to a particle crossing just one pixel without depositing energy to any of its neighbours. The peak at 5 000 electrons represents instead the case of a particle crossing two neighbouring pixels while the large amount of low deposited energy is given by particles crossing more than two pixels and diffusion effects. Finally, one can notice that the distributions obtained for the charge deposit with the fast simulation are not in perfect agreement with the ones obtained from the official simulation. These inconsistencies arise from effects that are not simulated in this context, such as the radiation damage that is expected to increase the diffusion of electrons, which are present in the official simulation. However, this simulation allows to obtain reliable results in terms of detector performance as shown in Section 4.6.

Given that the VeloPix ASIC operates in binary readout mode in normal data taking, the total charge must be compared to a threshold value (`ChargeThreshold` = 1000 electrons) in order to transform the histogram in a bitmap. Moreover a noise term accounting for the electronic noise should be added by sampling from a Gaussian distribution with a standard deviation σ given by the parameter `ElectronicNoise` (130 electrons). In "real-life", VeloPix ASIC produces super-pixel packets grouping together arrays of 2×4 pixels and corresponding to a 32-bit word. For each VP sensor, super-pixels are arranged in a raw bank, where only active super-pixel are listed (zero suppression). The simulation of the raw bank format can be useful for performance studies of FPGA-based clustering algorithms, such the one reported in Ref. [137]. However, this level of complexity is not needed for the purpose of this work and so neglected.

All the parameters used to describe the VP sensor response and digitization are

summarised in Table 4.2.

Parameter	Value	Unit
`StepSize`	5	µm
`MaxNumSteps`	150	
`evPerElectron`	3.6	eV
`ChargeUniform`	70	electrons/ µm
`MinChargeTail`	10	electrons
`Temperature`	253.15	K
`BiasVoltage`	105	V
`ChargeThreshold`	1000	electrons
`ElectronicNoise`	130	electrons

Table 4.2: Parameters of the algorithm used to describe the deposit of charge in the VP sensor and its digitization.

The pixel occupancy defined as the probability of a pixel being active is measured for the station closest to the interaction point (where it is expected to be the highest) as a function of the radial distance from (0,0) in the Upgrade-I scenario and reported in Figure 4.10. The pixels in this station, which are closest to the beam line, exhibit an occupancy of ∼0.12% while it decreases as a function of radius as the pixel pitch is constant over the whole detector. This is in agreement with what stated in Ref. [95] for Upgrade-I conditions.

4.4.2 Monte Carlo truth association

While the information from `MChits` is used to deposit charge into the pixels of the detector, a vector representing the true tracks `MCTracks` is created. This container is necessary to obtain benchmarking quantities when compared with the reconstructed tracks, referred to as `Tracks`. Each `MCTrack` contains the information of the `MCparticle` together with the collection of the `MChits` produced by the particle in the interaction with the VP layers. Here, the `MChit` encloses the information of all the pixels where non-zero charge has been released. In particular, each pixel is identified by means of the so-called `channelID`.

4.5 Track reconstruction

The reconstruction of a track starts from the clustering of the active pixels creating a set of reconstructed hits. These are then combined together in the pattern recognition algo-

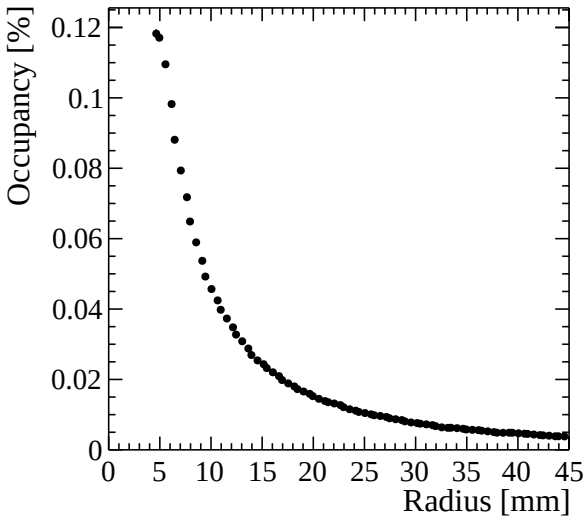

Figure 4.10: Pixel occupancy measured in the station closest to the interaction point ($z = 0$) as a function of the radial distance from (0,0) in Upgrade-I scenario conditions.

rithm in order to form realistic tracks. The track reconstruction algorithm is inherited from `RecDev/v30r6p1` and `Brunel/v60r6p1` [130] and described in the following.

4.5.1 Clustering

Clustering is the process of identifying groups of neighbouring pixels on one sensor. In this simplified simulation, the cluster finding algorithm is applied in each VP module, instead of each sensor, avoiding double counting effects from neighbouring pixels belonging to different sensors[2]. A cluster is defined as an isolated group of eight-way connected active pixels. This means that diagonal neighbours are treated at the same way as horizontal and vertical neighbours. Thus, a pixel in the centre of the layer has eight neighbours (hence the name), a pixel at the edge has five and a corner pixel has three. Clusters are allowed to have arbitrary size. Figure 4.11 depicts a few examples of possible clusters.

Since in normal data taking conditions the pixel readout is binary, the pixel on a module can therefore be represented by a two-dimensional array of bit. This representation corresponds to a black-and-white bitmap image of the pixel grid on a module, as shown in Figure 4.11. The task of finding clusters then correspond to the problem of finding all groups of connected "black" pixels in the bitmap. In this simulation, the clustering

[2]However, in "real-life" VP this effect is expected to be modest as the occupancy of pixels in the region in between two sensors is smaller than that of the central pixels by a factor 0.1 or less.

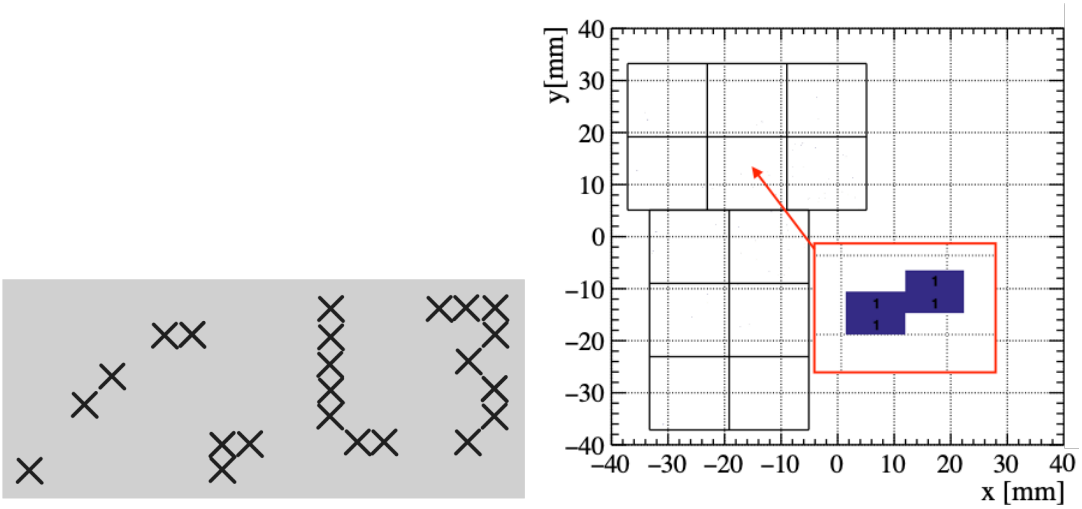

Figure 4.11: Example of possible (left) eight-way connected clusters and (right) bitmap image of the active pixel grid on a module.

is implemented with the following recursive approach where a loop in the pixels of the bitmap is done.

1. if a pixel is found to be active, create a cluster and

- **a)** add the pixel to the cluster;
- **b)** remove the pixel from the bitmap;
- **c)** make a loop on the eight-way connected neighbours of the pixel in the bitmap; if an active pixel is found, repeat the instructions from a).

2. store the cluster and move to the next pixel.

Adding a pixel to a cluster involves maintaining the sums of x and y coordinates of all contributing pixels and keeping track of the cluster size. This is necessary to compute the centre of the cluster after it is finished.

Figure 4.12 on the left shows the distributions of the differences between the global x coordinates of the reconstructed cluster and the coordinates of the associated simulated hit. Similar results are found for y coordinates. Hit resolution distributions for single-pixel clusters and two-pixel clusters are also shown. They constitute ∼47% and ∼36% of all clusters, respectively, as can be seen from Figure 4.12 on the right. Averaging over all cluster sizes, the RMS of the residual distribution is found to be approximately 12 µm in both x and y.

At the end of the clustering process, a set of `Hits`, each of them containing the 3-dimensional coordinates of the cluster center and the `channelIDs` of the corresponding

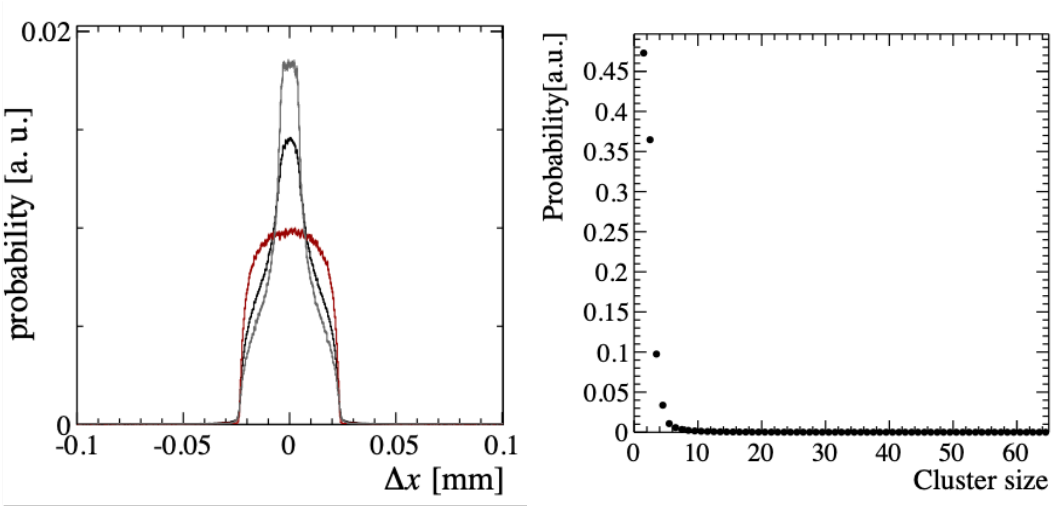

Figure 4.12: (left) residual distribution of global x-coordinates for (red) single-pixel clusters, (grey) two-pixel clusters and (black) all clusters. (right) distribution of cluster sizes in Upgrade-I events.

pixels, is created for each module. A transformation from local to global coordinates is also applied for the purpose of the track finding algorithm.

4.5.2 Patter recognition

The VP pattern recognition employs a local track following method. Track candidates are seeded by looking for pairs of unused hits on neighbouring same-side modules which are compatible with track slopes in the LHCb acceptance, *i.e.* $|dx/dz| < 0.4$ and $|dy/dz| < 0.4$. The search starts from downstream, *i.e.* at the module with the largest z-position: the algorithm first searches for (and extrapolates) pairs of hits on modules 52 and 50, followed by pairs of hits on modules 51 and 49, and so on. This seed track is then extrapolated in the upstream direction and the extrapoled position x_p, y_p on the next same-side module is calculated, as shown in Figure 4.13. The closest hit within a search window around the predicted position on a sensor is added if it passes a cut on the maximal scattering angle. If no compatible hit is found the search is extended to modules on the other side. The search is abandoned if no hits on three consecutive stations have been found.

Track candidates with less than three hits are rejected. In case of tracks comprising only three hits, a cut on the track χ^2 (obtained from a least-squares straight-line fit) is applied[3]. If the candidate track passes all the requirements, all the hits on the track are

[3]At present the hit position errors (which are used for calculating the weights in the track fit) are approximated by $\Delta x = \Delta y = p/\sqrt{12}$ where p is the pixel pitch (55 µm for the VP sensor).

tagged as used. The search continues until the end of the forward region of the detector ($z > -100$ mm) and then starts again from upstream, *i.e.* from the backward region of the detector ($z < 100$ mm).

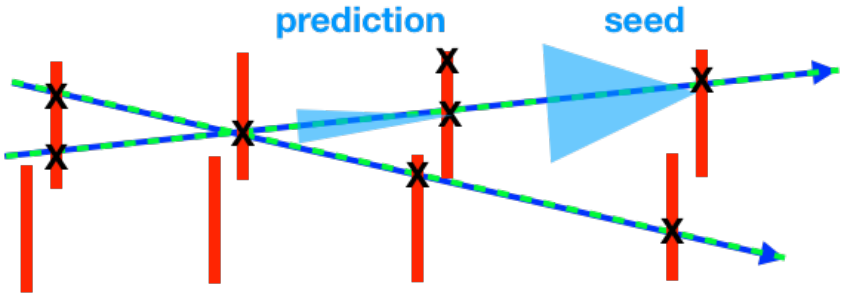

Figure 4.13: Sketch representing the track following method applied for VP track finding. Blue arrows represent particle traversing the VP stations, X(s) represent hits on the modules and green dashed lines the reconstructed tracks.

As a result of this process, each temporary track object corresponding to a collection of `Hits` is stored in the container `Tracks`. The structure of `Tracks` is identical to `MCTracks` with the difference that the information regarding the `MCParticle`(s) which originated the track is lost. If the z-position at which the track is closest to the beam line is larger than the maximal z-coordinate of all measurements, the track is flagged as a backward track, otherwise it is flagged as a forward track.

4.6 Performances and validation

This section covers the performance evaluation of the Upgrade-I VELO with the presented simulation and its validation with respect to the official LHCb simulation. Key measures of the performance include track reconstruction efficiency and ghost probability. Other important quantities such as the impact parameter resolution, the pixel occupancy and the hit resolution which do not have any dependence on the track reconstruction algorithms but only depend on the design of the detector have already been introduced and shown in Figures 4.7, 4.10 and 4.12, respectively.

The performance of the pattern recognition algorithm is measured in simulation by comparing correctly reconstructed tracks with reconstructible tracks obtained from truth information. The following definitions, inherited from the official LHCb tracking framework, are used:

- A particle (`MCTrack`) is reconstructible if it has `MCHits` on three or more modules.
- A particle (`MCTrack`) is considered reconstructed if at least 70% of the hits on a

track (`Track`) are associated to this particle. Here, a `MCHits` is matched to a `Hit` if they share at least one `channelID`, *i.e.* one pixel.

- If more than one reconstructed track (`Track`) is associated to a particle (`MCTrack`) the extra tracks are counted as clone tracks.
- A ghost track or fake track is a track (`Track`) which can not be associated to any simulated particle (`MCTrack`).

Finally, the pattern recognition *efficiency* is defined as

$$\frac{\text{N of reconstructed } \texttt{MCTracks} \text{ associated with at least one } \texttt{Track}}{\text{N of reconstructible } \texttt{MCTracks}}. \tag{4.15}$$

This parameter can be calculated for several sub-sample of particles (`MCTracks`), such as the VELO particles defined as a forward particle with pseudo-rapidity $2 < \eta < 5$ and not being an electron. These criteria select with a very high purity interesting particles from the point of view of the LHCb physics programme. Electrons are excluded due to the massive presence of secondary particles, such as δ-rays[4], which have no physical interest. Another category may be the long particles, defined as the one having hits also in the tracking layers downstream the LHCb magnet as shown in Figure 2.10. Since these objects are not simulated in the fast simulation, a definition consistent with the official one can not be applied. However, the VELO track efficiency is more than sufficient and will be considered as the preferred benchmark. The second important figure of merit is the *ghost probability*, given by

$$\frac{\text{N of reconstructed } \texttt{Tracks} \text{ not associated with any } \texttt{MCTrack}}{\text{N of reconstructed } \texttt{Tracks}}. \tag{4.16}$$

In addition to assuring analysts of the good quality of the data collected, it is particularly important to estimate the performance of the full LHCb track reconstruction at Hlt1 level where a combination between the tracks built in the different sub-detectors is done in order to create the final LHCb tracks. The higher the ghost rate is in the VELO, the more VELO tracks will not be matched with tracks from the other sub-detectors and then the more time will be needed for this process to be completed by the computing farm.

It is also interesting to investigate the performance as a function of the number of reconstructed primary vertices. This gives an indication of the robustness against pile-up. A reconstructed primary vertex (PV) is defined in the LHCb framework as a primary vertex with at least 4 reconstructed true tracks[5]. Figure 4.14 shows the behaviour of the tracking efficiency and ghost rate as a function of the number of PVs for the fast

[4]Ionization products with enough energy to exit from medium.

[5]The information of the primary vertex is also stored in `MCParticle` and as a consequence in `MCTrack`.

simulation together with the official one. As expected the two parameters are sensitive to the number of primary vertices. In fact, it can be seen that the performances get worse as the pile-up increases, as a consequence of the rise of the possible combinations. Integrated values for the performance parameters are reported in Table 4.3 for the official and fast simulation. They are about 98% and 0.5% for VELO efficiency and ghost rate, respectively.

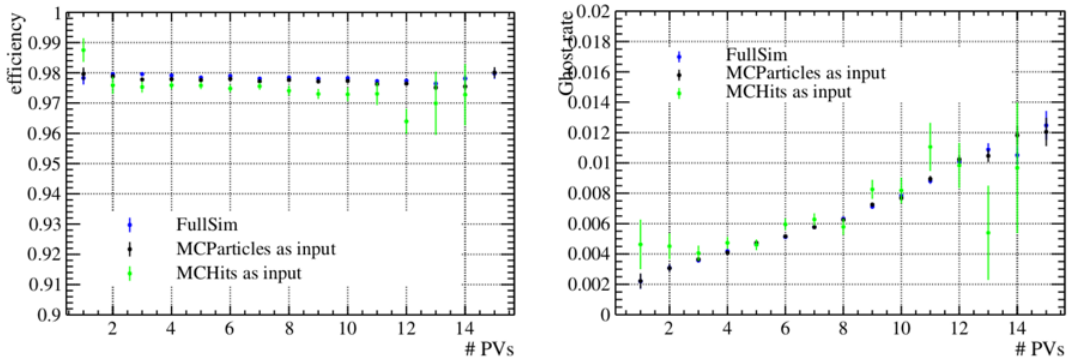

Figure 4.14: Pattern recognition performance of the Upgrade-I VELO as function of the number of primary vertices measured with the (blue) official LHCb simulation and the fast simulation with (black) `MCParticles` and (green) `MCHits` as input. (left) Reconstruction efficiency for VELO particles. (right) Ghost rate. Simulated events containing $B^0 \to K^* \mu^- \mu^+$ decays are used.

Upgrade-I Simulation	VELO efficiency[%]	Ghost Prob.[%]
Official LHCb	97.8	0.44
`MCParticles` as input	98.0	0.50
`MCHits` as input	97.8	0.48

Table 4.3: Pattern recognition performance parameters for VeloPix at Upgrade-I conditions. These parameters are measured using simulated events containing $B^0 \to K^* \mu^- \mu^+$ decays.

4.6.1 Validation

The validity of the fast simulation has been tested with a comparison with the official one in all the key quantities. In particular, the validity of the simulation of the sensor response and its digitisation is demonstrated by looking at the probability distribution of active

pixels as reported in Figure 4.15 on the top, for the Upgrade-I conditions. Similarly, the procedure of clustering and track finding are validated with the distribution of the number of reconstructed clusters and reconstructed tracks as shown in Figure 4.15 on the bottom. All the distributions are found to be compatible between the fast simulation and the official one, demonstrating that the input and the output of each algorithm are well reproduced, despite simplifications.

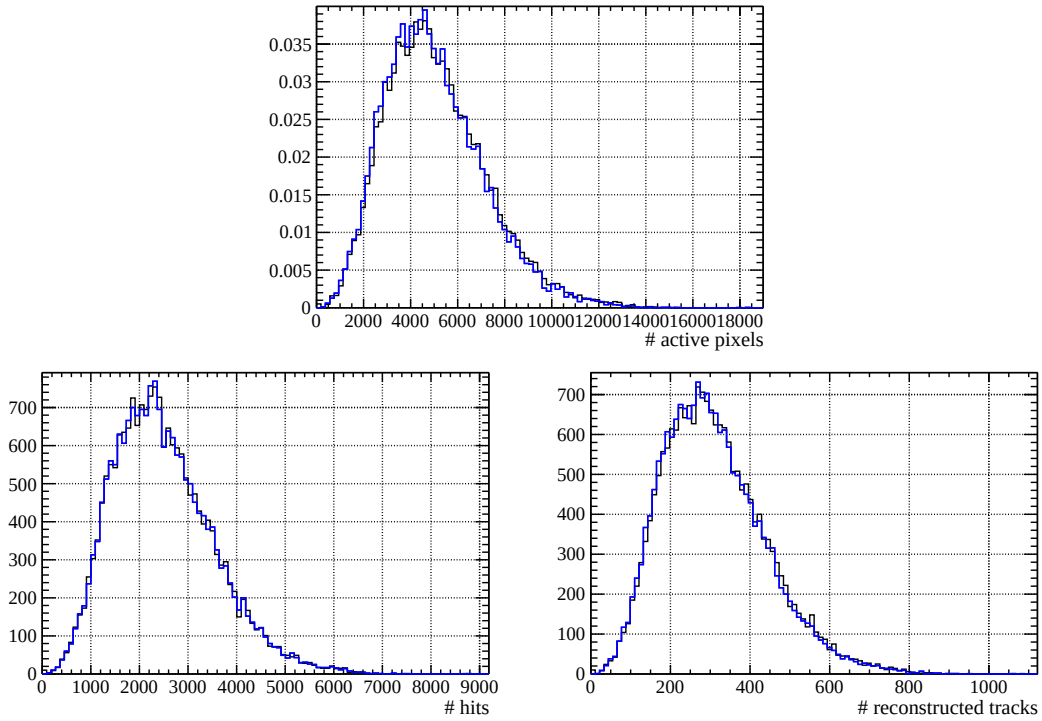

Figure 4.15: Probability distribution for the number of (top) active pixels, (bottom left) clusters and (bottom right) reconstructed tracks with (black) fast simulation with `MCParticles` as input and (blue) official LHCb simulation in Upgrade-I scenario conditions. Similar results are obtained with `MCHits` as input.

Figure 4.14 and Table 4.3 report the tracking performances measured with the fast simulation taking as input `MCParticles` and `MCHits` together with the results obtained with the official LHCb simulation. As one can notice, no significant discrepancy is present and both the methods developed for fast simulation are considered to be reliable.

4.7 The Upgrade-II scenario

The fast simulation framework presented in the previous section is now tested in the harsher Upgrade-II scenario. It is important to mention that, so far, no official LHCb

simulation can run in Upgrade-II conditions and the framework developed in this section offers a powerful probe to explore this scenario and study possible improvements.

As reported in Figure 4.16 (left), if the design of the VeloPix is maintained for the Upgrade-II VELO, the occupancy is expected to increase by about one order of magnitude with respect to Upgrade-I (see Figure 4.10 on the left). On the contrary, Figure 4.16 (right) shows that the distribution of the cluster size is almost unchanged when compared with Upgrade-I results in Figure 4.12 (right). In fact, between Upgrade-I and Upgrade-II the fraction of clusters formed that two or more pixels only changes from 53% to 55% while the fraction of pixel fired by at least two particles slightly increases from 2% to 3%, meaning that the logic of the clustering algorithm based on a bitmap image is still valid[6]. The tracking performances are reported in Figure 4.17 showing a significant worsening of efficiency and ghost probability with respect to the Upgrade-I, especially for the latter which increases of about a factor 10 bringing a huge impact on the computing time used in the Event Filter Farm.

Considering the values reported in Table 4.3 for VELO efficiency and ghost probability as a target of the future VELO in Upgrade-II conditions, improvements in detector design are needed. In particular, in this high track multiplicity environment the addition of the time coordinate in tracking algorithm is considered to be precious for the correct assignment of tracks to primary and decay vertices, as anticipated in Section 2.8, and for the reduction of combinatorial track candidates. A possible solution is using sensors with time information. A 3D pixel sensor is under development within the TimeSpot project [138] founded by INFN. Preliminary study show a time resolution of $\sim$15 ps and a good radiation tolerance [105]. In the following, the simulation of this sensor is introduced while the geometry of the detector is maintained. Even if both the methods for fast simulation are reliable and give similar results, only `MCHits` as input will be considered for a better description of the multiple scattering effects and a more accurate estimation of the time assigned to each hit by `Geant4`.

4.7.1 The TimeSpot sensor

In a silicon sensor, the time of response is proportional to the inter-electrode distance L while the signal amplitude is proportional to the thickness of the sensor Δ. Silicon sensors are typically "planar", *i.e.* they consist of a high resistivity doped silicon bulk, 200-300 μm thick, with a single ohmic contact on the backside and a matrix of contiguous implants on the front side, as described in Figure 4.18 (left). In this case $L = \Delta$ and therefore, if one wants to improve the timing of the sensor is forced to reduce the signal amplitude. 3D silicon sensors, instead, have a novel geometry where vertical columnar

[6]If the average cluster size would significantly increase, this would mean that the fraction of clusters with the contributions of more than one particle is increased. Then, if this fraction is significant, a non-negligible impact on the tracking performances is expected. To contrast this effect, one solution would be a smaller pitch size for the pixel detector.

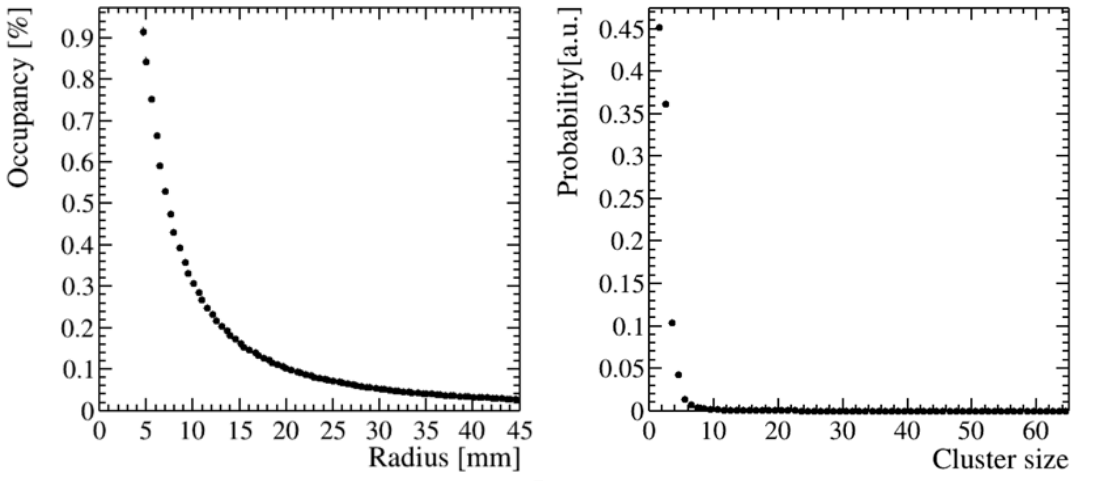

Figure 4.16: (left) Pixel occupancy measured in the station closest to the interaction point ($z = 0$) as a function of the radial distance from (0,0). (right) Distribution of the cluster size. Upgrade-II scenario conditions are used in simulation.

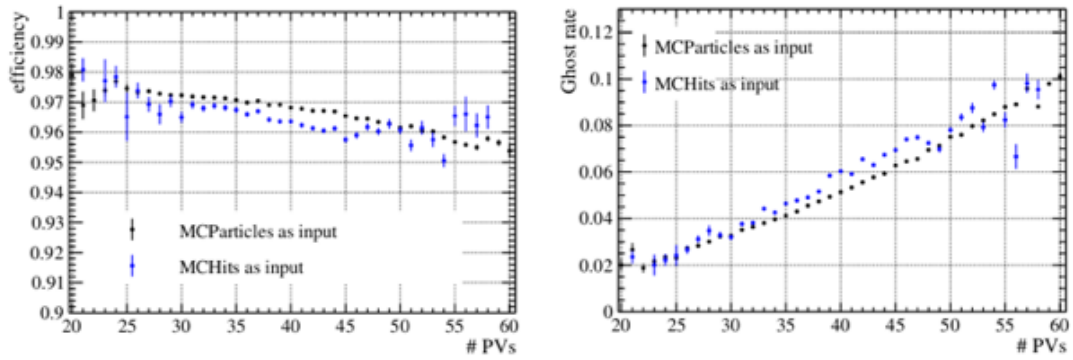

Figure 4.17: Pattern recognition performance of the VeloPix as function of the number of primary vertices in Upgrade-II conditions, measured with the fast simulation using (black) `MCParticles` and (blue) `MCHits` as input. (left) Reconstruction efficiency for VELO particles. (right) Ghost rate. Simulated events containing $B^0 \to K^* \mu^- \mu^+$ decays are used.

electrodes penetrate the silicon substrate, as shown in Figure 4.18 (right). Here, the collection distance can be significantly reduced (up to 50 µm or less) without affecting the signal amplitude. In this way a large freedom is left for the optimization of the performances through the geometry customization.

In order to guarantee the fast time application required by the Upgrade-II VELO, the sensor studied in the TimeSpot project has a inter-electrode distance of ∼20 µm. The

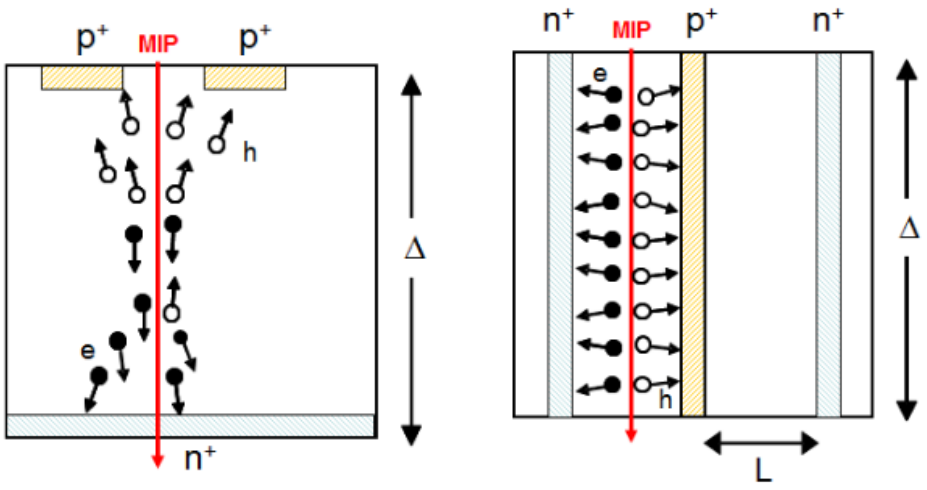

Figure 4.18: Sketch representing the behaviour of (left) planar and (right) 3D silicon sensors.

pixel has a $n-p$ doping profile, which allows an efficient electron collection at increasing radiation damage. Each pixel has three vertical electrodes: two biasing electrodes on its ends and one collecting electrode in the middle. The latter is referred to as "trench", while the formers simply as electrodes. The dimensions of the trench is chosen in order to balance two opposite effects: on one side, a long trench minimizes the weak field area between trenches, on the other small distance between trenches increases pixel capacitance, causing a worsening in time resolution. The geometry of the TimeSpot sensor is reported in Figure 4.19. The pitch of the sensor is 55 µm as for the VP sensor, while its thickness its reduced to 150 µm with respect to 200 µm in the VP sensor. The trench, positioned at the center of the sensor, occupies a volume of $40 \times 5 \times 135$ µm ^{3} while each electrode $2.5 \times 55 \times 150$ µm ^{3}.

Table 4.4 reports the parameters used to describe the TimeSpot (TS) sensor together with the one used for the VP sensor. In the fast simulation, `MCHits` coming from the `Gauss`+`Geant4` simulation of the VP sensor are used as input. Therefore, some adjustments need to be done accounting for these differences. The deposited charge is scaled by a factor 0.75 considering the smaller thickness of the TS sensor. However, since only `MCHits` are considered, multiple scattering effects can not be "rescaled" and are then overestimated in the current simulation. The trench and the electrodes correspond to non-sensitive regions of the pixel described as an area of 5×40 µm ^{2} and 2.5×55 µm ^{2} respectively, along the full thickness of the detector, as shown in Figure 4.20. The presence of these "holes" in the TS sensor will bring a drop in efficiency, as demonstrated in the following. As a consequence of the required precise time information, an advantage of the TimeSpot sensor is that diffusion effects along the (x, y) plane are expected to be

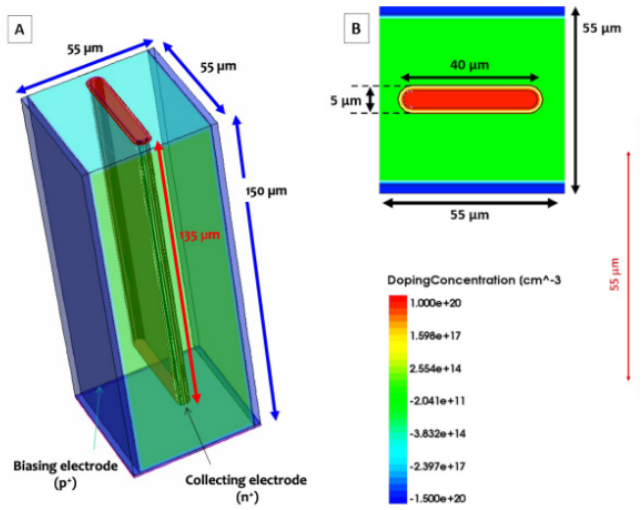

Figure 4.19: Geometry of the pixel of the TimeSpot sensor.

negligible and for this reason are not simulated. From preliminary TimeSpot studies, the electronic noise is assumed to have a RMS of about 300 electrons and therefore a threshold of 5σ is considered to activate the pixel. Despite a time resolution per pixel of 15 ps has been achieved by the TimeSpot collaboration, a more realistic resolution should be considered when the sensor is inserted in the more complex data taking framework of LHCb. For this reason, time resolutions of 20, 30 and 50 ps have been considered in this study.

Sensor parameters	TimeSpot	VeloPix
`Pitch`	55 µm	55 µm
`Depth`	150 µm	200 µm
`InactiveArea`	$5 \times 40 + 5 \times 55$ µm ^{2}	none
`Diffusion`	none	in z
`ElectronicNoise`	300 electrons*	130 electrons
`ChargeThreshold`	1500 electrons*	1000 electrons
`TimeResolutionPerPixel`	20, 30, 50 ps	none

Table 4.4: Parameters used in the simulation of the TimeSpot sensor compared with the one used for the VeloPix. The parameters values tagged with a "*" come from preliminary studies.

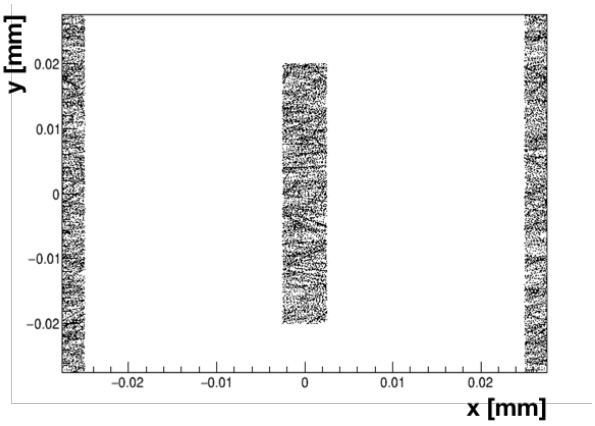

Figure 4.20: Inactive area as simulated for the TimeSpot sensor. In this plot, the charge deposit positions entering in the non-sensitive area are represented.

4.7.2 Introducing the time information

In this section, it is explained how the time information is introduced in the fast simulation and then in the algorithm of track reconstruction. In `Gauss`, the timing of each primary vertex (PV) is not simulated, *i.e.* $t_{PV} = 0$. However, the time of each `MChit` t_{MCHit} is calculated when the particle is propagated through the detector by `Geant4` starting from the time of creation of its primary vertex. In the same way also the time of the origin and end vertex of each `MCParticle` is calculated. In the current simulation, a simple model is used to assign to each primary vertex (PV) a corresponding time of production. Since the total crossing angle between the beams is small ($\sim$0.1 μrad), the bunches are assumed to hit each other head-on. In addition, in the model the transversal dimension of the bunches is also neglected since it is much smaller than the longitudinal dimension. Under these assumptions, the bunches are described as Gaussian distributions $G_{\pm}$, with standard deviation σ_z and means moving along the z axis at the speed of light c in opposite directions. The corresponding distribution in z and t of the PVs is the product of the two Gaussian functions, bringing to

$$G_{PV} = G_{+}(z + ct) \cdot G_{-}(z - ct) \propto \exp\left(\frac{2z^2 + 2(ct)^2}{2\sigma_z^2}\right), \tag{4.17}$$

which can be rewritten as

$$G_{PV} \propto \exp\left(\frac{z^2}{2(\sigma_z/\sqrt{2})^2}\right) \cdot \exp\left(\frac{t^2}{2(\sigma_z/(c\sqrt{2}))^2}\right). \tag{4.18}$$

From this basic argument, it is possible to see that the z and time distributions of the PVs are uncorrelated and have standard deviations $\sigma_z(\mathrm{PV}) = \sigma_z/\sqrt{2}$ and $\sigma_t(\mathrm{PV}) = \sigma_z/(c\sqrt{2})$, respectively. Using the value $\sigma_z = 90$ mm for the size of the bunch, $\sigma_z(\mathrm{PV}) = 63$ mm

and $\sigma_t(\text{PV}) = 212$ ps are found. Therefore, in the simulation t_{PV} is extracted from a Gaussian centered at zero and width $\sigma_t(\text{PV})$. The time of all `MChits` is then corrected by adding the t_{PV} contribution. At the same way also the origin and end vertex times of the `MCParticle` can be updated. In the case of a `MCParticle` as input, the simulation of the time to be associated to the `MCHit` is evaluated as

$$t_{MChit} = t_{OV} + \frac{1}{c\beta}|z_{MChit} - z_{OV}|\frac{p}{p_z}. \tag{4.19}$$

Given that multiple scattering effects and energy losses act on the particle traversing the material changing its 3-dimensional momentum, directly taking `MCHits` from the official LHCb simulation as input is a safer approach.

In the simulation of the TS sensor response, when a charge is deposited in a pixel its time t_{MChit} is smeared considering a certain resolution σ_t=`TimeResolutionPerPixel`. Hence, when a particle hits neighbouring pixels, the time assigned to each pixel is independent from the one in the neighbouring pixels. This consideration is supported by the fact that the time resolution is driven by electronic noise effects which are therefore independent from the pixels. In the case of more than one particle
hitting the pixel (3% of the active pixels), the following approximation is done:
the time assigned to the pixel is only given by the particle hitting the sensor first.

The clustering algorithm is modified by also asking neighbouring pixel to have $|\Delta t| < 3\sigma_t$ and then the time information assigned to the cluster is calculated by averaging the times measured in all its pixels. The cut at $3\sigma_t$ is however of small impact, given that most of the clusters see the contribution of just one particle and if more than one particle share the same cluster they most probably are correlated, *e.g.* being secondary particles from the same decay, and then already sharing similar hit times. This is also demonstrated by the fact that the cluster size distribution does not change significantly between the Upgrade-I and Upgrade-II conditions (see Figure 4.12 and Figure 4.16, respectively).

The highest impact of the time information is found in the pattern recognition algorithm which is modified with the following assumptions. Considering that the velocity of the particle can be approximated to the speed of light c and presuming a certain direction of the particle (forward/backward), given a hit (x_1, y_1, z_1) found in a module with a certain time t_1 it is possible to predict the time t_2 for a second hit (x_2, y_2, z_2) to be found in the next module:

$$t_2 = t_1 \pm \sqrt{(x_2 - x_1)^2 + (y_2 - y_1)^2 + (z_2 - z_1)^2}/c. \tag{4.20}$$

Then, in the track following method, only the hits satisfying

$$|t_{pred} - t_{reco}| < 3\sigma_t, \tag{4.21}$$

with t_{reco} being the time associated to the reconstructed hit and t_{pred} the predicted one from the previous measurements, are considered in the search for pairs to build a seed

and in its extrapolation to the subsequent modules. This simple requirement, as will be seen in the following, will be particularly useful in improving the track reconstruction performances. Improvements are possible, for example by considering σ_t to be different for clusters of different size. However, no further investigations have been done so far.

4.7.3 Performances with the TimeSpot sensor

In this section, the performances of a future VELO using the TimeSpot sensor and maintaining the current geometry of the VeloPix are measured in Upgrade-II conditions.

The VELO efficiency and the ghost probability as a function of the number of PV are reported in Figure 4.21 for different time resolution per pixel $\sigma_t = 20$, 30 and 50 ps. For reference, also the performances obtained with the VeloPix and with the TimeSpot without the time information ($\sigma_t = \infty$) are shown, together with the average parameter values observed in Upgrade-I conditions. The integrated values for the performance parameters are also reported in Table 4.5. In the table, the average number of combinations of hits considered by the track following algorithm, N_{CPUtime}, is also reported for each configuration in order to give an idea of the improvements on the required CPU time. It is possible to notice that, if the time information is not accounted, the performances of a TimeSpot VELO are worse than the ones using the VeloPix sensor. The reason has to be found in the less collected charge per particle traversing the module due to the smaller thickness, and the existence of non-sensitive regions, combined with a higher electronic noise and a consequent higher threshold used to switch on the pixel. However, when the time information is considered the performance of the TimeSpot VELO improves. In particular, the ghost rate results to be highly sensitive to σ_t and is reduced up to 0.7% when $\sigma_t = 20$ ps. As regards the VELO efficiency, it slightly depends on σ_t and it is found to be about 1% lower that what is obtained with the VeloPix sensor. If one consider the VP performances obtained in Upgrade-I (Table 4.3) as a target of the future detector, one can notice that the TimeSpot sensor in the current design gives quite good results. However, improvements concerning the detector geometry can be done as explained in the following section.

4.7.4 Performances with different tilting angles

The presence of a trench and of the electrodes along the thickness of the sensor bring to non-sensitive regions in the pixel (shown in Figure 4.20) and therefore to a consistent loss in efficiency as reported in Figure 4.21. Given that the dimension of these "holes" in the xz plane is 5×150 μm ^{2} a tilting angle of about 2° applied in this plane to each module, in order to increase the path of the particle within the sensor, can be exploited in order to recover this loss in efficiency. This number is estimated considering that particles traverse the module perpendicularly which is in general not true. Therefore, in order to estimate the best tilting angle, the simulation needs to be run with different values.

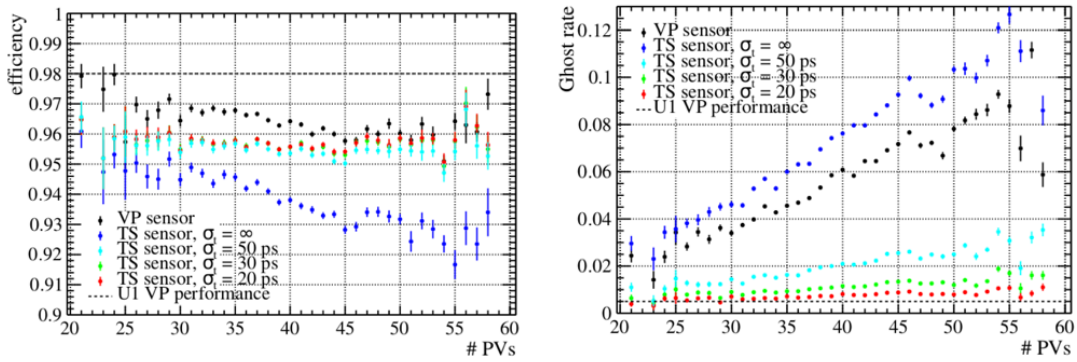

Figure 4.21: Pattern recognition performance of the VELO as function of the number of primary vertices in Upgrade-II conditions, measured with the fast simulation using the TimeSpot sensor with pixel resolution of (red) 20 ps, (green) 30 ps, (cyan) 50 ps or (blue) ∞, or using (black) the VeloPix sensor. The integrated values observed in Upgrade-I conditions with the VeloPix sensor are also represented as a reference with a black-dashed line. (left) Reconstruction efficiency for VELO particles. (right) Ghost rate. Simulated events containing $B^0 \to K^* \mu^- \mu^+$ decays are used.

Upgrade-II Sensor (σ_t)	VELO efficiency[%]	Ghost Prob.[%]	N_{CPUtime} [10^3]
VeloPix (∞)	96.4	5.6	29.8
TimeSpot (∞)	93.5	7.0	30.2
TimeSpot (50 ps)	95.4	2.0	19.6
TimeSpot (30 ps)	95.6	1.1	16.2
TimeSpot (20 ps)	95.6	0.7	14.2

Table 4.5: Pattern recognition performance parameters for VELO using VeloPix and TimeSpot sensors at Upgrade-II conditions. These parameters are measured using simulated events containing $B^0 \to K^* \mu^- \mu^+$ decays.

In order to increase the path of a particle within the sensor, the modules positioned at opposite sides with respect to the beam line have to be rotated with different angles with a "fish bone" structure, as shown in Figure 4.22. Moreover, opposite angles should also be considered for particles going backward or forward. However, since the VELO efficiency parameter used as benchmark only relies on forward particles, the modules are rotated with the same angle independently by their z position. Another point that needs to be raised is the fact that the L-shape geometry of the module is not ideal for rotations in the xz plane (where $x = 0$, $z = z_{module}$ is used as axis), in fact while most of the module sees an increase in efficiency, as can be deduced from Figure 4.12 about 1/12 of the module lays in a region where the path of the particles decreases (as an average

effect) and then a smaller efficiency is expected. However, these regions are far from the beam line and are not expected to be significantly populated. Therefore, the impact of these inefficient regions is expected be negligible.

From the point of view of the simulation, the rotation is applied directly in the official LHCb simulation in order to obtain consistent `MCHits`. In this way, multiple scattering effects and production of secondary particles are correctly accounted. The `MCHits` are then transformed in the local coordinates of each module for the deposit of charge in the pixels. After that clusters are found, the `Hit` are then transformed in global coordinates for the pattern recognition algorithm. In the official LHCb simulation, an upgraded version of the `Gauss` simulation framework is used, characterized by the introduction of a new approach in the detector description. `DD4Hep` [139] is a detector description toolkit that provides experiment-independent libraries for conditions management and visualization of the geometry. Thanks to its flexibility, this toolkit has allowed to easily change the geometry of the detector considering different tilting angles.

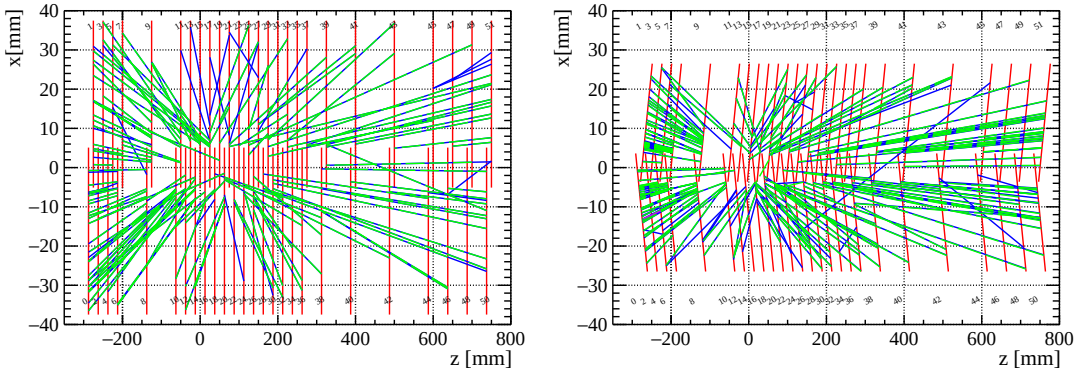

Figure 4.22: Display of the same pp event in the xz plane with the modules (left) positioned vertically with respect to the beam line and (right) rotated in the plane xz by 45°. Each module is represented with a red line, the `MCParticles` traversing the detector are represented with blue lines while the reconstructed `Tracks` are depicted as green-dashed lines. Upgrade-I conditions are used, as an example. The dimensions of the L-shaped modules seem not to be conserved between the two plots. Indeed, this is a simple consequence of the z and y axes being scaled for a different factor. Only promptly produced particles are shared between the two configurations, while secondary particles may not be the same or be produced in different positions and angles as a conquence of the interaction with the detector material.

The idea of using tilting angles in order to recover the loss in efficiency arising from the trench and the electrodes is synthesised in Figure 4.23 where Upgrade-I conditions are used in the simulation. When no tilting angle is applied the effect of the non-sensitive regions impacts on the reconstruction efficiency of the track. However, when a sufficiently large angle is applied, inefficiency is recovered. From Figure 4.23, one can also notice

that the efficiency achieved with the TimeSpot sensor will always be slightly lower than the one observed with the VeloPix in Upgrade-I, with the caveat made in the simulation of the TS sensor (see Section 4.7.1).

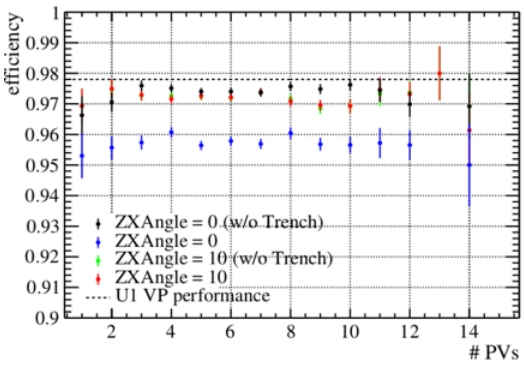

Figure 4.23: Reconstruction efficiency for VELO particles in a possible VELO using the TimeSpot sensor as function of the number of primary vertices simulated in Upgrade-I conditions, using the modules positioned vertical with respect to the beam line (blue) with and (black) without non-sensitive regions, and using the modules rotated by an angle 10° with respect to the beam line (red) with and (green) without non-sensitive regions. The integrated values observed in Upgrade-I conditions with the VeloPix sensor are also represented as a reference with a black-dashed line. Simulated events containing $B^0 \rightarrow K^* \mu^- \mu^+$ decays are used.

Finally, different tilting angles are explored in Upgrade-II scenario. In the official LHCb simulation, three samples using 1°, 3° and 5° as tilting angle, have been produced and the respective `MCHits` used as input for the fast simulation. The resulting performances are reported in Figure 4.24 as a function of the number of primary vertices while the integrated values are reported in Table 4.6. As one can notice, the reconstruction efficiency increases with the tilting angle from 1° to 3° and seems to have reached a plateau between 3° and 5°, where no improvement is found at increased angles. To investigate better this behaviour more simulations at different angles are needed, as it is probable that better performances can be achieved with intermediate angles. As concerns the ghost rate, it can be seen that it only has a slight dependence on the tilting angle. Figure 4.25 reports the probability distribution of the cluster size with the different tilting angles together with their average values. As expected, while the average path of a particle through the sensor increases also the size of the cluster increases. Since 3° and 5° give comparable results in terms of performances, 3° is preferred because of the smaller size of the clusters, that means less CPU time required by the clustering algorithm. In Figure 4.24, performances at the tilting angle of 3° are also shown introducing the time information with a resolution per pixel of 50 ps, considered to be a minimum requirement for the future Upgrade-II detector. The combination of the time information together

with the application of a tilting angle, results to give the best performance for a possible future VELO. However, even if the current result does not reproduce exactly the VeloPix performances expected for the Upgrade-I, considered as a target, it allows the VELO to run at a much higher luminosity, 7.5 times larger with respect to Upgrade-I, with only a loss of 1% in tracking performance. This will permit to achieve the physics goals of LHCb for the Upgrade-II scenario and in particular fulfill the expectations with respect to the number of collected events to carry out high-precision measurements.

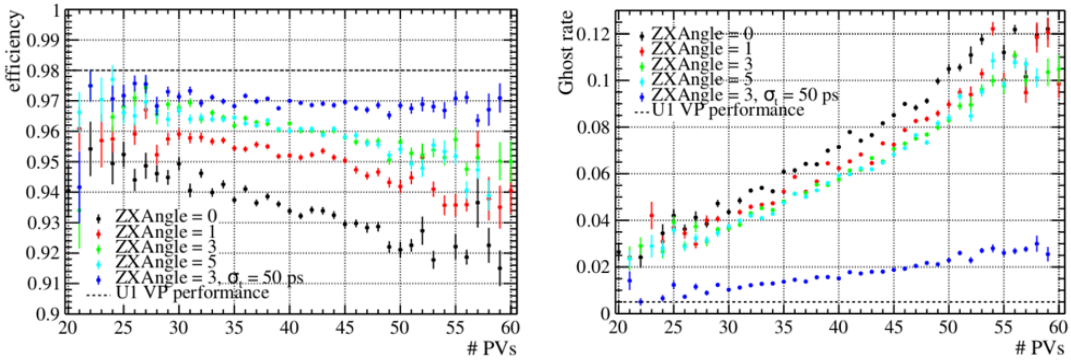

Figure 4.24: Pattern recognition performance of the VELO as function of the number of primary vertices in Upgrade-II conditions, measured with the fast simulation using the TimeSpot sensor with tilting angle in the xz plane of (black) 0°, (red) 1°, (green) 3°, (cyan) 5° or (blue) 3° with the addition of the time information with a resolution of 50 ps per hit. The integrated values observed in Upgrade-I conditions with the VeloPix sensor are also represented as a reference with a black-dashed line. (left) Reconstruction efficiency for VELO particles. (right) Ghost rate. Simulated events containing $B^0 \to K^* \mu^- \mu^+$ decays are used.

This results have to be considered as preliminary since the simulation of the TimeSpot sensor (see Section 4.7.1) may be too pessimistic. In addition, the wrong tilting angle assigned in the backward region of the detector may slightly increase the ghost rate. Other aspect that can be investigated regards the use of σ_t measured in each cluster from the average of the pixel in order to obtain more stringent requirements when pairs of hits are combined to build a track. This can also be joined with the increase of the cluster size given from larger tilting angles.

Upgrade-II TimeSpot sensor θ_{xz} (σ_t)	VELO efficiency[%]	Ghost Prob.[%]
0° (∞)	93.5	7.0
1° (∞)	95.7	5.0
3° (∞)	96.3	4.8
5° (∞)	96.1	4.7
3° (50 ps)	96.9	1.6

Table 4.6: Pattern recognition performance parameters for VELO using TimeSpot sensors with different tilting angles applied in the xz plane and time resolution. These parameters are measured using simulated Upgrade-II events containing $B^0 \to K^* \mu^- \mu^+$ decays.

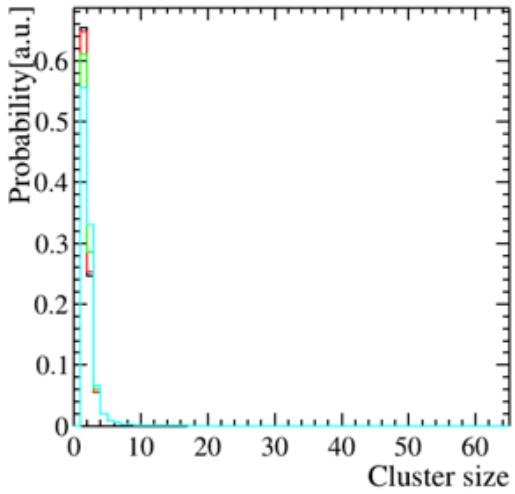

Figure 4.25: Distribution of cluster sizes in Upgrade-II events with different tilting angles applied in the xz plane being (black) 0°, (red) 1°, (green) 3° and (cyan) 5°. The average values obtained for the cluster size are 1.60, 1.60, 1.65 and 1.71 for $\theta = 0$, 1°, 3° and 5°, respectively.

4.8 A FPGA-friendly algorithm in the fast simulation

In this section, a new track reconstruction algorithm is proposed. It is highly parallelized and particularly suitable for implementation in FPGA with a pipe-lined architecture[7].

[7]In computing, a "pipeline" is a set of data-processing elements connected in series, where the output of one element is the input of the next one. The elements of a pipeline can be (and are often) executed in parallel.

It is intended to reconstruct straight 3-dimensional tracks with the addition of the time information. Being a 4D real-time algorithm, it aims to be a perfect candidate in the prospect of a future VELO for Upgrade-II. This work is also within the work package 4 of TimeSpot project and has already been tested in simulation and implemented in FPGAs [140]. However, its development is still ongoing and the coordination with the simulation of the VELO detector is mandatory for its success. In particular, in this section the FPGA-friendly algorithm is integrated in the fast simulation and preliminary results for its performances in the Upgrade-II scenario are presented.

The algorithm is based on the identification of pairs of hits in adjacent modules, called *stubs*. Each stub (or track[8]) is characterized by five parameters $(x_+, x_-, y_+, y_-, t_0)$ with $(x_\pm, y_\pm) = ((x_f \pm x_l)/2, (y_f \pm y_l)/2)$ and $z_\pm = (z_f \pm z_l)/2)$, where z_f, z_l are the z-coordinates of the first and last tracking planes, respectively, and (x_f, y_f) and (x_l, y_l) are the coordinates of the track at z_f and z_l, respectively. In particular, (x_+, y_+) corresponds to the coordinates of the intersection of the track with a reference plane placed at z_+ and will be relevant in the following, while (x_-, y_-) are related to the tangent of the track angles. A more classical definition of the 3D track can be given as

$$\begin{aligned} x(z) &= x_0 + m_x z, \\ y(z) &= y_0 + m_y z, \end{aligned} \tag{4.22}$$

where x_0, y_0 are the coordinates of particle at $z = 0$, and m_x and m_y are the track slopes. The relation between the two sets of coordinates is given by the following equations:

$$\begin{aligned} x_- &= m_x z_-, \\ y_- &= m_y z_-, \\ x_+ &= x_0 + m_x z_+, \\ y_+ &= y_0 + m_y z_+. \end{aligned} \tag{4.23}$$

Including the time coordinate to the track definition, as extension of the 3D definition, it is necessary to define the time of the track t_0 as the time of the particle at $z = 0$, according to

$$t(z) = t_0 + \frac{z}{c}\sqrt{m_x^2 + m_y^2}, \tag{4.24}$$

where the particle is assumed to travel at the speed of light c.

A stub is formed by any combination of hits that is compatible with reconstructible track, *i.e.* in the LHCb acceptance region. Assuming (x_1, y_1, z_1, t_1) and (x_2, y_2, z_2, t_2) are

[8]In fact, a stub is the simplest possible track given that the minimum number of hits in a track to theoretically reduce to zero its number of degrees of freedom is two, if hit resolution and multiple scattering effects are ignored.

the coordinates of the first and second hit of a stub candidate, respectively, the stub coordinates are evaluated as

$$\begin{aligned} x_{-,stub} &= \frac{x_1 z_- - x_2 z_-}{z_1 - z_2}, \\ x_{+,stub} &= \frac{x_1(z_+ - z_2) - x_2(z_+ - z_1)}{z_1 - z_2}, \\ y_{-,stub} &= \frac{y_1 z_- - y_2 z_-}{z_1 - z_2}, \\ y_{+,stub} &= \frac{y_1(z_+ - z_2) - y_2(z_+ - z_1)}{z_1 - z_2}, \\ t_{0,stub} &= \frac{t_1 + t_2}{2} - \frac{z_1 + z_2}{2c\sqrt{1 + (x_-/z_-)^2 + (y_-/z_-)^2}}. \end{aligned} \tag{4.25}$$

The velocity of the particle can be estimated as an additional stub parameter and is defined as $|\vec{x_1} - \vec{x_2}|/(t_1 - t_2)$, where $\vec{x_1} = (x_1, y_1, z_1)$ and $\vec{x_2} = (x_2, y_2, z_2)$. The velocity is used only during the stub construction for the estimation of t_0, while the reconstructed tracks are always assumed to be associated with particles travelling at the speed of light. In fact, if the velocity determined from the stub is not compatible with the speed of light c then the candidate stub is rejected.

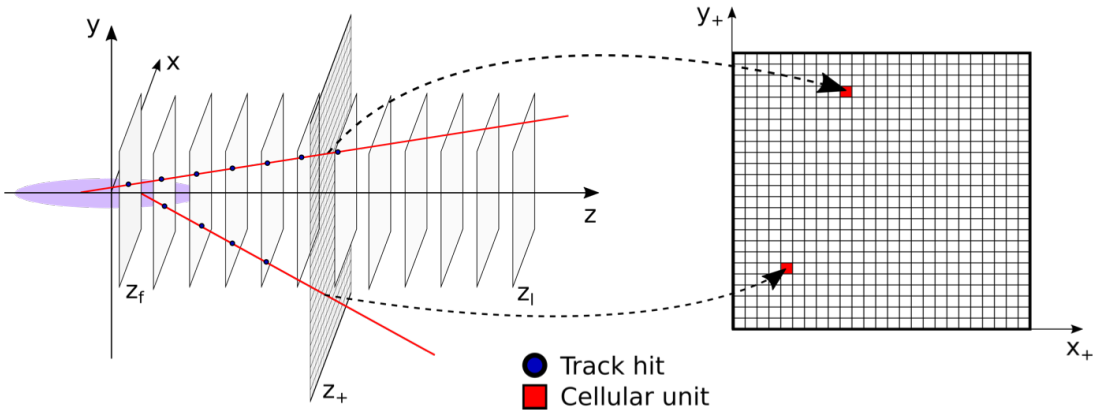

Figure 4.26: Layout of a VELO-like detector and visual representation of the grid of cellular units, distributed over a reference plane placed at $z = z_+$.

The pattern recognition algorithm consists in the association of multiple stubs to a track candidate according to their projection to a reference plane. In particular, the stub projections at $z = z_+$ that are defined by (x_+, y_+) are considered. A grid of cellular units is allocated in the sub-space of the track parameters (x_+, y_+) and is labelled by

the couple of indexes (i, j). In this 4D real-time tracking algorithm a cellular unit is associated with a bundle of tracks that intersect the reference plane in the coordinates (x_{i+}, y_{j+}) as shown in Figure 4.26. The other stub parameters (x_-, y_-, t_0) are free to assume any value, provided that these are compatible with the geometrical acceptance and timing cuts. Each cellular unit evaluates a Gaussian response according to the distance of the cell in the reference plane from the measured stub, whose coordinates are (x_{k+}, y_{k+}). This squared distance is defined as

$$s^2_{ijk} = (x_{k+} - x_{i+})^2 + (y_{k+} - y_{j+})^2, \tag{4.26}$$

and the response to a single stub is defined as

$$W_{ijk} = N_{ijk} \cdot \exp\left(-\frac{s^2_{ijk}}{2\sigma^2}\right), \tag{4.27}$$

with

$$N_{ijk} = \begin{cases} 1 \text{ if } |s_{ijk}| < \Delta \\ 0 \text{ otherwise} \end{cases}, \tag{4.28}$$

where Δ and σ are parameters to be adjusted for optimal response. In particular, Δ is about the size of the grid step in the case of uniformly distributed cellular units, and the value of σ is comparable to Δ. The total response (weight function) of each cellar unit is evaluated as the average of the contributions from the measured stubs. A contribution is considered negligible, hence not included in the average, if $N_{ijk} = 0$. The weight function is then defined by the following equation:

$$W_{ij} = \frac{1}{N_{ij}} \sum_k W_{ijk}, \tag{4.29}$$

where

$$N_{ij} = \sum_k N_{ijk}. \tag{4.30}$$

It is worth noting that the weight function only depends on the x_+, y_+ quantities from the measured stubs while the three additional quantities can be evaluated by each cellular units from the (x_{-k}, y_{-k}, t_{0k}) stub parameters of the k-th stub and used for geometrical and timing acceptance cuts. For each cellular unit they correspond to:

$$\begin{aligned} x_{-ij} &= \frac{1}{N_{ij}} \sum_k x_{-ijk}, \\ y_{-ij} &= \frac{1}{N_{ij}} \sum_k y_{-ijk}, \\ t_{0ij} &= \frac{1}{N_{ij}} \sum_k t_{0ijk}, \end{aligned} \tag{4.31}$$

where

$$\begin{aligned} x_{-ijk} &= N_{ijk}\, x_{-k}, \\ y_{-ijk} &= N_{ijk}\, y_{-k}, \\ t_{0ijk} &= N_{ijk}\, t_{0k}. \end{aligned} \tag{4.32}$$

The evaluation of the weight function can be performed in parallel since it only depends on the inputs from the measured stubs and a track is identified by a local maximum of the weight function. The function N_{ij} for the local maxima is required to be greater than a certain threshold. In fact the value N_{ij} corresponds to the number of stubs that belong to the candidate track, in the simplest case in which stubs from different tracks excite different cellular units. In this simulation the minimum number of stubs required to identify a track has been set to 2, *i.e.* at least 4 hits per track.

The presented algorithm has been integrated in the fast simulation framework in order to estimate the performances of a future possible VELO detector using the TimeSpot sensor in the Upgrade-II scenario. In particular, this real-time algorithm replaces the track following method described in Section 4.5.2, taking as input the `Hits` reconstructed in the clustering process. Here, the stubs are build from the exclusive pairing of adjacent stations, however more inclusive pairing schemes can be studied. In the Upgrade-I VELO geometry, a station is intended to be composed by two L-shaped modules positioned at opposite sides (left and right) of the x axis with respect to the beam line, as shown in Figure 2.17. Then, the modules 0 and 1 are coupled with the the modules 2 and 3 to build the first set of stubs and so on, for a total of 13 pairs of stations. Different cuts, based on spatial parameters of the stub and on the difference in time between the two measured hits, have been applied to reject misidentified stub candidates that are not compatible with a realistic track. The parameter values used in these cuts are tuned based on events where only one track have been simulated as a benchmark for evaluating the quality of the reconstruction. Tighter cuts can be applied considering only "interesting" particles, such as VELO particles, long particles or the ones from b-hadron events. In the presence of a high number of tracks different contribution can decrease the quality of the reconstruction and increase the number of ghost tracks. The worsening of the resolution is in general due to the contamination of the weight function near the local maximum corresponding to an identified tracks. This effect depends on the granularity of the grid and it is reduced when increasing the number of cellular units, *i.e.* the resources that can be allocated in a FPGA. However, an increased granularity of the grid does not bring further improvements once the size of each cell is smaller than Δ, representing the hit resolution effect on (x_+, y_+).

Since (x, y) coordinates of the hits in pp collision events are not uniformly distributed, the (r', ϕ') coordinates, corresponding to the radial distance and the angle in the x_+y_+ plane transformed in order to be uniformly distributed between 0 and 1, are preferred to equally distribute the work load to all the cellular units. The weight function of

the cellular units is shown in Figure 4.27 for an event in Upgrade-I, as an example. Figure 4.27 also acts as event display where each reconstructed `Track` is represented by at least 2 occurrences in a cellar unit and it is marked with a red circle. In addition, reconstructible `MCTracks` are marked with green circles.

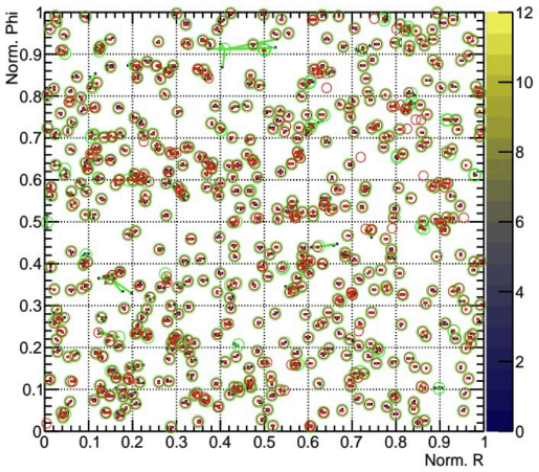

Figure 4.27: Representation of a cellular unit grid in the (r', ϕ') coordinates in the reference plane $z_+ = 400$ mm for an event of the Upgrade-I. In this plot only true MC particles, with their track parameters, are used to "fill" the histogram representing the cellular unit. Reconstructible `MCTracks` are marked with green circles linked to the corresponding (r', ϕ') point(s). Multiple scattering effects alter the track parameters values and therefore more points in the (r', ϕ') plane can be identified by the same particle. Reconstructed `Tracks` are marked with red circles. They are defined with at least 2 occurrencies in the cellular unit containing all the allowed combinations of stubs, including the fake ones.

A preliminary study has been performed for an event of 32 PVs belonging to the Upgrade-II scenario. The (r', ϕ') plane at $z_+ = 400$ mm has been considered as reference for the track finding. Here, the cuts applied to the (x_-, y_-, t_0) track parameters are tuned in order to have 100% efficiency in the creation of stubs coming from reconstructible tracks, *i.e.* with 4 hits in the detector. The outcome of the current algorithm returns a VELO efficiency of about 80% and a ghost rate larger than 20%, as can also be seen in terms of the weighting function in Figure 4.28. Despite the results are far from the target values for the performance parameters desired, they represent a good starting point for further improvements. In particular, the present algorithm do not split the tracks in forward and backward regions as done in the track following method. Having two reference plane, *e.g.* one for stubs with hits having $z > -100$ mm and another one for hits with $z < 100$ mm, would lighten the population of the grid and then improve the performances. Moreover, also the z position of the tracking reference plane can be

modified. Finally, also the geometry itself of the detector can be modified, with tracking layers at different z position to optimize the stub creation from paired stations.

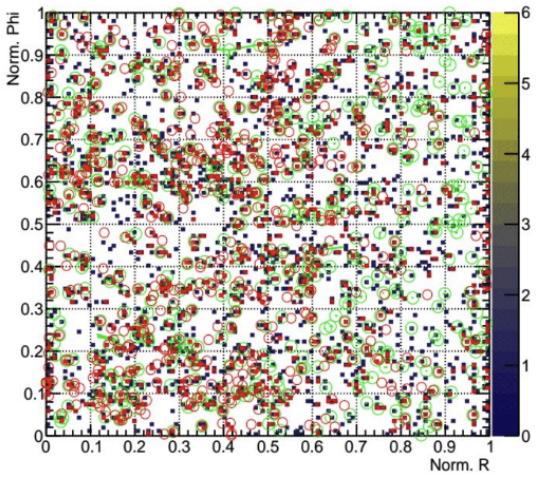

Figure 4.28: Representation of a cellular unit grid in the (r', ϕ') coordinates in the reference plane $z_+ = 400$ mm for an event of 32 PVs of the Upgrade-II. In this plot only true MC particles, with their track parameters, are used to "fill" the histogram representing the cellular unit. Reconstructible `MCTracks` are marked with green circles linked to the corresponding (r', ϕ') point(s). Multiple scattering effects alter the track parameters values and therefore more points in the (r', ϕ') plane can be identified by the same particle. Reconstructed `Tracks` are marked with red circles. They are defined with at least 2 occurrencies in the cellular unit containing all the allowed combinations of stubs, including the fake ones.

4.9 Conclusions

In the Upgrade-II scenario, the fulfillment of the VeloPix (VP) detector is severely hampered with strong consequences on its performance, especially in terms of ghost probability and efficiency in the reconstruction algorithm. Thanks to the introduction of the time information, the 3D sensor developed by the TimeSpot collaboration is proposed to supersede the VP sensor. Preliminary results concerning the simulation of this sensor in the current VP geometry and the application of a tilting angle to the module to increase the pixel efficiency, give the best performance for a possible future VELO. Considering a realistic time resolution per pixel of 50 ps, the VELO particle efficiency is estimated to be ∼97% while the ghost rate ∼ 1.6%. These results represent a huge improvement from what is expected if the VP VELO is run in Upgrade-II conditions and not far from expected performances ($\epsilon_{VELO} = 98\%$ and $P(ghost) = 0.5\%$). Therefore, further effort

is needed for a more realistic simulation together with an improved design and track reconstruction algorithm. In addition, studies involving an alternative pattern recognition algorithm using an FPGA-friendly algorithm are also ongoing, in order to achieve track finding in real-time.

Conclusions

This thesis reports the search for time-integrated violation of the *CP* symmetry in the Cabibbo-suppressed $D^0 \to K^-K^+$ decays, namely $\mathcal{A}^{CP}(K^-K^+)$. The analysis is performed at the LHCb detector using proton-proton collisions recorded from 2015 to 2018 at the centre of mass energy of 13 TeV. The data used corresponds to an integrated luminosity of 5.7 fb^{-1}. The flavour of the charm mesons is defined from the charge of the pion in $D^{*+} \to D^0\pi^+$ and $D^{*-} \to \overline{D}^0\pi^-$ decays. Nuisance asymmetries are constrained from $D^{*+} \to D^0(\to K^-\pi^+)\pi^+$, $D^+ \to K^0_S\pi^+$, $D^+ \to K^-\pi^+\pi^+$, $D_s^+ \to K^0_S K^+$ and $D_s^+ \to \phi\pi^+$ decays. When D^+ meson is involved, the results are named D^+-method, while in the case of D_s^+ meson, D_s^+-method. The results are

$$\mathcal{A}^{CP}(K^-K^+)|D^+ = (13.6 \pm 8.8\,(\text{stat}) \pm 1.6\,(\text{syst})) \cdot 10^{-4},$$
$$\mathcal{A}^{CP}(K^-K^+)|D_s^+ = (2.8 \pm 6.7\,(\text{stat}) \pm 2.0\,(\text{syst})) \cdot 10^{-4},$$

with an overall correlation $\rho_{\mathcal{A}^{CP}} = 0.06$. They are found to be compatible within one standard deviation and their combination is measured to be

$$\mathcal{A}^{CP}(K^-K^+) = (6.8 \pm 5.4\,(\text{stat}) \pm 1.6\,(\text{syst})) \cdot 10^{-4},$$

in agreement with the previous LHCb results and the current world average. This result is the world's most precise measurement of this quantity to date. Combining $\mathcal{A}^{CP}(K^-K^+)$ with the time-integrated *CP* asymmetry difference, $\Delta A_{CP} = \mathcal{A}^{CP}(K^-K^+) - \mathcal{A}^{CP}(\pi^-\pi^+)$, and the time-dependent *CP* asymmetry, ΔY, measured with $D^0 \to K^-K^+$ and $D^0 \to \pi^-\pi^+$ decays, the direct *CP* asymmetries in $D^0 \to K^-K^+$ and $D^0 \to \pi^-\pi^+$ decays, a^d_{KK} and $a^d_{\pi\pi}$, result to be

$$a^d_{KK} = (7.7 \pm 5.7) \cdot 10^{-4},$$
$$a^d_{\pi\pi} = (23.2 \pm 6.1) \cdot 10^{-4},$$

where the errors include systematic and statistical uncertainties and the correlation between the two values is $\rho(a^d_{KK}, a^d_{\pi\pi}) = 0.88$. The values differ from zero for 1.4 and 3.8 standard deviations, respectively. In particular, $a^d_{\pi\pi}$ shows an evidence for direct *CP* violation in $D^0 \to \pi^-\pi^+$ decays.

In this thesis, a preliminary study regarding the performance evaluation for a future VertexLocator (VELO) for LHCb Upgrade-II is also reported. In particular, the possibility of using the 3D silicon sensor developed within the TimeSpot project is explored. The study relies on a fast simulation which includes the simulation of the sensor response and the track reconstruction algorithm, taking as input Monte Carlo particle information from the standard LHCb simulation of proton-proton events. The fast simulation has been validated with several benchmarks in the LHCb-Upgrade scenario. Considering a preliminary parametrisation of the sensor with a time resolution per pixel of 50 ps, the reconstruction efficiency for VELO tracks is estimated to be 97% while the ghost rate is 1.6%. Those preliminary results are not far from the current performance of the LHCb-Upgrade VELO detector and show the importance of time measurements for a vertex detector working in the High-Luminosity era.

Bibliography

[1] R. Aaij et al. Observation of *CP* violation in charm decays. *Phys. Rev. Lett.*, 122: 211803, 2019. doi: 10.1103/PhysRevLett.117.211803.

[2] T. D. Lee and C. N. Yang. Question of parity conservation in weak interactions. *Phys. Rev.*, 104:254–258, Oct 1956. doi: 10.1103/PhysRev.104.254.

[3] C. S. Wu et al. Experimental test of parity conservation in beta decay. *Phys. Rev.*, 105:1413–1415, Feb 1957. doi: 10.1103/PhysRev.105.1413.

[4] R. L. Garwin et al. Observations of the failure of conservation of parity and charge conjugation in meson decays: the magnetic moment of the free muon. *Phys. Rev.*, 105:1415–1417, Feb 1957. doi: 10.1103/PhysRev.105.1415.

[5] M. Goldhaber et al. Helicity of neutrinos. *Phys. Rev.*, 109:1015–1017, Feb 1958. doi: 10.1103/PhysRev.109.1015.

[6] G Lüders. On the equivalence of invariance under time reversal and under particle-antiparticle conjugation for relativistic field theories. *Dan. Mat. Fys. Medd.*, 28: 1–17, 1954. URL `https://cds.cern.ch/record/1071765`.

[7] G. Luders. Proof of the TCP theorem. *Annals Phys.*, 2:1–15, 1957. doi: 10.1016/0003-4916(57)90032-5. [Annals Phys.281,1004(2000)].

[8] J. H. Christenson, J. W. Cronin, V. L. Fitch, and R. Turlay. Evidence for the 2π Decay of the K_2^0 Meson. *Phys. Rev. Lett.*, 13:138–140, Jul 1964. doi: 10.1103/PhysRevLett.13.138.

[9] S. L. Glashow. Partial Symmetries of Weak Interactions. *Nucl. Phys.*, 22:579–588, 1961. doi: 10.1016/0029-5582(61)90469-2.

[10] S. Weinberg. A model of leptons. *Phys. Rev. Lett.*, 19:1264–1266, Nov 1967. doi: 10.1103/PhysRevLett.19.1264.

[11] A. Salam and J.C. Ward. Electromagnetic and weak interactions. volume 13, pages 168–171, 1964. doi: 10.1016/0031-9163(64)90711-5.

[12] N. Cabibbo. Unitary symmetry and leptonic decays. *Phys. Rev. Lett.*, 10:531–533, Jun 1963. doi: 10.1103/PhysRevLett.10.531.

[13] S. L. Glashow, J. Iliopoulos, and L. Maiani. Weak Interactions with Lepton-Hadron Symmetry. *Phys. Rev.*, D2:1285–1292, 1970. doi: 10.1103/PhysRevD.2.1285.

[14] G. S. Abrams et al. The Discovery of a Second Narrow Resonance in e^+e^- Annihilation. *Phys. Rev. Lett.*, 33:1453–1455, 1974. doi: 10.1103/PhysRevLett.33.1453. [Adv. Exp. Phys.5,150(1976)].

[15] J. J. Aubert, U. Becker, P. J. Biggs, J. Burger, M. Chen, G. Everhart, P. Goldhagen, J. Leong, T. McCorriston, T. G. Rhoades, M. Rohde, S. C. C. Ting, S. L. Wu, and Y. Y. Lee. Experimental Observation of a Heavy Particle J. *Phys. Rev. Lett.*, 33:1404–1406, Dec 1974. doi: 10.1103/PhysRevLett.33.1404.

[16] M. Kobayashi and T. Maskawa. *CP* Violation in the Renormalizable Theory of Weak Interaction. *Prog. Theor. Phys.*, 49:652–657, 1973. doi: 10.1143/PTP.49.652.

[17] S. W. Herb et al. Observation of a Dimuon Resonance at 9.5-GeV in 400-GeV Proton-Nucleus Collisions. *Phys. Rev. Lett.*, 39:252–255, 1977. doi: 10.1103/PhysRevLett.39.252.

[18] F. Abe et al. Observation of top quark production in $\bar{p}p$ collisions. *Phys. Rev. Lett.*, 74:2626–2631, 1995. doi: 10.1103/PhysRevLett.74.2626.

[19] S. Abachi et al. Search for high mass top quark production in $p\bar{p}$ collisions at $\sqrt{s} =$ 1.8 TeV. *Phys. Rev. Lett.*, 74:2422–2426, 1995. doi: 10.1103/PhysRevLett.74.2422.

[20] B. Aubert et al. Observation of *CP* violation in the B^0 meson system. *Phys. Rev. Lett.*, 87:091801, 2001. doi: 10.1103/PhysRevLett.87.091801.

[21] K. Abe et al. Observation of large *CP* violation in the neutral B meson system. *Phys. Rev. Lett.*, 87:091802, 2001. doi: 10.1103/PhysRevLett.87.091802.

[22] R. Aaij et al. First observation of *CP* violation in the decays of B_s^0 mesons. *Phys. Rev. Lett.*, 110(22):221601, 2013. doi: 10.1103/PhysRevLett.110.221601.

[23] B. Aubert et al. Evidence for $D^0 - \bar{D}^0$ Mixing. *Phys. Rev. Lett.*, 98:211802, 2007. doi: 10.1103/PhysRevLett.98.211802.

[24] M. Starič et al. Evidence for D^0-$\bar{D}^0$ mixing. *Phys. Rev. Lett.*, 98:211803, May 2007. doi: 10.1103/PhysRevLett.98.211803.

[25] A. D. Sakharov. Violation of *CP* Invariance, c Asymmetry, and Baryon Asymmetry of the Universe. *Pisma Zh. Eksp. Teor. Fiz.*, 5:32–35, 1967. doi: 10.1070/PU1991v034n05ABEH002497. [Usp. Fiz. Nauk161,61(1991)].

[26] R. D. Peccei. The Strong *CP* Problem and Axions. page 3–17, 2008. ISSN 0075-8450. doi: 10.1007/978-3-540-73518-2_1.

[27] C. A. Baker et al. Improved Experimental Limit on the Electric Dipole Moment of the Neutron. *Phys. Rev. Lett.*, 97:131801, Sep 2006. doi: 10.1103/PhysRevLett.97.131801.

[28] G. R. Farrar and M. E. Shaposhnikov. Baryon asymmetry of the universe in the standard electroweak theory. *Phys. Rev.*, D50:774, 1994. doi: 10.1103/PhysRevD.50.774.

[29] P. Huet and E. Sather. Electroweak baryogenesis and standard model *CP* violation. *Phys. Rev.*, D51:379–394, 1995. doi: 10.1103/PhysRevD.51.379.

[30] M. B. Gavela, P. Hernandez, J. Orloff, and O. Pene. Standard model *CP* violation and baryon asymmetry. *Mod. Phys. Lett.*, A9:795–810, 1994. doi: 10.1142/S0217732394000629.

[31] P.A. Zyla et al. Review of Particle Physics. *Progress of Theoretical and Experimental Physics*, 2020(8):083C01, 2020. doi: 10.1093/ptep/ptaa104.

[32] L. Evans. The large hadron collider. *New Journal of Physics*, 9(9):335, 2007. doi: 10.1088/1367-2630/9/9/335.

[33] Y. Fukuda et al. Evidence for oscillation of atmospheric neutrinos. *Phys. Rev. Lett.*, 81:1562–1567, 1998. doi: 10.1103/PhysRevLett.81.1562.

[34] Ikaros I. Y. Bigi. *CP* violation: An Essential mystery in nature's grand design. *Surveys High Energ. Phys.*, 12:269–336, 1998. doi: 10.1080/01422419808228861. [Proc. Int. Sch. Phys. Fermi137,451(1998)].

[35] M. Bona et al. The 2004 UTfit collaboration report on the status of the unitarity triangle in the standard model. *JHEP*, 07:028, 2005. doi: 10.1088/1126-6708/2005/07/028.

[36] M. Bona et al. Model-independent constraints on $\Delta F = 2$ operators and the scale of new physics. *JHEP*, 03:049, 2008. doi: 10.1088/1126-6708/2008/03/049.

[37] L. Wolfenstein. Parametrization of the Kobayashi-Maskawa Matrix. *Phys. Rev. Lett.*, 51:1945, 1983. doi: 10.1103/PhysRevLett.51.1945.

[38] Y. Grossman, Y. Nir, and G. Perez. Testing New Indirect *CP* Violation. *Physical Review Letters*, 103(7), Aug 2009. ISSN 1079-7114. doi: 10.1103/physrevlett.103.071602.

[39] A. L. Kagan and M. D. Sokoloff. Indirect *CP* violation and implications for D^0-$\overline{D}^0$ and B_s^0-$\overline{B}_s^0$ mixing. *Physical Review D*, 80(7), Oct 2009. ISSN 1550-2368. doi: 10.1103/physrevd.80.076008.

[40] V. Weisskopf and E. Wigner. Berechnung der natürlichen linienbreite auf grund der diracschen lichttheorie. *Physical Review DZeitschrift für Physik*, 63, 1930. ISSN 0044-3328. doi: 10.1007/BF01336768.

[41] R. Aaij et al. Observation of the mass difference between neutral charm-meson eigenstates. *Phys. Rev. Lett.*, 127:111801, 2021. doi: 10.1103/PhysRevLett.127.111801.

[42] Y. S. Amhis et al. Averages of b-hadron, c-hadron, and τ-lepton properties as of 2018. *Eur. Phys. J.*, C81:226, 2021. doi: 10.1140/epjc/s10052-020-8156-7. Updated results and plots available at `https://hflav.web.cern.ch/`.

[43] A. J. Buras. *Gauge Theory of Weak Decays: The Standard Model and the Expedition to New Physics Summits*. Cambridge University Press, 2020. doi: 10.1017/9781139524100.

[44] R. Aaij et al. Observation of $D^0 - \overline{D}^0$ oscillations. *Phys. Rev. Lett.*, 110(10):101802, 2013. doi: 10.1103/PhysRevLett.110.101802.

[45] A. L. Kagan and L. Silvestrini. Dispersive and absorptive *CP* violation in $D^0 - \overline{D^0}$ mixing. *Phys. Rev. D*, 103(5):053008, 2021. doi: 10.1103/PhysRevD.103.053008.

[46] R. Aaij et al. Search for time-dependent *CP* violation in $D^0 \to K^+K^-$ and $D^0 \to \pi^+\pi^-$ decays. *Phys. Rev.*, D104:072010, 2021. doi: 10.1103/PhysRevD.104.072010.

[47] R. Aaij et al. Measurement of the charm mixing parameter $y_{CP} - y_{CP}^{K\pi}$ using two-body D^0 meson decays. 2021. submitted to PRD. arXiv: 2202.09106.

[48] Y. Grossman and S. Schacht. The emergence of the $\Delta U = 0$ rule in charm physics. *Journal of High Energy Physics*, 2019(7), Jul 2019. ISSN 1029-8479. doi: 10.1007/jhep07(2019)020.

[49] J. Brod, Y. Grossman, A. L. Kagan, and J. Zupan. A consistent picture for large penguins in $D^0 \to \pi^+\pi^-$, K^+K^-. *Journal of High Energy Physics*, 2012(10), Oct 2012. ISSN 1029-8479. doi: 10.1007/jhep10(2012)161.

[50] Y. Grossman, A. L. Kagan, and Y. Nir. New physics and *CP* violation in singly Cabibbo suppressed D decays. *Phys. Rev. D*, 75:036008, Feb 2007. doi: 10.1103/PhysRevD.75.036008.

[51] H. Li, C. Lu, and F. Yu. Branching ratios and direct *CP* asymmetries in $D \to PP$ decays. *Phys. Rev. D*, 86:036012, Aug 2012. doi: 10.1103/PhysRevD.86.036012.

[52] H. Cheng and C. Chiang. Direct *CP* violation in two-body hadronic charmed meson decays. *Phys. Rev. D*, 85:034036, Feb 2012. doi: 10.1103/PhysRevD.85.034036.

[53] A. Khodjamirian and A. A. Petrov. Direct *CP* asymmetry in $D \to \pi^-\pi^+$ and $D \to K^-K^+$ in QCD-based approach. *Physics Letters B*, 774:235–242, Nov 2017. ISSN 0370-2693. doi: 10.1016/j.physletb.2017.09.070.

[54] M. Golden and B. Grinstein. Enhanced *CP* violations in hadronic charm decays. *Physics Letters B*, 222(3):501–506, 1989. ISSN 0370-2693. doi: 10.1016/0370-2693(89)90353-5.

[55] F. Buccella, A. Paul, and P. Santorelli. $SU(3)_F$ breaking through final state interactions and *CP* asymmetries in $D \to PP$ decays. *Phys. Rev. D*, 99:113001, Jun 2019. doi: 10.1103/PhysRevD.99.113001.

[56] D. Pirtskhalava and P. Uttayarat. *CP* violation and flavor SU(3) breaking in D-meson decays. *Physics Letters B*, 712(1):81–86, 2012. ISSN 0370-2693. doi: 10.1016/j.physletb.2012.04.039.

[57] T. Feldmann, S. Nandi, and A. Soni. Repercussions of flavour symmetry breaking on *CP* violation in D-meson decays. *Journal of High Energy Physics*, 2012(6), Jun 2012. ISSN 1029-8479. doi: 10.1007/jhep06(2012)007.

[58] G. Hiller, M. Jung, and S. Schacht. $SU(3)$-flavor anatomy of nonleptonic charm decays. *Phys. Rev. D*, 87:014024, Jan 2013. doi: 10.1103/PhysRevD.87.014024.

[59] Y. Grossman and D. J. Robinson. SU(3) sum rules for charm decay. *Journal of High Energy Physics*, 2013(4), Apr 2013. ISSN 1029-8479. doi: 10.1007/jhep04(2013)067.

[60] S. Müller, U. Nierste, and S. Schacht. Sum Rules of Charm *CP* Asymmetries beyond the $\mathrm{SU}(3)_F$ Limit. *Phys. Rev. Lett.*, 115:251802, Dec 2015. doi: 10.1103/PhysRevLett.115.251802.

[61] F. Buccella, M. Lusignoli, G. Miele, A. Pugliese, and P. Santorelli. Nonleptonic weak decays of charmed mesons. *Phys. Rev. D*, 51:3478–3486, Apr 1995. doi: 10.1103/PhysRevD.51.3478.

[62] E. Franco, S. Mishima, and L. Silvestrini. The Standard Model confronts *CP* violation in $D^0 \to \pi^+\pi^-$ – and $D^0 \to K^+K^-$. *Journal of High Energy Physics*, 2012(5), May 2012. ISSN 1029-8479. doi: 10.1007/jhep05(2012)140.

[63] R. Aaij et al. Measurement of *CP* asymmetry in $D^0 \to K^-K^+$ and $D^0 \to \pi^-\pi^+$ decays. *JHEP*, 07:041, 2014. doi: 10.1007/JHEP07(2014)041.

[64] R. Aaij et al. Measurement of *CP* asymmetry in $D^0 \to K^+K^-$ decays. *Phys. Lett.*, B767:177, 2017. doi: 10.1016/j.physletb.2017.01.061.

[65] R. Aaij et al. Evidence for *CP* violation in time-integrated $D^0 \to h^-h^+$ decay rates. *Phys. Rev. Lett.*, 108:111602, 2012. doi: 10.1103/PhysRevLett.108.111602.

[66] Amarjit Soni. Resonance enhancement of Charm *CP*, 2019. doi: 10.48550/arXiv.1905.00907.

[67] A. Dery, Y. Grossman, S. Schacht, and A Soffer. Probing the $\Delta U = 0$ Rule in Three Body Charm Decays, 2021. doi: 10.48550/arXiv.2101.02560.

[68] H. Cheng and C. Chiang. Revisiting *CP* violation in $D \to PP$ and VP decays. *Phys. Rev. D*, 100:093002, Nov 2019. doi: 10.1103/PhysRevD.100.093002.

[69] D. Wang, C. Jia, and F. Yu. A self-consistent framework of topological amplitude and its SU(N) decomposition. *Journal of High Energy Physics*, 2021(9), Sep 2021. ISSN 1029-8479. doi: 10.1007/jhep09(2021)126.

[70] D. Atwood and A. Soni. Searching for the origin of *CP* violation in Cabibbo-suppressed D-meson decays. *Progress of Theoretical and Experimental Physics*, 2013(9), 09 2013. ISSN 2050-3911. doi: 10.1093/ptep/ptt065.

[71] M. Chala, A. Lenz, A. V. Rusov, and J. Scholtz. ΔA_{CP} within the Standard Model and beyond. *Journal of High Energy Physics*, 2019(7), Jul 2019. ISSN 1029-8479. doi: 10.1007/jhep07(2019)161.

[72] A. Dery and Y. Nir. Implications of the LHCb discovery of *CP* violation in charm decays. *Journal of High Energy Physics*, 2019(12), Dec 2019. ISSN 1029-8479. doi: 10.1007/jhep12(2019)104.

[73] R. Bause, H. Gisbert, M. Golz, and G. Hiller. Exploiting *CP* asymmetries in rare charm decays. *Phys. Rev. D*, 101:115006, Jun 2020. doi: 10.1103/PhysRevD.101.115006.

[74] LHCb Collaboration. Physics case for an LHCb Upgrade II - Opportunities in flavour physics, and beyond, in the HL-LHC era. Technical report, CERN, Geneva, Aug 2018. URL `https://cds.cern.ch/record/2636441`. ISBN 978-92-9083-494-6.

[75] R. Aaij et al. Measurement of the difference of time-integrated *CP* asymmetries in $D^0 \to K^-K^+$ and $D^0 \to \pi^-\pi^+$ decays. *Phys. Rev. Lett.*, 116:191601, 2016. doi: 10.1103/PhysRevLett.116.191601.

[76] A. A. Alves, Jr. et al. The LHCb Detector at the LHC. *JINST*, 3:S08005, 2008. doi: 10.1088/1748-0221/3/08/S08005.

[77] R. Aaij et al. Measurement of the b-quark production cross section in 7 and 13 tev pp collisions. *Phys. Rev. Lett.*, 118:052002, Feb 2017. doi: 10.1103/PhysRevLett.118.052002.

[78] R. Aaij et al. Measurements of prompt charm production cross-sections in pp collisions at $\sqrt{s} = 13$ TeV. *JHEP*, 03:159, 2016. doi: 10.1007/JHEP03(2016)159, 10.1007/JHEP09(2016)013, 10.1007/JHEP05(2017)074. [Erratum: JHEP05,074(2017)].

[79] G. Arnison et al. Experimental observation of isolated large transverse energy electrons with associated missing energy at s=540 GeV. *Physics Letters B*, 122(1): 103–116, 1983. ISSN 0370-2693. doi: 10.1016/0370-2693(83)91177-2.

[80] G. Arnison et al. Experimental observation of lepton pairs of invariant mass around 95 GeV/c2 at the CERN SPS collider. *Physics Letters B*, 126(5):398–410, 1983. ISSN 0370-2693. doi: 10.1016/0370-2693(83)90188-0.

[81] P. R. Barbosa-Marinho et al. *LHCb VELO (VErtex LOcator): Technical Design Report*. Technical Design Report LHCb. CERN, Geneva, 2001. URL `http://cds.cern.ch/record/504321`.

[82] R. Antunes-Nobrega et al. *LHCb reoptimized detector design and performance: Technical Design Report*. Technical Design Report LHCb. CERN, Geneva, 2003. URL `https://cds.cern.ch/record/630827`.

[83] Silicon Tracker UZH group. Lhcb silicon tracker - material for publications. URL `http://lhcb.physik.uzh.ch/ST/public/material/index.php`.

[84] P. R. Barbosa-Marinho et al. *LHCb inner tracker: Technical Design Report*. Technical Design Report LHCb. CERN, Geneva, 2002. URL `https://cds.cern.ch/record/582793`.

[85] R. Arink et al. Performance of the LHCb Outer Tracker. *JINST*, 9(01):P01002, 2014. doi: 10.1088/1748-0221/9/01/P01002.

[86] R. Aaij et al. LHCb Detector Performance. *Int. J. Mod. Phys.*, A30(07):1530022, 2015. doi: 10.1142/S0217751X15300227.

[87] L. Dufour. High-precision measurements of charge asymmetries at LHCb, 2019. CERN-THESIS-2019-281.

[88] A. Papanestis and C. D'Ambrosio. Performance of the LHCb RICH detectors during the LHC Run II. Technical Report LHCB-PUB-2017-012. CERN-LHCb-PUB-2017-012, CERN, Geneva, Mar 2017. URL `https://cds.cern.ch/record/2255885`.

[89] C. Lippmann. Particle identification. *Nucl. Instrum. Meth.*, A666:148–172, 2012. doi: 10.1016/j.nima.2011.03.009.

[90] S. Amato et al. *LHCb calorimeters: Technical Design Report*. Technical Design Report LHCb. CERN, Geneva, 2000. URL `https://cds.cern.ch/record/494264`.

[91] A. A. Alves, Jr. et al. Performance of the LHCb muon system. *JINST*, 8:P02022, 2013. doi: 10.1088/1748-0221/8/02/P02022.

[92] R. Aaij et al. Design and performance of the LHCb trigger and full real-time reconstruction in Run 2 of the LHC. Performance of the LHCb trigger and full real-time reconstruction in Run 2 of the LHC. *JINST*, 14:P04013. 43 p, Dec 2018. doi: 10.1088/1748-0221/14/04/P04013. URL `https://cds.cern.ch/record/2652801`.

[93] S. Benson, V. V. Gligorov, M. A. Vesterinen, and J. M. Williams. The LHCb Turbo Stream. *J. Phys. Conf. Ser.*, 664(8):082004, 2015. doi: 10.1088/1742-6596/664/8/082004.

[94] LHCb Collaboration. Letter of Intent for the LHCb Upgrade. Technical report, CERN, Geneva, Mar 2011. URL `https://cds.cern.ch/record/1333091`.

[95] LHCb Collaboration. LHCb VELO Upgrade Technical Design Report. Technical report, Nov 2013. URL `https://cds.cern.ch/record/1624070`.

[96] LHCb Collaboration. LHCb Tracker Upgrade Technical Design Report. Technical report, Feb 2014. URL `https://cds.cern.ch/record/1647400`.

[97] O. Aberle et al. *High-Luminosity Large Hadron Collider (HL-LHC): Technical design report*. CERN Yellow Reports: Monographs. CERN, Geneva, 2020. doi: 10.23731/CYRM-2020-0010. URL `https://cds.cern.ch/record/2749422`.

[98] J. Albrecht, M. J. Charles, L. Dufour, M. D. Needham, C. Parkes, G. Passaleva, A. Schopper, E. Thomas, V. Vagnoni, M. R. J. Williams, and G. Wilkinson. Luminosity scenarios for LHCb Upgrade II. Technical report, CERN, Geneva, Jan 2019. URL `https://cds.cern.ch/record/2653011`.

[99] N. Harnew et al. Status of the TORCH time-of-flight project. *Nucl. Instrum. Meth., A*, 952:161692. 4 p, Dec 2018. doi: 10.1016/j.nima.2018.12.007. URL http://cds.cern.ch/record/2706078.

[100] R. Aaij et al. Precise determination of the B_s^0–$\overline{B}_s^0$ oscillation frequency. Precise determination of the B0s-B0sbar oscillation frequency. *Nature Phys.*, 18:1–5. 20 p, Apr 2021. doi: 10.1038/s41567-021-01394-x. URL https://cds.cern.ch/record/2764338.

[101] R. Aaij et al. Test of lepton universality in beauty-quark decays. 2021. to appear in Nature Physics. arXiv: 2103.11769.

[102] R. Aaij et al. Observation of the Doubly Charmed Baryon Ξ_{cc}^{++}. *Phys. Rev. Lett.*, 119:112001, Sep 2017. doi: 10.1103/PhysRevLett.119.112001.

[103] R. Aaij et al. Search for the doubly charmed baryon Ξ_{cc}^{+}. 2019. submitted to Science China Physics, Mechanics & Astronomy. arXiv: 1909.12273.

[104] K. Akiba et al. Considerations for the VELO detector at the LHCb Upgrade II. Technical report, CERN, Geneva, Jan 2022. URL https://cds.cern.ch/record/2800144.

[105] A. Lai et al. First results of the timespot project on developments on fast sensors for future vertex detectors. *Nuclear Instruments and Methods in Physics Research Section A: Accelerators, Spectrometers, Detectors and Associated Equipment*, 981:164491, 2020. ISSN 0168-9002. doi: https://doi.org/10.1016/j.nima.2020.164491. URL https://www.sciencedirect.com/science/article/pii/S0168900220308883.

[106] R. Aaij et al. Measurement of the $D^{\pm}$ production asymmetry in 7 TeVpp collisions. *Phys. Lett.*, B718:902, 2013. doi: 10.1016/j.physletb.2012.11.038.

[107] W. D. Hulsbergen. Decay chain fitting with a Kalman filter. *Nucl. Instrum. Meth.*, A552:566–575, 2005. doi: 10.1016/j.nima.2005.06.078.

[108] M Needham. Momentum scale calibration using resonances. Technical report, CERN, Geneva, Jul 2008. URL https://cds.cern.ch/record/1115072. LHCb-2008-037.

[109] N. L. Johnson. Systems of frequency curves generated by methods of translation. *Biometrika*, 36:149–176, 1949. doi: 10.1093/biomet/36.1-2.149.

[110] M. Pivk and F. R. Le Diberder. sPlot: A statistical tool to unfold data distributions. *Nucl. Instrum. Meth.*, A555:356–369, 2005. doi: 10.1016/j.nima.2005.08.106.

[111] W. Fetscher et al. Regeneration of arbitrary coherent neutral kaon states: A new method for measuring the K0 anti-K0 forward scattering amplitude. *Z. Phys. C*, 72:543–547, 1996. doi: 10.1007/s002880050277.

[112] A. Gsponer et al. Precise Coherent K_S Regeneration Amplitudes for C, Al, Cu, SN and Pb Nuclei From 20-GeV/c to 140-GeV/c and Their Interpretation. *Phys. Rev. Lett.*, 42:13, 1979. doi: 10.1103/PhysRevLett.42.13.

[113] R. A. Briere and B. Winstein. Determining the phase of a strong scattering amplitude from its momentum dependence to better than 1-degree: The Example of Kaon regeneration. *Phys. Rev. Lett.*, 75:402–405, 1995. doi: 10.1103/PhysRevLett.75.402.

[114] S. Stahl. Measurement of *CP* asymmetry in muon-tagged $D^0 \to K^-K^+$ and $D^0 \to \pi^-\pi^+$ decays at LHCb. Jun 2014. CERN-THESIS-2014-274.

[115] An introduction to PYTHIA 8.2. *Computer Physics Communications*, 191:159–177, 2015. ISSN 0010-4655. doi: 10.1016/j.cpc.2015.01.024.

[116] G. Barrand et al. GAUDI: The software architecture and framework for building LHCb data processing applications. 2000. doi: 10.1016/S0010-4655(01)00254-5. URL `https://cds.cern.ch/record/467678`.

[117] R. Aaij et al. Measurement of $D_s^\pm$ production asymmetry in pp collisions at $\sqrt{s}$ =7 and 8 TeV. *JHEP*, 08:008, 2018. doi: 10.1007/JHEP08(2018)008.

[118] R. Aaij et al. Measurement of b-hadron fractions in 13 TeVpp collisions. *Phys. Rev.*, D101:031102(R), 2019. doi: 10.1103/PhysRevD.100.031102.

[119] G. A. Cowan, D. C. Craik, and M. D. Needham. RapidSim: an application for the fast simulation of heavy-quark hadron decays. *Comput. Phys. Commun.*, 214: 239–246, 2017. doi: 10.1016/j.cpc.2017.01.029.

[120] L. Anderlini et al. The PIDCalib package. Technical report, CERN, Geneva, Jul 2016. URL `https://cds.cern.ch/record/2202412`.

[121] A. Davis et al. Measurement of the $K^-\pi^+$ two-track detection asymmetry in Run 2 using the Turbo stream. LHCb-INT-2017-023.

[122] L. Lyons, D. Gibaut, and P. Clifford. How to combine correlated estimates of a single physical quantity. *Nucl. Instrum. Meth.*, A270:110, 1988. doi: 10.1016/0168-9002(88)90018-6.

[123] E. Gersabeck et al. Search for time-integrated *CP* violation in $D^0 \to h^-h^+$modes using self-tagged $DD^{*\pm} \to D^0(h^-h^+)\pi$ decays with 3 fb^{-1}. Aug 2014. LHCb-ANA-2014-075.

[124] F. Betti et al. Observation of *CP* violation in charm decays. Apr 2018. LHCb-ANA-2018-016.

[125] R. Aaij et al. Updated measurement of decay-time-dependent *CP* asymmetries in $D^0 \to K^+K^-$ and $D^0 \to \pi^+\pi^-$ decays. *Phys. Rev.*, D101:012005, 2020. doi: 10.1103/PhysRevD.101.012005.

[126] R. Aaij et al. Measurement of the *CP* violation parameter A_Γ in $D^0 \to K^+K^-$ and $D^0 \to \pi^+\pi^-$ decays. *Phys. Rev. Lett.*, 118:261803, 2017. doi: 10.1103/PhysRevLett.118.261803.

[127] R. Aaij et al. Measurement of indirect *CP* asymmetries in $D^0 \to K^-K^+$ and $D^0 \to \pi^-\pi^+$ decays using semileptonic B decays. *JHEP*, 04:043, 2015. doi: 10.1007/JHEP04(2015)043.

[128] G. Cowan. Error analysis with weighted events. https://www.pp.rhul.ac.uk/∼cowan/stat/notes/errors_with_weights.pdf.

[129] LHCb Collaboration. Expression of Interest for a Phase-II LHCb Upgrade: Opportunities in flavour physics, and beyond, in the HL-LHC era. Technical report, CERN, Geneva, Feb 2017. URL `https://cds.cern.ch/record/2244311`.

[130] T. Bird et al. VP Simulation and Track Reconstruction. Technical report, CERN, Geneva, Oct 2013. URL `https://cds.cern.ch/record/1620453`.

[131] M. Clemencic et al. The LHCb Simulation Application, Gauss: Design, Evolution and Experience. Oct 2010. URL `https://cds.cern.ch/record/1302049`.

[132] P. V. Vavilov. Ionization losses of high-energy heavy particles. *Sov. Phys. JETP*, 5:749–751, 1957.

[133] L. Landau. On the energy loss of fast particles by ionization. *J. Phys. (USSR)*, 8: 201–205, 1944.

[134] H. Bichsel. Straggling in thin silicon detectors. *Rev. Mod. Phys.*, 60:663–699, Jul 1988. doi: 10.1103/RevModPhys.60.663.

[135] H. A. Bethe. Molière's theory of multiple scattering. *Phys. Rev.*, 89:1256–1266, Mar 1953. doi: 10.1103/PhysRev.89.1256.

[136] Gerald R. Lynch and Orin I. Dahl. Approximations to multiple Coulomb scattering. *Nucl. Instrum. Meth. B*, 58:6–10, 1991. doi: 10.1016/0168-583X(91)95671-Y.

[137] F. Lazzari et al. Real-time cluster finding for LHCb silicon pixel VELO detector using FPGA. *J. Phys.: Conf. Ser.*, 1525:012044. 6 p, 2020. doi: 10.1088/1742-6596/1525/1/012044. URL `https://cds.cern.ch/record/2744309`.

[138] Lai, A. and others. TimeSpot Project - The Challenge. URL `https://web.infn.it/timespot/index.php`.

[139] M. Frank et al. DD4hep: A Detector Description Toolkit for High Energy Physics Experiments. *J. Phys. Conf. Ser.*, 513:022010, 2014. doi: 10.1088/1742-6596/513/2/022010.

[140] M. Petruzzo. A 4D real-time tracking device for the LHCb Upgrade II, Apr 2019. CERN-THESIS-2019-076.

Acknowledgements

I would like to use this small space to express my gratitude to all the people who have contributed in one way or another to this thesis. The past years have been quite complicated, also as a consequence of the pandemic that interrupted most of human interaction and impeded efficient work. However, this didn't stop my passion for the reasearch.

First of all, I want to thank my supervisor Angelo Carbone for the support he gave me in starting new projects and, more importantly, for the day and night assistance. I also want to aknowledge the LHCB-Bologna group, in particular Daniele Manuzzi, Stefano Perazzini, Fabio Ferrari, Lorenzo Capriotti and Vincenzo Vagnoni for the nice time spent together among physics discussions, speculations, and a few beers as well.

The measurement of $\mathcal{A}^{CP}(K^-K^+)$ wouldn't be possible without the help of the other proponents, namely Laurent Dufour, Federico Betti and Sascha Stahl. In particular, I want to thank Laurent for the smart suggestions, Federico for the careful understanding and Sascha for the 360° view of the LHCb experiment that brought valuable comments to further improve the content of this document. Inestimable advices have also been addressed during the internal review of the LHCb collaboration, in particular by the people belonging to the Charm working group. It is worth to mention Michael J. Morello, Tommaso Pajero, Lars Eklund, Sneha Malde and Michael Alexander for their deep questioning on possible neglected systematic uncertainties.

In the last years, I also enjoyed a lot the time spent in the development of new detectors. Thus, I want to thank Nicola Neri, Marco Petruzzo, Stefania Vecchi and Benedetto Siddi for the help in studying the perfomance a future Vertex-Locator in the Upgrade-II scenario, and the people involved in the Time-Spot project for the realisation of such a nice sensor. Finally, I also want to thank the LHCb-PLUME group I joined while I was based at CERN for the commissioning of the sub-detector. Thanks for the patience and entuthiasm in explaining the various details.

Thanks also to the people I met as an indirect consequence of my PhD studies. Some of them was already in my history, others were completely new to me, but they all gave me something beautiful and unexpected. In particular, I want to thank Alessandra, Carlo and Michela. Grazie a Luisa ed Arianna per essere state così speciali. Ringrazio anche Catherine e Claudia, Ilaria, Pio, Sabri e Marty che sebbene avessero le loro sfide importanti da superare non si sono mai tirate indietro. Grazie a Michele che in un modo

o nell'altro è sempre presente in ogni mia decisione. Infine, grazie alla mia famiglia: non ce lo diciamo spesso ma vi voglio bene!